UNIVERSIDAD POLITÉCNICA DE MADRID
Escuela Técnica Superior de Ingenieros Industriales

Control a Multi-Ducted Fan UAV Using Thrust Vectoring

D O C T O R A L T H E S I S

Submitted for the degree of Doctor by:

Mohammad Sadeq Ale Isaac Khoueini
M.Sc. in Aerospace Engineering

Madrid, 2024

UNIVERSIDAD POLITÉCNICA DE MADRID
Escuela Técnica Superior de Ingenieros Industriales

Doctoral Degree in Automatic Control and Robotics

Control a Multi-Ducted Fan UAV Using Thrust Vectoring

D O C T O R A L T H E S I S

Submitted for the degree of Doctor by:

Mohammad Sadeq Ale Isaac Khoueini
M.Sc. in Aerospace Engineering

Under the supervision of:
Prof. Pascual Campoy Cervera
Dr. Ahmed Refaat Ragab

Madrid, 2024

Title: Control a Multi-Ducted Fan UAV Using Thrust Vectoring

Author: Mohammad Sadeq Ale Isaac Khoueini

Doctoral Programme: Automatic Control and Robotics

Thesis Supervision:

Prof. Pascual Campoy Cervera, Full Professor, Responsible for the Computer Vision and Aerial Robotics Group, Centre for Automation and Robotics (CAR), Universidad Politécnica de Madrid (UPM-CSIC), 28006 Madrid, Spain.(Supervisor)

Dr. Ahmed Refaat Ragab, Postdoctoral Researcher at Department of Electrical Engineering, University Carlos III of Madrid, 28919 Leganés, Spain and Associate Professor at Department of Network, Faculty of Information Systems and Computer Science, October 6 University, Giza 12511, Egypt.

External Reviewers:

Thesis Defense Committee:

Thesis Defense Date:

I would like to express my gratitude to all those who supported me throughout this journey.
To my family, whose unwavering love and encouragement have been my anchor.
To my mentors, whose guidance and wisdom have illuminated my path.
To my friends, who stood by me with laughter and camaraderie.
This endeavor wouldn't have been possible without your collective kindness and belief in me.
-Sadeq

Acknowledgement

I would like to express my sincere gratitude to my supervisor, Prof. Pascual Campoy, and my advisor, Dr. Ahmed Refaat Ragab, for their continuous support, patience, and guidance throughout my PhD journey. Their insightful feedback and encouragement have been invaluable.

I am also grateful to my committee members, Prof. Manual Ferre and Prof. Martin Molina, for their constructive comments and suggestions, which greatly improved the quality of my research.

I am thankful for the financial support provided by Drone Hopper S.L. and the resources provided by the Computer Vision and Aerial Robotics Group, Centre for Automation and Robotics (CAR) at Universidad Politécnica de Madrid.

My deepest thanks to my colleagues and friends in the Robotics Lab for their collaboration and stimulating discussions, as well as my colleagues at the company for their support and innovative ideas. I would particularly like to thank Dr. Hriday Bavle, Dr. Adrián Carrio, and Marco Andrés Luna for their assistance with data analysis at the university, and Pablo Flores Peña for his financial support at the company.

I am deeply grateful to my family, especially my parents, for their unwavering support and encouragement.

Lastly, I want to thank everyone who has contributed to my journey in one way or another. This accomplishment would not have been possible without all of them.

Abstract

Unmanned aerial vehicles (UAVs) have emerged as versatile flying systems, finding applications in various sectors, ranging from surveillance and firefighting to reconnaissance and cargo transport. The classification of UAVs spans micro to full-scale, depending on their weight, including payloads. Of particular interest in this thesis are heavy UAVs, as they are capable of carrying substantial payloads and are integral to operations such as crop spraying, long-range monitoring, and portable communication. Achieving extended flight endurance, a critical requirement for many missions has led to the prominence of thermal engines among propulsion systems.

In contradiction, thermal engines introduce mechanical challenges, chief among them being latency in response. Addressing this issue requires innovative control algorithms, especially as conventional control methods often rely on engine propellers for both position and attitude control. The use of distinct actuators to regulate the system introduces redundancy, enhancing stability and safety margins. As a result, the control of heavy UAVs entails multiple layers of complexity.

This comprehensive Ph.D. thesis, comprising three Q1 journal papers, delves into groundbreaking control methodologies, with a specific emphasis on the implementation of thrust vectoring through flap vanes. The overarching goal of this research is to address inherent attitude instabilities, streamline mechanical intricacies, and significantly augment flight endurance, with a primary focus on the domain of heavy UAVs.

Additionally, the thesis embarks on an exploration of the evolution of UAVs from military to civilian applications and introduces the concept of the Unmanned Aerial System (UAS), encompassing the entire ecosystem, including UAVs, Ground Control Stations (GCS), communication systems, and networking components.

Motivated by the "WILD HOPPER" project, which seeks to design a heavy-duty UAV for firefighting operations, the author's role is to develop a suitable control algorithm. The "WILD HOPPER" platform offers unique advantages, including precise payload release capabilities and the ability to operate effectively during nighttime missions, complementing existing aerial firefighting methods.

The thesis clearly defines the problem statement, highlighting key design steps. These steps encompass the investigation of potential control solutions, a comprehensive analysis of aerodynamic interactions, the development of a mathematical model, and a deep dive into the challenges associated with flap vanes under various operating conditions.

The proposed control solution is structured into three primary levels: attitude control and position control, concentrating on the vertical and attitude parameters. It capitalizes on the main propellers to generate the vertical thrust and flap vanes to maintain the system stability and augment flight endurance. The controller's functionality is further fortified through the incorporation of redundant actuation mechanisms.

The research objectives are ambitious, aiming to contribute significantly to the advancement of control methodologies for heavy multi-ducted fan UAVs. These objectives encompass the development of a comprehensive mathematical model, the formulation of innovative control strategies, and the validation of these control techniques through rigorous simulations and real-world experiments.

In conclusion, this Ph.D. thesis is dedicated to advancing the control of multi-ducted fan UAVs through thrust vectoring. The research seeks to address the unique challenges posed by heavy UAVs, with a primary focus on stability improvement and prolonged flight endurance. The proposed control solutions and innovative methodologies hold the promise of making substantial contributions to the field of UAV control.

Resumen

Los vehículos aéreos no tripulados (UAVs) han emergido como sistemas voladores versátiles, encontrando aplicaciones en varios sectores, desde vigilancia y extinción de incendios hasta reconocimiento y transporte de carga. La clasificación de los UAVs abarca desde micro hasta escala completa, dependiendo de su peso, incluyendo cargas útiles. De particular interés en esta tesis son los UAV pesados, ya que son capaces de transportar cargas sustanciales y son fundamentales para operaciones como la pulverización de cultivos, monitoreo a larga distancia y comunicación portátil. Lograr una resistencia de vuelo prolongada, un requisito crítico para muchas misiones, ha llevado a la prominencia de los motores térmicos entre los sistemas de propulsión.

Por otro lado, los motores térmicos introducen desafíos mecánicos, siendo uno de los más destacados la latencia en la respuesta. Abordar este problema requiere algoritmos de control innovadores, especialmente porque los métodos de control convencionales a menudo dependen de las hélices del motor tanto para el control de la posición como de la actitud. El uso de actuadores distintos para regular el sistema introduce redundancia, mejorando la estabilidad y los márgenes de seguridad. Como resultado, el control de UAV pesados implica múltiples capas de complejidad.

Esta tesis de doctorado integral, que comprende tres artículos de revistas Q1, profundiza en metodologías de control innovadoras, con un énfasis específico en la implementación de la vectorización de empuje a través de aletas. El objetivo general de esta investigación es abordar las inherentes inestabilidades de actitud, simplificar las complejidades mecánicas y aumentar significativamente la resistencia en vuelo, con un enfoque principal en el ámbito de los UAV pesados.

Además, la tesis emprende una exploración de la evolución de los UAV desde aplicaciones militares hasta aplicaciones civiles e introduce el concepto del Sistema de Aeronave No Tripulada (UAS), que abarca todo el ecosistema, incluyendo UAV, Estaciones de Control en Tierra (GCS), sistemas de comunicación y componentes de redes.

Motivado por el proyecto "WILD HOPPER", que busca diseñar un UAV resistente para operaciones de extinción de incendios, el autor tiene como tarea desarrollar un algoritmo de control adecuado. La plataforma "WILD HOPPER" ofrece ventajas únicas, que incluyen la capacidad de liberar cargas útiles con precisión y la capacidad de operar de manera efectiva en misiones nocturnas, complementando los métodos existentes de extinción de incendios aéreos.

La tesis define claramente el enunciado del problema, resaltando los pasos clave de diseño. Estos pasos comprenden la investigación de posibles soluciones de control, un análisis exhaustivo de las interacciones aerodinámicas, el desarrollo de un modelo matemático y una inmersión profunda en los desafíos asociados con las aletas en diversas condiciones de operación.

La solución de control propuesta se estructura en tres niveles principales: control de actitud, control de posición y control de trayectoria, centrándose en los parámetros verticales y de

actitud. Capitaliza las hélices principales para generar el empuje vertical y las aletas para mantener la estabilidad del sistema y aumentar la resistencia en vuelo. La funcionalidad del controlador se fortalece aún más mediante la incorporación de mecanismos de actuación redundantes.

Los objetivos de investigación son ambiciosos, con el propósito de contribuir significativamente al avance de las metodologías de control para UAVs pesados de múltiples motores. Estos objetivos incluyen el desarrollo de un modelo matemático completo, la formulación de estrategias de control innovadoras y la validación de estas técnicas de control mediante rigurosas simulaciones y experimentos en el mundo real.

En conclusión, esta tesis de doctorado se dedica a avanzar en el control de UAVs de múltiples motores a través de la vectorización de empuje. La investigación busca abordar los desafíos únicos planteados por los UAV pesados, con un enfoque principal en la mejora de la estabilidad y la resistencia en vuelo prolongada. Las soluciones de control propuestas y las metodologías innovadoras tienen el potencial de realizar.

Table of Contents

List of Figures

List of Tables

List of Publications

This thesis by compendium is based on the work and results presented in the following three **Q1** journal publications, which best summarize and highlight the scientific dissemination shown in Appendix C, hereby referenced in the text as **PI**, **PII**, **PIII**, and **PAd**:

PI Isaac, M.S.A., Ragab, A.R., Garcés, E.C., Luna, M.A., Peña, P.F., and Cervera, P.C. (2022). *Mathematical Modeling and Designing a Heavy Hybrid-Electric Quadcopter, Controlled by Flaps.* Journal of Unmanned Systems, 10(03), pp.241-253, doi:10.1142/S2301385022500133.

PAd Ale Isaac, M.S., Luna, M.A., Ragab, A.R., Ale Eshagh Khoeini, M.M., Kalra, R., Campoy, P., Flores Peña, P., and Molina, M. (2022). *Medium-Scale UAVs: A Practical Control System Considering Aerodynamics Analysis.* Journal of Drones, 6(9), p.244, doi:10.3390/drones6090244.

PII Ale Isaac, M.S., Ragab, A.R., Luna, M.A., Ale Eshagh Khoeini, M.M., and Campoy, P. (2023). *Thrust Vectoring Control for Heavy UAVs, Employing a Redundant Communication System.* Journal of Sensors, 23(12), p.5561, doi:10.3390/s23125561.

PIII Ale Isaac, Pena, P.F., Luna, M.A., Ragab, A.R., and Cervera, P.C. (2024). *Sensing and Control Integration for Thrust Vectoring in Heavy UAVs: Real-World Implementation and Performance Analysis.* Journal of Unmanned Systems, doi:10.1142/S2301385025500396.

Publication **PI** proposed a general mathematical model of a heavy multirotor, considering a specific geometry of a quadcopter with coaxial propellers. All of the internal and external forces and moments were determined to have a precise model. Then, a nonlinear robust control model was designed to stabilize the mentioned drone. To examine the performance of the controller, components were CAD modeled and analyzed through the simulation in the MATLAB Simscape, which contains dynamic space for 3D platforms. The main control terms of this paper were summarized in the controller surfaces. Once the system was supposed to be stabilized only by Flap vanes, then by Electric Ducted Fans (EFDs), and finally, using both. Eventually, a real platform was designed, called Duty-Hopper to be analyzed as a real-world model further.

Publication **PAd** continued the control issue of heavy drones using EDFs for a different platform and investigated the possibility of carrying heavy payloads of liquid and solid types. This latter was surveyed in a collaborative paper prior to work Ragab et al., 2021, and the results were used to model a real but smaller model and examine the controller efficiency. Also, some aerodynamic analyses were conducted to smooth the exhaust vortices of the engines. Then, in order to conquer the instabilities that came from the liquid payload, an adaptive model reference controller (MRAC) was used to update the controller parameters, and a new simulation model was designed in Gazebo to utilize a better dynamic space model. Finally, simulation results were compared to practical results.

Publication **PII** continued the controller improvements in the final platform, which is a heavy hexa ducted fan. While, the aerodynamic effects of blade numbers and blade pitch angle were analyzed to perform a better design. Additionally, a sliding mode technique was used as the nonlinear controller to compensate for internal uncertainties that came from servos and external disturbances. Through this paper, the main controller surfaces were flap vanes, and the main purpose of choosing flaps was to maintain long flight autonomy using thermal engines. Eventually, through the results, the performance of a cascade PID controller was compared to the proposed robust method.

Publication **PIII** completed the enhancements to the controller on the WILD HOPPER platform through several real-world tests and refinement of the robust controller parameters. The main contribution of this paper was to integrate the improvements from previous studies and validate them through practical tests to optimize the controller's performance. Furthermore, this publication defined the standard terms and Technology Readiness Level (TRL) protocols for each project phase. The paper described the entire framework, detailing the progression from smaller-scale models to the final operational platform. It also examined the enhanced dynamic model designed to improve thrust generated by ducted fans. Based on the mathematical model of the duct and the improvements from prior research, the final parameters and terms were established to accurately calculate duct forces and moments used in the controller inputs. The final control loop was analyzed under various disturbances, affecting both internal and external loops, which correspond to the attitude and position control loops. Finally, the paper compared the performance of the refined controller to a cascade PID-tuned controller, demonstrating the effectiveness of the improvements.

In all publications **PI**, **PII**, **PIII**, and **PAd**, the author of this thesis was responsible for the analysis, design, implementation, testing, and validation of the techniques, as well as writing the papers' manuscripts. Also, the co-authors in each publication contributed magnificently to improving the theoretical design, as well as the implementation and revision of the manuscripts.

Abbreviations and Acronyms

AOI Angle of Incidence

ASMC Adaptive Sliding Mode Control

BFF Body-Fixed Frame

CAR Centre of Automation and Robotics

CLF Control Lyapunov Function

COG Centre of Gravity

COM Centre of Mass

COP Centre of Pressure

CVAR Computer Vision and Aerial Robotics Group

DF Ducted Fan

DCM Direction Cosine Matrix

DOD United States Department of Defense

DOF Degrees Of Freedom

DP Ducted Propeller

ECU Engine Control Unit

EDF Electric Ducted Fan

EFF Earth-Fixed Frame

EKF Extended Kalman Filter

GCS Ground Control Station

GPS Global Positioning System

GUI Graphical User Interface

H-UAS Heavy-Lift Unmanned Aerial System

IMAV International Mirco-Aerial Vehicle competition

IMU Inertial Measurement Unit

KF Kalman Filter

MDF Multi Ducted Fan

MIMO Multi Input Multi Output

MPC Model Predictive Control

MRAC Model Reference Adaptive Control

LQR Linear Quadratic Regulator

PD Proportional-Derivative

PID Proportional-Integral-Derivative

RPAV Remotely Piloted Aerial Vehicles

SDF Single Ducted Fan

SITL Software In The Loop

SMC Sliding Mode Control

SPR Strictly Positive Real

TDF Tandem Ducted Fan

TVC Thrust Vector Control

UAS Unmanned Aerial System

UAV Unmanned Aerial Vehicle

UKF Unscented Kalman Filter

UPM Universidad Politécnica de Madrid

UVCS Unmanned Vehicle Control System

XML Extensible Markup Language

Chapter 1

Introduction

The present Doctoral Thesis concentrates on several aspects of autonomous aerial vehicles, called Unmanned Aerial Vehicles (UAVs), including nonlinear control design for distinct control surfaces, aerodynamic improvements, thermal motor enhancements, simulation modeling, and implementation considerations. During the history of UAVs, especially Multi-Ducted Fans (MDFs), a few cases could be found in Thrust Vector Control (TVC) was successful; nonetheless, this method aims for high efficiency regarding flight autonomy. For the first time, TVC, using flap vanes, stabilized a heavy MDF, which carries heavy payloads and has a long flight endurance.

During the twentieth century, the concept of unmanned Aerial Vehicles (UAVs) or drones emerged as aircraft that operated without human pilots or crew members on board. Originally, UAV or Remotely Piloted Aerial Vehicles (RPAV) was coined and developed for military aviation, which became widely used to describe such aircraft. However, its application has since expanded beyond the military and into civilian domains. To encompass the complexities of the entire system, the terminology evolved from UAV to Unmanned Aerial System (UAS). The UAS concept incorporates not only the UAV itself but also the Ground Control Station (GCS), communication systems, and networking components LNC Prakash et al., 2023. The Federal Aviation Administration (FAA) and the United States Department of Defense (DOD) adopted the terms UAS and Remotely Piloted Aerial System (RPAS) in 2005 to outline their UAS roadmap until 2030 of the Secretary of Defense, 2005. UAVs can be operated remotely through human piloting or can possess varying degrees of autonomy with the assistance of an Autopilot (AP), ranging from semi-autonomous to fully autonomous capabilities Elmokadem and Savkin, 2021, Mohsan et al., 2023.

Additionally, a Ducted Fan (DF) or Ducted Propeller (DP) refers to a mechanical fan or propeller installed inside a cylindrical duct or shroud. This configuration, as studied in previous research Abrego et al., 2002, Ko et al., 2007, allows for the enhancements to create a Multiple Ducted Fan (MDF) system. The MDF system incorporates a coherent geometry that optimizes the arrangement of DFs to generate the necessary thrust force during flying missions. Depending on their installation direction, DFs can function as longitudinal or vertical thrusters. To meet specific output requirements, DFs undergo optimizations based on factors such as inlet arc shape, duct wall length, and outlet-to-inlet area ratio. These

considerations ensure the DFs are precisely designed for optimal performance and efficiency. The integration of DFs and the utilization of MDF systems contribute to advancements in aerospace engineering, enhancing thrust generation and maneuverability in various flight scenarios.

UAVs have garnered significant attention from researchers thanks to their wide-ranging applications and exceptional performance capabilities. These versatile aircraft have found extensive utility in both civil and military domains, delivering groundbreaking solutions while minimizing risks for operators. In the civil sector, UAVs have proved invaluable in aerial photogrammetry and videography, cultivation analysis and crop monitoring, firefighting, search and rescue operations, infrastructure inspection, and environmental monitoring. In the military realm, they have diverse applications such as surveillance and reconnaissance, target acquisition and object tracking, battlefield support, and combat operations González-deSantos, 2022. Furthermore, the emergence of Vertical Takeoff and Landing (VTOL) systems, particularly the promising Multi Ducted Fans (MDFs), has added another dimension to their attractiveness, offering enhanced agility, stability, and versatility for a wide range of applications. Specifically, heavy clusters of UAVs are spread in myriad applications such as firefighting, large package delivery, agricultural protection, passenger transportation, communicative portable stations, and military patrol. Attending such beneficial aerial systems in the industry requires high stability and safe flights, especially in the case of human carriage. Meanwhile, to satisfy the mentioned applications, long-range and high-endurance platforms will be aimed; consequently, heavy drones necessitate quite a lot of power to serve long missions.

UAVs can be classified based on various factors and their extensive usage. These classifications include weight-based, mission-based, flight endurance or range-based, payload-based, and more. Among these, the weight and payload capacity of UAVs plays a significant role in their categorization. According to research in Ale Isaac et al., 2023, Ale Isaac et al., 2024, UAVs are categorized as micro, small, medium, and large-scale platforms. In the European Union aviation safety regulations, weight classifications are defined as Class A1 (less than 900 g), Class A2 (less than 4 kg), Class A3 (less than 25 kg), and additional categories for weights exceeding 25 kg. Similarly, the global NATO-STANAG 4670 UAS category classifies UAVs as nanoscale (less than 250 g), microscale (less than 2 kg), small scale (less than 25 kg), medium scale (less than 150 kg), and large scales (more than 150 kg) Zeng et al., 2016, Castrillo et al., 2022. Denoting that larger UAVs offer the advantage of carrying heavier cargo payloads over longer distances, recent research and industries focused on such platforms. While mini-scale UAVs have considerable limitations in terms of flight endurance and payload capacity.

Furthermore, the concept of control in UAVs encompasses a comprehensive system that ensures the stability of an aircraft through a combination of software and hardware components. The design of controller systems can vary depending on the complexity of the drone, ranging from linear methods suitable for simpler drones to nonlinear and higher-order controllers tailored for more intricate aerial robotics. This concept is commonly referred to as the Unmanned Vehicle Control System (UVCS). Within the realm of UVCSs, conventional linear methods, such as feedback linearization and Linear Quadratic Regulator (LQR) focus on simplifying the problem by dividing it into multiple layers and employing Proportional Integral Derivative (PID) algorithms for control, which disregarding the missed characteristics of the system due

to linearizing, these controllers generally function acceptably. On the other hand, nonlinear approaches, including backstepping, dynamic inversion, and adaptive and robust controllers, encompass the entire dynamics of the vehicle and establish a nonlinear model to achieve stabilization.

1.1 Motivation

Throughout the history of aviation, Ducted Fans (DFs) have not been widely employed as thrust generators in conventional Vertical Take-Off Landing (VTOL) vehicles. This is primarily due to their inherent static and dynamic instabilities, as well as the mechanical complexities involved in their design and construction. However, the advent of Multi Ducted Fans (MDFs) has revolutionized the field by effectively addressing these challenges. By redistributing the Center of Gravity (COG) towards the whole system's geometric center, which is different from a single DF, MDFs significantly enhance stability. Furthermore, the presence of ducts surrounding the propellers helps eliminate undesired yawing torques, thus greatly improving rotational maneuvers, a common issue encountered in VTOLs. Although the utilization of MDFs remains limited in research and industrial platforms, their potential is increasingly recognized.

As stated before, the heavy UAVs' wide-ranging applications became evident. These aerial systems play a crucial role in various domains, necessitating utmost stability and safe flight operations, particularly in payload carriage and taxi air scenarios. To ensure safety, the integration of robust engines, enclosed platforms, and auxiliary actuator units becomes imperative. These components collectively provide the required power, safeguard the structure and vital elements, and fulfill standard control requirements. Additionally, to meet the demands of diverse applications, high-endurance platforms are designed to sustain autonomous flight throughout entire missions, eliminating the need for mid-flight refueling. However, heavy drones require substantial power to support long-range missions, posing challenges for electrical battery systems. The trade-off between power generation and battery weight calls for alternative solutions, leading to the utilization of fossil fuels and thermal engines. Thermal engines offer extended thrust capabilities while utilizing way lighter fuel compared to batteries. Nevertheless, the presence of mechanical uncertainties and propulsive system complexities necessitates the implementation of a precise control system capable of addressing both internal instabilities and external disturbances. Furthermore, it is important to note that thermal engines exhibit a certain level of response latency, influenced by factors such as fuel injection speed, combustion process, and energy exhaust. In contrast, electrical engines offer a significantly higher frequency of response, enabling designers to regulate them effectively using Electrical Speed Controllers (ESCs) to ensure synchronized input signals. Lastly, the utilization of thermal engines is highly sought after due to their ability to provide extended flight endurance, making them a preferred choice for weight-sensitive applications.

While addressing the thermal engine challenge, the implementation of a hierarchical control strategy becomes crucial. The propellers play a key role in generating the necessary thrust to lift the drone to the desired altitude, with their velocity being controlled by Engine

Control Units (ECUs) designed explicitly for this purpose. Equipped with microprocessors, the ECUs continuously compare sensor inputs with lookup tables stored in their memory, making adjustments to actuators and valves on the engine to ensure a balanced distribution of generated thrust across all motors. This initial phase of ascending the drone is referred to as the altitude controller, followed by the position-holding and attitude stabilization phase that requires additional augmentation of actuators. Various solutions have been proposed to address this issue, including the utilization of rotatable components, swash plates, collective pitch propellers, and switch controllers, which are explored further in 2. However, an optimized solution lies in the incorporation of Thrust Vector Control (TVC) through the ducts' exhaust. This approach not only bypasses the non-usable airstream but also aims to stabilize the drone's attitude while simultaneously overcoming mechanical issues such as helicopter calibrations.

In summary, to address the need for heavy UAVs with large payloads, Multi-Ducted Fans (MDFs) were developed. These fans utilize thermal energy to generate thrust, enabling extended flight autonomy. Furthermore, the incorporation of Thrust Vectoring Control (TVC) through flap vanes placed at the ducts' outlets enhances system stability while reducing mechanical complexities. The project WILD HOPPER*, funded by the European Commission, focused on designing a Heavy-Duty UAV specifically for firefighting operations during the day and night. DRONE HOPPER S.L.[1] was entrusted with achieving the project objectives, which involved designing and manufacturing the platform. Meanwhile, the author of this thesis was responsible for developing an appropriate control algorithm for the target drone. The project had several defined conditions:

M.1 WILD HOPPER is a 600-liter platform designed for forest firefighting. Unlike electric drones, which are limited to fire monitoring due to insufficient lifting power, this platform utilizes technologies developed by DRONE HOPPER to combat wildfires worldwide effectively.

M.2 The enhanced capabilities of WILD HOPPER make it a valuable complement to existing aerial methods, particularly for night operations. This significantly reduces wildfire duration by providing continuous aerial support for extinguishing activities when conventional aerial means, such as hydroplanes and helicopters, are grounded at night.

M.3 WILD HOPPER offers advantages such as precise release capabilities derived from the dynamic characteristics of a multirotor platform. Coupled with a proprietary water jet nebulization system, it achieves high efficiency compared to traditional means. Helicopters and hydroplanes carrying similar or greater volumes of water typically drop it from high altitudes, limited by their operational envelope. As an autonomous vehicle, WILD HOPPER ensures the safety of human lives by managing operations from a secure ground base.

M.4 The cost-effective nature of WILD HOPPER makes it an accessible platform for small and medium regional bodies to own their fast-response resources. Its reduced complexity translates to lower ownership costs.

[1] https://www.drone-hopper.es/ (accessed on: 07/09/2023)

M.5 WILD HOPPER facilitates swarm operations by enabling coordination among multiple units, thereby maximizing efficiency. Peña et al., 2022

Considering the mentioned conditions, the final WILD HOPPER platform has certain specifications that the designed controller criteria will stabilize, as shown in Table 1.1.

Table 1.1: Summary of requirements for the designed platform defined by the project rules.

Maintainability	
The system supplies thermal engines for a long autonomy of up to 3 hours. The thermal power supplier is equipped with several electrical batteries for redundancy and emergent landing to feed Electrical Ducted Fans (EDFs) installed next to the main ducts for an adequate time to land safely.	
Structural Design	
Platform Type	Hexa Ducted Fan (HDF)
Duct No.	6
Duct Diameter	125 cm
Propeller No.	6
Servo Flap No.	12
Flap Vane No.	12
Flap Vane Model	NACA-0015
Battery No.	6
Battery Types	LIPO 16000 mAH
EDF No.	4
EDF Type	SCHUBELER, DS-215-DIA HST
On-Board Sensors	
Inertial Measurement Unit (IMU)	
Redundant GPS System	
On-Board Computer	Jetson Xavier Developer Kit[2]
RGB and Thermal Camera	

1.2 Problem Statement

The focus of this thesis is on the control of a heavy MDF using thrust vectoring through flap vanes. The significance of this research can be summarized by the following key design steps:

P.1 Investigating potential control solutions for the heavy MDF and conducting a comparative analysis of each approach to identify the optimal solution. This analysis led to the adoption of thrust vectoring as the chosen method.

P.2 Analyzing the aerodynamic interactions between the heavy MDF and the flap vanes, with the aim of improving the efficiency and functionality of the control surfaces.

P.3 Developing a comprehensive mathematical model for the heavy MDF and formulating a novel control strategy to enhance system stability.

P.4 Exploring the challenges associated with utilizing flap vanes under various conditions, including the introduction of internal uncertainty through random noise and external disturbances such as wind gusts. Additionally, the controller functionality is enhanced by incorporating redundant actuation mechanisms, including EDFs, into the system.

By addressing these design steps, this thesis aims to make significant contributions to the advancement of control methodologies for heavy MDFs, with a particular focus on the application of thrust vectoring and the optimization of flap vane control in various operating conditions.

The control solution proposed in this thesis can be divided into three main levels, as depicted in Figure 1.1. These levels can be regarded as the low-level controller loop, where stable points are determined using a single integrator, regardless of the position loop, where the stable points are defined using a double integrator.

Figure 1.1 illustrates the system diagram, which begins with the reference values provided to the altitude and attitude controllers. These controllers generate the desired values for the actuators. The altitude controller outputs the necessary thrust force for a desired altitude, and the Engine Control Unit (ECU) plays a crucial role in this process by translating the altitude controller commands. It utilizes a predefined lookup table to continuously calculate the logical inputs for the thermal engines, thereby generating the required vertical thrust. The necessary power for this operation is produced by the propellers, which are driven by the engines.

In another layer, the attitude controller receives the desired Euler angles, namely Roll, Pitch, and Yaw angles (ϕ, θ, and ψ), which are generated by a position controller loop. These Euler angles are utilized to determine the desired moments necessary for the proper functioning of the servo flaps located at the exit of the ducts. The flap vanes are set to their standard values to generate the required lift force for each attitude action, ensuring the stabilization of the drone.

Furthermore, in the event of an emergency situation, an additional layer of control is implemented to address the critical circumstances using electrical power. This third layer begins with a motor mixing system, which receives both vertical and attitude commands

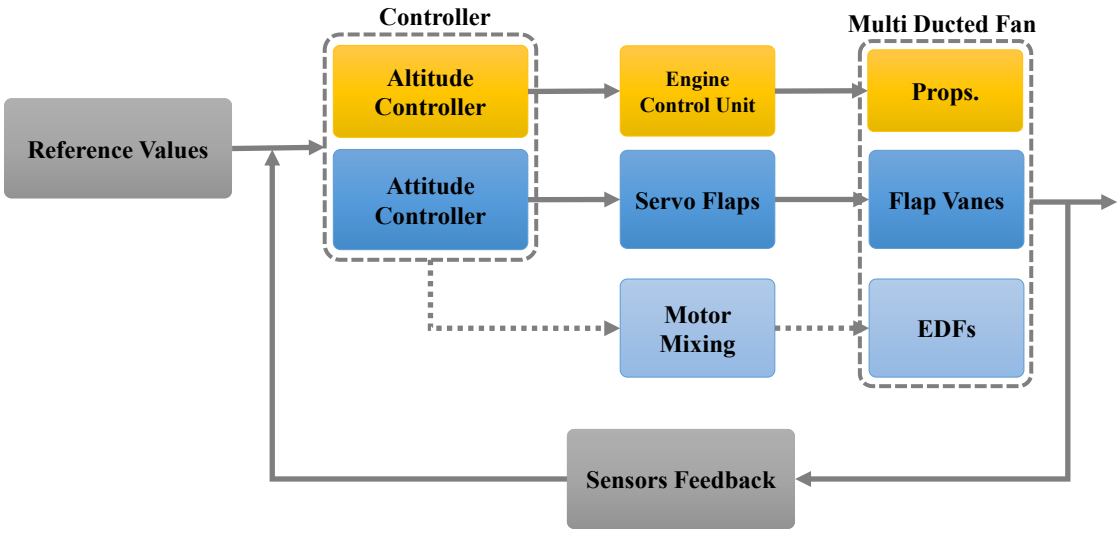

Figure 1.1: A diagram of the controller system interacting with the MDF plant.

from the controller. Its primary function is to convert these commands into standard Pulse Width Modulation (PWM) signals, which are then utilized by the EDFs. The EDFs generate sufficient thrust for a short-duration flight, thereby stabilizing both the position and attitude of the drone until a safe landing can be executed. This particular aspect serves as a redundant system, ensuring that any potential failures or disruptions have minimal impact on the overall system.

Overall, this thesis aims to enhance the control capabilities of heavy MDFs through the integration of thrust vectoring and the optimization of flap vane control, enabling improved performance and versatility in diverse operational scenarios.

1.3 Objectives

The main objective of this thesis by compendium that is elaborately addressed through **PI** Isaac et al., 2022, **PII** Ale Isaac et al., 2023, **PIII** Ale Isaac et al., 2024, and **PAd** Ale Isaac et al., 2022 could be summarized into a single sentence: *to* ***develop, implement, and validate*** *novel* ***control techniques*** *to regulate the flap vanes in a* ***thrust vectoring system****, in order to solve and improve the attitude instabilities of heavy UAVs, reduce the mechanical complexities of the system, and* ***increase flight endurance*** *by employing thermal engines to generate vertical thrust.* In order to accomplish the mentioned objective, there are several sub-objectives followed in this thesis.

O.1 System Design: Initiate the design process by brainstorming ideas for modeling a heavy Unmanned Aerial Vehicle (UAV) and progressing towards the conceptual and detailed design of a multirotor system integrated with thermal engines. The aim is to eventually evolve this design into a Multi Ducted Fan (MDF) model, which effectively eliminates

unwanted yaw moments and enhances thrust efficiency. The initial step involves CAD modeling of a primary design based on a conventional hexacopter. Subsequently, the model can be refined by incorporating additional components such as ducts, Electrical Ducted Fans (EDFs), controller surfaces, flap vanes, and other necessary elements.

O.2 System Modeling: Develop an accurate mathematical model for the stable designed MDF model. This involves achieving the static and dynamic model of the target drone, considering the system's degrees of freedom and the specific elements incorporated, such as coaxial propellers. Additionally, it accounts for the possibility of a liquid payload, which may introduce additional degrees of freedom due to compounded movements, forces, and moments.

- **Aerodynamic Considerations:** Conduct comprehensive aerodynamic modeling and analysis to refine the final model. This analysis includes an examination of critical components such as the propellers, prop pitch angles, duct diameters, inlet arcs, and servo locations. Furthermore, particular attention is given to the interactions between the attitude controller surfaces and the freestream airflow as required in-depth analysis to ensure optimal functionality and efficiency.

O.3 Control Development: This research aims to explore nonlinear attitude control methods specifically tailored for UAVs, with a particular focus on MDFs. The control development can be divided into two parts: the *General Control*, which addresses standard conditions applicable to conventional drones, and the *Specific Control*, which focuses on stabilizing the MDF system based on the defined controller surfaces and specific actuator configuration outlined in O2.

- **Methods Comparison:** The designed control system shall be thoroughly evaluated in both theoretical analysis and integrated system performance. To achieve enhanced efficiency, a comparison of the functionality of each presented nonlinear control method will be conducted. The selected method with the best performance will then be further evaluated through experimental testing, as outlined in O.4.

- **Force Allocation Module (FAM):** The control system shall work in conjunction with a FAM designed in the Autopilot (AP), which generates logical outputs for distinct actuator types, including the primary propellers, servo flaps, and EDFs. This module is crucial for efficiently distributing the desired forces and moments among the various actuators, ensuring effective control and maneuverability of the MDF system.

O.4 System Validation The proposed control methods and aerodynamic improvements will undergo validation in both simulation and real-world experiment platforms. The validation process includes laboratory testing using dynamic simulators that closely mimic real-world conditions. Especially for a heavy MDF system, the simulation should accurately replicate the dynamics and potential failures while incorporating wind disturbances to assess performance under challenging scenarios. Additionally, real-world experiments will be conducted to validate the attitude control performance and further enhance functionality.

1.4 Contributions

This thesis makes several significant contributions to the design, development, testing, and validation of attitude control systems for UAVs. The main contributions are as follows:

C.1 Distinct complete prototypes are modeled, improved, and tested to approach the final heavy MDF setup, as ordered:

C.1.1 FAN HOPPER: A small-scale hexacopter platform weighing up to 40 Kg. It serves as the primary platform for exploring the controllability of electrically powered drones with EDFs. The prototype features a redundant battery system and the capability to recover from single-engine failures.

C.1.2 DUTY HOPPER: A medium-scale Quad Ducted Fan (QDF) platform with a maximum weight of 250 Kg. It incorporates coaxial propellers and EDFs for redundancy. The prototype focuses on examining the controllability of QDF systems using thrust vectoring with flap vanes in scenarios involving motor failures, wind disturbances, and the presence or absence of EDFs.

C.1.3 WILD HOPPER: A large-scale Hexa Ducted Fan (HDF) platform capable of carrying payloads up to 600 Kg. This prototype builds upon previous experiments and includes improved components. It is equipped to handle liquid payloads and features EDFs as an emergency backup. WILD HOPPER represents the final configuration that meets the requirements outlined in Section 1.1.

C.2 Different nonlinear algorithms are designed, adapted to the model, and validated through the tests:

C.2.1 Model Reference Adaptive Controller (MRAC): This controller is implemented on the FAN HOPPER and DUTY HOPPER prototypes to handle internal system uncertainties. It incorporates an adaptation law that accounts for payload release, both for solid and liquid payloads, as the weight decreases over time.

C.2.2 Sliding Mode Controller (SMC): This controller is designed to enhance control system performance in the presence of external errors or failure modes. The SMC provides stability when the MRAC fails to reach a stable point within a given time frame. It performs effectively during heavy flights by utilizing more efficient commands to actuate the servo flaps.

C.3 Mathematical Modeling of Dynamic Systems: Mathematical models are developed for each prototype, consisting of a complete 6DOF dynamic system. In one case involving liquid payloads, a 7DOF system is modeled (as described in the collaborative article Ragab et al., 2021). The attitude control systems for all prototypes adhere to the conditions set by Cinematic and kinematic equations to ensure proper stabilization.

C.4 Comprehensive Laboratory Validation: This process is conducted to analyze the performance of the control algorithms in each prototype. The validation process involves simulating the prototypes in two different dynamic environments: Matlab Simulink SimScape and the Gazebo platform. This allows for improving the models and assessing

the fault tolerance of the control methods. A comparative analysis of the different methods is carried out to identify the most effective solution and prepare for real-world tests.

C.5 Experimental Validation: This procedure is conducted for each prototype to assess the functionality of the system under various conditions. This process includes subjecting the prototypes to different failure scenarios, such as engine failures as well as external disturbances. The aim is to evaluate the robustness and performance of the control systems in practical scenarios.

1.5 Outline

This thesis is structured as a compendium of publications, providing a comprehensive elucidation of the diverse solutions outlined in three primary publications (**PI**, **PII**, and **PIII**), accompanied by an additional paper (**PAd**), all tailored to realize the research objectives underscored in Section 1.3. The publications are appended at the end, and the thesis is divided into several chapters, each summarizing the contributions of the included articles.

In the first chapter, the introduction, motivation, thesis objectives, and contributions are presented. The content of the remaining chapters is summarized below:

Chapter 2 reviews the state of the art in the field of the methods and applications under research, with a special focus on linear and nonlinear control approaches for VTOLs' autonomous flights, emphasizing MDFs, payload variability during flight, and control surfaces utilized in the research.

Chapter 3 introduces the methodology employed in both the development of the thesis and the evaluation of the results obtained, detailing general terms and specific control algorithms utilized and publication evolution.

Chapter 4 details the comprehensive design process of each principal platform developed during the doctoral project, including the FAN HOPPER, DUTY HOPPER, and WILD HOPPER.

Chapter 5 provides an in-depth dynamic modeling analysis of the ducted fan platforms examined in the thesis and publications **PI**, **PII**, **PIII**, and **PAd**.

Chapter 6 discusses the general and specific control systems developed and presented in the thesis and publications **PI**, **PII**, **PIII**, and **PAd**.

Chapter 7 presents the simulation and experimental results and discussion. The main results published in **PI**, **PII**, **PIII**, and **PAd** are showcased, including the functional enhancement of various designs until the final operational platform.

Chapter 8 presents the overall conclusions for this doctoral thesis and provides an overview of future works.

Chapter 9 is dedicated to the publications, covering **PI**, **PII**, **PIII**, and **PAd**.

Furthermore, the focus extends to the detailed exposition of Thrust Vector Control (TVC) algorithms expounded across the publications, partitioned into two principal categories: a general control solution and a specific control solution for MDFs. Stability analyses are briefly scrutinized, accompanied by a comprehensive discourse on simulation outcomes juxtaposed against empirical test results. The pivotal contributions, encapsulated in **C.1 - C.5**, are highlighted in Section 1.4. For more extensive insights, readers are encouraged to peruse the encompassed published works **PI**, **PII**, **PIII**, and **PAd**, integral to this thesis compilation, along with supplementary publications briefly outlined in this dissertation. A visual summation is provided in Figure 1.2, offering a flow chart that captures the intricate interconnections and dependencies binding the publications.

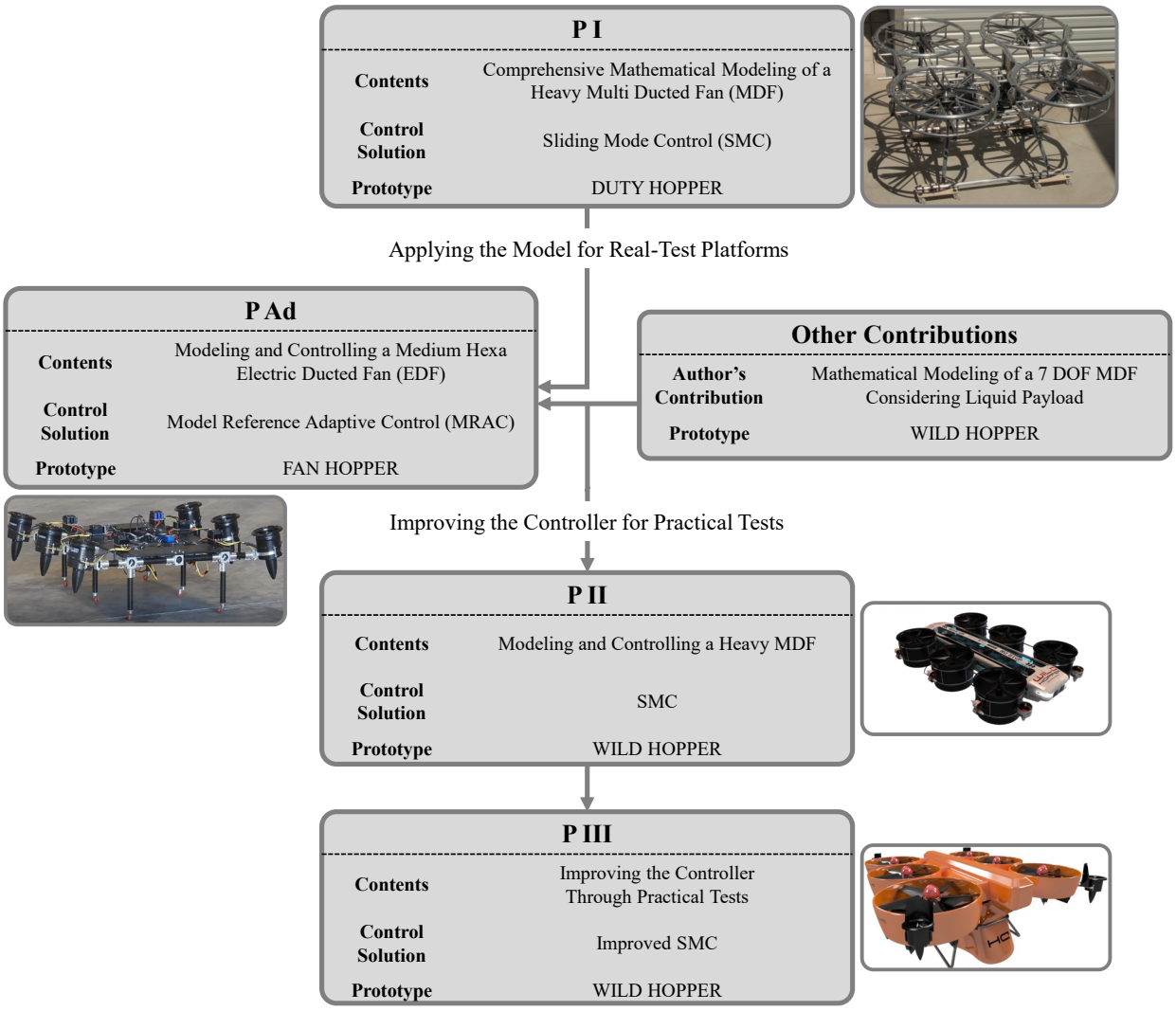

Figure 1.2: Flow chart illustrating the publications summarized in this thesis by compendium.

The sequence of publications, **PI**, **PII**, **PIII**, and **PAd** follows a coherent and structured progression. It begins with **PI**, where the mathematical model is introduced, providing a foundation for subsequent developments. **PAd** transitions to real-world implementation,

focusing on the medium-scale FAN HOPPER platform, applying and evaluating the MRAC under payload conditions. **PII** integrates an SMC algorithm into the large-scale WILD HOPPER hexa MDF system to enhance platform stability, building upon the results from previous work. Finally, **PIII** culminates these efforts by enhancing the control performance through real-world flight tests and comparing the results with those of a cascade PID controller. An extended contribution is made by introducing an advanced model accommodating liquid payload dynamics, enriching the conventional 6DOF model to a more intricate 7DOF representation, and ensuring a progressive and thorough exploration of control strategies across diverse platforms. More details about the contributions of each paper are provided earlier in Section .

Chapter 2

Literature Review

In recent years, significant research efforts have been devoted to the field of heavy aerial robotics with a primary focus on achieving long autonomous flights and efficient carriage of heavy payloads. This chapter presents a comprehensive review of the literature in this area, highlighting various control approaches and methodologies applied to UAVs and especially MDFs. Additionally, it explores the application of aerial robots in diverse industrial contexts and international competitions, with specific emphasis on the methods presented in **PI**, **PII**, **PIII**, and **PAd**.

2.1 Control Approaches for UAVs with long Autonomy

Over the last decade, researchers have delved into a diverse array of strategies for governing UAVs with long-flight endurance, as outlined by the study detailed in Bin Junaid et al., 2017 presents an inventive approach to recharging the battery of a compact AR. Drone through wireless means. This pioneering wireless charging method involves the drone meticulously following predefined waypoints to a marked location, where it receives a recharge. The drone then resumes its flight after this replenishing phase. According to the authors' assertions, this mission significantly enhances wireless power transfer efficiency, yielding an impressive 75% improvement over conventional flights of this drone, which possesses a limited battery capacity. Furthermore, the study suggests that incorporating solar panels or rapid charging techniques could yield even more substantial gains. While this research holds undeniable value, it is important to recognize potential limitations when applied to larger-scale scenarios. Achieving pinpoint landing accuracy with specific sensors might pose challenges, particularly in contexts where suitable landing sites are scarce or absent.

While in Cabanas et al., 2021 the authors embarked on enhancing both flight duration and the thrust-to-weight ratio through the utilization of an innovative hybrid system. This endeavor involved the creation and demonstration of a prototype hybrid generator that melds cutting-edge electronics with a fresh approach employing a supercapacitor array. This dual-pronged strategy aimed to conserve fuel, elevate the thrust-to-weight ratio, optimize conversion losses,

and avert the risk of internal combustion unit overheating. By controlling throttle generation, energy consumption was judiciously managed. The authors devised an ECU-like system using FPGA technology, which accommodated specific control loops for each component. The proposed concept underwent rigorous evaluation via MATLAB Simulink, yielding impressive outcomes. Despite the commendable strides achieved, it's worth noting that the current form of the working prototype remains distant from industrial readiness, primarily due to its unwieldy integrated casing, rendering it unsuitable for most aircraft. This is compounded by the existence of several established hybrid industrial solutions already in existence.

Further investigation into the realm of aerial systems underscores the predominant use of electrical batteries, a trend that could potentially be addressed through structural enhancements to minimize battery consumption and extend flight durations. However, it is worth noting that thermal engines offer a distinct advantage, boasting superior performance compared to their electrical counterparts. A striking testament to the potential of meticulous aerodynamic design, lightweight carbon-fiber construction, and the incorporation of advanced Lithium-ion cells is exemplified by the CONDOR Dronetools, 2021, crafted by the Spanish company Dronetools™that has achieved a remarkable feat, showcasing flight durations surpassing the one-hour mark. Nonetheless, it is essential to acknowledge that while this achievement is impressive, this UAV remains constrained in terms of payload capacity and size. The deficiency in carrying a substantial payload is evident as well in other studies, Ronchi et al., 2020, Viera-Torres et al., 2020, and Parshin et al., 2021, highlighting a noticeable gap in the realm of Heavy-Lift Unmanned Aircraft Systems (H-UASs) within the category of multi-rotors.

Another real case utilized for a long autonomy application is GAIA manufactured by FoxtechFPV™"Foxtech Nova 2400 Generator", n.d., which is equipped with a hybrid engine generator called NOVA that is able to generate a power maximum of 2400 W, which is lower during a flight, which disregarding a more flight endurance it performs but a conspicuously low thrust-to-weight ratio that characterizes existing H-UAS could be seen.

2.2 Control Approaches for Single Ducted Fans (SDFs)

Among all UAV types, this emphasizes on SDFs due to specific characteristics they have, as exemplified by the work in Townsend et al., 2020. Here, an ingenious concept of an aerial manipulator equipped with a coaxial SDF was introduced, specifically tailored for intricate tasks within confined environments. Central to this innovative control approach was an adaptive methodology aimed at sustaining the drone's stability, particularly during intricate manipulator interactions. The integration of an impedance controller further ensured equilibrium during physical contact. The practical implementation featured a fusion of cutting-edge hardware, such as the Navio2 onboard controller and Dynamixel XH430 intelligent actuator, accompanied by a sophisticated OptiTrack camera positioning system. Despite its success in dynamic scenarios, the closed-source nature of the onboard controller limited the seamless integration of alternative solutions, restricting the practical deployment to simulation-based evaluation.

The study presented in Jeong et al., 2020 unveiled an inventive aerial array system centered

around an SDF configuration. Notably, their focus rested on introducing dynamic alterations to the physical structure, particularly involving Center of Gravity (COG) adjustments and inertial moment modifications to render the system reconfigurable. A comprehensive exploration of dynamic control implementation ensued, revealing a proportional relationship between the assembly of multiple components and the corresponding influence on the plant through actuators. Their investigation highlighted the pivotal roles played by control influence and mechanical interconnections within the array system, with external forces and moments exerting comparatively lesser impact. Leveraging an open-source simulation software called "DF design code", the researchers meticulously analyzed and predicted propulsion designs for asymmetric combinations. This entailed the determination of thrust and torque models, derived from geometric configurations and motor RPM information. Focusing on two distinct array types –four-module-based and five-module-based configurations– the study ultimately determined that a closely set, statically stable combination offered the most suitable configuration. It is worth noting that while this endeavor contributed valuable insights into mathematical modeling and dynamic reconfiguration, practical validation through empirical results remained absent.

In Asl and Moosapour, 2017, a groundbreaking nonlinear control approach was introduced, merging backstepping and fast terminal sliding mode control for SDF engines. This innovative method harnessed thrust vectoring to counteract internal uncertainties and external disturbances. The strategy aimed to expedite system state convergence to equilibrium points within a finite time. The enhanced algorithm yielded an Adaptive Backstepping Fast Terminal Sliding Mode Controller (ABFTSMC) by combining the BFTSMC with improved uncertainty estimation. The researchers examined diverse scenarios, employing sinusoidal and step functions as inputs along with external disturbances. Simulation outcomes in MATLAB-Simulink revealed enhanced transient mode response, heightened robustness, and superior disturbance rejection compared to SMC and Adaptive Sliding Mode Controller (ASMC). The study affirmed ABFTSMC's potential to stabilize closed-loop systems and enhance desired value tracking. However, it's worth noting that this work focused solely on simulations and lacked experimental tests or an exploration of the proposed dynamic model.

In contrast, Jeong et al., 2015 introduced a Linear Quadratic Tracking (LQT) controller tailored for hover, transition, and cruise modes. Enhancing this approach, they incorporated an Integrator to mitigate steady-state errors by accumulating tracking integral terms into the state vector. Employing 3D simulations, which included waypoint navigation and accounted for miscalculated wind disturbances, they validated the reduction of steady-state errors. Notably, the simulation involved a numerical process leveraging wind tunnel data. However, it's important to highlight that this paper introduced a linear tracker for a nonlinear system, lacking the ability to address nonlinearities stemming from dynamic equations. Furthermore, practical results were conspicuously absent from the study.

However, Jeong et al., 2015 presented a range of nonlinear strategies to govern SDFs. Notably, they delved into the placement of the COG, a factor that influences the system's zero dynamics. Paradoxically, an optimally positioned COG from a mechanical standpoint can inadvertently introduce instability to the vehicle's controller. Furthermore, their comprehensive investigation extended to the analysis of force and moment generation modules within SDFs, particularly

in response to varying environmental conditions. The paper outlined the deployment of a backstepping controller and partial feedback linearizing techniques to enhance state feedback. It's noteworthy, however, that the conclusions of this work are predominantly based on simulation results without experimental validation.

In a distinct approach, Chen et al., 2019 concentrated on the mechanical-structural parameter design of an individual SDF, employing Lyapunov Exponents (LEs) to establish a quantifiable relationship between these parameters and the UAV's motion stability. The novel utilization of LEs facilitated the optimization of structural parameters to enhance dynamic stability. Notably, the paper emphasizes that LE remains invariant in dynamic systems. A noteworthy assertion highlights the optimization of mechanical-structural parameters, which significantly influence stability. Despite their commendable efforts, it is important to acknowledge that the inherent instabilities associated with an SDF might challenge the efficacy of a PD controller. This remains pertinent even after enhancements to structural parameters, a point that warrants further exploration beyond the scope of the presented work.

In a different investigation, Yu et al., 2001 conducted a comparative exploration of various nonlinear control design techniques by applying them to a planar model of an SDF engine. The comparison encompassed linear methodologies like Linear Quadratic Regulator (LQR) and nonlinear methods, divided into two phases: one involving the derivation of a Control Lyapunov function (CLF), and the other utilizing an existing CLF for controller generation. The authors endeavored to integrate these phases within a Model Predictive Control (MPC) framework, demonstrating that the hybrid approach outperformed individual techniques. It's worth noting that while the work is valuable, the conclusion highlights its simulation nature, and achieving the practical implementation of the Caltech SDF still requires an extensive process.

In another study by Shan et al., 2016, an attitude controller was introduced, employing a robust servomechanism LQR approach. Notably, the authors optimized the controller through variations in the penalty function weight coefficient. However, it's worth mentioning that their practical implementation raises questions, as they utilized a commercial Ardupilot-Mega (APM) 2.0 as the flight controller. The integration of their algorithm into the chip firmware remains unclear. Despite this, their experiments demonstrated consistent performance even in the presence of real-world noise, a phenomenon not commonly observed in the context of SDFs, which often exhibit multiple instabilities.

While Naldi et al., 2010 focused on an SDF aimed at stabilizing a nonlinear control law enabling robust tracking of various aircraft dynamics, including lateral, longitudinal, vertical, and heading references. The authors achieved this by developing mathematical models for SDFs with four and eight-flap configurations. They further implemented a cascade control structure involving an inner attitude loop and an outer horizontal loop. The study's outcomes are significant, demonstrating stability in both vertical and attitude aspects. However, it's important to note that the research was limited to laboratory settings, and for broader industrial applications, additional refinement and processes would be necessary.

2.3 Control Approaches for Multi-Ducted Fans (MDFs)

Approaching the issue of this thesis context, improving a DF to MDF has several merits, including much more static and dynamic stability due to moving the COG toward a point in the middle of DFs and higher thrust power to carry heavier payloads. To this end, some research focused on controlling MDFs, as the study outlined by Muehlebach and D'Andrea, 2017, researchers focused on a triangular EDF system, specifically honing in on TVC as a critical stabilizing factor. Employing a linear cascade controller, they achieved stable hover performance with minimal disruptions, efficiently regulating angular rates at high frequencies. The controller was split into two components: an onboard gyroscope for real-time angular rate measurement and an offboard calculation module for position and attitude control. Communication with the PX4 autopilot ensured coordination. Notably, mounting the motor controller (YGE 90HV) at the exit nozzle provided cooling through airflow. However, this work primarily relied on controlled settings with motion capture, potentially limiting real-world applicability. Offline primary controller components posed vulnerability to delays or data loss due to connection issues. Battery reliance led to constrained operational times for energy-intensive DFs. While hover stability was validated, further exploration of diverse flight maneuvers remains a promising avenue.

Whereas in a distinct research endeavor detailed by Tobias and Horn, 2008, a comprehensive simulation methodology for a TDF system was presented, encompassing intricate considerations of aerodynamic interactions and the mathematical underpinnings of flap vanes. This simulation was realized using MATLAB Simulink, offering a versatile and modular framework for TDF analysis. Delving into the intricacies of airflow dynamics within the duct, the study scrutinized the destabilizing effects on the nose-down pitching moment during the transition from edge-wise to axial flight modes at low velocities. By fine-tuning the deflection angle of the vanes, the researchers reported enhancements in transient behavior. This work contributes significantly to theoretical insights and aerodynamic investigations of MDFs, especially those akin to the Urban Aeronautics X-Hawk and the 29-inch UAV, which served as inspirational sources; however, its real-world applicability might necessitate further implementation beyond the confines of the simulation environment.

In a related study, discussed by Miwa et al., 2012, researchers focused on an MDF flying object consisting of two EDFs connected by a vertical wooden bar. The unique feature of their design was the rotatable installation of the EDFs, functioning like a hinge to induce roll, pitch, and yaw rotations. Employing a PD controller initially, the system encountered a persistent steady-state error, prompting the integration of an integral term, which effectively mitigated this error. While the effort showcased valuable insights, the positioning of the battery and equipment on the wooden bar introduced an imbalance by shifting the COG to a higher point relative to the EDF plane. This configuration likely contributed to the observed steady-state error. Furthermore, the study highlighted a limitation in endurance, attributed to the low battery capacity not suitable for powering two EDFs.

However, in another research, Xu et al., 2015 proposed a novel TDF for drones, featuring small EDFs and larger TDFs controlled by a robust static H_∞ output feedback technique. The controller effectively stabilizes and decouples body-frame velocities and yaw angle states, even

in the presence of disturbances and EDF tilting. The study also addresses time delays caused by open-loop gain roll-off using system identification. However, the approach's applicability to industrial platforms is limited due to component disharmony and complexities associated with decoupling.

In a related study by Fan et al., 2018, a compact MDF was introduced, utilizing two DFs for vertical stabilization and two EDFs for attitude control. The study employed a structured multi-loop feedback attitude controller based on H_∞ synthesis, encompassing a low-order attitude controller and multi-loop feedback for cross-attitude decoupling and reference signal tracking. Controller parameter tuning was conducted using a non-smooth optimization method. Although the approach demonstrates promise, further investigation is recommended to address significant uncertainties, disturbances, or actuator/sensor faults, as also asserted by the authors.

In essence, the literature review delves into a range of control algorithms, succinctly encapsulated in Figure 2.1. It becomes evident that controllers displaying heightened robustness demonstrate superior resistance to external disruptions. Similarly, the adaptability of controllers manifests its prowess in scenarios where the system's internal dynamics shift or the payload undergoes modifications, altering the system's overall weight. The landscape predominantly showcases electric aerial vehicles, with a few exceptions utilizing thermal energy to sidestep motor intricacies. Nevertheless, this emphasis on electric setups often comes at the expense of extended flight autonomy. Recognizing these prevailing trends, this thesis bridges the gap by addressing both autonomy and stability, thus advocating for a thermal MDF configuration bolstered by TVC.

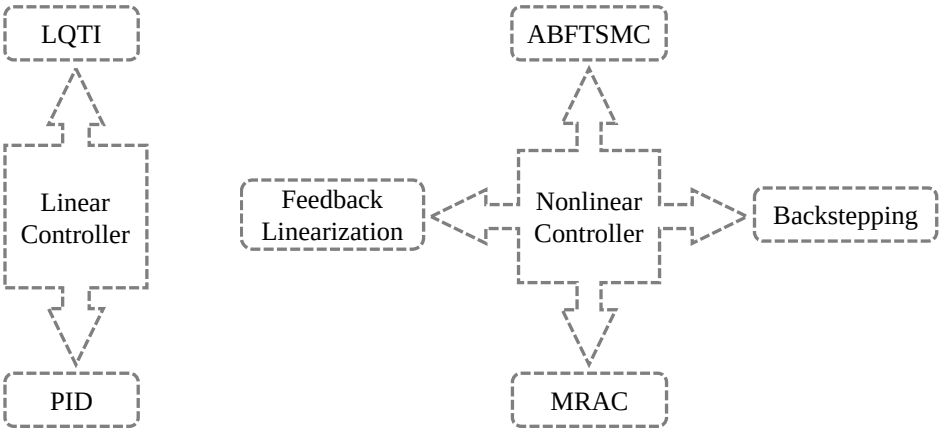

Figure 2.1: Diverse Control Strategies Explored in Literature.

Chapter 3

Methodology

3.1 Introduction

As outlined in Chapter 1, this thesis focuses on the control of heavy UAVs with a specific emphasis on applying TVC using flap vanes. The research methodology employed in this thesis can be classified according to the *Applied Research* presented by Kothari, 2004, which differentiates the context from fundamental (basic) research in terms of purpose, context, and methods. Applied research aims to solve practical problems, whereas basic research seeks to study certain issues without immediate practical application. The key elements of this thesis are elaborated as follows:

Purpose: The purpose of **PI** is to solve the mathematical modeling and dynamics of heavy Multi-Ducted Fan (MDF) UAVs while applying flap vanes to stabilize the attitude using Sliding Mode Control (SMC). In **PAd**, the focus is on solving the control issue defined previously in a real platform and evaluating the controller's performance under motor failure and external noises. Lastly, **PII** and **PIII** aim to enhance the control issue by implementing Thrust Vector Control (TVC) using flap vanes for heavy platforms.

Context: The context of this thesis is highly valuable due to the industry's long-standing need for easy-to-set-up UAVs that can carry heavy payloads for extended flight autonomy. This requirement is addressed in **PI**, **PII**, **PIII**, and **PAd**, where a system is developed to supply thermal energy for extended flight autonomy and equipped with a controller that avoids mechanical complexities and is rational for such a system.

Methods: The methods used in **PI**, **PII**, **PIII**, and **PAd** involve advanced control algorithms, particularly Sliding Mode Control, applied in a novel way to achieve TVC using flap vanes. The design is easily extendable for similar platforms, and the application of SMC offers the advantage of easy tuning compared to conventional Proportional-Integral-Derivative (PID) controllers.

Furthermore, the methodology utilized in this thesis is a combination of the system engineering

method derived from the system engineering process organized in Bahill and Gissing, 1998. This process is abbreviated as "S.I.M.I.L.A.R." and encompasses the following steps, which are also shown in Figure 3.1:

State the problem: Clearly define the research problem and objectives related to controlling heavy UAVs and applying TVC using flap vanes.

Investigate alternatives: Explore and evaluate various alternatives and approaches for achieving the desired control objectives. This may involve a literature review, feasibility studies, and analysis of existing control techniques.

Model the system: Develop mathematical models and simulations to represent the dynamics and behavior of heavy UAVs with TVC using flap vanes. This step involves formulating equations and algorithms to describe the control system.

Integrate solutions: Integrate the developed models and control algorithms into the heavy MDF's overall system architecture. This includes hardware and software integration, testing, and verification.

Launch the system: Implement the control system with TVC using flap vanes on a prototype or experimental platform. This involves the physical realization and deployment of the developed control algorithms.

Assess performance: Evaluate and analyze the control system's performance in various scenarios and operational conditions. This involves flight testing, data collection, and performance evaluation metrics.

Reevaluate: Continuously assess and reevaluate the control system to identify areas for improvement, address any limitations, and refine the design to enhance the performance of the TVC system with flap vanes.

The applied research approach adopted in this thesis allows for practical implementation and validation of control techniques for heavy UAVs with TVC using flap vanes. By following the "S.I.M.I.L.A.R." methodology, this research aims to address the challenges and requirements specific to the field of control for heavy UAVs and contribute to advancing TVC technology. This section could be summarized as several sequences:

Problem definition: The core challenge of this project is initially identified, and potential solutions are presented. The genesis of this thesis's problem stems from a crucial industrial demand, particularly advantageous for advancing thermal heavy UAVs, with a special focus on multi-rotors. For a comprehensive understanding, readers are directed to Section 1.2. In **PI**, the bedrock of the issue is fortified by establishing the dynamic model of heavy MDFs, setting the stage for subsequent publications. Subsequently, in **PII** and **PAd**, the problem scope is broadened to encompass real-world control challenges. Finally, **PIII** hones in on refining the problem statement to enhance both the controller and dynamic modeling for the ultimate prototype.

Mathematical hypothesis: Drawing from the problem statement and objectives outlined in Section 1.3, the development of a comprehensive mathematical hypothesis took precedence in order to establish the system's dynamic model. This phase stands as the crux of our modeling

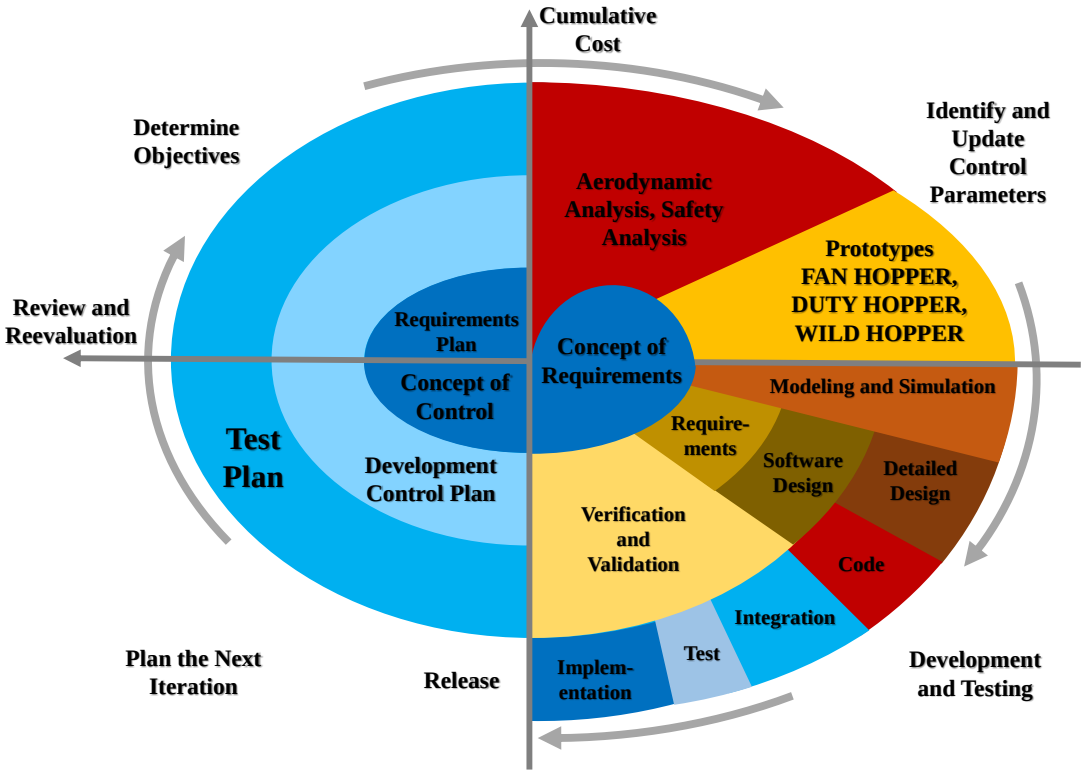

Figure 3.1: Methodology approach model followed in this thesis, according to the "S.I.M.I.L.A.R." Bahill and Gissing, 1998, and the spiral procedure defined by Boehm, 1988 .

effort; while other setbacks might necessitate revisiting specific components, a failure at this juncture would demand a complete reevaluation and rectification of the mathematical model across all processes. In light of this, **PI** has meticulously expounded upon this critical phase, serving as a cornerstone for subsequent research. Meanwhile, **PII** and **PAd** have explored the dynamics of time-invariant systems, focusing on refining the controller to accommodate fluid-type payload releases and associated changes in system weight, thereby introducing additional degrees of freedom. Finally, **PIII** has integrated control techniques with mathematical advancements, notably adopting the Lyapunov candidate approach to encompass the entirety of attitude angles within the control procedure.

Aerodynamic analysis: plays a crucial role in enhancing the design phase by optimizing components for advanced industrial prototypes. In this pursuit, a comprehensive examination was conducted on every aspect of the initial two prototypes, encompassing main engines, EDFs, ducts, flap vanes, and propellers. This meticulous analysis informed the refinement of the vane airfoil model, where the effects of deflection angle (α) on lift and drag forces were explored, culminating in the selection of the NACA-0015 airfoil for **PII**. In **PAd**, the investigation delved into EDF utilization for drone lift, entailing a multi-stage optimization of the aerodynamic configuration. Commencing with addressing vortex issues via the addition of a stator to counter rotation challenges, the approach progressed to incorporate concatenated ducts to improve transient stability and ground interaction. This configuration's success

against a single rotor alternative, coupled with in-depth studies on injector strategies and vapor volume fractions, contributed to system refinement. In **PII**, the optimal number of rotor blades was studied, with a conclusion favoring an 8-blade configuration, suggesting tip angles for enhanced thrust generation.

Prototype development: The evolution phase encompasses three principal prototypes, as illustrated in Figure 3.1, each with distinct characteristics. The "DUTY HOPPER," a robust platform, took center stage in **PI** as a laboratory quad-MDF prototype, serving to investigate the feasibility of attitude control using flap vanes. This initial iteration underwent subsequent refinement in components following its physical construction. The "FAN HOPPER," a hexa medium-sized prototype equipped with six turbofan EDFs and capable of carrying a moderate payload, assumed prominence in **PAd**. Here, the focus was on refining control theories established in **PI** and evaluating the performance of both the controller and the devised dynamic model. The culminating prototype, "WILD HOPPER," a hexa MDF featured in **PII** and **PIII**, seamlessly integrated simulation and experimental studies to enhance controller functionality for industrial applications. Notably, several auxiliary prototypes were designed and constructed throughout the design process, instrumental in resolving internal uncertainties within thermal engines and addressing peculiar controller challenges. However, these auxiliary prototypes, although pivotal, deviate from the primary objectives of this thesis and, therefore, are not expounded upon here.

Simulation and experimental testing: Rooted in its industrial context, comprehensive testing was conducted through both simulation and practical methods to identify vulnerabilities and areas of divergence between intended conditions and real-world outcomes. The initial step, detailed in **PI**, engaged a 3D spatial model tightly interlinked with dynamic components, harnessing MATLAB SimScape within Simulink. This platform facilitated the augmentation of controller actuators, refinement of control surfaces, and fine-tuning of controller parameters, culminating in visualized flight simulations. In the pursuit of an improved dynamic model, the project transitioned to Gazebo SW in **PAd**, leveraging its robust dynamic engine to simulate prototype reactions. However, transitioning from simulation to reality presented an array of challenges encompassing cabling intricacies, communication discrepancies, and mechanical nuances. Subsequent real-world assessments, primarily outlined in **PII** and **PIII**, were anchored in resolving these issues while maintaining the simulation as a vital feedback loop for refining the control system's efficacy. This harmonious interplay between simulation and experimentation facilitated a comprehensive understanding of system behavior and iteratively enhanced the control paradigm.

Validation and verification: The practical validation of the proposed solutions is a critical step to ascertain the feasibility and effectiveness of the designed prototypes. Throughout the research process, a series of experiments were conducted to validate the aerodynamic enhancements and control algorithms. In **PI**, laboratory tests were carried out on the heavy "DUTY HOPPER" prototype to assess the response of the EDFs and validate the dynamic model's performance. This testing phase enabled insights into rotor behavior and aided in improving controller performance. In **PAd**, real-world implementation of the model was accomplished with the "FAN HOPPER" prototype, which facilitated rigorous testing of the controller's response and overall stability during flight on a medium-sized platform. The results

from these experiments informed the progression to the larger prototype, "WILD HOPPER," discussed in **PII** and **PIII**. In this context, the focus shifted to thermal propulsion systems, and testing was conducted to validate the efficiency of the system under various payloads and scenarios. These experimental validations collectively contribute to the robustness and practicality of the proposed solutions, ensuring that the designed prototypes perform as intended in real-world conditions.

3.2 Technology Readiness Levels (TRLs)

In addition to the outlined methodology followed throughout the course of this thesis, the assessment of developed technologies in **PI**, **PII**, **PIII**, and **PAd** has been guided by applying TRLs to gauge their level of maturity. TRLs represent a method for gauging technological maturity during the acquisition phase of a program, originating from NASA's efforts in the 1970s as documented by Sadin et al., 1989. This method establishes a measurement scale spanning from 1 to 9, offering a standardized sequence of states. The primary objective of employing TRLs is to support managerial decision-making concerning technology development and transition. It serves as one of the tools required to effectively oversee the progression of research and development activities within an organization, as highlighted by Deutsch et al., 2010. By utilizing the TRL measurement scale, the advancement of a technology or system can be effectively traced, ranging from initial ideas documented in publications to fully compliant industry products. Consequently, TRLs are increasingly adopted by professionals such as engineers, scientists, innovators, and investors across various international organizations. The graphical representation of distinct technology readiness levels is depicted in Figure 3.2. Also, the progression of **PI**, **PII**, **PIII**, and **PAd** is illustrated in Figure 3.2, aligning each publication with its corresponding prototype as indicated in Figure 1.2.

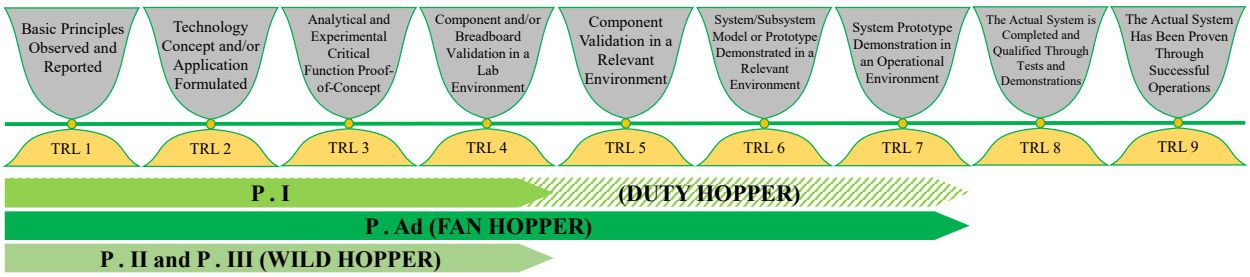

Figure 3.2: Brief descriptions of TRL levels and their progression within each publication.

Moreover, this thesis aligns with the TRL framework, establishing a standardized method to benchmark the developed research and technologies within the context of other related scientific endeavors. The terminology employed herein is precisely defined as follows:

Laboratory Environment Involves confined laboratory analysis and a test bench to formulate and validate the system's dynamics, albeit on a limited scale, as a preliminary step for more advanced experiments. This phase focuses on theoretical groundwork and lacks

operational application or a relevant model for comprehensive testing. **PI** addresses this level, and the subsequent year saw enhancements to the prototype studied, rendering it operational.

Relevant Environment Entails testing and refining a partially operational model, simulating operational challenges, and highlighting component functionality. This level bridges the gap between theoretical groundwork and complete operational deployment. **PII** and **PIII** delve into this level of testing and enhancement.

Operational Environment Characterized by a suitable operational setting in which the system is optimized for actual deployment. This phase encompasses refining specific functionalities and addressing operational requirements. **PAd** follows this progression to achieve an operational level of development.

This research aimed to adhere to the standard Technology Readiness Levels (TRLs) model; however, it experienced some degree of overlap with the established standards. As illustrated in Figure 3.2, **PI** reached TRL-4, signifying completion of laboratory studies and analyses. Subsequently, the "DUTY HOPPER" prototype underwent significant expansion, progressing to an operational environment level and corresponding to TRL-7. Similarly, **PAd** meticulously followed the design, simulation, and operational testing stages for the "FAN HOPPER" prototype, achieving a TRL-7. Lastly, **PII** and **PIII** elevated the combined experimental approach, advancing the "WILD HOPPER" model to TRL-4, while retaining the potential for future improvements to attain operational status due to thorough preparation and study. A concise overview of the TRLs is compiled in Table 1 from Annex D, providing a short reference for each level.

3.3 Publication Evolution

This section provides a brief overview of the key elements discussed and discovered in each publication. The findings from the previous sections will be summarized, outlining the progression of the project as reflected in these publications, thus creating a clear roadmap of the improvements and developments made over time.

3.3.1 Mathematical Modeling and Laboratory Environment (PI)

This publication mainly focused on the mathematical design of the heavy prototype "DUTY HOPPER," which at that time was in a laboratory mode, and the year after the publication, this work improved in modeling and design and finally became operational. The important notes of this paper are outlined as follows:

Mathematical Modeling: Detailed mathematical modeling is extensively discussed and refined in Sections 5.1 and 5.2.

Aerodynamic Considerations: Although briefly explained in Section 4, this section is better explained in **PI**.

Geometry Modeling: Various aspects are considered during the design phase, ranging from material selection for the entire body to minute details like screws, engines, airfoil profiles, and propeller types. An early non-confidential prototype of the "DUTY HOPPER" is showcased in Figure 4.2.

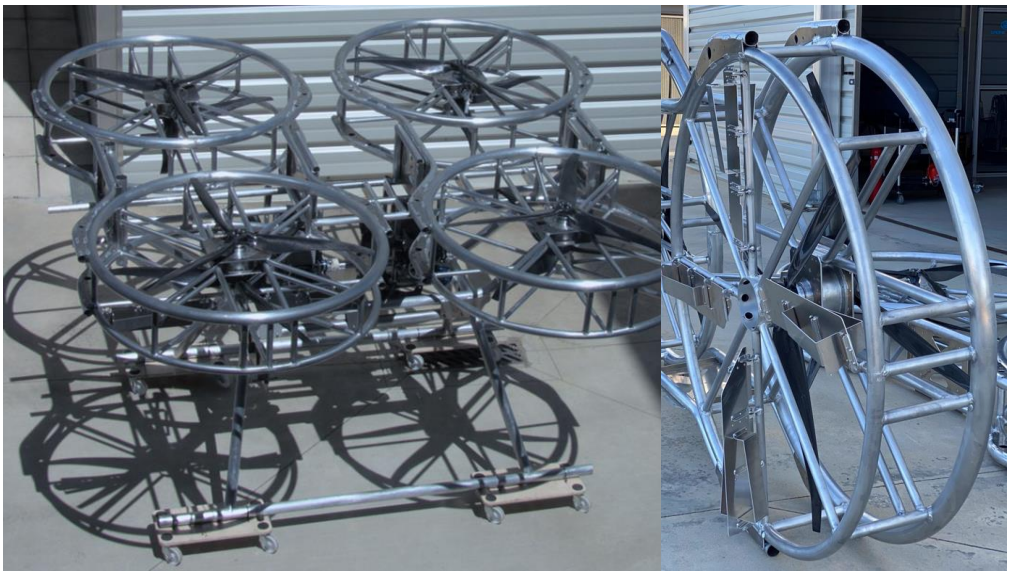

Figure 3.3: An initial non-confidential real schematic of the "DUTY HOPPER" prototype.

Control Strategy: The control algorithm employed to manage the intricate dynamics of the "DUTY HOPPER" is a Sliding Mode Control (SMC) strategy, properly detailed in Subsections 6.1.2 and 6.2.3. The ultimate control law outlined in this publication is as follows:

$$
\begin{aligned}
\ddot{x}_d &= -\lambda \dot{e}_x - K \tanh\left(S_x\right), \\
\ddot{y}_d &= -\lambda \dot{e}_y - K \tanh\left(S_y\right), \\
U_1 &= m\left(\ddot{z}_d - \lambda \dot{e}_z\right) - K \tanh\left(S_z\right), \\
U_2 &= \frac{I_x}{l}(\ddot{\phi}_d - \lambda \dot{e}_\phi) - K \tanh\left(S_\phi\right), \\
U_3 &= \frac{I_y}{l}(\ddot{\theta}_d - \lambda \dot{e}_\theta) - K \tanh\left(S_\theta\right), \\
U_4 &= I_z(\ddot{\psi}_d - \lambda \dot{e}_\psi) - K \tanh\left(S_\psi\right)
\end{aligned}
\tag{3.1}
$$

Simulation: The comprehensive modeling and simulation work is conducted using the MATLAB Simulink-SimScape platform. This simulation provided invaluable insights into components such as flap vane servos and allowed for an in-depth exploration of the dimensions of flap vanes relative to the duct's height, as observed in 7.1.

3.3.2 Operational Desing (PAd)

This publication is a continuation of Part I and focuses on achieving a more comprehensive understanding of aerodynamic elements to enhance overall modeling. It particularly emphasizes

a medium-sized platform called the "FAN HOPPER" as the initial step in real-world design. The research also investigates controller failures to improve performance for a larger prototype, the "DUTY HOPPER," as mentioned in Section 3.3.1. The paper provides a thorough examination of the target platform's functionality, covering laboratory analysis to final practical tests. The key steps and contributions of this paper are summarized as follows:

Medium-Scale Platform Concepts: This section offers concise geometry definitions and key insights from the design phase, with a particular focus on aerodynamic analysis. An official physical model of the "FAN HOPPER" is visually represented.

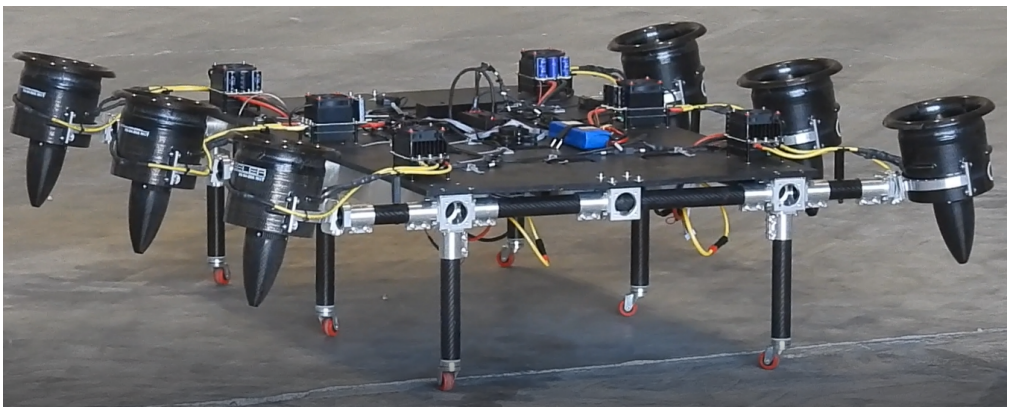

Figure 3.4: An official unrestricted real schematic of the "DUTY HOPPER" prototype.

Time-Varying Dynamics: A comprehensive understanding of the design's behavior, accounting for both solid and fluid payloads, is obtained through the study of time-varying dynamics. Further details are elaborated in Section 5.2.

Control Strategy: The control approach introduced in this paper revolves around MRAC to effectively account for variations in payload mass during flight. This control algorithm is rigorously examined and comprehensively defined in Subsections 6.1.1 and 6.2.2. Furthermore, the proposed control law bears resemblance to Equations 6.2 through 6.20, with detailed insights into its structure and functionality. The Lyapunov candidate function, along with a proof of its stability, is presented in Equations 6.7 and 6.8. These elements collectively form a robust foundation for the control strategy outlined in this research.

Simulation:, the simulation transitioned from MATLAB to Gazebo to provide enhanced insights into the dynamic performance of the controller and enhance the work thanks to the precise dynamic space of Gazebo. A concise overview of this transition process is detailed in the paper. Additionally, a notable outcome illustrating the consequences of an EDF failure during flight is presented in 7.1:

3.3.3 Improved Design (PII and PIII)

The culmination of experiences gained from multiple projects and the initial prototypes showcased in both **PI** and **PAd** forms the basis of final publications. It encompasses an array of facets, including design improvements, aerodynamic considerations, advancements in

the communication system, refined control methodologies, comprehensive simulations, and real-world field tests. Initially intended to emphasize the meticulously designed "DUTY HOPPER" model and its controller functionality, the paper evolved to encompass the final iteration of the "WILD HOPPER." This strategic shift marked a step closer to realizing the overarching project objective. Unfortunately, due to budgetary constraints, the project has been temporarily halted. However, there is optimism that it will resume in the close future, ultimately establishing itself as a thriving industrial platform among the select few thermally-powered MDFs currently operational. The key highlights of **PII** and **PIII** are summarized as follows:

Communication System: These papers commence by exploring various communication enhancements implemented in the platform, aimed at establishing robust external links between the MDF and the Ground Control Station (GCS), along with enhancing internal communication between the AP and the onboard computer with other subsystems. These improvements are detailed in **PII** and **PIII**. Additionally, the paper discusses the conceptual transition from the auxiliary usage of the EDFs, as employed in the previous prototype, to the implementation of a safe-landing concept, thereby eliminating the need for a redundant system. Further insights into this transformation can be found in Section 4. Figure 4.3 provides a conceptual schematic of the "WILD HOPPER," accompanied by detailed descriptions.

Aerodynamic Considerations: The **PII**'s aerodynamic approach primarily concentrated on optimizing the duct shape and blade geometry to enhance thrust production, as emphasized in Section 4.

Control Strategy: The control strategy employed in these papers was an optimized combination of the SMC presented in **PI** and the MRAC proposed in **PAd**. This control approach outperforms previous methods by accounting for both internal and external nonlinearities and uncertainties, making it a robust SMC technique. The controller theory and equations are detailed in Subsections 6.1.2 and 6.2.3.

Chapter 4

System Design

The overall system is treated as a unified mass, exhibiting either a 6 DOF or a 7 DOF configuration depending on the nature of the payload (solid or liquid). The translational movements encompass surge, sway, and heave, while the rotational aspects encompass roll, pitch, and yaw, which are graphically depicted in Figure 4.3, corresponding to the Euler angles ϕ, θ, and ψ. To elucidate further, the control solutions described across **P.I, P.II, and P.III** primarily address vertical dynamics and attitude, forming the foundation of the low-level control loop. Meanwhile, the high-level control loop, encompassing position control is delegated to the onboard AP, thereby consolidating the main objective of these publications is the provision of a tailored attitude controller that outperforms standard industrial PID solutions. These conventional PID controllers often entail time-consuming parameter tuning for specific platforms. Since many industrial APs already possess effective position controllers, an exhaustive reiteration of the entire process is rendered redundant. In fact, empirical observations reveal that, in many cases, the inherent firmware of APs stabilizes more proficiently than intricate nonlinear techniques to stabilize the position. However, the realm of attitude control presents a distinct scenario. Leveraging the unique characteristics of each platform, meticulous exploration can yield notably enhanced performance compared to conventional APs. This very essence underscores the essence of this thesis by compendium. Hereof, the overall moments and thrust forces generated by both main propellers and EDFs of the three platforms are demonstrated in Figures 4.1, 4.2, and 4.3. Moreover, the two main **Body-Fixed Frame (BFF)** and **Inertial Frame** where the dynamic equations are driven are highlighted and will be elaborated further.

Moreover, during the designing process, comprehensive consideration of multiple factors was pivotal in achieving the ultimate goal. As mentioned in Section 1.3, the conclusive development of the MDF encompassed pivotal criteria, namely the incorporation of an adept TVC mechanism utilizing flap vanes and an emphasis on attaining prolonged flight autonomy. These critical aspects guided the design approach, enabling a streamlined and expeditious progression. As an initial step towards delving into the realm of MDFs, a scaled-down prototype was meticulously crafted. This prototype served as a valuable tool for gaining deeper insights into the intricate dynamics of EDFs and exploring the realms of stability enhancement to optimize controller performance, as delineated in **PAd**. Thus, the meticulously

tailored MDF, referred to as "FAN HOPPER" in this publication, boasts distinctive attributes, which are succinctly enumerated below:

FAN HOPPER embodies a 6DOF hexa MDF system, leveraging electric propulsion technology that emulates the operational characteristics of conventional thermal engines. This design choice provides an avenue to explore and address the inherent uncertainties reminiscent of thermal motors within this context. Rigorous aerodynamic analyses were conducted, leading to significant enhancements across the entire platform. Notably, the innovative duct design yielded multiple benefits, including the attainment of a streamlined inlet and outlet airflow even at elevated horizontal velocities. Moreover, a remarkable reduction in undesired yaw moments, historically associated with instability in high-powered multi-rotor propellers, was observed. This achievement is particularly noteworthy as the constrained space between the duct wall and the rotor blades virtually eliminates yawing, thereby contributing to enhanced stability. Consequently, the consideration of rotor rotation direction becomes superfluous, and as illustrated in Figure 4.1, the EDFs exhibit uniform rotation due to their near-zero yawing moments. Furthermore, as depicted in the figure, empirical investigations led to the incorporation of an optimized Angle of Incidence (AOI), enhancing stabilization during yawing. This concept is further described in **PII**, providing a better insight into its implementation and impact.

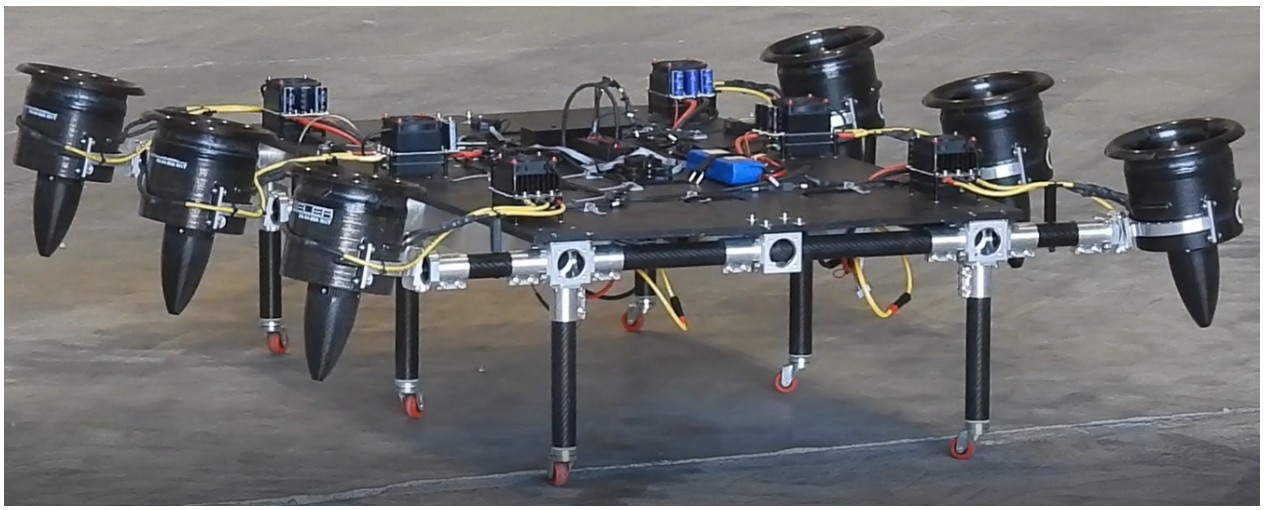

Figure 4.1: The general coordinate system based on the FAN HOPPER prototype; T_i and M_i are thrusts and moments generated by the EDFs, δ is the Angel of Incidence (AOI) of EDFs according to experiment, $\{\}_b$ is the subscript for the body-fixed frame, and $\{\}_E$ is the subscript for the inertial frame.

In the next step, a significant milestone was achieved by developing a larger-scale prototype intended to be fitted with thermal engines, thereby advancing toward the ultimate objective. This design endeavor was fortified by meticulous modeling, expounded upon in **PI**, which furnished a comprehensive mathematical representation of the dynamic system governing the extensive MDF. Noteworthy traits of this UAV, dubbed "DUTY HOPPER," are succinctly outlined as follows.

DUTY HOPPER is a 6DOF quad MDF system harnessing thermal propulsion technology through the integration of two longitudinally aligned motors. This configuration also boasts the capability to accommodate Lipo batteries for supplementary attitude stabilization. Detailed in **PI**, it marked the pioneering instance of laboratory modeling and design. Subsequently, to enhance controller performance, several tests were conducted, including the incorporation of diverse payloads (solid and liquid), culminating in the development of a standardized prototype. By utilizing thermal engines, this platform obviates the need for ESCs in the main ducts, instead adopting an ECU system to translate AP commands for propeller control and maintain a consistent angular velocity across all propellers using a simple PID for different RPM bounds, ensuring safe takeoff and landing. Attitude regulation is achieved via flap vanes, as depicted in Figure 4.2, wherein commanded surge, sway, and heave movements are doubly derived to suitably control Euler angles ϕ, θ, and ψ. Furthermore, Figure 4.2 elucidates the configuration of each duct, the inlet airflow, and a schema of rotational flap vanes that are described further in 5.2. Comprehensive insights into these aspects are unveiled in **PII** and **PIII**. Notably, based on experimental findings, each flap's rotation is constrained within a $\pm 15°$ range to avert mechanical interference with other flap rotations during both modeling and operational phases.

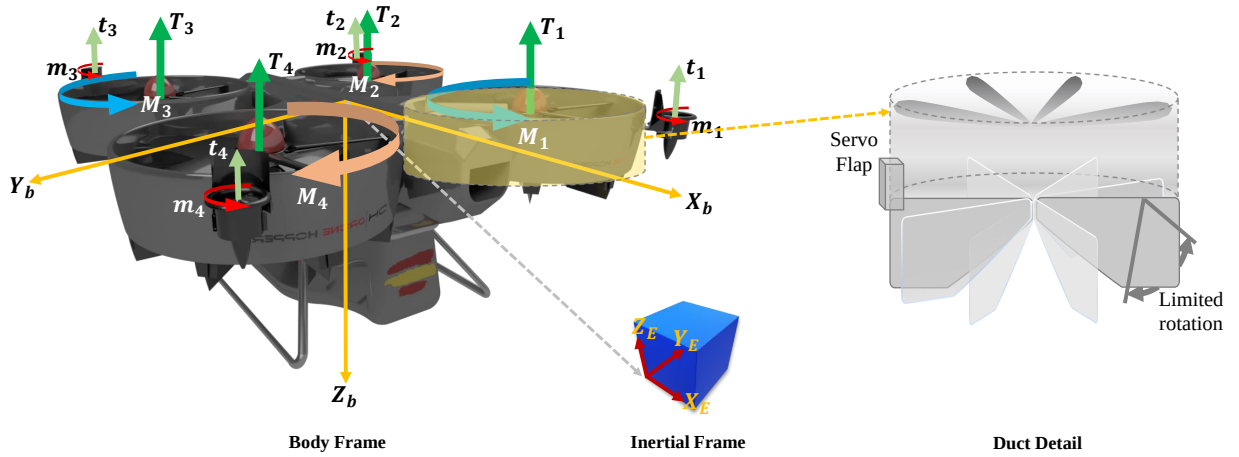

Figure 4.2: The general coordinate system based on the DUTY HOPPER prototype; T_i and M_i are thrusts and moments generated by the main ducts, t_i and m_i are thrusts and moments generated by the EDFs, $\{\}_b$ is the subscript for the body-fixed frame, and $\{\}_E$ is the subscript for the inertial frame.

Finally, in the concluding stage, a synthesis of the preceding experiments led to the development of an advanced, larger-scale prototype tailored for integration with thermal engines. The comprehensive evolution encompassing enhanced modeling, refined control algorithms, and meticulous simulations culminated in **PII** and **PIII**. This iteration witnessed significant advancements in power supply, safety measures, communication systems, auxiliary EDF concepts, and overall geometry. Aptly named "WILD HOPPER," this ultimate prototype encapsulates these refinements in a coherent design as follows.

WILD HOPPER is a hexa MDF platform featuring 6 DOF, equipped with six main ducts and four auxiliary EDFs for safety and emergency situations, as elaborated in **PII** and **PIII**. This prototype operates on two power sources: primary propellers are fueled by thermal energy, while EDFs are powered by Lipo batteries. The payload compartment can handle up to 60% of the total weight. The configuration, depicted in Figure 4.3, outlines forces, moments, rotations, movements, and frame connections between the **BFF** and **Inertial Frame**. The model has been extensively enhanced. Notable improvements include refining the aerodynamic model with blade tip angle adjustments and blade count optimization for superior thrust. The communication system received upgrades, incorporating redundancy for reliable short and long-distance links. Employing a TVC strategy, the control system employs geometrically enhanced flap vanes as control surfaces, evolved iteratively during design.

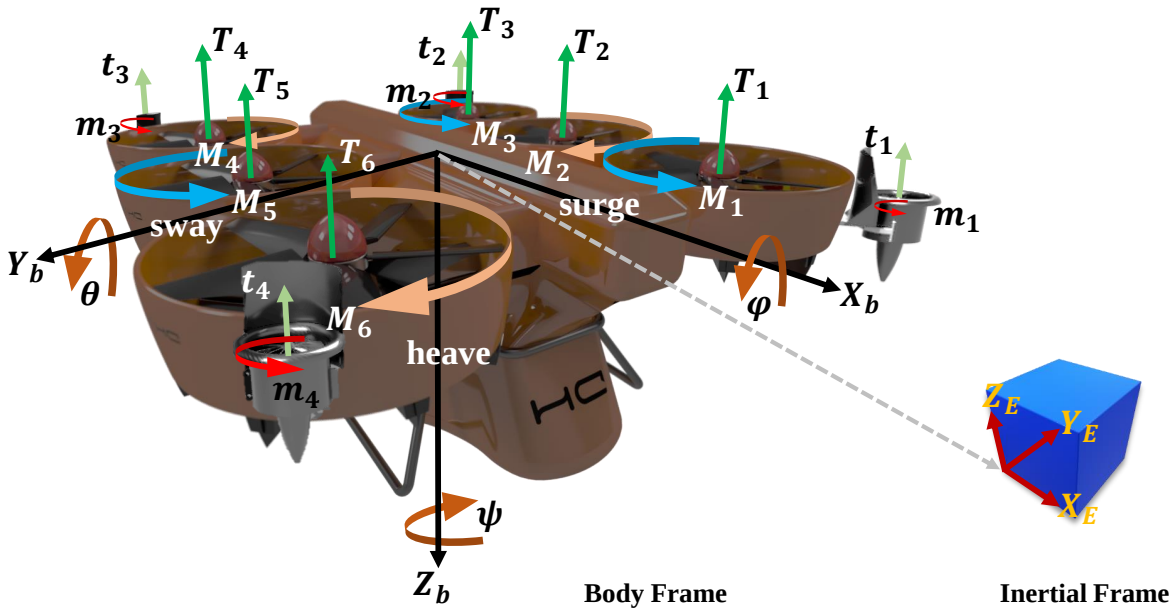

Figure 4.3: The general coordinate system based on the final WILD HOPPER prototype; T_i and M_i are thrusts and moments generated by the main ducts, t_i and m_i are thrusts and moments generated by the EDFs, $\{\}_b$ is the subscript for the body-fixed frame, and $\{\}_E$ is the subscript for the inertial frame.

Chapter 5

System Dynamics

This section aims to provide a comprehensive insight into the author's work by offering an in-depth understanding of the applied modeling, design, and control methodologies across three distinct platforms. Each level of development, spanning from **PI** to **PIII** and **PAd**, is accompanied by insightful cues for cross-referencing. The core objective of this section is to offer a comprehensive elucidation of the mathematical equations and control algorithms utilized in the publications. This is particularly important as the publications necessitate succinct descriptions in a standardized format, thereby warranting a more elaborate exposition here. The section is organized into two primary subsections: "General Modeling" and "Specific Modeling". These terms encompass both conventional MDFs or general multirotor types initially and subsequently narrow down to delineate the model of an MDF steered by TVC utilizing flap vanes. To ensure uniformity, the equations are harmonized based on the final hexa "WILD HOPPER" prototype as illustrated in Figure 4.3.

5.1 General Modeling (PI and PAd)

Given the 6DOF rigid body of an MDF as a complex Multi-Input Multi-Output (MIMO) system due to its nonlinear configuration, the governing equations can be derived from the Newton-Euler equation set. These equations are formulated with respect to either the **BFF** or **Earth-Fixed Frame (EFF)**, which are denoted as subscript $\{\}_b$ and $\{\}_e$, respectively.

$$
\begin{aligned}
\mathbf{v_b} &= \begin{bmatrix} u & v & w \end{bmatrix}^T, \\
\omega_\mathbf{b} &= \begin{bmatrix} p & q & r \end{bmatrix}^T, \\
\mathbf{I_b} &= \begin{bmatrix} I_{xx} & 0 & 0 \\ 0 & I_{yy} & 0 \\ 0 & 0 & I_{zz} \end{bmatrix}, \\
\mathbf{F_b} &= F_{\text{grav}} + F_{\text{fuse}} + F_{\text{prop}} + F_{\text{duct}} + F_{\text{edf}} + F_{\text{fv}}, \\
\mathbf{M_b} &= M_{\text{gyro}} + M_{\text{prop}} + M_{\text{duct}} + M_{\text{edf}} + M_{\text{fv}}, \\
\dot{\mathbf{v}}_\mathbf{b} &= -\omega_\mathbf{b} \times \mathbf{v_b} + \frac{1}{m_b}(\mathbf{F_b} + F_{\text{grav}}), \\
\dot{\omega}_\mathbf{b} &= \mathbf{I_b}^{-1}(\mathbf{M_b} - \omega_\mathbf{b} \times \mathbf{I_b} \times \omega_\mathbf{b}),
\end{aligned}
\tag{5.1}
$$

In Equations 5.1, $\mathbf{v_b}$ corresponds to the velocity vector in the BFF, and $\omega_\mathbf{b}$ represents the angular velocity vector in the same frame. The variables u, v, and ω denote the airframe velocities in the BFF, while p, q, and r refer to the angular rates around the respective axes. Furthermore, F_b and M_b denote the total forces and moments acting in the BFF. The quantities $\dot{\mathbf{v}}_\mathbf{b}$ and $\dot{\omega}_\mathbf{b}$ symbolize the time derivatives of the velocity and angular velocity vectors, respectively. The parameters m_b and $\mathbf{I_b}$ signify the body mass and inertia, respectively. Due to the Hexa MDF's symmetrical geometry, only diagonal inertias are taken into account in the inertia matrix, where $I_{xx} = I_x$, $I_{yy} = I_y$, and $I_{zz} = I_z$. The subscripts (e.g., fv $\simeq$ flap vanes, grav $\simeq$ gravity, fuse $\simeq$ fuselage, etc.) indicate various factors contributing to the forces and moments, which are elaborated on in more detail in **PI**.

It's worth noting the distinction between F_{prop} and F_{duct}, which may initially seem equal, but they serve distinct roles, and both contribute to force generation in the BFF. This distinction is as follows.

> **Propeller Thrust ($\mathbf{F_{prop}}$)**: The primary thrust in a DF system originates from the propeller or fan itself. As the fan's blades rotate, they create an airflow that generates thrust by propelling the air in the opposite direction, in accordance with Newton's third law of motion. This thrust is the central driver of propulsion.
>
> **Duct Thrust ($\mathbf{F_{duct}}$)**: The duct that surrounds the fan plays a critical role in optimizing the propeller's performance. By guiding and channeling the airflow generated by the fan, the duct minimizes air loss and enhances the system's overall efficiency. While the duct doesn't generate thrust in the same direct manner as the propeller, its design significantly influences the system's total thrust generation. This aspect is particularly emphasized in the context of **PI**, **PII**, **PIII**, and **PAd**, where the overall system efficiency is a focus.

Subsequently, by translating the velocities and attitudes between the BFF and the Inertial frame yields:

$$
\begin{aligned}
\mathbf{r} &= \begin{bmatrix} x & y & z \end{bmatrix}^T, \\
\alpha &= \begin{bmatrix} \phi & \theta & \psi \end{bmatrix}^T, \\
\mathbf{C_{eb}} &= \begin{bmatrix} c(\psi)c(\theta) & c(\psi)s(\theta)s(\phi) - s(\psi)c(\phi) & c(\psi)s(\theta)c(\phi) + s(\psi)s(\phi) \\ s(\psi)c(\theta) & s(\psi)s(\theta)s(\phi) + c(\psi)c(\phi) & s(\psi)s(\theta)c(\phi) - c(\psi)s(\phi) \\ -s(\theta) & c(\theta)s(\phi) & c(\theta)c(\phi) \end{bmatrix}, \\
\mathbf{v_e} &= \begin{bmatrix} \dot{x} & \dot{y} & \dot{z} \end{bmatrix}^T = \mathbf{C_{eb}}\mathbf{v_b}, \\
\dot{\alpha} &= \begin{bmatrix} 1 & s(\phi)t(\theta) & c(\phi)t(\theta) \\ 0 & c(\phi) & -s(\phi) \\ 0 & s(\phi)/c(\theta) & c(\phi)/c(\theta) \end{bmatrix} \omega_\mathbf{b},
\end{aligned}
\tag{5.2}
$$

In Equations 5.2, the symbol $\mathbf{r}$ represents the location vector observed in the EFF, while $\mathbf{C_{eb}}$ stands for the rotation matrix that corresponds to the airframe's yaw, pitch, and roll transformations from the Earth-Fixed Frame to the BFF. This pivotal matrix is known as the Direction Cosine Matrix (DCM). The functions $s()$, $c()$, and $t()$ signify the sine, cosine, and tangent functions, respectively. The symbol α refers to the Euler angles vector, while $\mathbf{v_e}$ represents the velocity vector in the EFF, which is equivalent to the velocity vector in the BFF after being multiplied by the rotation matrix. Additionally, the time derivatives of the Euler angles are determined by the angular velocity in the BFF and are multiplied by the rotational matrix to account for the transformation.

By substituting the moments into the Newton-Euler equation, the specified dynamic equations can be determined. Further, the rotation dynamics equations can be obtained by considering the acceleration in EFF and the BFF, resulting in:

$$
\begin{aligned}
\mathbf{F_b} &= \begin{bmatrix} F_{b_x} & F_{b_y} & F_{b_z} \end{bmatrix}^T, \\
\mathbf{M_b} &= \begin{bmatrix} M_{b_x} & M_{b_y} & M_{b_z} \end{bmatrix}^T, \\
\mathbf{F_{b_x}} &= m_b(\dot{u} + gs(\theta) + qw - rv), \\
\mathbf{F_{b_y}} &= m_b(\dot{v} - gc(\theta)c(\phi) + ru - pw), \\
\mathbf{F_{b_z}} &= \mathbf{F_b} - m_b(\dot{w} - gc(\theta)c(\phi) + pv - qu), \\
\mathbf{M_{b_x}} &= I_x\dot{p} + (I_z - I_y)qr - I_p\omega_p q, \\
\mathbf{M_{b_y}} &= I_y\dot{q} + (I_x - I_z)rp + I_p\omega_p p, \\
\mathbf{M_{b_z}} &= I_z\dot{r} + (I_y - I_x)pq + I_p\dot{\omega}_p - Q, \\
\rightarrow \dot{\omega}_\mathbf{b} &= \begin{bmatrix} \dot{p} & \dot{q} & \dot{r} \end{bmatrix}^T = \begin{pmatrix} \left((I_y - I_z)qr + I_p\omega_p q + \mathbf{M_{b_x}}\right)/I_x \\ \left((I_z - I_x)rp - I_p\omega_p p + \mathbf{M_{b_y}}\right)/I_y \\ \left((I_x - I_y)pq - I_p\dot{\omega}_p + \mathbf{M_{b_z}} + Q\right)/I_z \end{pmatrix}, \\
\rightarrow \dot{\mathbf{v}}_\mathbf{b} &= \begin{bmatrix} \dot{u} & \dot{v} & \dot{w} \end{bmatrix}^T = \begin{pmatrix} \mathbf{F_{b_x}}/m_b - gs(\theta) + rv - qw \\ \mathbf{F_{b_y}}/m_b + gc(\theta)c(\phi) + pw - ru \\ (\mathbf{F_b} - \mathbf{F_{b_z}})/m_b + gc(\theta)c(\phi) + qu - pv \end{pmatrix}
\end{aligned}
\tag{5.3}
$$

Through Equations 5.3, the symbols I_p and ω_p refer to the inertia and angular rate of the propellers, respectively. Additionally, M_{b_x}, M_{b_y}, and M_{b_z} represent the moments along different axes in the BFF, while F_{b_x}, F_{b_y}, and F_{b_z} denote forces on the corresponding coordinate axes in the BFF. The term Q denotes the propeller's anti-torque, and g represents the gravitational acceleration.

Now, let's consider a duct and delve into the dynamic equation corresponding to the aerodynamic interactions with the duct and the turning effects induced by the propeller, as illustrated in Figure 5.1.

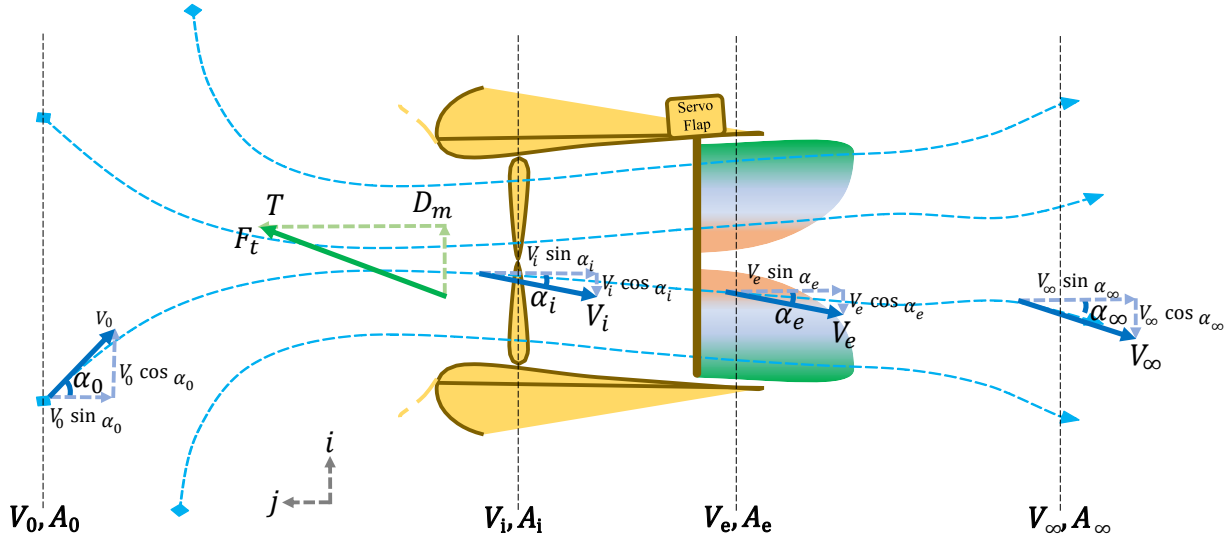

Figure 5.1: Schematic of the free airstream passing through a duct, analyzed in four stages: upstream, propeller inlet, outlet, and downstream.

Figure 5.1 provides a visual representation of the various stages of the free airstream as it traverses through a duct. These stages encompass the upstream, propeller inlet, outlet, and downstream portions. Subscripts $\{\}_0$ correspond to the upstream airflow well before it enters the duct, $\{\}_i$ pertains to the inlet airflow, $\{\}_e$ signifies the exit or outlet airflow, and $\{\}_\infty$ represents the downstream airflow much further from the duct. Additionally, α, V, and A respectively denote the airflow angle, velocity, and planar area at each stage. Additionally, angles α_i and α_e, corresponding to the airflow angle within the duct inlet and the airflow angle at the outlet of the duct, respectively, can be determined as follows:

$$
\begin{aligned}
\alpha_{\mathbf{i}} &= \alpha_0 + k_i \left(\frac{\pi}{2} - \alpha_0 \right), \\
\alpha_{\mathbf{e}} &= \alpha_0 + k_e \left(\frac{\pi}{2} - \alpha_0 \right), \\
\alpha_\infty &= \alpha_0 + k_\infty \left(\frac{\pi}{2} - \alpha_0 \right),
\end{aligned}
\tag{5.4}
$$

In Equations 5.4, the terms k_i, k_e, and k_∞ correspond to flow turning efficiency factors influenced by the inlet propeller plane, the outlet plane, and the downstream region far from

the duct. It's important to note that in various articles, notably Shan et al., 2016, Wang et al., 2014, Tobias and Horn, 2008, Xiaoliang et al., 2018, and Zhang et al., 2016, a single airflow angle is commonly utilized for both α_e and α_∞. This approach simplifies the assumption or utilizes an average value for the angle of deflection at a specific downstream point, often situated far from the duct exit. This choice facilitates an understanding of the aerodynamic behavior without delving into the intricacies of specific flow interactions. Now, based on the airflow angle at various stages, the velocities at the upstream, duct inlet, outlet, and downstream can be expressed as follows:

$$\begin{aligned}
\mathbf{V_0} &= V_0\cos(\alpha_0)i - V_0\sin(\alpha_0)j,\\
\mathbf{V_i} &= V_0\cos(\alpha_\mathbf{i})i - (V_0\sin(\alpha_\mathbf{i}) + v_i)j,\\
\mathbf{V_e} &= V_0\cos(\alpha_\mathbf{e})i - (V_0\sin(\alpha_\mathbf{e}) + v_e)j,\\
\mathbf{V}_\infty &= V_0\cos(\alpha_\infty)i - (V_0\sin(\alpha_\infty) + v_\infty)\,j,
\end{aligned} \tag{5.5}$$

Using Equations 5.5, the terms v_i, v_e, and v_∞ represent the induced speeds caused by the airflow as it passes through the duct. Besides, the induced exit velocity is also well-known as slipstream velocity Zhao, 2009. These speeds are oriented vertically, in the same direction as the vertical axis. Furthermore, as shown in Figure 5.1, the total force vector generated by the duct system is denoted as F_t, which is assumed to comprise a vertical thrust component, T, and a horizontal momentum drag component, D_m. Specifically, T encompasses the combined thrust produced by both the propeller and the duct itself, leading to the equation:

$$\begin{aligned}
\mathbf{F_{duct_t}} &= D_m i + Tj,\\
\mathbf{T} &= F_{prop} + F_{duct} = F_{prop}(1 + k_{aug})
\end{aligned} \tag{5.6}$$

In Equation 5.6, the symbol k_{aug} denotes the Thrust Augmentation Factor (TAF), which signifies the influence of the duct's lift effect. A TAF value of 1 indicates that the total thrust generated is twice that of the propeller thrust alone. This rationale underscores the selection of the DF model, as it effectively enhances the overall system efficiency. Now, when taking into account the airflow mass rate, as well as the horizontal and vertical thrust forces, the following expressions are applicable:

$$\begin{aligned}
\dot{\mathbf{m}} &= \rho A_i V_i,\\
\mathbf{T} &= \dot{\mathbf{m}}\,(\mathbf{V_e} - V_0)\\
&\xrightarrow{\text{Simplifying}} \mathbf{T} = \dot{\mathbf{m}}(\mathbf{V}_\infty - V_0)\\
&\xrightarrow{\text{Simplifying}} \mathbf{T} = \dot{\mathbf{m}}(\sin(\alpha_\infty) - \sin(\alpha_0))V_0 + v_\infty,\\
\mathbf{D_m} &= \dot{\mathbf{m}}\,(\cos(\alpha_0) - \cos(\alpha_e))\,V_0\\
&\xrightarrow{\text{Simplifying}} \mathbf{D_m} = \dot{\mathbf{m}}\,(\cos(\alpha_0) - \cos(\alpha_\infty))\,V_0
\end{aligned} \tag{5.7}$$

Equations 5.7 are obtained assuming the conservation of energy, momentum, and the mass flow rate from the inlet of the duct to the downstream. ρ is the density of the airstream, and

for simplifying the $\alpha_e = \alpha_\infty$ and $V_e = V_\infty$. Finally, the whole force generated by the duct system is determined as follows,

$$\mathbf{F_{duct_t}} = 2\rho A_i \left(\frac{1}{1+k_{aug}} \left(V_0 \sin(\alpha_i) + v_i \right) - V_0 \sin(\alpha_0) \right) \sqrt{V_0^2 + 2V_0 v_i \sin(\alpha_i) + v_i^2} \tag{5.8}$$

The total force, denoted as $\mathbf{F_{duct_t}}$ in Equation 5.8, can also be expressed and simplified in a vectorized manner as follows. Additionally, based on the equations detailed in 5.1 and described in **PI**, the remaining forces and moments acting on the BFF can be presented as follows:

$$\begin{aligned}
\mathbf{F_{grav}} &= \begin{bmatrix} -mg\sin\theta \\ mg\cos\theta\sin\phi \\ mg\cos\theta\cos\theta \end{bmatrix}, \\
\mathbf{F_{fuse}} &= -0.5\rho \begin{bmatrix} C_{D_x} u_b |u_b| A_{side} \\ C_{D_y} v_b |v_b| A_{side} \\ C_{D_z} w_b |w_b| A_{top}, \end{bmatrix}, \\
\mathbf{F_{prop}} &= 0.5\rho A_i b \Omega_p^2 \begin{bmatrix} C_{D_{bl}} \sin\alpha_{bl} \sin\theta_{bl} \\ -C_{D_{bl}} \sin\alpha_{bl} \sin\theta_{bl} \\ C_{L_{bl}} \cos\alpha_{bl} \cos\theta_{bl} \end{bmatrix}, \\
\mathbf{F_{duct}} &= D_m + K_{aug} F_{prop} = 0.5\rho C_{D_{duct}} \begin{bmatrix} A_e u_0 |u_0| \\ A_e v_0 |v_0| \\ A_i K_{aug} V_i |V_i| \end{bmatrix}, \\
\mathbf{M_{gyro}} &= NJ\omega \begin{bmatrix} -q \\ p \\ 0 \end{bmatrix}, \\
\mathbf{M_{duct}} &= \begin{bmatrix} F_{duct_y} r \\ F_{duct_x} r \\ F_{duct_z} l_d \end{bmatrix}
\end{aligned} \tag{5.9}$$

In Equations 5.9, certain parameters are defined as follows: N represents the number of propellers, J denotes the rotor inertia, while p and q correspond to the angular rates of the propellers, discussed by Fan et al., 2018, Johnson and Turbe, 2006. It is important to note that this equation is applicable when the angular rates are assumed to be semi-constant, irrespective of any aggressive flight behavior. Additionally, C_D stands for the drag coefficient of the fuselage, A_{side} represents the cross-sectional area of the drone, assuming symmetry on both sides, and A_{top} denotes the top area of the MDF. The blade pitch is denoted as θ_{bl}, and the blade incidence angle is represented by α_{bl}, which in hover flight conditions, both θ_b and α_b are considered negligible due to their small values. The Ω_p corresponds to the propeller angular velocity, b is the thrust factor of the propeller, and $C_{D_{bl}}$ and $C_{L_{bl}}$ are the drag and lift coefficients of the propeller blades. The parameter $C_{D_{duct}}$ stands for the duct moment coefficient, serving as a proportionality constant that relates the moment to the dynamic

pressure caused by crosswind effects, introduced by Johnson and Turbe, 2006. Referring to Figure 5.1, the variables V_0 represent the duct inlet air velocity, r corresponds to the duct exit radius, l_d is the diagonal distance between the Center of Pressure (COP) of the duct to the COG of the MDF, and finally, V_0, A_i, V_e, and A_e represent the rotor plane and duct exit velocities and areas, respectively.

5.2 Specific Modeling (PI, PII, PIII, and PAd)

In this subsection, the author aims to highlight the distinctive features of this thesis pertaining to **PI**, **PII**, **PIII**, and **PAd**. The equations presented here have been integral to the design process of the three primary prototypes and have undergone practical validation.

Starting from the ground up, envisioning a scenario involving a large MDF in which the payload could be either solid or fluid, the equations of motion for a solid mass were derived in the previous Subsection 5.1. Now, turning the attention to the latter payload type – fluid, which is applicable to the real case of the "DUTY HOPPER" prototype. In this context, the dynamics of the liquid within the drone's repository introduce an additional degree of freedom due to the newly induced motions and rotations. This could potentially lead to an expanded system with up to 96DOF, as discussed in **PAd**. However, to simplify the problem, only one degree is added to the system. These newly derived equations represent a 7DOF system. For a more in-depth understanding, readers are encouraged to explore publications that delve into the dynamics of DFs with manipulators, such as those authored by Zhang et al., 2018 and Zhang et al., 2020.

Taking into account Figure 5.1 and Equations 5.4, it becomes imperative to account for even minor phenomena that might go unnoticed in conventional scenarios due to the large scale of the MDF. An example of such a consideration is the Wake Skew Angle (WSA) of the airflow, which correlates with α_i, α_e, and α_∞ as depicted in Figure 5.1. This entails:

$$\begin{aligned}
\xi_{\mathbf{i}} &= \arctan\left(\frac{V_0\cos(\alpha_i)}{V_0\sin(\alpha_i)+v_i}\right),\\
\xi_{\mathbf{e}} &= \arctan\left(\frac{V_0\cos(\alpha_e)}{V_0\sin(\alpha_e)+v_e}\right),\\
\xi_{\infty} &= \arctan\left(\frac{V_0\cos(\alpha_\infty)}{V_0\sin(\alpha_\infty)+v_\infty}\right)
\end{aligned} \tag{5.10}$$

In Equations 5.10, the symbol ξ denotes the WSA, representing the angle that characterizes the skewness of the wake airflow. This angle quantifies the misalignment between the direction of the wake and the flight path of the drone. On the other hand, the high spinning of the propeller induces a drag force, resulting in a swirling motion of the flow. This effect introduces a swirl velocity into the flow, which can be described as follows:

$$\omega_{\mathbf{swirl}} = \frac{M_{prop}}{\frac{1}{2}\rho A_i V_i r_{prop}^2} \tag{5.11}$$

In Equation 5.11, M_{prop} represents the propeller torque, and r_{prop} is the radius of the propeller. The swirl velocity has a direct influence on the vertical component of the flap vanes' velocity. Taking into account the previously mentioned V_e in both horizontal and vertical directions, it yields:

$$\mathbf{V_e} = \begin{bmatrix} u_e \\ v_e \\ w_e \end{bmatrix} = \begin{bmatrix} V_e \sin(\alpha_e) \\ 0 \\ V_e \cos(\alpha_e) \end{bmatrix} \tag{5.12}$$

In Equations 5.12, $\mathbf{u_e}$ and $\mathbf{w_e}$ represent the two components of the total outlet velocity, corresponding to the x and z axes, respectively. Introducing the flap vane velocity components in all three dimensions as V_{fv}, we arrive at the following set of equations:

$$\begin{aligned} \mathbf{V_{fv}} &= \begin{bmatrix} u_{fv} & v_{fv} & w_{fv} \end{bmatrix}^T, \\ \mathbf{V_{fv}} &= \begin{bmatrix} 0 & 0 & -1 \\ -1 & 0 & 0 \\ 0 & 1 & 0 \end{bmatrix} \begin{bmatrix} \cos(\delta_{fv}) & -\sin(\delta_{fv}) & 0 \\ \sin(\delta_{fv}) & -\cos(\delta_{fv}) & 0 \\ 0 & 0 & 1 \end{bmatrix} \begin{bmatrix} \mathbf{u_e}\cos(\delta_{fv}) \\ \mathbf{u_e}\sin(\delta_{fv}) \\ -\mathbf{w_e} \end{bmatrix} + \begin{bmatrix} 0 \\ 0 \\ r\omega_{\mathbf{swirl}} \end{bmatrix}, \\ \rightarrow \mathbf{V_{fv}} &= \begin{bmatrix} \mathbf{u_e}\sin(\delta_{fv}) \\ -\mathbf{u_e}\cos(\delta_{fv}) \\ r\omega_{\mathbf{swirl}} - \mathbf{w_e} \end{bmatrix} \end{aligned} \tag{5.13}$$

Equation 5.13 introduces three crucial variables: u_{fv}, v_{fv}, and w_{fv}, signifying the chordwise, spanwise, and normal constituents of the flap vane velocity. These variables derive their values from the influence of the outlet airstream exhaust emanating from the duct. The parameter δ_{fv}, equivalent to the vane's deflection angle or the widely acknowledged azimuthal angle ϕ, constitutes a pivotal aspect. This angle delineates the divergence between the vertical axis and the projection of the COP of the vane upon the horizontal plane. For an intricate depiction of the utilized flap vanes, refer to Figure 5.2. This illustrative diagram aptly showcases the three principal rotations imperative for generating roll, pitch, and yaw moments in the pursuit of optimal functionality.

Furthermore, let's represent the downwash angle induced by the duct, which is usually negative due to the propeller that creates an airflow that is directed downward. It is also related to the lift force of the duct by the following expression:

$$
\begin{aligned}
\gamma_{\mathbf{d}} &= \frac{\mathbf{F_{duct}}}{\dot{m} v_e}, \\
\gamma_{\mathbf{d}} &= \begin{bmatrix} \gamma_{d_x} \\ \gamma_{d_y} \end{bmatrix} = \begin{bmatrix} \mathbf{F_{duct}} / \left(\rho \pi r^2 \left((v_i - v_z)^2 + v_x^2\right)\right) \\ \mathbf{F_x} / \left(\rho \pi r^2 \left((v_i - v_z)^2 + v_y^2\right)\right) \end{bmatrix}, \\
\mathbf{V_{fv}} &= \begin{bmatrix} u_{fv} \\ v_{fv} \\ w_{fv} \end{bmatrix} = \begin{bmatrix} u_{fv_p} & u_{fv_r} & u_{fv_y} \\ v_{fv_p} & v_{fv_r} & v_{fv_y} \\ w_{fv_p} & w_{fv_r} & w_{fv_y} \end{bmatrix}, \\
\delta_{\mathbf{fv}} &= \begin{pmatrix} \alpha_{fv} \\ \beta_{fv} \\ \epsilon_{fv} \end{pmatrix} = \begin{pmatrix} \delta_{fv} + \arctan 2\left(-u_{fv_p} - v_{fv_p} l_{fv}, v_i - w_{fv_p}\right) - \gamma_{\mathbf{d_x}} \\ -\delta_{fv} + \arctan 2\left(-v_{fv_r} - u_{fv_r} l_{fv}, v_i - w_{fv_r}\right) - \gamma_{\mathbf{d_y}} \\ \delta_{fv} + \arctan 2\left(-v_{fv_y} l_{fv}, v_i - w_{fv_y}\right) \end{pmatrix}
\end{aligned}
\tag{5.14}
$$

In Equations 5.14, the downwash angle (γ_d) is calculated based on the total duct thrust (as defined in Equation 5.8), the mass airflow passing through the duct (refer to Equation 5.7), and the exit velocity. This equation unveils the significant impact of the downwash angle on the final azimuthal angle of the flap vanes. In practical scenarios, such as the "WILD HOPPER" platform with a wide-diameter exhaust, the downwash angle deviates from the ideal conditions considered during the design process. This deviation carries implications, particularly for large-scale systems. Considering the three rotational angle axes for the vane azimuthal angle, we have α_{fv} (longitudinal direction), β_{fv} (lateral direction), and ϵ_{fv} (vertical direction). To account for the entire body's angular velocity, induced velocity (v_i) at the flap vane neighborhood is factored in. Additionally, the distance between the Center of Gravity (COG) of the MDF and the Center of Pressure (COP) of the flap vane (or their aerodynamic center), represented as l_{fv}, plays a crucial role in these calculations. For a more detailed discussion on these aspects, refer to Johnson and Turbe, 2006. The velocity of the flap vanes is expressed in Equations 5.14 as a 3×3 matrix, delineating each element corresponding to pitch ($\{\}_{fv_p}$), roll ($\{\}_{fv_r}$), and yaw ($\{\}_{fv_y}$) flap vanes.

The downwash angle influences various aspects, notably the effectiveness of control surfaces. It does so by altering the relative airflow over these surfaces and modifying the effective angle of attack of the flap vanes. Since control surfaces are essentially movable flat-plate lifting structures, changes in their angles can significantly affect their ability to generate lift or control forces. The downwash angle can be further divided into surge and sway components, denoted as γ_{d_x} and γ_{d_y}. Notably, it lacks a Z-component in conventional flight situations, primarily pertaining to horizontal airflow patterns around the aircraft.

Broadly, in this thesis, there exist two types of flap vanes: lateral and longitudinal. Longitudinal vanes (roll flaps) align similarly with the X-axis (pitch flaps), while lateral vanes align with the Y-axis direction, and yaw flaps are a combination of these two, as illustrated in Figure 5.2. This visual also showcases three unique vane arrangements alongside a singular duct outfitted with all flap vanes for component exposition. These arrangements share a consistent perspective, "Top-Down View," from a third eye toward the MDF model. In this view, the positive X-axis denotes the rightward direction, the positive Y-axis extends downward, and the positive Z-axis projects into the page. Importantly, each axis corresponds to a positive

moment rotation in adherence to Fleming's right-hand rule. These three modes are elucidated as follows:

Upper-Left (a): The generation of rolling moments involves the coordinated movement of all longitudinal flap vanes set at the same azimuthal angle. This synchronized action uniformly produces a moment along the roll axis (X-axis), as indicated by the circular green arrow.

Upper-Right (b): Generating yawing moments requires the collaboration of four frontal and four rear intersectional flap vanes, all set at identical azimuthal angles. This cooperative configuration creates an equilibrium moment around the yaw axis (Z-axis), depicted by the green arrow extending towards the page.

Bottom-Left (c): To produce pitching moments, uniform adjustments of all lateral flap vanes at the same azimuthal angle are essential. This concerted effort results in a balanced moment around the pitch axis (Y-axis), represented by the green arrow.

Bottom-Right (d): This section presents a schematic of a single duct housing two pairs of flap vanes: two lateral flap vanes, denoted as fv_{lat}, and two longitudinal flap vanes, labeled as fv_{lng}. In this context, the term fv signifies a flap vane, while F_{fv} symbolizes the force exerted by a flap vane oriented in the opposite direction of its corresponding azimuthal angle. This phenomenon is also clearly depicted in Figure 5.3. Additionally, the arrangement of each servo flap is illustrated in Figure 5.2(d), showcasing the asymmetrical layout of the servo installations. The decision to employ two servo flaps instead of four is driven by efficiency, as it eliminates the need for disparate angle production and yields more harmonized force generation. This advantageous design choice is further emphasized in the magnified circle adjacent to the duct. At the other end of the servo bar, a flexible joint is connected to the duct's wall, facilitating smooth rotation of the flaps bar under the influence of servo-generated moments.

As depicted in Figure 5.2, the "WILD HOPPER" platform utilizes a hexagonal geometry with a set of vanes positioned at the duct exits. This arrangement consists of twelve pairs of vanes that are strategically configured for optimal control and effective functionality in influencing a sizeable payload. The term "pair" signifies that each duo of flap vanes is linked by a shaft and managed by a singular servo flap, efficiently rotating both vanes. This configuration offers several advantages:

Reduced Mechanical Complexity: Unlike the case where two adjacent flaps are managed by distinct servo flaps, which can result in non-uniform rotations and internal instability, the paired vane setup minimizes mechanical complications.

Simplified Control and Computation: Operating fewer vanes concurrently requires less computational effort by the autonomous platform (AP), contributing to a safer flight operation.

Error Prevention: The design prevents unintended rotations due to erroneous control commands that might lead to the interference of intersecting vanes, potentially compromising the entire control system.

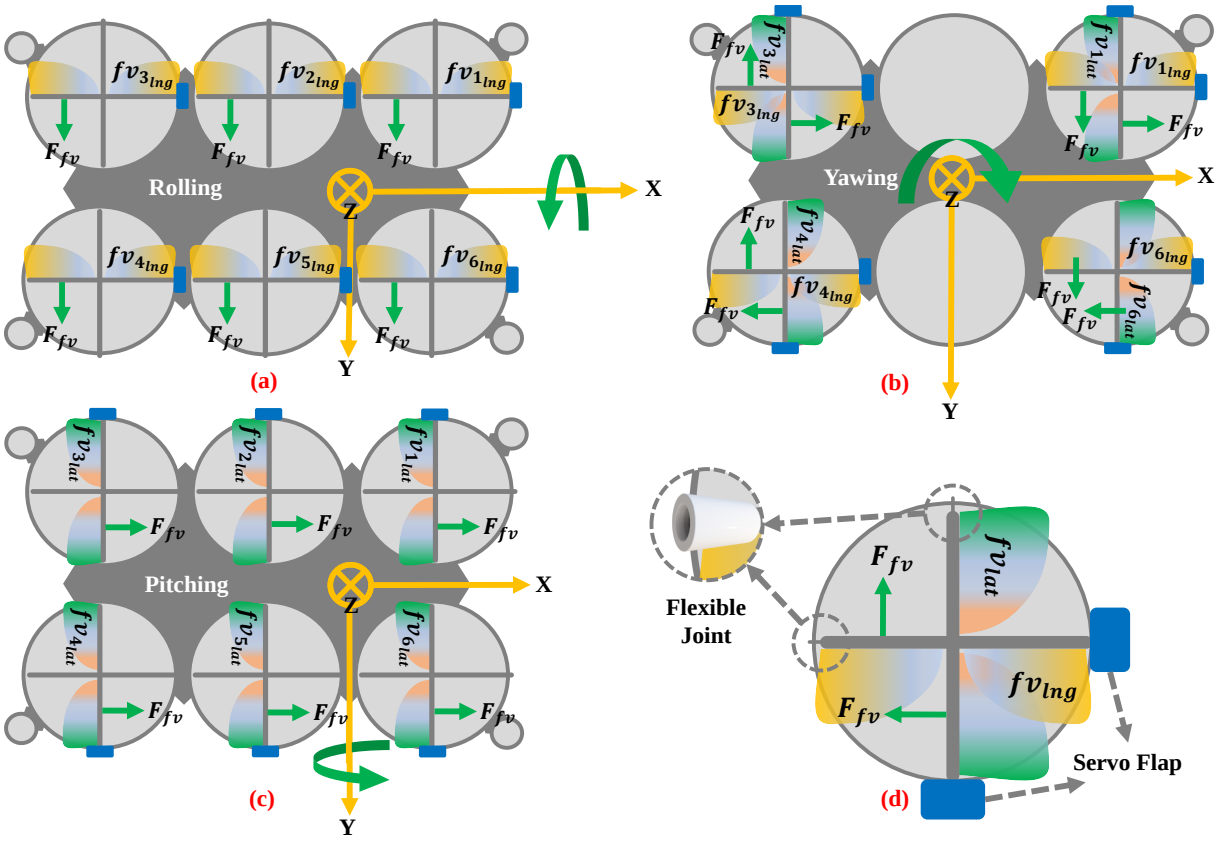

Figure 5.2: Top-Down view schematic of twelve pairs of flap vanes on the "WILD HOPPER" prototype, strategically positioned at the duct outlets to generate specific moments: (a) Rolling moment, (b) Yawing moment, (c) Pitching moment. In (d), a detailed view of a single duct featuring two pairs of vanes is depicted.

Enhanced Moment Generation: By synchronizing the rotation of paired vanes, the resulting moment is more potent compared to separate rotations. The harmonious alignment of azimuthal angles in a vane pair magnifies their combined effect, thus enhancing overall controller surface efficiency.

In this setup, six pairs of vanes are allocated for roll moment generation, an additional six for pitch moment, and eight pairs positioned at the drone's front and rear sides for yaw moment production. Notably, the "DUTY HOPPER" prototype (also seen in Figure 4.2) initially adopted a redundancy approach with thirty-two pairs of vanes: eight for roll, eight for pitch, eight diagonal pairs for yaw moments, and eight for redundancy. This configuration aimed to ensure moment generation continuity in the face of vane failures. However, this approach was abandoned due to intricate mechanical and servo control challenges, including varying calibration points and difficulty in harmonizing the overall system response, which hindered precise controllability compared to desired commands.

As depicted in Figure 5.3, the incoming airflow is directed into a duct as the MDF moves along the longitudinal X-axis. Positioned near the duct's outlet, the two servo flaps exert control on the exhaust airflow, prompting a reactive response from the flap vanes to the

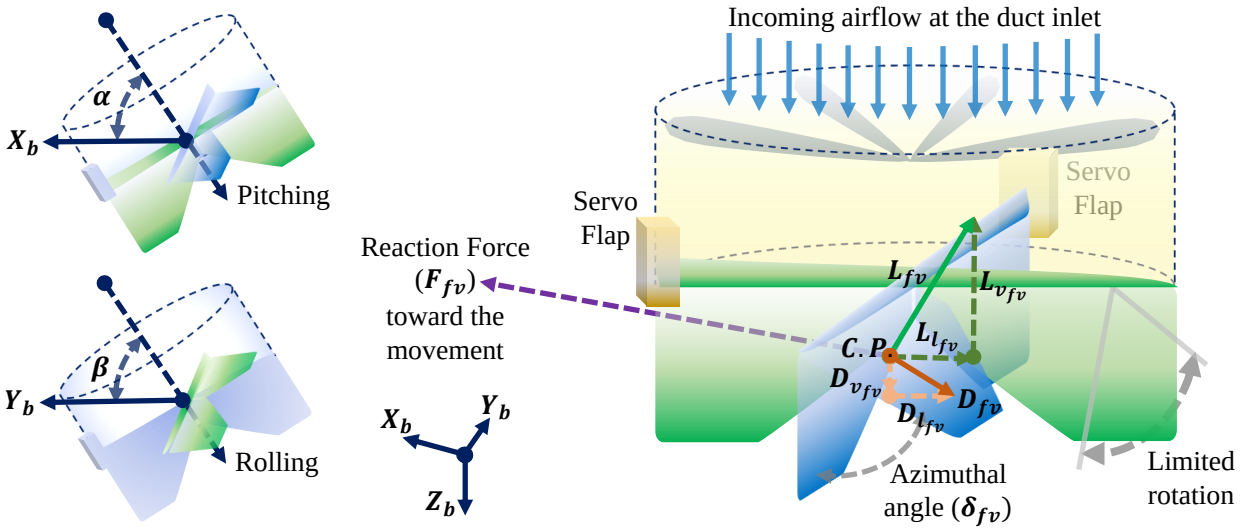

Figure 5.3: Schematic of a duct with two pairs of flap vanes rotating, illustrating generated forces and reaction force.

exiting airflow. In this dynamic, a pair of forces emerge L_{fv} and D_{fv}, signifying the creation of Lift and Drag forces for each set of vane pairs. An important consideration is the azimuthal angle, δ_{fv}, which is restricted within the $\pm 15°$ range to prevent interference with adjacent cross-linked vanes. This precaution, as previously discussed in 4, safeguards against potential disruptions. Furthermore, Figure 5.3 demonstrates two potential deflections of the single duct. The deflection corresponding to longitudinal movement is denoted as α, while the angle associated with lateral movement is designated as β. Moreover, the derived force acting on the flap is central to defining the flap force equation set, which can be expressed as follows:

$$\begin{aligned}
\mathbf{L_{fv}} &= L_{l_{fv}} i + L_{v_{fv}} j = L_{fv} \cos(\delta_{fv}) i + L_{fv} \sin(\delta_{fv}) j, \\
\mathbf{D_{fv}} &= D_{l_{fv}} i + D_{v_{fv}} j = -D_{fv} \sin(\delta_{fv}) i + D_{fv} \cos(\delta_{fv})) j, \\
\mathbf{T_{fv}} &= L_{v_{fv}} i - D_{v_{fv}} j = \mathbf{L_{fv}} \sin(\delta_{fv}) - \mathbf{D_{fv}} \cos(\delta_{fv}), \\
\mathbf{F_{fv}} &= L_{l_{fv}} i + D_{l_{fv}} j = \mathbf{L_{fv}} \cos(\delta_{fv}) + \mathbf{D_{fv}} \sin(\delta_{fv}),
\end{aligned} \tag{5.15}$$

Equation 5.15 presents the breakdown of the lift force into distinct lateral and vertical components, denoted as $L_{l_{fv}}$ and $L_{v_{fv}}$, respectively. Similarly, the drag force is divided into lateral and vertical components, represented by $D_{l_{fv}}$ and $D_{v_{fv}}$ for a flap vane. The aggregate thrust force produced by the flap vane, denoted as T_{fv}, results from combining the vertical components of both lift and drag forces. In contrast, the lateral force generated by the flap, marked as F_{fv}, arises from the summation of both lateral components of lift and drag forces. This interesting observation reveals that the lateral components of the decomposed lift and drag forces act in parallel, enhancing the MDF's forward momentum with increased force. Conversely, the vertical components oppose each other, thereby contributing to the overall thrust generated by the main propeller during flight. For the sake of simplification, the formulation assumes that the reaction lateral force of the flaps, F_{fv}, is equivalent to the primary force produced, and any negative sign is disregarded, as illustrated in Figures 5.2

and 5.3.

Importantly, the resultant movement of the system is directed in the opposite direction of the flap's rotation, a direct consequence of Newton's third law, which states that every action is met with an equal and opposite reaction. Simultaneously, it's worth noting that the final roll or pitch angle of an individual duct corresponds with the azimuthal angle of the flaps due to the lateral force they generate. This congruence underscores the integral relationship between forces and angles, showcasing the intricate interplay that governs the system's behavior. Now, to determine the terms defined in Equations 5.15, a list of corresponding aerodynamic parameters can be detailed as follows:

$$\begin{aligned}
\mathbf{q_{fv}} &= \frac{1}{2}\rho(\mathbf{V_b} + v_e)^2, \\
\mathbf{C_{L_{fv}}} &= C_{L_{0_{fv}}} + C_{L_{\delta_{fv}}} + \frac{c_{fv}}{2v_e}\left(C_{L_{\dot{\delta}_{fv}}}\dot{\delta}_{fv} + C_{L_{q_{fv}}}\mathbf{q_{fv}}\right), \\
\mathbf{C_{D_{fv}}} &= C_{D_{0_{fv}}} + \frac{(\mathbf{C_{L_{fv}}} - C_{L_{0_{fv}}})^2}{\pi e AR}, \\
\mathbf{L_{fv}} &= \mathbf{q_{fv}} A_{fv} \mathbf{C_{L_{fv}}}, \\
\mathbf{D_{fv}} &= \mathbf{q_{fv}} A_{fv} \mathbf{C_{D_{fv}}},
\end{aligned} \tag{5.16}$$

Equations 5.16 break down as follows: ρ symbolizes the density of the outgoing airstream from the duct, while $v_e = v_\infty$ denotes the exhaust velocity of the duct. The variables A_{fv}, $\mathbf{q_{fv}}$, and c_{fv} correspond to the sectional area of the flap vane exposed to the passing airstream, the dynamic pressure that is raised due to summation of the velocity of the MDF in the BFF and the exit velocity, and the chord of the flap, respectively. The term AR stands for the Aspect Ratio of the vane, and e is the efficiency factor derived from the aerodynamic shape of the flap (with $e < 1$). Meanwhile, $\mathbf{C_{L_{fv}}}$ and $\mathbf{C_{D_{fv}}}$ pertain to the lift and drag coefficients of the vane, respectively. In addition, $C_{L_{0_{fv}}}$ represents the zero-drag lift coefficient, while $C_{D_{0_{fv}}}$ denotes the zero-lift drag coefficient of the vane.

Finally, the dynamic model of a servo flap, which is utilized to actuate the flap vanes as depicted in Figure 5.3, can be represented by the following transfer function:

$$H(s) = \frac{K}{s^2 + 2\zeta\omega_n s + \omega_n^2} \tag{5.17}$$

In Equation 5.17, $H(s)$ is the transfer function of the servo flap, s represents the complex frequency variable (Laplace domain), K denotes the system gain, signifying the amplification factor of the control signal, ζ is the damping ratio, indicating how the system responds to external disturbances and affects the overshoot and settling time, and ω_n represents the natural frequency of the system, indicating how rapidly the system reacts to changes in the input. These parameters can be defined according to the physical characteristics of the servo, as discussed by Fan et al., 2018.

Chapter 6

System Control

This section aims to streamline the control algorithms presented in publications **PI**, **PII**, and **PIII** based on the dynamics model and mathematical equations discussed in the previous section. The section is further divided into two subsections: "General Control" and "Specific Control." In the latter, we delve into the core principles of the proposed control methodology, while the former focuses on the particular design, parameters, and assumptions specific to this thesis.

6.1 General Control (PI, PII, and PIII)

Having thoroughly examined the dynamics and mathematical modeling of the MDF platform, this subsection, alongside the subsequent one, succinctly encapsulates the essence of the control algorithm put forth in **PI**, **PII**, and **PIII**. The aim is to provide a comprehensive overview of the equations presented in the publications while grasping the underlying hypotheses. To address the inherent nonlinearities of the MDF's dynamic model, both this thesis and **PI**, **PII**, and **PIII** introduce nonlinear control solutions. These solutions are tailored to maintain the model's nonlinearity, thus preserving the core attributes of the primary system. Broadly, two distinct methodologies are showcased: Sliding Mode Control (SMC) and Model Reference Adaptive Control (MRAC). The sequence of publication enhancements unfolds as follows: **PI** initiates with SMC, followed by **PAd** where MRAC is introduced to internalize system parameters. Finally, the culmination of these approaches is realized through Adaptive SMC (ASMC) in **PII** and **PIII**. This subsection delves into the core principles of each approach, elucidating their underlying mechanisms. Subsequently, the focus will shift to highlighting the specialization of each method as a TVC approach through the utilization of flap vanes in the ensuing subsection. The overall control schematic for both methods is depicted in Figure 6.1, encompassing several distinct assumptions and components as outlined below:

Reference Values: These are the input values assumed for the control system, denoted as x_r, y_r, z_r, and ψ_r in case of providing by the mission or is determined by $\psi_d = \arctan(e_y/e_x)$, i,e., the distance of each of pair of waypoints in Y-axis over their difference

in X-axis. Typically determined by a guidance or path-planning system, these values are encapsulated within a matrix of ${}_{3\times n}$ or ${}_{4\times n}$ elements, where n signifies the number of waypoints input as control references, depending on the yaw angle.

Position Controller (PC): Also referred to as the outer-loop or upper-level controller, this component involves double integration, transforming attitude values into position values. In essence, human commands are interpreted as positions, which, through double differentiation, yield the desired attitude angle values. After subsequent double integration, the desired position values are derived. Through this thesis, **PI**, **PII**, **PIII**, and **PAd**, a simple Proportional-Derivative (PD) controller is employed to manage the defined position values of x and y, and a distinct controller for z.

Vertical Controller (VC): This part is also considered as the position controller but is independent of the attitude angles and known as the vertical controller. This section is considered one of the focus points of this thesis to be controlled, which generates the desired thrust command expressed as $U_{altitude} = \begin{bmatrix} U_{z_d} \end{bmatrix}$.

Attitude Controller (AC): Often known as the inner-loop or lower-level controller, which constitutes the core of the control mechanism. Central to this thesis, the attitude controller integrates the desired Euler angles calculated by the PC to generate necessary attitude moments, thereby stabilizing the attitude system, which is $U_{att} = \begin{bmatrix} U_{\phi_d} & U_{\theta_d} & U_{\psi_d} \end{bmatrix}^T$.

Electric Control Unit (ECU): As discussed in 1.2, the ECU serves as a vital regulator. Utilizing a PID (Proportional-Integral-Derivative) controller, it translates desired control outputs into commands for the main propulsion units. In this case, the main propulsion units consist of thermal engine-powered fan blades or propellers. The ECU receives data from sensors and employs algorithms to optimize engine performance, manage emissions, and enhance efficiency. Additionally, the ECU manages the injection of fuel for the chosen gasoline-powered internal combustion engines within the project.

Servo Flap Dynamics (SFD): The Servo Flap Dynamics component plays a crucial role in regulating inputs for servo flaps, which function as control surfaces. Similar to the ECU, the SFD translates desired moments for control into standard Pulse Width Modulation (PWM) signals. These PWM signals are then utilized by servo motors to actuate the control surfaces, specifically flap vanes.

EDF Motor Dynamics (EDF-MD): Designed for emergency situations, the EDF Motor Dynamics component serves as the "Secondary" output of the PC system. It activates only when primary systems such as the ECU or thermal engines experience failure. The EDF-MD component provides the necessary PWM signals to control EDF motors, ensuring a contingency propulsion system.

Secondary Attitude Dynamics (SAD): Building upon the EDF-MD component, Secondary Attitude Dynamics maintains the functionality of the system in critical situations. It supplies power to the Lipo batteries located near the thermal engines, allowing for emergency thrust generation over a limited duration. This aspect is further elaborated in **PIII**.

Attitude Dynamics (AD): The primary Attitude Dynamics component is responsible for generating the required moments for various attitude rotations, including roll, pitch, and yaw. This function is achieved through the manipulation of servo flaps and flap vanes, which are illustrated in Figures 5.2 and 5.3.

Position Dynamics (PD): The Position Dynamics component governs the physical movements of the MDF system. This is achieved through coordination with sensors such as gyroscopes, GPS modules, and other relevant devices. Feedback from these sensors is relayed to the controller, enabling the dynamic adjustment of control parameters for precise positioning.

Disturbances ($\mathbf{D_{PD}}$ and $\mathbf{D_{AD}}$): Finally, the Disturbances segments, represented as D_{PD} and D_{AD}, account for the uncertainties and nonlinearities present in the real-world laboratory environment. These elements are crucial for simulating real-world conditions and enhancing the robustness of the system against potential disturbances. The impact of these disturbances is further explored and demonstrated in the results of both **PII** and **PIII**.

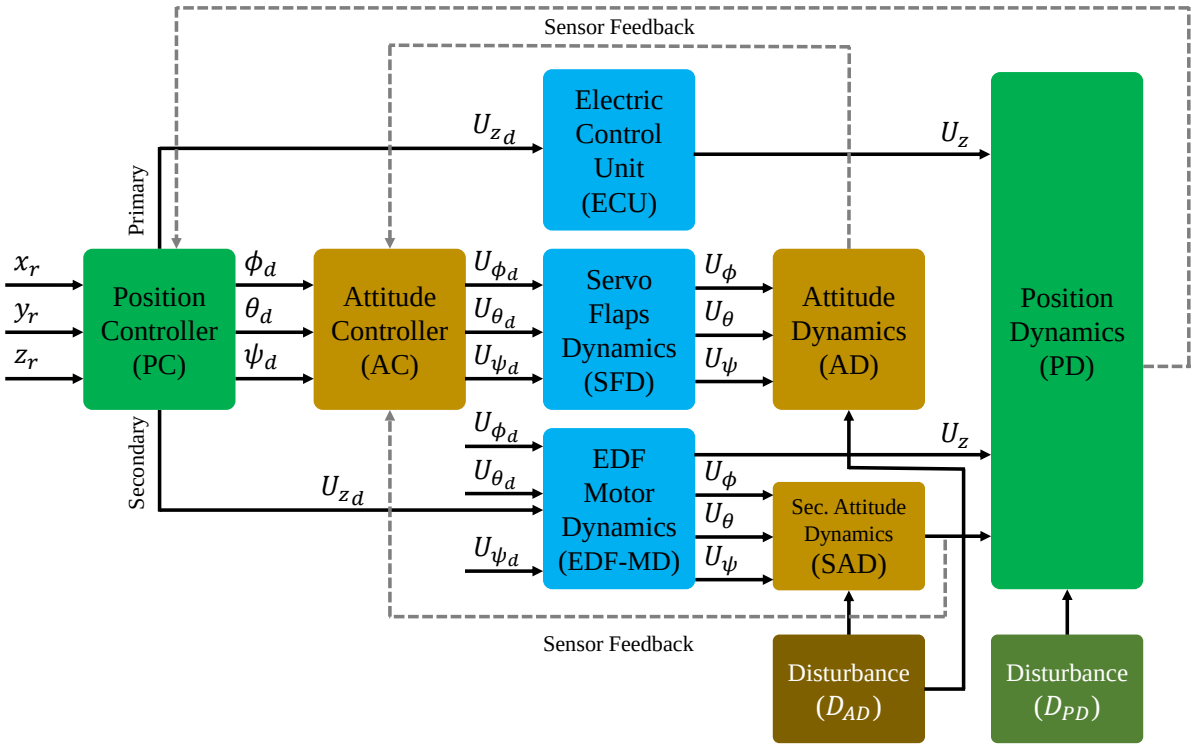

Figure 6.1: Diagram illustrating the overarching control scheme implemented across **PI**, **PII**, and **PIII** for precisely regulating the heavy hexa MDF system known as the "WILD HOPPER."

6.1.1 Model Reference Adaptive Control (MRAC, PAd)

The specific MRAC method utilized in this thesis is based on a Lyapunov candidate to guarantee the stability of the system. The overall schematic of the MRAC is very similar to Figure 6.1, with the difference that the feedback loop contains the adaptively updated parameters and further details are provided in **PAd**.

Characterizing the 6 DOF MDF system of the "WILD HOPPER" and accounting for its inherent nonlinearities, a closed-loop transfer function for the reference model is formulated, as outlined below:

$$\mathbf{G_m(s)} = \frac{Y(s)}{R(s)} = \frac{C(s)P(s)}{1 + C(s)P(s)H(s)} \tag{6.1}$$

In Equation 6.1, $C(s)$ represents the transfer function of the controller, $P(s)$ corresponds to the transfer function of the hexa MDF's dynamic characteristics, and $H(s)$ denotes the transfer function of the feedback loop encompassing sensors and actuators.

In the context of our specific case study, when considering the interplay of nonlinearities and the coupling of two attitude angles (ϕ and θ) with lateral and longitudinal movements (surge and sway), the dynamics of the hexa MDF can be effectively captured by a set of second-order ordinary differential equations. This characteristic leads us to categorize the system as a second-order system, owing to the fact that its mathematical representation involves second-order differential equations. By simplifying the feedback path in this manner, the reference model's behavior in a more streamlined manner is outlined below:

$$\mathbf{G_m(s)} = \frac{w^2}{s^2 + 2\xi\omega s + \omega^2} \rightarrow \ddot{y}_m + \underbrace{2\xi\omega}_{a_1}\dot{y}_m + \underbrace{\omega^2}_{a_2} y_m = \underbrace{\omega^2}_{a_3} u_c \tag{6.2}$$

In Equation 6.2, The symbol "u_c" represents the control reference input or control reference signal, signifying the intended behavior that the controlled system is meant to follow. In contrast, the control input denoted as "u" is dynamically tuned to ensure that the real-time response of the system aligns with the target behavior set by "u_c." The objective is to iteratively adjust "u" such that the system's actual behavior closely corresponds to the desired response outlined by "u_c." The value of u_c influences how quickly the system adapts to changes and disturbances. $\{\}_m$ refers to a parameter of the model. Now, achieving our goal hinges on estimating the parameters of the reference system through the controller assumed transformation function outlined in Equation 6.3. To accomplish this, the disparity between the assumed and reference systems shall be ascertained.

$$\mathbf{G_m(s)} = \frac{1}{s(s+a)} = \frac{1}{s^2 + as} \tag{6.3}$$

In Equation 6.3, the parameter a is the target of estimation as the adaptive model converges toward the reference model. With this in mind, let's define the adaptive control law as follows:

$$u = \theta_1 u_c - \theta_2 \dot{y} - \theta_3 y \tag{6.4}$$

In Equation 6.4, the symbols $\theta_{\{i=1,2,3\}}$ denote the adaptive parameters that are targeted for updates to facilitate controller adaptation. As a result, by simplifying Equations 6.2 and 6.3, the following expressions emerge:

$$\begin{aligned}
&\ddot{y} - \ddot{y}_m - a_1\dot{y}_m - a_2 y_m + a_1\dot{y} + a_2 y \\
&= -(a+\theta_2)\dot{y} - \theta_3 y + (\theta_1 - b)u_c + a_1\dot{y} + a_2 y, \\
&\textit{knowing that: } e = y - y_m \textit{ , } \dot{e} = \dot{y} - \dot{y}_m \textit{ ,and } \ddot{e} = \ddot{y} - \ddot{y}_m \\
&\rightarrow \ddot{e} + a_1\dot{e} + a_2 e = -\underbrace{(\theta_2 + a - a_1)}_{\widetilde{\theta}_2}\dot{y} - \underbrace{(\theta_3 - a_2)}_{\widetilde{\theta}_3} y + \underbrace{(\theta_1 - a_3)}_{\widetilde{\theta}_1} u_c, \\
&\rightarrow e = \frac{1}{s^2 + a_1 s + a_2}\begin{bmatrix} -\dot{y} & -y & u_c \end{bmatrix}\begin{bmatrix} \widetilde{\theta}_2 \\ \widetilde{\theta}_3 \\ \widetilde{\theta}_1 \end{bmatrix}, \\
&\rightarrow e = \frac{1}{s^2 + 2\xi w s + w^2}\begin{bmatrix} -\dot{y} & -y & u_c \end{bmatrix}\begin{bmatrix} \widetilde{\theta}_2 \\ \widetilde{\theta}_3 \\ \widetilde{\theta}_1 \end{bmatrix}
\end{aligned} \tag{6.5}$$

By incorporating the blue terms into both sides of Equations 6.5, the formula is further simplified. Shifting from the time domain to the Laplace domain facilitates the examination of the final transfer function. In cases where all the terms are evidently positive, the system can be classified as minimum-phase. However, due to the discrepancy in the degree between the numerator and denominator being greater than one, the system doesn't fulfill the conditions for being Strictly Positive Real (SPR), necessitating analysis. Unfortunately, the application of Kalman Yakubovich's Lemma, as proposed by Andrievsky et al., 1996, is impractical. Instead, the issue can be addressed using state-space equations outlined as follows:

$$
\begin{aligned}
&\begin{cases} \dot{X} = AX + BU \\ Y = CX + DU \end{cases} \\
&\xrightarrow{\text{Assuming}} A = \begin{bmatrix} 0 & 1 \\ -a_2 & -a_1 \end{bmatrix}, B = \begin{bmatrix} 0 & 1 \end{bmatrix}^T, C = \begin{bmatrix} 0 & 1 \end{bmatrix}, D = 0 \\
&\rightarrow \begin{bmatrix} \dot{e}_1 \\ \dot{e}_2 \end{bmatrix} = \begin{bmatrix} 0 & 1 \\ -a_2 & -a_1 \end{bmatrix} \begin{bmatrix} e_1 \\ e_2 \end{bmatrix} + \begin{bmatrix} 1 \\ 0 \end{bmatrix} \begin{bmatrix} -\dot{y} & y & u_c \end{bmatrix} \begin{bmatrix} \widetilde{\theta}_2 \\ \widetilde{\theta}_3 \\ \widetilde{\theta}_1 \end{bmatrix} \\
&\rightarrow \begin{bmatrix} \dot{e}_1 \\ \dot{e}_2 \end{bmatrix} = \begin{bmatrix} 0 & 1 \\ -\omega^2 & -2\xi\omega \end{bmatrix} \begin{bmatrix} e_1 \\ e_2 \end{bmatrix} + \begin{bmatrix} 0 \\ 1 \end{bmatrix} \begin{bmatrix} -\dot{y} & y & u_c \end{bmatrix} \begin{bmatrix} \widetilde{\theta}_2 \\ \widetilde{\theta}_3 \\ \widetilde{\theta}_1 \end{bmatrix} \\
&\rightarrow \begin{bmatrix} \dot{\widetilde{\theta}}_2 \\ \dot{\widetilde{\theta}}_3 \\ \dot{\widetilde{\theta}}_1 \end{bmatrix} = -\Gamma \begin{bmatrix} -\dot{y} \\ y \\ u_c \end{bmatrix} \begin{bmatrix} 0 & 1 \end{bmatrix} P \begin{bmatrix} e \\ \dot{e} \end{bmatrix}, (P : A^T P + PA = -I)
\end{aligned}
\tag{6.6}
$$

In Equations 6.6, the matrices Γ and P are established as Diagonal Positive Definite (DPD) matrices, sharing a consistent dimension. The formulation of the MRAC method, as outlined through Equations 6.1 - 6.6, adapts according to the specific system in focus, notably, in reference to the **PAd** model, which encompasses a twelve-dimensional state vector, the sizes of matrices Γ and P are tailored to match this dimensionality. This alignment ensures the effective application of MRAC principles within the unique characteristics of the **PAd** system ("FAN HOPPER" prototype). Also, in the given context, the ultimate $\dot{\widetilde{\theta}}_{i=1,2,3}$ vector signifies the augmented adaptation parameters, incorporating the simplifications introduced within Equations 6.5. These simplifications facilitate the determination of the central adaptation parameters. To establish the stability of the asserted Model Reference Adaptive Control (MRAC), the Lyapunov candidate introduced in **PAd** is adopted. It's important to note that the Lyapunov candidate presented in **PII** and **PIII** pertains to an ASMC method, distinct from a pure adaptive controller, which is the focus here. To establish the stability of the system, a Positive Definite Function (PDF) is introduced as a Lyapunov candidate. The critical step in this proof involves demonstrating that the derivative of this function exhibits negativity, thereby validating its negative definiteness.

$$
V = \frac{1}{2} e^T P e + \beta^T F \beta \tag{6.7}
$$

In Equations 6.7, the symbol V represents the Lyapunov function, while e signifies the aforementioned error term. The matrix Θ corresponds to the previously defined update matrix. Notably, the matrix F is diagonal in nature, functioning as a dot product when applied between two vectors. Consequently, both terms yield the same dimensionality. In light of these considerations, the simplification of the derivative of the Lyapunov candidate takes the following form:

$$
\begin{aligned}
\dot{V} &= \frac{1}{2}(\dot{e}^T P e + e^T P \dot{e}) + \dot{\Theta}^T F \Theta + \Theta^T F \dot{\Theta} \\
\rightarrow \dot{V} &= \frac{1}{2}((\dot{X} - \dot{X}_m)^T P e + e^T P (\dot{X} - \dot{X}_m)) + 2F\Theta^T \dot{\Theta} \\
\rightarrow \dot{V} &= \frac{1}{2}((A_m e + \underbrace{\cdots}_{\zeta\Theta})^T P e + e^T P (A_m e + \zeta\Theta)) + 2F\Theta^T \dot{\Theta} \\
\rightarrow \dot{V} &= \frac{1}{2} e^T (\underbrace{(A_m^T P + p A_m)}_{-I} e + \underbrace{\Theta^T \zeta^T P e}_{\Delta} + \underbrace{e^T P \zeta \Theta)}_{\Delta^T} + 2F\Theta^T \dot{\Theta} \\
\rightarrow \dot{V} &= \underbrace{-\frac{1}{2} e^T I e}_{ND} + \frac{1}{2}\Theta^T \underbrace{(Pe + e^T P \zeta \Theta + 4F\Theta^T \dot{\Theta})}_{\textit{shall equate to 0}}
\end{aligned}
\tag{6.8}
$$

In Equations 6.8, A_m signifies the Jacobian matrix of the reference model, while ζ serves as a condensed representation denoting the amalgamation of matrix product updates. In the context of the simplified derivative function, the initial term pertains to Negetive-Definite (ND). In contrast, the focus shifts to the second term, where the assumption of $\Theta^T = 0$ is deemed inadmissible. Instead, the condition necessitates that the equation $Pe + e^T P\zeta\Theta + 4F\Theta^T\dot{\Theta} = 0$ holds to ensure the unequivocal negativity of this particular term. This stipulation is vital for maintaining the requisite definiteness and consistency within the overall expression.

6.1.2 Sliding Mode Control (SMC, PI, PII, and PIII)

This controller plays a prominent role in both **PI** and ASMC strategies within **PIII**, offering distinct advantages. Its robustness against an array of external disturbances, such as wind gusts, fluctuations in payload weight, and uncertainties in dynamics, makes it particularly appealing. Furthermore, being a nonlinear controller, it aligns well with the complex nature of our nonlinear MDF system. Significantly, this method excels in rejecting disturbances through the imposition of a sliding surface on the system trajectory. This approach actively compels the trajectory to align with the sliding surface, enabling effective disturbance rejection. In the context of a state-space representation involving an nth-order derivative of the system's state vector, the determination of the sliding surface is expressed as:

$$
\begin{aligned}
& x^{(n)} = Ax + Bu + \delta(x) \rightarrow x^{(n)} = f(x) + u \\
& \rightarrow S = \left(\frac{d}{dt} + \lambda\right)^{(n-1)} (\dot{x} - \dot{x}_d) \rightarrow S = \left(\frac{d}{dt} + \lambda\right)^{(n-1)} e
\end{aligned}
\tag{6.9}
$$

In Equation 6.9, the symbol $\delta(x)$ denotes system uncertainties and nonlinearities encapsulated within the disturbance function. It's assumed that δ remains within the bounds $\delta(x) < k$, where k is a positive constant representing the maximum anticipated disturbance magnitude. Additionally, the symbol λ represents the sliding surface gain or slope coefficient, determined based on the weighting of the uncertainties. The introduction of the sliding variable S serves to quantify the tracking error, e, that emerges between the desired trajectory X_d and the

actual trajectory X of the system. The overarching objective is to drive the sliding variable S towards zero, thereby aligning the actual state values with the desired state. In this specific scenario where $n = 2$ and it corresponds to a straightforward MDF system, the formulation of the sliding surface is elaborated as follows:

$$S = \dot{e} + \lambda e = \dot{x} - \dot{x}_d + \lambda(x - x_d) \tag{6.10}$$

Indeed, a significant challenge within the sliding mode control method lies in the careful definition of the sliding surface. However, when viewed in a general and simplified manner, one can assert that the sliding surface ideally mirrors the system's error. This error signifies the disparity that necessitates a reduction to zero within the intended system.

$$\begin{aligned} \dot{S} &= \ddot{x} - \ddot{x}_d + \lambda(\dot{x} - \dot{x}_d), \\ \xrightarrow{\ddot{x}=f(x)+u} u_{eq} : \dot{S} &= 0 \rightarrow u_{eq} = X_d - \lambda\dot{e} \end{aligned} \tag{6.11}$$

In Equations 6.11, the u_{eq} stands for the equivalent control input, which is a part of the total control input specifically designed to drive the system onto the sliding surface and maintain sliding mode behavior. As seen the control input has appeared in the first derivative of the sliding variable. Therefore, the relative degree of the system is equal to 1. Now, let's define the complete control input, encompassing both the equivalent control input, denoted as u_{eq}, and the uncertain term of the system. This can be expressed as follows:

$$u = u_{eq} - d \times sign(s), \tag{6.12}$$

In Equation 6.12, the term $sign(s)$ embodies the switching or uncertainty component within the control law. This term accommodates system uncertainties, external disturbances, or any unaccounted dynamics that could influence the system's behavior. Its purpose is to enhance the robustness of the control system when confronted with uncertain factors that might impact the system's performance. To determine the unknown parameter d, a Lyapunov candidate is introduced. This candidate is not only Positive-Definite (PD) itself but also has a Negative-Definite (ND) derivative, as shown below. To mitigate the chattering phenomenon, which can cause undesirable high-frequency oscillations, the $\tanh s$ function is employed instead of the abrupt $sign(s)$ function. Additionally, for improved and swifter stability convergence, it is assumed that the derivative of the Lyapunov candidate is not only ND but also significantly more negative than a predefined positive value, μ. This choice ensures stability within a finite timeframe.

$$
\begin{aligned}
\textbf{updating: } \mathbf{u} &= \mathbf{u_{eq}} - \mathbf{d} \times \tanh(\mathbf{s}), \\
V(x) &= S^2/2 \rightarrow dV(x)/dt = s\dot{s}, \\
\textit{necessitates that: } \dot{V}(x) &\leq -\mu \rightarrow s\dot{s} \leq -\mu|s| \\
\textit{knowing that: } s\left(x^{(n)} = Ax + Bu + \delta(x)\right) &= s\left(-db\tanh(s) + \delta(x)\right) \\
\rightarrow -db|s| + |s\delta(x)| = -db|s| + |s||\delta(x)| &= |s|\left(-db + |\delta(x)|\right) \leq -\mu|s| \\
\rightarrow -db + k \leq -\mu \rightarrow \boxed{d \geq (\mu + k)/b}&
\end{aligned}
\tag{6.13}
$$

Hence, by adhering to the condition $d \geq (\mu+k)/b$, the stability of the system can be effectively ensured. This condition plays a pivotal role in bolstering the control system's ability to resiliently counter uncertainties and disturbances, thereby facilitating the achievement of both stability and precise tracking of the intended trajectory.

6.2 Specific Control (PI, PII, PIII, and PAd)

In the previous subsection, the fundamental principles underpinning the control algorithms employed in **PI**, **PII**, **PIII**, and **PAd** were provided, manifesting in the explicit form of equations. This discourse culminated in the representation of these equations, now applied concretely to the ultimate hexa-MDF platform. Here, the platform stands as the experimental subject for the concurrent application and comparison of both the MRAC and SMC methods.

When defining the state and input vectors, two approaches are evident: one based on the state values as followed in **PI**, **PII**, and **PAd**, and the other aligned with state values utilized in studies concerning conventional DFs. While the state matrix defined in **PIII** comprises an expandable model that is elaborated upon within the paper itself. In all scenarios, the input matrix remains consistent, as outlined below:

$$
\begin{aligned}
\mathbf{X} &= \begin{bmatrix} x & \dot{x} & y & \dot{y} & z & \dot{z} & \phi & \dot{\phi} & \theta & \dot{\theta} & \psi & \dot{\psi} \end{bmatrix}^T, \\
\mathbf{X_{alt}} &= \begin{bmatrix} u & v & w & p & q & r & \phi & \theta & \psi \end{bmatrix}^T, \\
\mathbf{U} &= \begin{bmatrix} u_z & u_\phi & u_\theta & u_\psi \end{bmatrix}^T
\end{aligned}
\tag{6.14}
$$

In Equations 6.14, $\mathbf{X_{alt}}$ corresponds to an alternative state matrix formulation as defined in other research works. In this section, the first model is considered in order to align the control framework with established DF standards, and regarding the second state vector with fewer input parameters, readers are encouraged to explore publications that considered this model, such as those authored by Wang et al., 2014, Zhang et al., 2016, Xiaoliang et al., 2018, and Emami and Banazadeh, 2015.

Specifically, $\mathbf{X_{alt}}$ is influenced by variables including the body-fixed frame (BFF) velocity ($\mathbf{V_b}$), Euler angles (α), and angular velocity in the BFF ($\omega_\mathbf{b}$), as previously defined in Equations 5.1 and 5.2. Also, u_z, u_ϕ, u_θ, and u_ψ refer to the total thrust, roll moment, pitch moment, and yaw moment, respectively.

6.2.1 Position Control

As previously discussed, planar position control is not the primary focus of this thesis, especially in sections from **PI** to **PIII**. During this phase, standardized Autopilots (APs) have proven to be highly efficient, outperforming custom laboratory designs. However, owing to the interplay between attitude and position loops and the necessity for simulating the entire process, a simplified Proportional-Derivative (PD) controller is employed for planar position control. This PD controller generates reference values for roll (ϕ) and pitch (θ) angles, which are then fed into the attitude controller. The equations facilitating this transformation are as follows:

$$\begin{aligned} \ddot{x} &= \frac{U_z}{m_b} \left(\cos(\phi)\sin(\theta)\cos(\psi) + \sin(\phi)\sin(\psi)\right), \\ \ddot{y} &= \frac{U_z}{m_b} \left(\cos(\phi)\sin(\theta)\sin(\psi) - \sin(\phi)\cos(\psi)\right), \end{aligned} \tag{6.15}$$

Given the control input vector defined in Equations 6.14, the acceleration of the planar position can be computed using Equations 6.15. Subsequently, to calculate the reference values for the Euler angles, the following equations are utilized:

$$\begin{aligned} \ddot{x}\sin(\psi) &= \frac{U_1}{m_b}\left(\frac{1}{2}\cos(\phi)\sin(\theta)\sin(2\psi) + \sin(\phi)\sin^2(\psi)\right), \\ \ddot{y}\cos(\psi) &= \frac{U_1}{m_b}\left(-\frac{1}{2}\cos(\phi)\sin(\theta)\sin(2\psi) + \sin(\phi)\cos^2(\psi)\right), \\ \underbrace{\sin(\phi)}_{\simeq\phi} &= \frac{m_b}{U_z}\left(\ddot{x}\sin(\psi) - \ddot{y}\cos(\psi)\right) \rightarrow \boxed{\phi_r = \frac{m_b}{U_z}\left(\ddot{x}_r\sin(\psi_r) - \ddot{y}\cos(\psi_r)\right)}, \\ \ddot{x}\cos(\psi) &= \frac{U_z}{m_b}\left(\cos(\phi)\sin(\theta)\cos^2(\psi) + \frac{1}{2}\sin(\phi)\sin(2\psi)\right), \\ \ddot{y}\sin(\psi) &= \frac{U_z}{m_b}\left(\cos(\phi)\sin(\theta)\sin^2(\psi) - \frac{1}{2}\sin(\phi)\sin(2\psi)\right), \\ \underbrace{\cos(\phi)}_{\simeq 1}\underbrace{\sin(\theta)}_{\simeq\theta} &= \frac{m_b}{U_z}\left(\ddot{x}\cos(\psi) + \ddot{y}\sin(\psi)\right) \rightarrow \boxed{\theta_r = \frac{m_b}{U_z}\left(\ddot{x}_r\cos(\psi_r) + \ddot{y}_r\sin(\psi_r)\right)} \end{aligned} \tag{6.16}$$

Equation 6.16 represents the nonlinear coupled equations for obtaining the parameters ϕ_r and θ_r. These equations can be expanded as discussed by Naldi et al., 2010:

$$\begin{bmatrix} \phi_r \\ \theta_r \end{bmatrix} = \begin{bmatrix} \arctan\left(\cos(\theta_r)\sin(\psi_r)\left(\ddot{x}_r f_{dr}\dot{x}_r + \ddot{y}_r f_{dr}\dot{y}_r\right) / \left(\ddot{z}_r - g\right)\right) \\ \arctan\left(\cos(\psi_r)\left(\ddot{x}_r f_{dr}\dot{x}_r\right) / \left(\ddot{z}_r - g\right) + \sin(\psi_r)\left(\ddot{y}_r f_{dr}\dot{y}_r\right) / \left(\ddot{z}_r - g\right)\right) \end{bmatrix} \tag{6.17}$$

In Equation 6.17, f_{dr} represents the nominal ram drag of the body divided by the total moments of the body in zero lift mode. Similar to Equations 6.15, in order to derive the nonlinear dynamics of the system for the vertical position parameter and Euler angles, the following expressions are used:

$$
\begin{aligned}
\ddot{z} &= \frac{U_z}{m_b}\left(\cos(\phi)\cos(\theta)\right) - g, \\
\ddot{\phi} &= \dot{\theta}\dot{\psi}\ \frac{I_y - I_z}{I_x} + \frac{J_r}{I_x}\dot{\theta}\Omega_r + \frac{l}{I_x}U_\phi, \\
\ddot{\theta} &= \dot{\phi}\dot{\psi}\ \frac{I_z - I_x}{I_y} + \frac{J_p}{I_y}\dot{\phi}\Omega_p + \frac{l}{I_y}U_\theta, \\
\ddot{\psi} &= \dot{\phi}\dot{\theta}\ \frac{I_x - I_y}{I_z} + \frac{1}{I_z}U_\psi
\end{aligned}
\tag{6.18}
$$

The Equations 6.15 and 6.18 mentioned earlier are inherently coupled and nonlinear. To facilitate the estimation of state transition matrix coefficients and understand the dynamics of the MDF system, it is necessary to linearize the model. The linearized form of aforementioned formulas can be expressed as shown in Equation 6.19:

$$
\begin{aligned}
\ddot{x} &= \underbrace{\frac{\Delta U_z}{m_b}(\theta + \phi\psi)}_{\simeq 0} + g\left(\theta + \underbrace{\phi\psi}_{\simeq 0}\right) \rightarrow \boxed{\ddot{x} = g\theta}, \\
\ddot{y} &= \underbrace{\frac{\Delta U_z}{m_b}(\theta\psi - \phi)}_{\simeq 0} + g\left(\underbrace{\theta\psi}_{\simeq 0} - \phi\right) \rightarrow \boxed{\ddot{y} = -g\phi}, \\
\ddot{z} &= \frac{\Delta U_z}{m_b} + g - g \rightarrow \boxed{\ddot{z} = \frac{\Delta U_z}{m_b}}, \\
\ddot{\phi} &= \underbrace{\dot{\theta}\dot{\psi}\frac{I_y - I_z}{I_x}}_{\simeq 0} + \underbrace{\frac{J_p}{I_x}\dot{\theta}\Omega_p}_{\simeq 0} + \frac{l}{I_x}U_\phi \rightarrow \boxed{\ddot{\phi} = \frac{l}{I_x}U_\phi}, \\
\ddot{\theta} &= \underbrace{\dot{\phi}\dot{\psi}\frac{I_z - I_x}{I_y}}_{\simeq 0} + \underbrace{\frac{J_p}{I_y}\dot{\phi}\Omega_p}_{\simeq 0} + \frac{l}{I_y}U_\theta \rightarrow \boxed{\ddot{\theta} = \frac{l}{I_y}U_\theta}, \\
\ddot{\psi} &= \underbrace{\dot{\phi}\dot{\theta}\frac{I_x - I_y}{I_z}}_{\simeq 0} + \frac{1}{I_z}U_\psi \rightarrow \boxed{\ddot{\psi} = \frac{1}{I_z}U_\psi}
\end{aligned}
\tag{6.19}
$$

6.2.2 Attitude Control: MRAC (PAd)

Two distinct approaches are being considered, once pertaining to the state vector $\mathbf{X}$, the state-space equations are outlined as follows:

$$
\begin{aligned}
A &= \begin{bmatrix}
0\,0\,0\,0\,0\,0 & 1-\omega_{\phi}^2 & 0 & 0 & 0 & 0 & 0 \\
0\,0\,0\,0\,0\,0 & 0 & 1-\omega_{\theta}^2 & 0 & 0 & 0 & 0 \\
0\,0\,0\,0\,0\,0 & 0 & 0 & 1-\omega_{\psi}^2 & 0 & 0 & 0 \\
0\,0\,0\,0\,0\,0 & 0 & 0 & 0 & 1-\omega_{\dot{\phi}}^2 & 0 & 0 \\
0\,0\,0\,0\,0\,0 & 0 & 0 & 0 & 0 & 1-\omega_{\dot{\theta}}^2 & 0 \\
0\,0\,0\,0\,0\,0 & 0 & 0 & 0 & 0 & 0 & 1-\omega_{\dot{\psi}}^2 \\
0\,0\,0\,0\,0\,0 & -2\xi_{\phi}\omega_{\phi} & 0 & 0 & 0 & 0 & 0 \\
0\,0\,0\,0\,0\,0 & 0 & -2\xi_{\theta}\omega_{\theta} & 0 & 0 & 0 & 0 \\
0\,0\,0\,0\,0\,0 & 0 & 0 & -2\xi_{\psi}\omega_{\psi} & 0 & 0 & 0 \\
0\,0\,0\,0\,0\,0 & 0 & 0 & 0 & -2\xi_{\dot{\phi}}\omega_{\dot{\phi}} & 0 & 0 \\
0\,0\,0\,0\,0\,0 & 0 & 0 & 0 & 0 & -2\xi_{\dot{\theta}}\omega_{\dot{\theta}} & 0 \\
0\,0\,0\,0\,0\,0 & 0 & 0 & 0 & 0 & 0 & -2\xi_{\dot{\psi}}\omega_{\dot{\psi}}
\end{bmatrix}, \\
B &= \begin{bmatrix}
0\,0\,0\,0\,0\,0 & 1/m_b & 0 & 0 & 0 & 0 & 0 \\
0\,0\,0\,0\,0\,0 & 0 & l/I_x & 0 & 0 & 0 & 0 \\
0\,0\,0\,0\,0\,0 & 0 & 0 & 0 & l/I_y & 0 & 0 \\
0\,0\,0\,0\,0\,0 & 0 & 0 & 0 & 0 & 0 & 1/I_z
\end{bmatrix}^T, U = \begin{bmatrix} m\ddot{z} & I_x\ddot{\phi} & I_y\ddot{\theta} & I_z\ddot{\psi}, \end{bmatrix}^T \\
C &= \begin{bmatrix} 0 \cdots_4 0 & 1 \cdots_4 1 \end{bmatrix}_{1\times 12} \ and \ D = O_{12\times 4}
\end{aligned}
\tag{6.20}
$$

In the equations given as 6.20, the symbols are defined as follows:

Matrix $A \in \mathbb{R}^{12\times 12}$ represents a matrix containing state coefficients, which is a more generalized version of the Jacobian matrix.

Matrix $B \in \mathbb{R}^{12\times 4}$ expresses how the controller inputs relate to the system's states.

Vector $U \in \mathbb{R}^4$ holds the values of controller inputs.

Matrix $C \in \mathbb{R}^{1\times 12}$ describes the connection between the system's states and its outputs.

Matrix $D \in \mathbb{R}^{12\times 4}$ serves as a static gain matrix, indicating the relationship between the system's outputs and inputs.

The subscripts $i = \phi, \theta, \psi, \dot{\phi}, \dot{\theta}, \dot{\psi}$ refer to specific values that are calculated through simulations. Additionally, the parameters within the B matrix are derived from the linearized fast dynamics of the hexacopter.

6.2.3 Attitude Control: SMC (PI, PII, and PIII)

Taking into account the position control method described in 6.2.1, along with the SMC concepts elaborated in **PIII**, the formulation for the comprehensive control input and the sliding surface/variable (S) can be expressed as follows:

$$
\begin{aligned}
u &= -k_1 Sign(S) + k_2 \tanh(k_3 S) \ when \ k_i : i \in 1,2,3, \\
S &= \frac{\sin(\psi_d - \psi)\cos(\theta_d - \theta)\cos(\phi_d - \phi) - \cos(\psi_d - \psi)\sin(\theta_d - \theta)}{\cos(\delta_{fv_d} - \delta_{fv})} \\
\rightarrow S &= \frac{\sin(e_{\psi})\cos(e_{\theta})\cos(e_{\phi}) - \cos(e_{\psi})\sin(e_{\theta})}{\cos(e_{\delta_{fv}})}
\end{aligned}
\tag{6.21}
$$

In Equation 6.21, the subscript $\{\}_d$ denotes the desired value. This sliding variable has the added advantage of encompassing all attitude variables. Ensuring that the Lyapunov candidate is PD, radially bounded, and decreasing along the sliding surface, the candidate function $V(s)$ and its time derivative can be expressed as follows:

$$
\begin{aligned}
V(s) &= \frac{1}{2}S^2PS \\
\rightarrow \dot{V}(s) &= \frac{1}{2}P(2S\frac{dS}{dt}S + S^2\frac{dS}{dt}) \\
\rightarrow \dot{V}(s) &= \left(\frac{S(e_\psi)C(e_\theta)C(e_\phi) - C(e_\psi)S(e_\theta)}{C(e_{\delta_{fv}})}\right)^2 \times \\
&\quad \frac{P\big(C(\delta_{fv_d})C(\phi_d)C(\delta_{fv})C(\phi)+S(\delta_{fv_d})S(\phi_d)S(\delta_{fv})S(\phi)+C(\delta_{fv_d})S(\theta_d)C(\delta_{fv})S(\theta)+S(\delta_{fv_d})C(\theta_d)S(\delta_{fv})C(\theta)\big)}{S(e_\psi)C(e_\theta)C(e_\phi)C(\delta_{fv_d})C(\delta_{fv})C(\phi)+S(\delta_{fv_d})S(\phi_d)S(\delta_{fv})S(\phi)+C(\delta_{fv_d})S(\theta_d)C(\delta_{fv})S(\theta)}
\end{aligned}
\tag{6.22}
$$

In Equations 6.22, the approximations $S() \cong \sin()$, $C() \cong \cos()$, and e represent the difference between the desired and actual values. Therefore, when considering the control law, the attitude controller in relation to the azimuthal angle of the flap vanes can be reformulated as:

$$
\begin{aligned}
U_{roll} &= I_x(\ddot{\delta}_{fv_d} - k_1\dot{e}_\phi) - k_1\tanh(k_3S) \\
U_{pitch} &= I_y(\ddot{\delta}_{fv_d} - k_2\dot{e}_\theta) - k_1\tanh(k_3S) \\
U_{yaw} &= I_z(\ddot{\delta}_{fv_d} - k_3\dot{e}_\psi) - k_2\tanh(k_1S)
\end{aligned}
\tag{6.23}
$$

By using Equations 6.23, the constants k_i with $i \in \{1, 2, 3\}$ will be determined through trial and error during the implementation phase, as discussed earlier in Equation 6.13. Ultimately, as a result of applying the control law, the attitude controller interfaces with the position controller.

Chapter 7

Results and Discussion

This section presents a clarified compilation of the results from all the publications, organized in a coherent order. These results encompass findings from both simulation and real flight experiments.

7.1 Simulation Experiments

Starting with publication **PI**, the culmination of the research is presented, featuring the performance results of different control approaches. These approaches include using only flap vanes, solely EDFs, or a combination of both. The results reveal that employing only flaps or EDFs can lead to latency issues. However, combining flaps and EDFs enhances system agility and significantly contributes to attitude control stability. This research strongly recommends the utilization of both flaps and EDFs in the control system. Furthermore, this hybrid system offers the advantage of extending flight time endurance through the use of gas engines. The key findings of this paper are summarized below:

Figure 7.1 illustrates the drone's actual and reference states along a predefined trajectory using only flaps. Results reveal that the control of Euler angles remains stable, except for yaw, which becomes unstable over time, indicating that the flaps struggle to manage the drone's rotation during turns. This instability affected the lateral movement of the drone, resulting in unstable movements along the horizontal trajectory. However, the altitude loop remained perfectly controlled, as it was unaffected by the flaps.

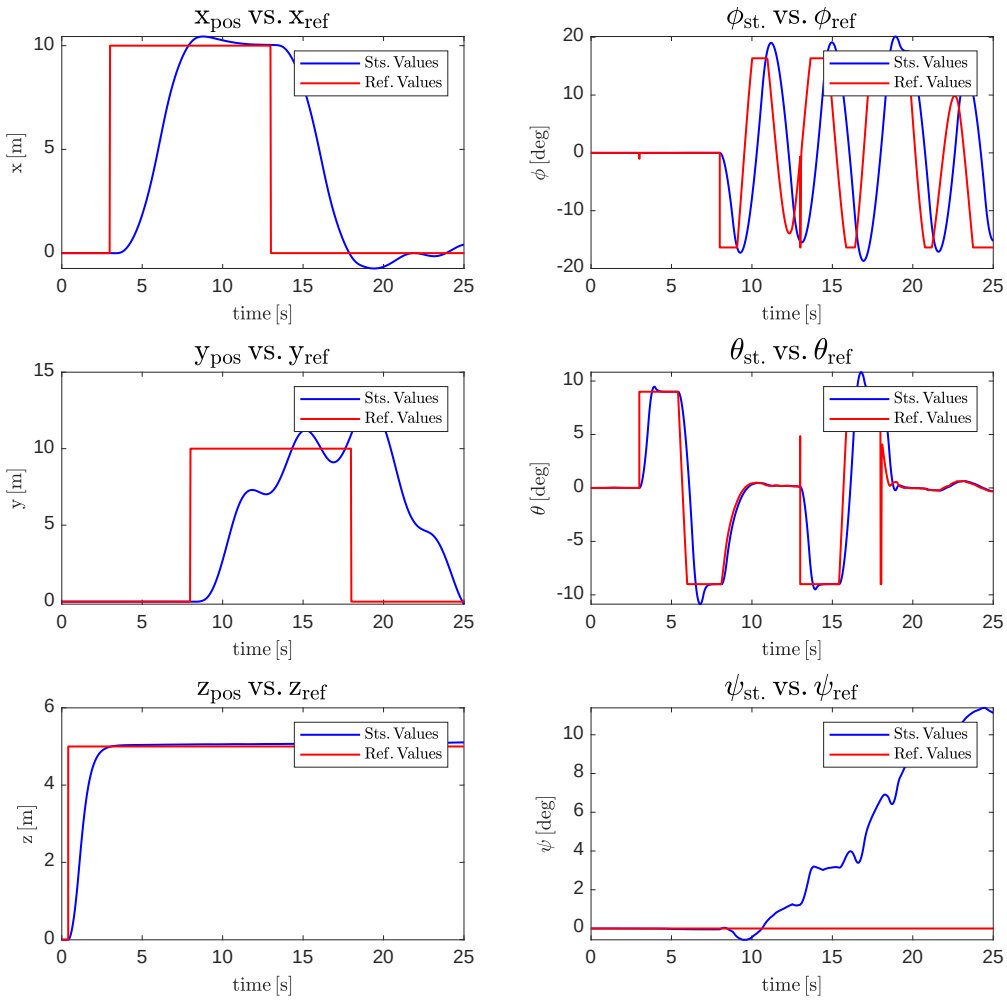

Figure 7.1: Comparison of the drone's actual state, reference positions, and attitude angles when $X_{\text{ref}} = 6$ m, $Y_{\text{ref}} = 6$ m, and $Z_{\text{ref}} = 5$ m, with the exclusive utilization of flap vanes.

Figure 7.2 displays the MDF's actual and reference states along a predetermined trajectory, employing solely EDFs. These fans were selected to provide functionality similar to that of flap vanes, albeit with approximately equal power. The results indicate that using only EDFs stabilizes the drone's attitude overall. However, similar to the case with flaps, yaw angle control proves challenging. This issue arises because the weight of the drone exceeds the stabilizing capabilities of the engine power, leading to instability in horizontal movement.

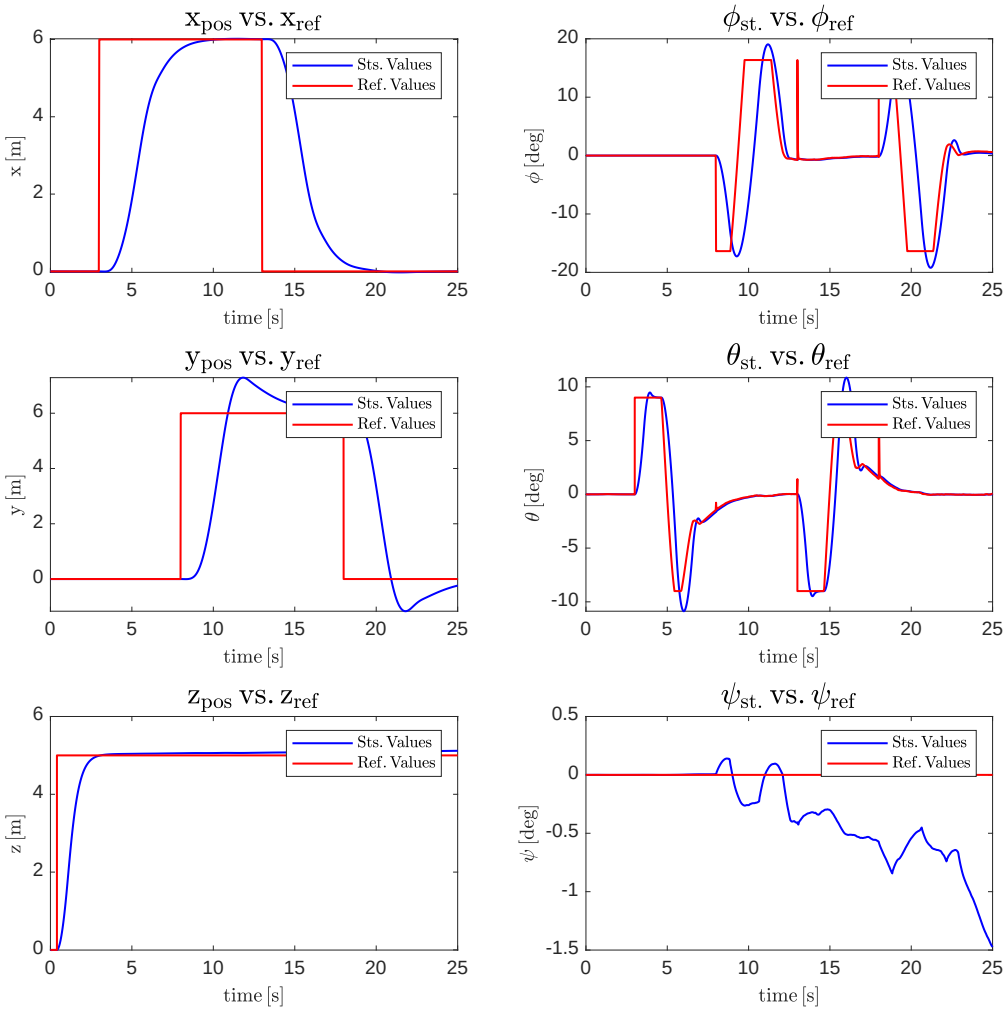

Figure 7.2: Comparison of the drone's actual state, reference positions, and attitude angles when $X_{\text{ref}} = 6$ m, $Y_{\text{ref}} = 6$ m, and $Z_{\text{ref}} = 5$ m, with the exclusive utilization of EDFs.

Figure 7.3 presents the MDF's actual and reference states along a predefined trajectory, utilizing both flap vanes and EDFs. The results indicate that this configuration effectively stabilizes the attitude system and, consequently, the horizontal movement of the MDF. This success can be attributed to the combined control provided by sufficient power from both systems. As observed in the figure, both the X and Y elements of the position are rapidly controlled with minimal overshoot. However, it's worth noting that the yaw stability still presents challenges at this stage, which were subsequently addressed in later iterations of the work.

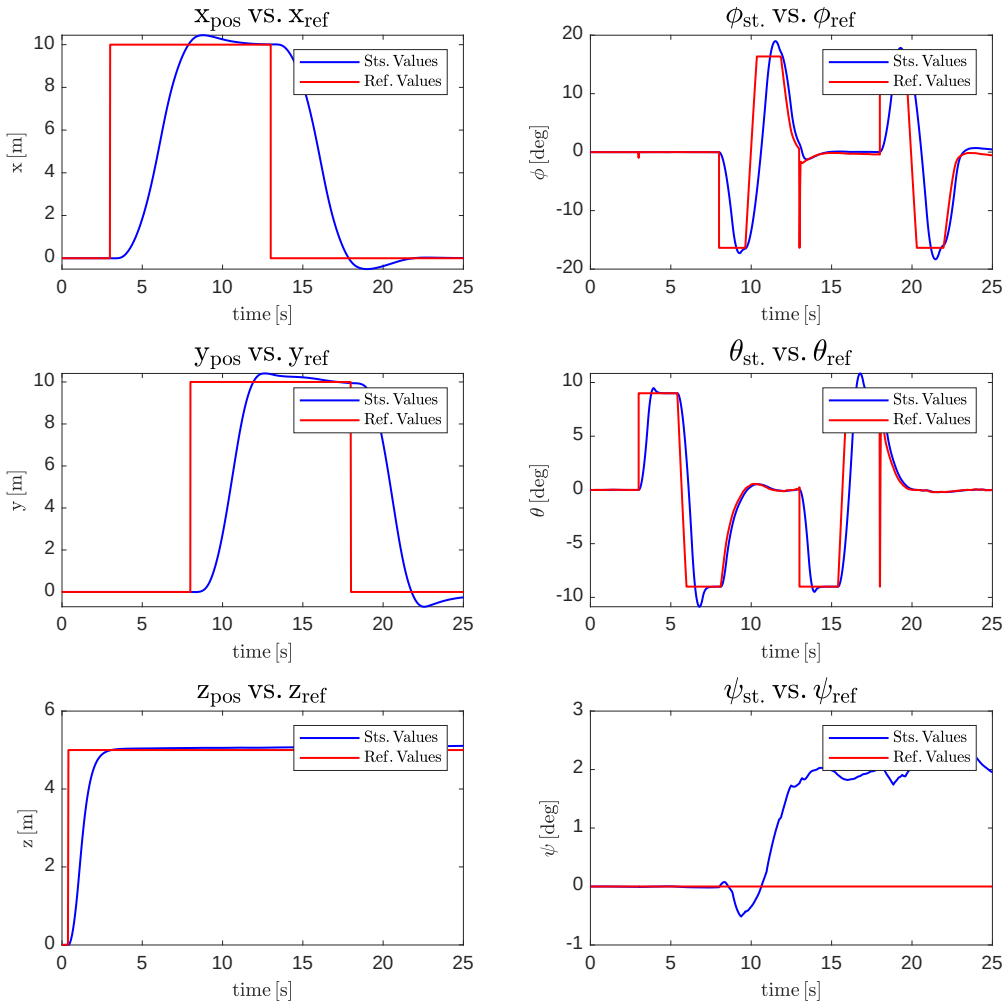

Figure 7.3: Comparison of the drone's actual state, reference positions, and attitude angles when $X_{ref} = 6$ m, $Y_{ref} = 6$ m, and $Z_{ref} = 5$ m, with the simultaneous utilization of both flaps and EDFs.

In the next publication and through the implementation of an adaptive controller, several enhancements were made to the mathematical model. This adaptive controller proved particularly effective in improving the efficiency of the controller, even when faced with failures during simulations. The optimized simulation results obtained in publication **PAd** are illustrated in Figure 7.4. During this simulation, a random failure of one EDF was introduced to observe the resulting instability while the MDF was in a stabilized motion. As depicted in the figure, despite the failure, both the roll and pitch of the MDF remained stable. However, there was a noticeable impact on the yaw, resulting in an irregular rotation. Despite this, the horizontal plane was effectively stabilized and controlled, showcasing the resilience of the MRAC in managing unexpected disturbances.

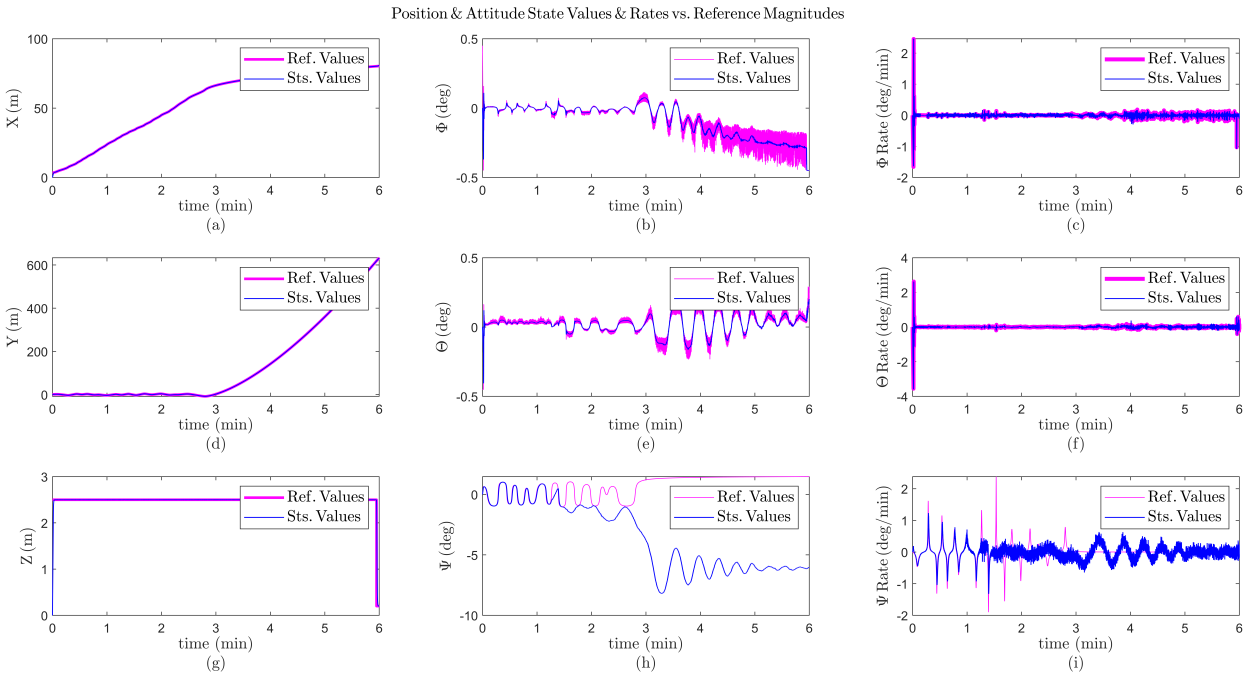

Figure 7.4: Analyzing the impact of a 5-minute failure in one of the EDFs. The results showcase the dynamics of the drone during this critical event. Specifically, (a), (d), and (g) correspond to the position controller, (b) and (c) the variation of the roll angle (ϕ) and the roll rate ($\dot{\phi}$ rate), respectively, (e) and (f) the pitch angle (θ) and the pitch rate ($\dot{\theta}$), respectively, (h) and (i) the yaw angle (ψ) and the yaw rate ($\dot{\psi}$) over time, respectively. These insights provide valuable information for assessing the system's stability and control strategies in the face of EDF failures.

Following with publication **PAd**, to compare and assess the performance of the proposed controller method, a semi-circular trajectory and then a rectangular route was chosen. This trajectory enables the examination of both turning points, where controllers often struggle to maintain a steady state, and abrupt, sharp turns, which introduce uncertainty to the control system. Additionally, random noise was introduced into the system to challenge its robustness further. The performance of this new method was compared to that of an ideal cascade PID controller operating on the same trajectory. For more detailed information about the test conditions and the noise function used in this study, please refer to **PII**. The results of this comparative analysis are presented below:

Figure 7.5 illustrates a realistic simulation depicting the horizontal movement of an MDF along a lengthy trajectory utilizing SMC. The term 'realistic' is employed because random external wind disturbances were introduced during the flight to assess the controller's functionality. Despite encountering harsh turns, the drone exhibits minor deviations, highlighting the effectiveness of the SMC implementation. Additionally, the smooth trajectory around the circular path demonstrates the efficacy of utilizing *tanh* in the sliding function to stabilize the attitude system.

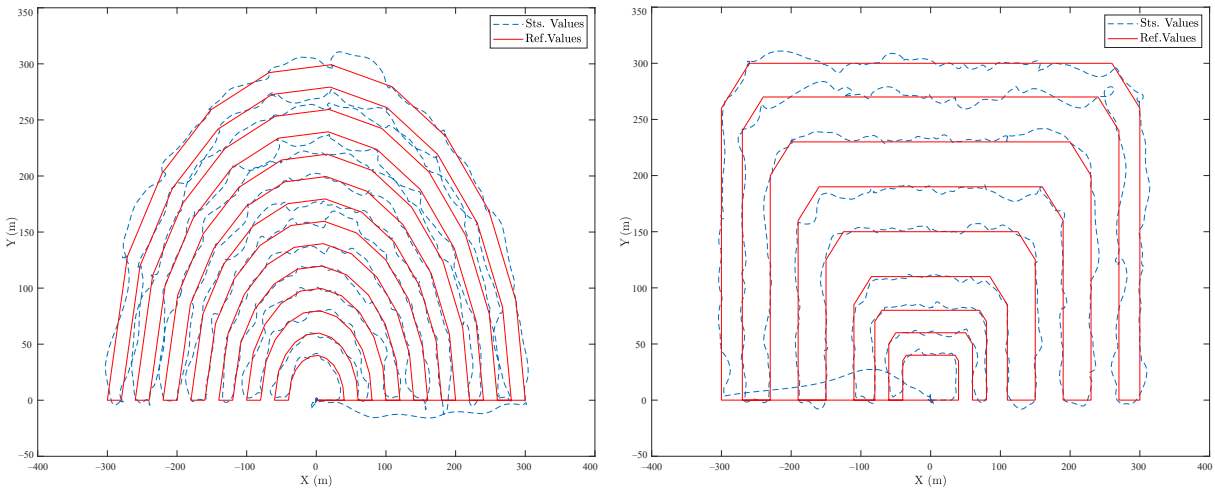

(a) Semi-circular trajectory. (b) Rectangular trajectory.

Figure 7.5: (Realistic Simulation): The horizontal projection of the reference and actual trajectory in the presence of random wind disturbances for two distinct flight paths.

Figure 7.6 presents the ideal simulation results of the MDF system navigating circular and rectangular trajectories using a cascade PID controller. The system is observed to exhibit superior control, evident from the minimal deviation experienced. It's important to note that these simulations were conducted under nominal conditions without the presence of any external disturbances.

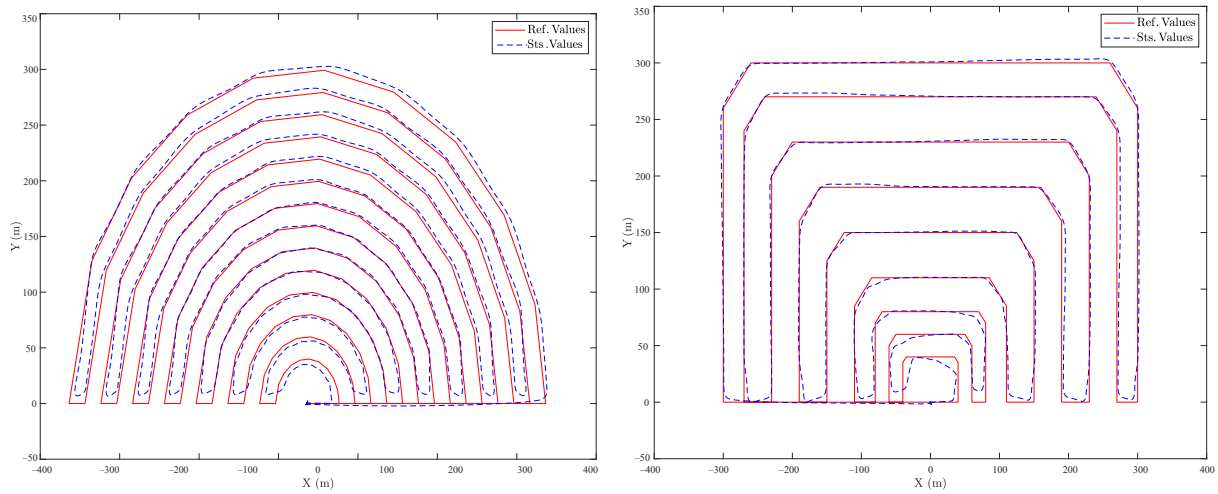

(a) Semi-circular trajectory. (b) Rectangular trajectory.

Figure 7.6: (Ideal Simulation): The horizontal projection of the reference and actual trajectory for two distinct flight paths controlled by a cascade PID controller.

Building upon previous research, the simulation process conducted in **PIII** was within the dynamic space of Gazebo on Ubuntu 18.04. The flap vanes joints were modeled as cylindrical

bars connected to servo-simulated springs, incorporating presumed bandwidth and amplitude gain margins. In the subsequent analysis, two figures illustrate the outcomes of two cruise flights conducted by the heavy Wild Hopper model over approximately 40 minutes for comparison. Figure 7.7 showcases the controller performance of a finely tuned PID controller. The top part depicts the altitude compared to the desired altitude, revealing a noticeable but manageable error. On the right, the total thrust of all propellers is presented, while the 3D plot illustrates the drone's trajectory throughout the flight. Zooming in on the movements, a five-line polygon of waypoints was defined to observe attitude performance at turning points. Over time, trajectory errors accumulate in the integrator, especially at turning points. However, these errors diminished thanks to the cascade loop compensating for the deviated lines. Notably, some errors emerged during ascents since the waypoints were not horizontally aligned. This indicates that the PID controller struggled to stabilize effectively when altitude changes occurred simultaneously. Nevertheless, it demonstrated merely acceptable results during hover and cruise flights.

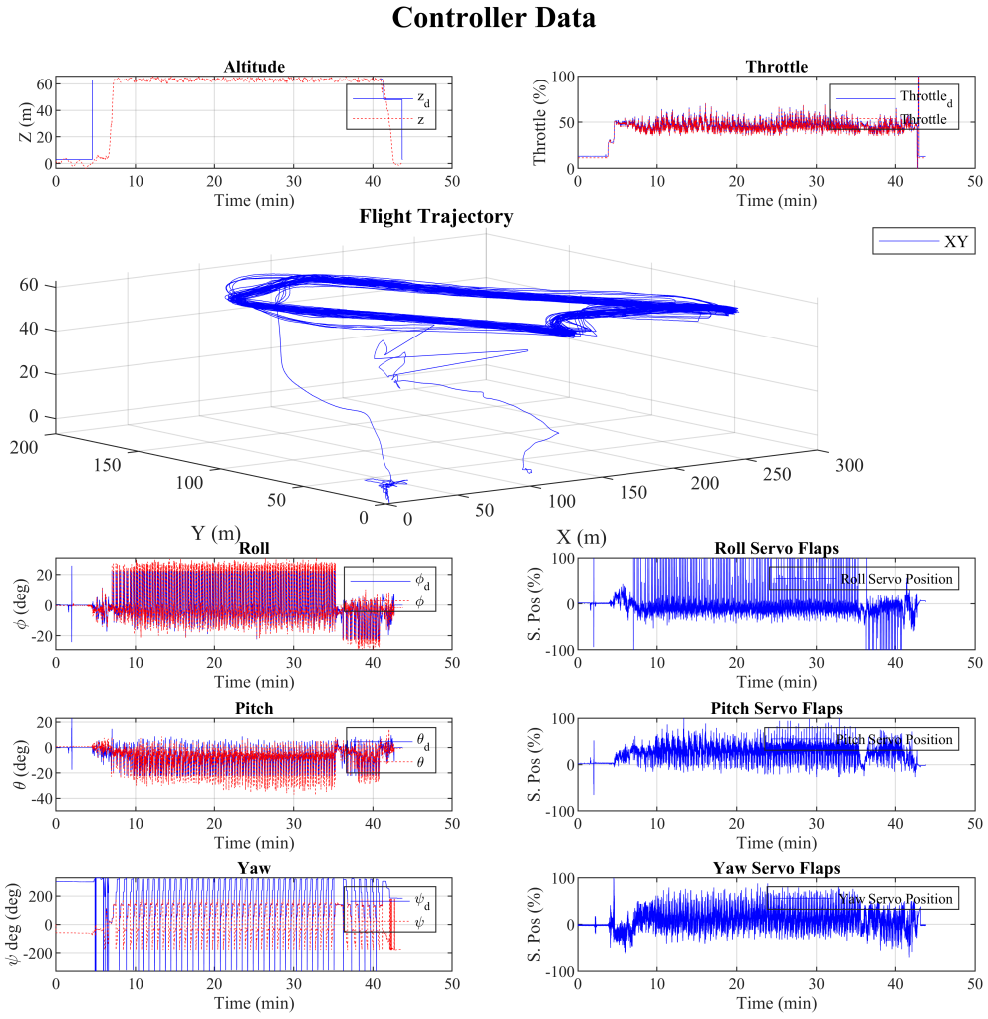

Figure 7.7: Simulation of Attitude controller performance during a cruise flight, controlled by a cascade PID and utilizing flap vanes.

The second simulation flight utilized the robust method introduced in **PIII**. As depicted in Figure 7.8, the overall flight trajectory mirrors that of the PID controller. In this simulation, a rectangular flight plan was initially executed. However, halfway through the flight, the rectangle underwent a 20-degree horizontal rotation to assess potential controller parameter accumulation. Remarkably, the controller effectively stabilized the flight, showcasing minimal attitude errors in the roll, pitch, and yaw loops. In contrast to the PID controller, this time, the ascending phase was more intense, and unexpectedly, moments of instability occurred during ascent that were beyond the controller's immediate control. However, the drone's swift movements effectively compensated for the instability, ensuring a safe landing.

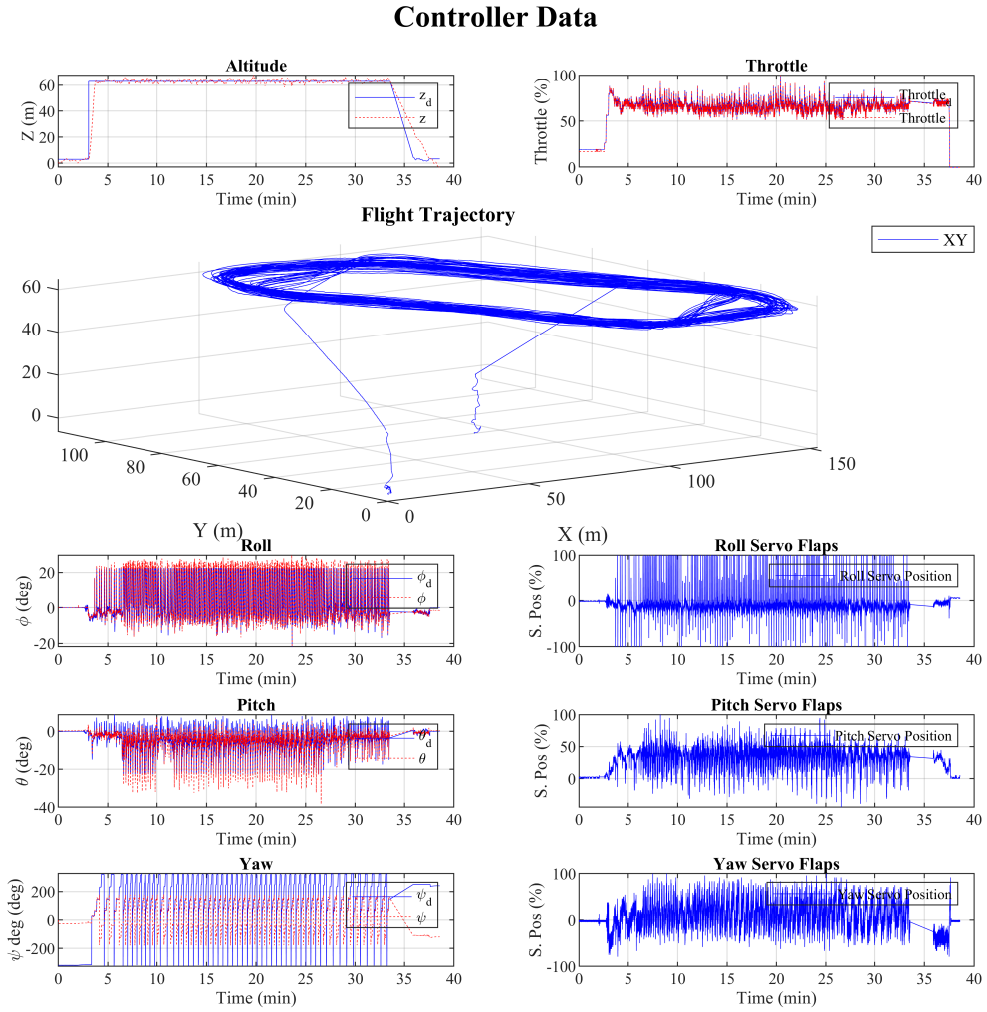

Figure 7.8: Simulation of Attitude controller performance during a cruise flight, controlled by the presented robust controller and utilizing flap vanes

7.2 Real-World Flight Experiments

Starting with publication **PAd** that presents the outcomes of numerous real flight tests conducted to validate the controller's effectiveness under diverse conditions. These flight test

results encompass hover and balance flights near the ground with a payload, hover flights with intermediate disturbances, and evaluations of the controller's performance during a flight with an EDF failure.

Figure 7.9 demonstrates the analytical results from a balance test. This test was conducted close to the ground, with altitudes varying up to 1.5 m and different payload weights. Additionally, the flight involved a copilot, where manual piloting was intentionally saturated by the autopilot's limitations to evaluate its responses. To ensure safety, the payload was suspended further from the fuselage using a rope. During the test, between the time interval of 6 s to 7.5 s, the pilot issued simultaneous roll and pitch commands of 15 degrees, along with a random yaw command, as illustrated in Figure 7.9(a-c). Despite the changes in attitude angles, the controller promptly stabilized the aircraft in less than 2 seconds, with only minor deviations.

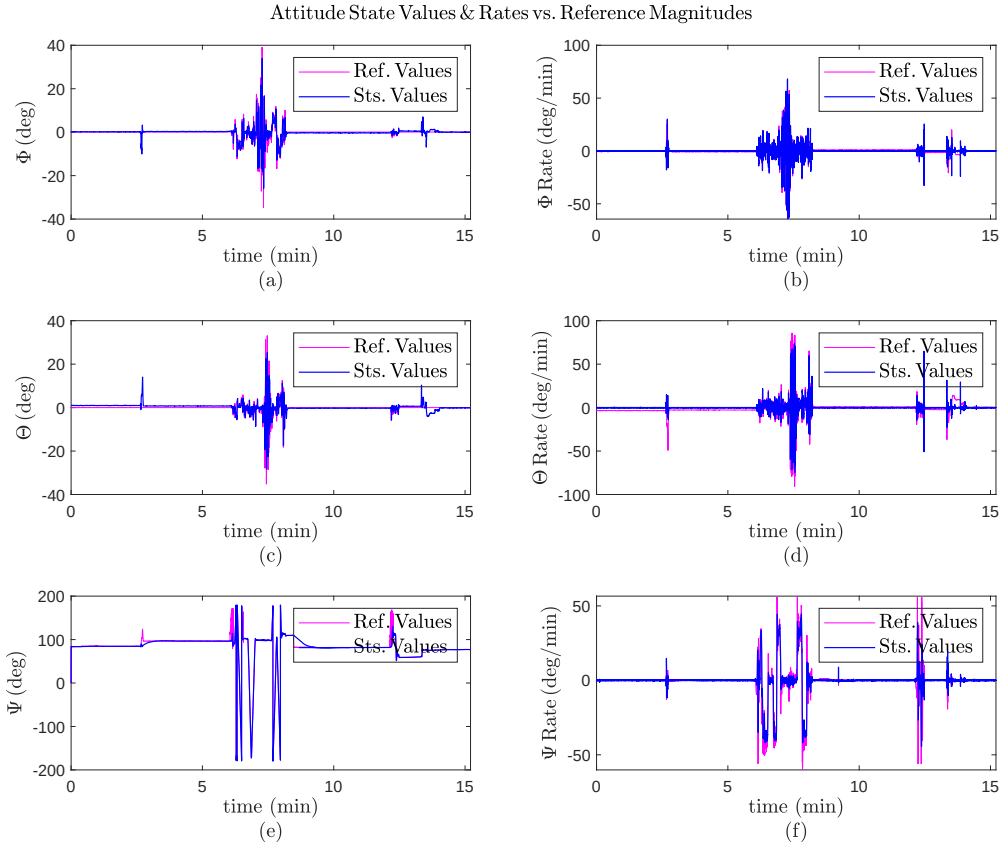

Figure 7.9: Balance test results over a 15-minute duration are presented as follows: (a) Time evolution of roll (ϕ) angle; (b) Time evolution of pitch (θ) angle; (c) Time evolution of yaw (ψ) angle; (d) Time evolution of roll rate ($\dot{\phi}$); (e) Time evolution of pitch rate ($\dot{\theta}$); (f) Time evolution of yaw rate ($\dot{\psi}$).

Thereafter, multiple flight tests were conducted at higher altitudes following the configuration of ground tests and tuning of PID parameters to ensure the FAN HOPPER's controllability. Two of these flight tests correspond to **PAd**, are presented here.

Figure 7.10 shows the results of a flight test lasting 18 minutes, including a sudden pilot disturbance occurring after 7.5 minutes. This disturbance led to an undershoot reaction from the attitude controller due to saturated inputs, as depicted in Figure 15a. However, stability was swiftly regained in less than 10 seconds, as the deviation was mitigated through a cascade approach. This approach effectively regulated both the roll angle and its rate, as demonstrated in Figure 7.10(b). Additionally, unexpected phenomena were observed in the pitch and yaw angles after 7.5 minutes, 9.5 minutes, and 13 minutes. The controller promptly dampened these phenomena, ensuring stable flight throughout the test duration.

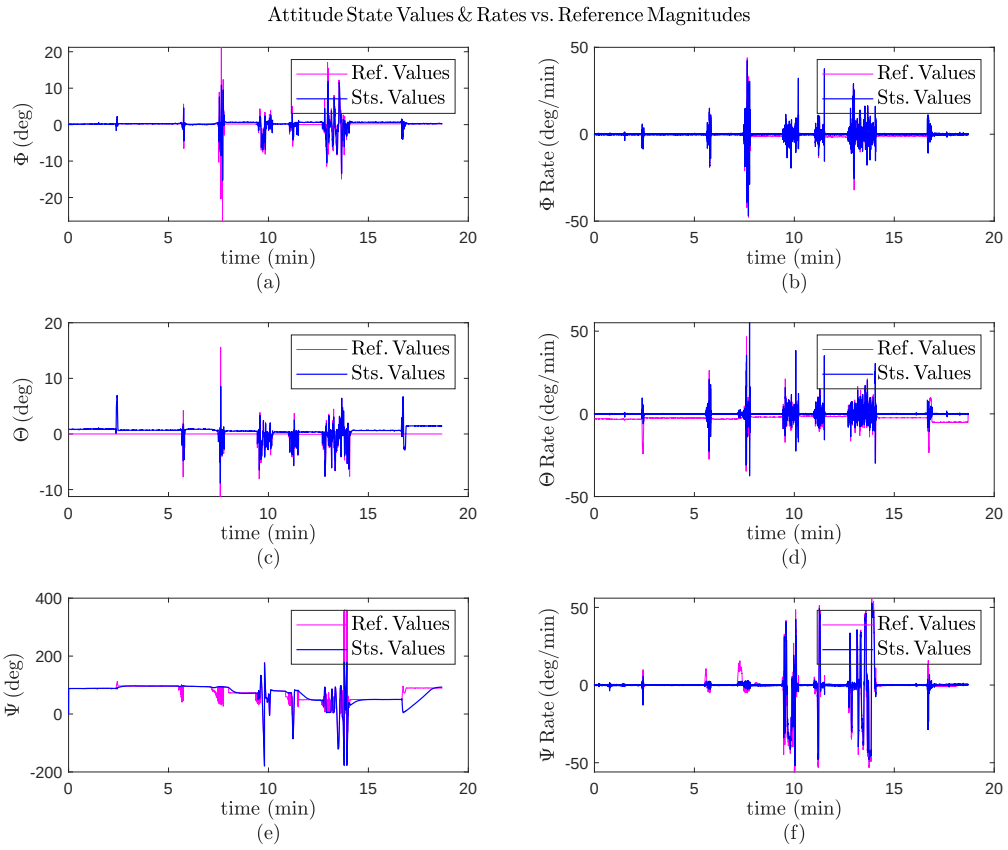

Figure 7.10: Practical results over an 18-minute duration with intermediate disturbances are depicted as follows: (a) Time evolution of roll (ϕ) angle; (b) Time evolution of pitch (θ) angle; (c) Time evolution of yaw (ψ) angle; (d) Time evolution of roll rate ($\dot{\phi}$); (e) Time evolution of pitch rate ($\dot{\theta}$); (f) Time evolution of yaw rate ($\dot{\psi}$).

Figure 7.11 displays results characterized by high disturbances that initially caused instability. However, these disturbances were promptly damped with sufficient agility. As illustrated in Figure 7.11, at the 10-minute mark, all attitude angles experienced simultaneous alterations: 10 degrees for roll, 8 degrees for pitch, and up to -200 degrees for yaw. Remarkably, these deviations were regulated in less than 2 seconds. At the 15-minute mark, one of the EDFs was intentionally unplugged from the system, resulting in a negligible transient error (less than 1 degree) in the pitch angle.

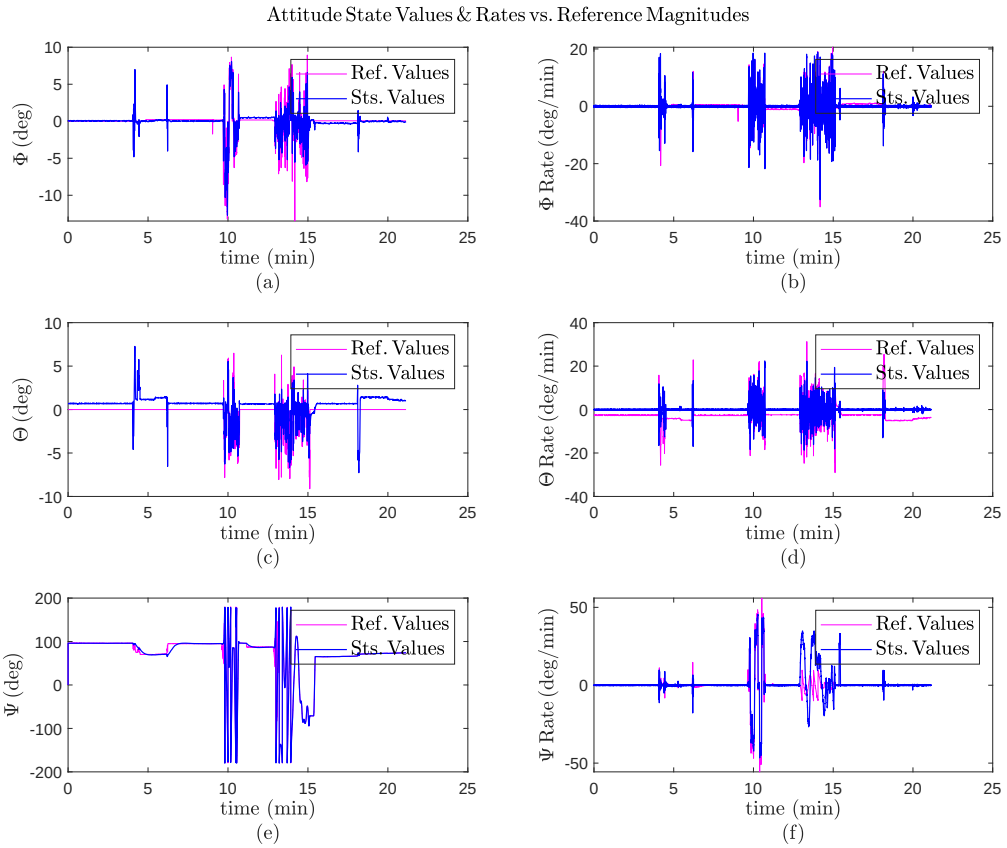

Figure 7.11: Practical results over a 22-minute duration with an EDF failure are presented as follows: (a) Time evolution of roll (ϕ) angle; (b) Time evolution of pitch (θ) angle; (c) Time evolution of yaw (ψ) angle; (d) Time evolution of roll rate ($\dot{\phi}$); (e) Time evolution of pitch rate ($\dot{\theta}$); (f) Time evolution of yaw rate ($\dot{\psi}$).

Subsequently, integrating various submodules required to assemble real components, a series of improved real-world results are presented in **PIII**. These results focus on five of the most successful missions performed by the redesigned and fine-tuned heavy-duty Duty Hopper prototype. It's worth noting that the initial schematic of this prototype was explored in detail in a previous study **PI**. Through successive iterations and improvements, this model has now reached Technology Readiness Level 7 (TRL-7), signifying its readiness for practical deployment, as outlined in 3.2.

The final results share a common timeframe, with flight durations ranging from 11 to 27 minutes. These experiments primarily assess the efficiency of the attitude controller, with the position loop intentionally excluded from consideration. To aid clarity and ease of interpretation, we also include the rates of the Euler angles in our results, with a specific focus on the changes in roll, pitch, and yaw servo flap positions, presented in comprehensive diagrams. Furthermore, it's important to note that the random noise equation employed for all flights remains consistent, as previously discussed in Ale Isaac et al., 2024, and is consistently applied in the context of this research.

The first result, illustrated in Figure 7.12, pertains to a brief hovering flight sequence. During

this flight, we intentionally introduced random noise into the yaw controller loop for 60 milliseconds, occurring in both the second and fourth minutes of the flight. The impact of this noise propagation is evident between the sixth and eighth minutes. However, as our diagrams vividly illustrate, the controller effectively managed this uncertainty, demonstrating its capability to stabilize the attitude even in the face of unexpected challenges.

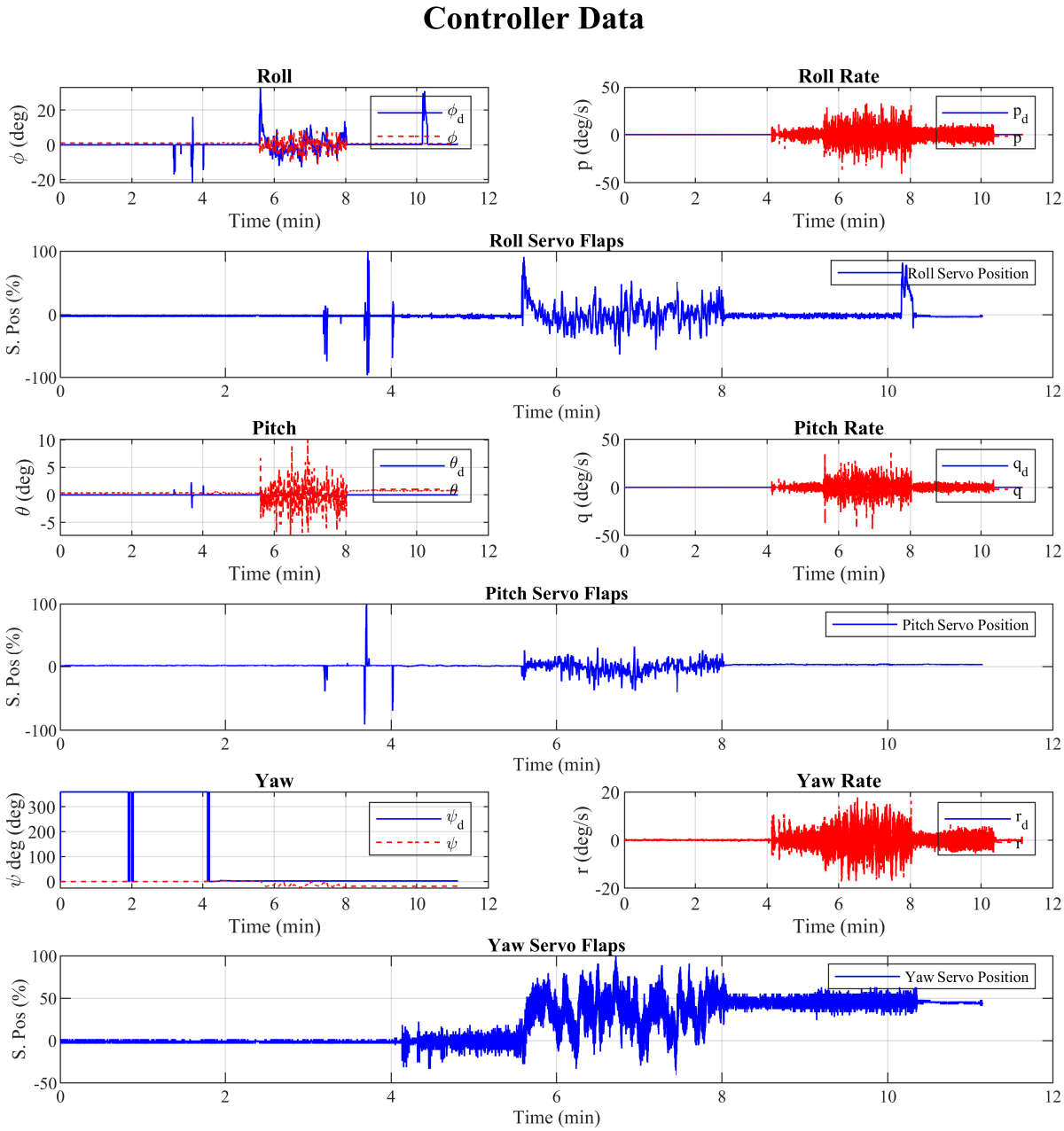

Figure 7.12: Attitude controller performance during a brief flight, enhanced by TVC utilizing flap vanes to stabilize the system against uncertainties applied on the yaw loop.

The second flight as shown in Figure 7.13, lasting approximately 19 minutes, featured two

instances of random nonlinearity application during an almost hover flight, coupled with a few angle-turning trajectories. These nonlinearities were introduced once in the roll loop and once in the pitch loop. Notably, the overall system promptly re-established regulation. However, in the yaw loop, some interference became apparent due to accumulated errors introduced during the extended duration of the flight. In this instance, the adaptive parameters struggled to fine-tune the loop. Importantly, it is worth noting that the interference, while observable, remained within predefined limits as the yaw angle remained saturated.

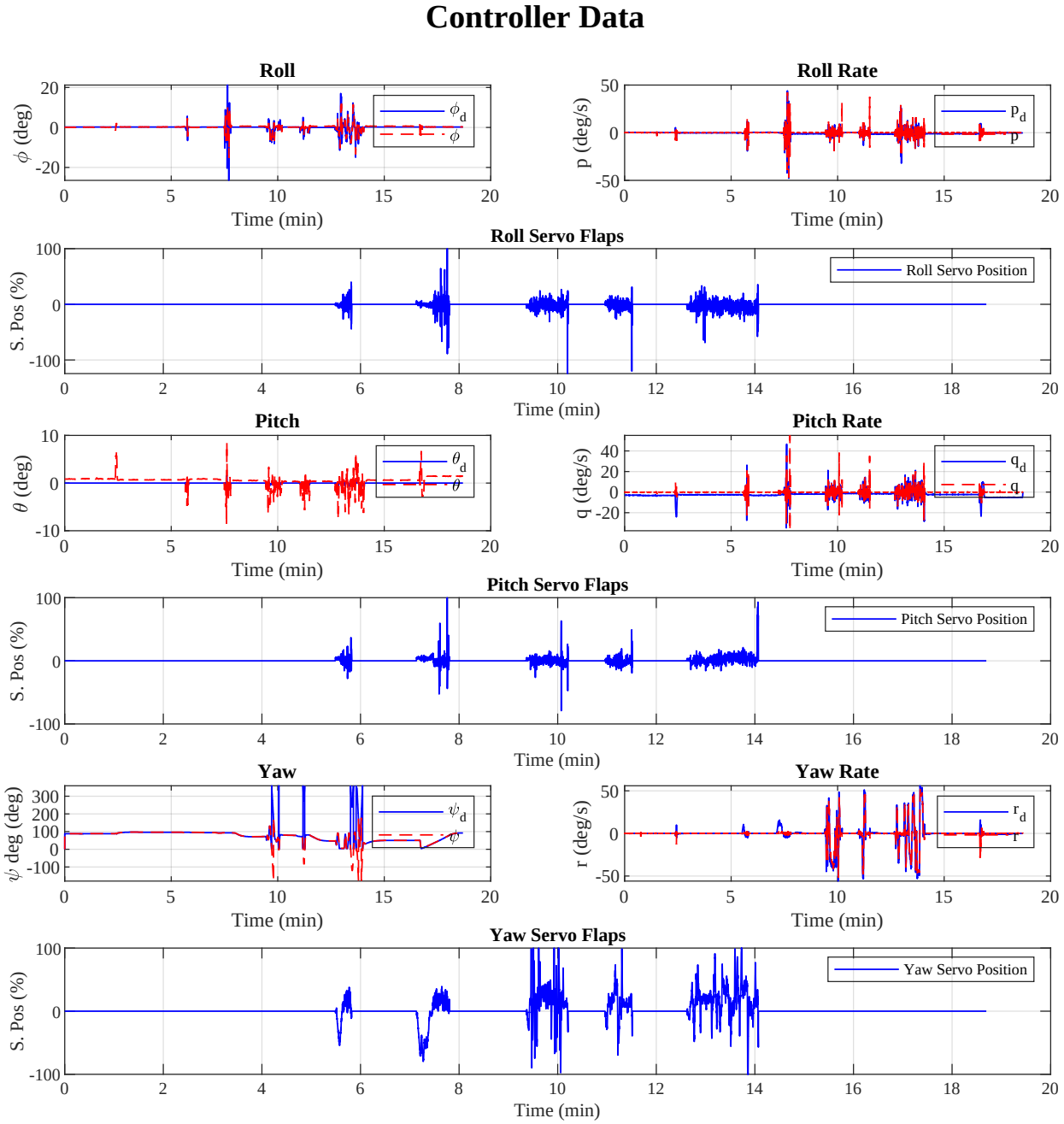

Figure 7.13: Attitude controller performance during a hover flight, enhanced by TVC utilizing flap vanes to stabilize the system against uncertainties applied on the roll and pitch loops.

The third flight, illustrated in Figure 7.14, comprised a 22-minute cruise phase during which random noise was deliberately introduced into both the roll and pitch control loops. These uncertainties manifested as brief, 50-millisecond disturbances, with one occurring in the roll loop during the tenth minute and another in the pitch loop during the fifteenth minute of the flight. The results of this flight demonstrate the system's impressive recovery and adaptability, with adaptive parameters promptly adjusted before and during the flight to restore stability. This flight was extended to observe the assessment of accumulated errors in the yaw control loop. As depicted in the figure, the yaw rate effectively compensated for the nonlinearity, leading to a rapid decrease in yaw loop disturbances, highlighting the effectiveness of the system's adaptive capabilities.

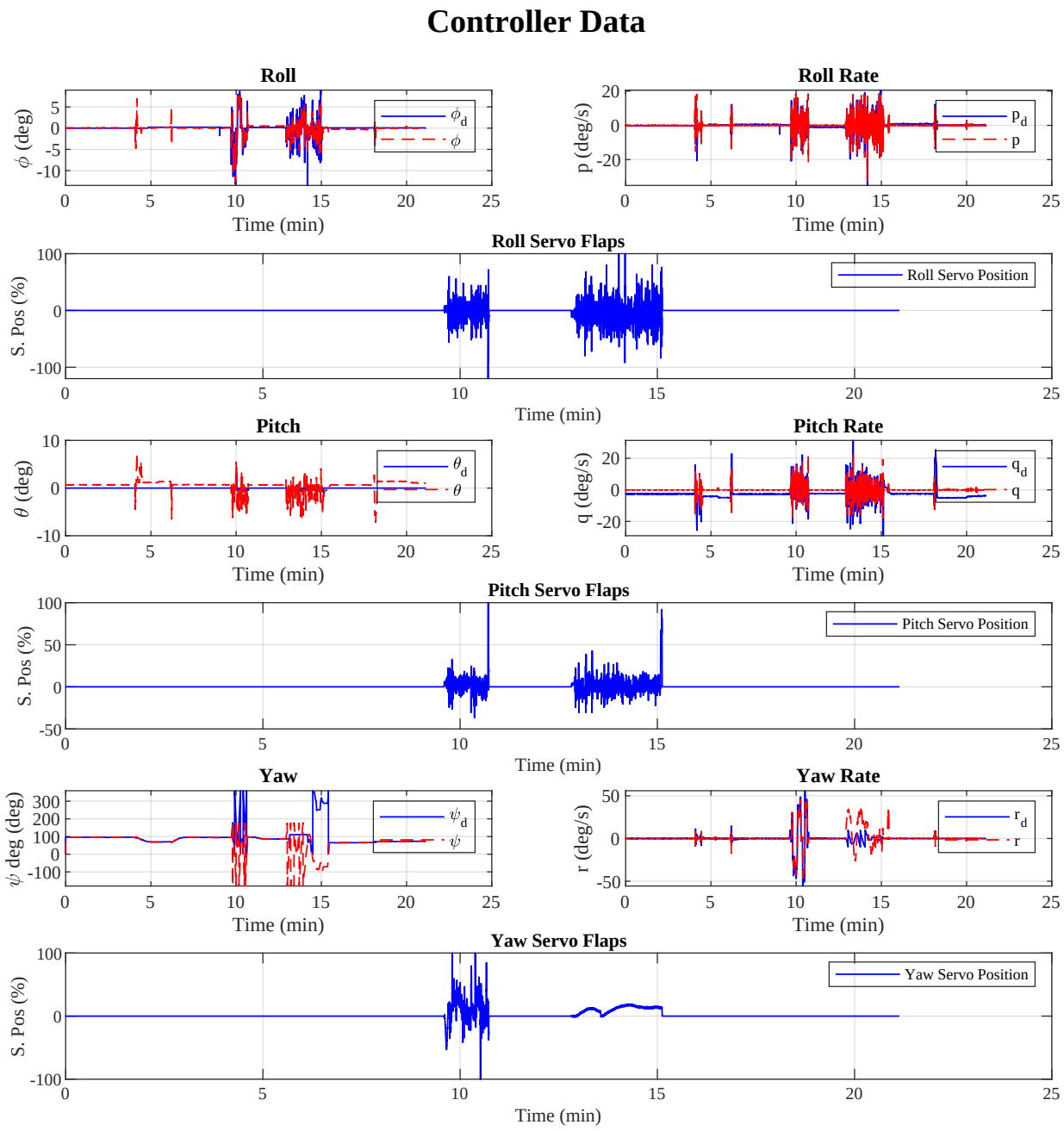

Figure 7.14: Attitude controller performance during a cruise flight with a rectangular trajectory, enhanced by TVC utilizing flap vanes to stabilize the system against an uncertainty applied on the yaw loop.

The last experiment, depicted in Figure 7.15, lasted for 27 minutes, following a rectangular trajectory. During the flight, a high noise was applied to the yaw loop in a turning moment of the rectangle in order to observe the performance of the controller. As seen in the plots, the noise is applied on the twentieth minute the reaction of the system was utilizing both roll and pitch servo flaps to overcome the nonlinearity seen in the system. The system was recovered after a minute and the flight continued normally.

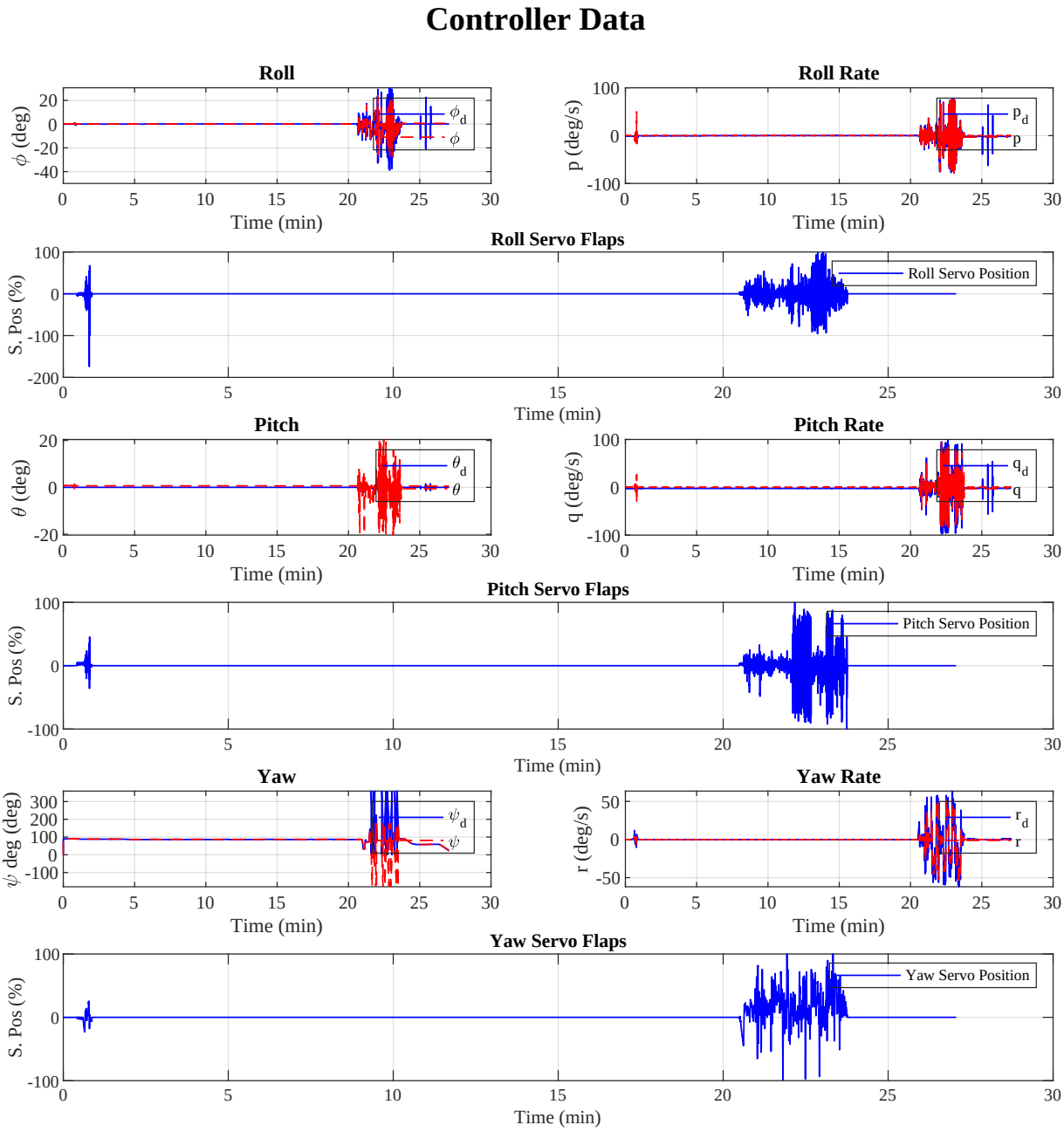

Figure 7.15: Attitude controller performance during a cruise flight with a rectangular trajectory, enhanced by TVC utilizing flap vanes to stabilize the system against uncertainties applied on the roll and pitch loops.

Chapter 8

Conclusions and Future Work

This thesis presented as a compendium, introduces a high-performance control system designed for both vertical and attitude control of a heavy Unmanned Aerial Vehicle (UAV) equipped with internal combustion thermal engines and configured with a Multi-Ducted Fan (MDF) layout. The research encompasses a comprehensive process that includes the following key phases:

Conceptual Design This phase involves the development of the fundamental concept for the Multi-Ducted Fans (MDFs). It includes defining project requirements outlined by the European Commission (as referenced in Section 1.4), establishing the system configuration, and determining key design parameters.

Preliminary Design This stage encompasses various critical aspects, such as mathematical modeling, aerodynamic analysis, structural design, selection of propulsion systems, and other essential considerations.

Detailed Design This phase encompasses simulation and practical validation processes aimed at preparing the prototype for industrial use. The research journey involved three hierarchical platforms, each designed to enhance the work level incrementally: The first platform was a medium-scale fully electric turbofan-powered hexa ducted fan named "FAN HOPPER" (as described in Sections 4, 4.1, and **PAd**). The second platform was a heavy quad ducted fan prototype with an initial stage concept for controlling the MDF using flap vanes, capable of carrying heavy payloads and powered by both thermal and electrical engines, referred to as "DUTY HOPPER" (explained in Sections 4, 4.2, and **PI**). The ultimate objective of the main project was to design a hexa ducted fan, empowered by thermal engines and auxiliary EDFs, with the capability to carry heavy payloads, known as "WILD HOPPER" (as detailed in Sections 4, 4.3, **PII**, and **PIII**).

Continuing with the primary objective of this thesis, which is to achieve precise attitude control, a comprehensive overview of the control strategy is provided in Section 4. The control algorithms introduced are specifically tailored for Thrust Vector Control (TVC) to suit the MDF configuration effectively. The key concepts and distinctive features of these controllers are elucidated as follows:

Controller Parameters The primary control focuses on two key aspects: vertical position or altitude and Euler angles, which encompass the attitude of the UAV, as illustrated in Figure 6.1.

Controller Actuators The altitude control relies on the thermal engines, which drive the primary propellers to generate thrust for the MDF. In emergency situations, the MDFs take on the role of thrust generation. For attitude control, the servo flaps act as the controller actuators, manipulating the flap vanes, which function as control surfaces. These components work together to produce the necessary forces and moments for stabilizing the MDF's attitude.

TVC using Model Reference Adaptive Control (MRAC) This controller is introduced, conceptually designed, and practically implemented on the "FAN HOPPER" platform to stabilize the MDF against internal uncertainties, particularly variations in payload weight (refer to Subsections 6.1.1, 6.2.2, and **PAd**).

TVC using Sliding Mode Control (SMC) This controller is developed to ensure stability against external uncertainties for both the "DUTY HOPPER" and "WILD HOPPER" prototypes (refer to Subsections 6.1.1, 6.2.2, **PI**, **PII**, and **PIII**).

Furthermore, the control process is complemented by extensive validation stages, encompassing both laboratory and operational phases, to assess the controller's functionality and performance during actual flights. This comprehensive testing approach initiates with MATLAB Simulink SimScape simulations, further enhanced by the Gazebo platform, culminating in real-world flight tests.

It's important to highlight that this collaborative endeavor represents the culmination of years of collective effort by a dedicated group. The author of this thesis played a pivotal role in designing the controller and devising control concepts, contributing significantly to the development of an operational and industrially viable system.

Future potential research endeavors encompass enhancing the airfoil design of the flap vanes to further optimize their functionality. Additionally, there is a prospect of finalizing the production of the "WILD HOPPER," enabling rigorous testing in more challenging maneuvers and under varying temperature conditions. This would serve to evaluate the performance of individual components and assess the adaptability of controller parameters in the face of diverse and plausible nonlinearities. These initiatives aim to advance the field of MDF UAVs and refine the capabilities of such systems for a wide range of applications.

Chapter 9

Publications

9.1 Publication I

Isaac, M.S.A., Ragab, A.R., Garcés, E.C., Luna, M.A., Peña, P.F. and Cervera, P.C. (2022). *Mathematical Modeling and Designing a Heavy Hybrid-Electric Quadcopter, Controlled by Flaps.* Unmanned Systems, 10(03), pp.241-253, doi:10.1142/S2301385022500133.

OPEN ACCESS
Unmanned Systems, Vol. 10, No. 3 (2022) 241–253

DOI: 10.1142/S2301385022500133

UNMANNED SYSTEMS
https://www.worldscientific.com/worldscinet/us

Mathematical Modeling and Designing a Heavy Hybrid-Electric Quadcopter, Controlled by Flaps

Mohammad Sadeq Ale Isaac[*,†], Ahmed Refaat Ragab[*,‡], Enrique Caballero Garcés[§], Marco Andres Luna[*,†,¶], Pablo Flores Peña[*], Pascual Campoy Cervera[†]

[*]*Drone Hopper Company, Spain*

[†]*Polytechnic University of Madrid, Spain*

[‡]*University of Carlos III of Madrid, Spain*

[§]*UC3M and Aerodynamics Engineer at Drone Hopper*

Systematic hybrid-electric unmanned aerial vehicles (UAVs) and, especially, quadcopters are so promising due to their long flight endurance and their usage in patrol and rescue missions which gain a high interest to be under examination and test scope by researchers; however, a complete mathematical design is required to fulfill theoretical complexities such as aerodynamic analysis and flight dynamics models related. This paper investigates salient sections from hypothesis to implementation. Researchers at Drone Hopper company have conducted various calculations to perform a precise novel platform called Duty-Hopper (DH). The benefit of this design is to control the attitude by flap vanes and electrical ducted fans (EDFs) when using gasoline engines; while, the principle propellers only lift the drone. This paper examines the attitude control system of DH, once using only flaps, then by only EDFs, and eventually, by compounding both. During this research, the scientific software used is ANSYS-Fluent and MATLAB-SimScape to analyze the entire body of the DH. Furthermore, a robust fault-tolerant controller is designed to immune the DH against internal and external errors. Our research reveals that using flaps is a feasible way to control attitude when it is augmented by EDFs.

Keywords: Hybrid-electric; UAV; quadcopter; duty-Hopper; EDF; flap.

1. Introduction

The hybrid-electric propulsion is a rather innovative technology system employed to combine the mechanical power generated by one (or more) electric drives with a thermal engine [7]. Hybrid-electric propulsive UAVs (HEP-UAVs) are highly valuable, thanks to removing heavy batteries and a long endurance; in counterpart, their disadvantage is the control challenge. They perform beneficial applications such as wildfire fighting, long-term inspection, carrying heavy payloads, and patrolling UAVs [13,24]. There are various researches investigating HEP-UAVs. Bravo *et al.* [25] concentrated on the similarities and differences of the pure HEPs compared to conventional ones and introduced a normalized analysis to improve light HEP configuration, approaching the pure one. Savvaris *et al.* [26] worked on control and optimization of light HEP systems, using a parallel configuration architecture and supervisory control to implement in-ground hardware-in-the-loop (HIL) tests. Ruscio [27] emphasized the propulsion aerodynamics and wing mass of the fast general aviation class and validated it by implementing on double-engine Beechcraft 76 and the X-57 Maxwell to be in both propulsive and hybrid forms. Capata *et al.* [28] proposed a conceptual design of an

Received 27 May 2021; Revised 3 September 2021; Accepted 3 September 2021; Published 19 November 2021. This paper was recommended for publication in its revised form by editorial board member, Wen-Hua Chen.
Email Address: ¶*marco.a@drone-hopper.com*

HEP-UAV feeding by ultramicrogas–turbine (UMGT), which powers an electric generator, concluding high-endurance flights, which is obtained by several aerodynamics analyses to optimize the specific fuel consumption. Nonetheless, Yung [16] made a survey on various propulsive and electric systems to compound an optimized simulated model, using both systems simultaneously, and according to this research, a HEP-UAV can save energy up to 6.5% compared to only a propulsive model. Throughout existing works, there is a gap for combining the theories and industrial form of HEP-UAVs. This research is undergoing to fill this space by presenting a rationale methodology and proving the statement. Generally speaking, HEP-UAVs require two completely independent systems which work simultaneously; thermal and electrical [16,24]. Principally, the system is powered by the gasoline engines, in which a shaft connects the rotating gears, and the main propellers maintain an adequate lift force to take-off, climb, and descend; however, this only relates to the throttle, since the gasoline engines do not respond abruptly, augmentation systems function for the rest of the control variables, including attitude values (ϕ, θ, and ψ) resulting in the lateral movement (x and y). This manner is better off, thanks to the gasoline motors, which make the HEP-UAV runway longer than electrical ones; however, this is mechanically complicated. There are various solutions, but the most efficient are variable-pitch governers or electric ducted fans (EDFs) to control the low-level control loop (attitude). Utilizing variable-pitch propellers as designated by Langkamp, [9], and Fresk in [18] requires an optimized point between pitch angle and motor RPM, which in the real world brings about many complexities such as controlling the swashplate rotation, internal errors of the pitch servos, and the gasoline engines. Furthermore, using servos for grand drones requires a long time of aerodynamics analysis to determine moments around blade hinges, then transforming to the pitch link and finally, find suitable servos. Therefore, it ought to concentrate on the latter technique, requiring less effort to harmonize the EDFs and choosing the best incident angle for the EDFs. Among all, Fan *et al.* [5] endeavored to demonstrate the attitude control efficiency using EDFs, which is an inspirable work; however, it needs a robust control method to prevent external errors and make the system traceable. Moreover, several researchers like [1,3,15,22] worked on the ducted fan solution, while all the works suffer from static instability of the model when flies, especially using flaps makes even the dynamic stability face problems. We have covered all aforementioned throats through this research by equipping the DH with four main ducts to move the center of mass (CoM) from the duct center to the quadcopter center, which causes the drone to fly stable. Actually, DH is considered as a powerful HEP-UAV, which utilizes the technology of multiple flaps movement to be stabilized with minimum error; more specifically, to rotate toward the longitudinal, lateral, and vertical axis, it has eight distinct flaps pairwise. Considering redundant elements for stability and several control layers, DH has four coaxial pairs of propellers, 4 EDFs, 32 flap blades; i.e. every set of the rotor has four pairs, then to control rolling moment, longitudinal pairs works to have the moment stabilized; for pitching moment, lateral ones, and for yawing, the two diagonals vice versa. Regardless of redundancy, this schematic helps the system work undeniably safely; even if it loses some, others compensate for a complete movement. Such a design has various benefits such as being structured, immune and effortless; using mechanical systems instead of electric parts makes the DH user-friend. Notwithstanding rotors of conventional quadcopters produce all forces and moments, a very hasten response is considered a salient factor for distinct maneuvers; however, separating roles helps the system be more functionalized. In addition, redundant mechanisms could be controlled much more immune than the situation all-in-one. Besides, unwanted moments and energy are removed to improve the DH model; thanks to aerodynamic duct-tubes confined geometry, to somehow, the rotor moments are canceled out, especially during hover flight or maneuvers, flaps are operating, so the velocity of the main rotors is semi-conservative. Therefore, DH saves quite a lot of energy rather than similar cases without flaps. Another benefit of flaps is the static stability, helping the system to converge on the balance mode. While in most of the drones, propellers function as the main control targets, here instead, flaps and EDFs are employed to act as the attitude controller, and the fixed propellers only lift the drone, clustered as low-speed throttlers specified for quadcopters. Noting the novel controller employed is a robust sliding-mode that targets external errors to eliminate, which is highly required in the industry. This paper is arranged as follows. Section 2 clarifies a complete dynamic model of the DH. Section 3 discusses the implemented scenario. Section 4 reveals the results obtained. Finally, Sec. 5 compares the models expressed.

2. Dynamic Model of the DH

According to this research, the dynamic model of a large quadcopter is remarkably challenging because of plenty of internal errors that most of them are due to the difference among thermal engines characteristics even with the same model, such as their power causing sudden imbalances during flight. We have considered such problems in the

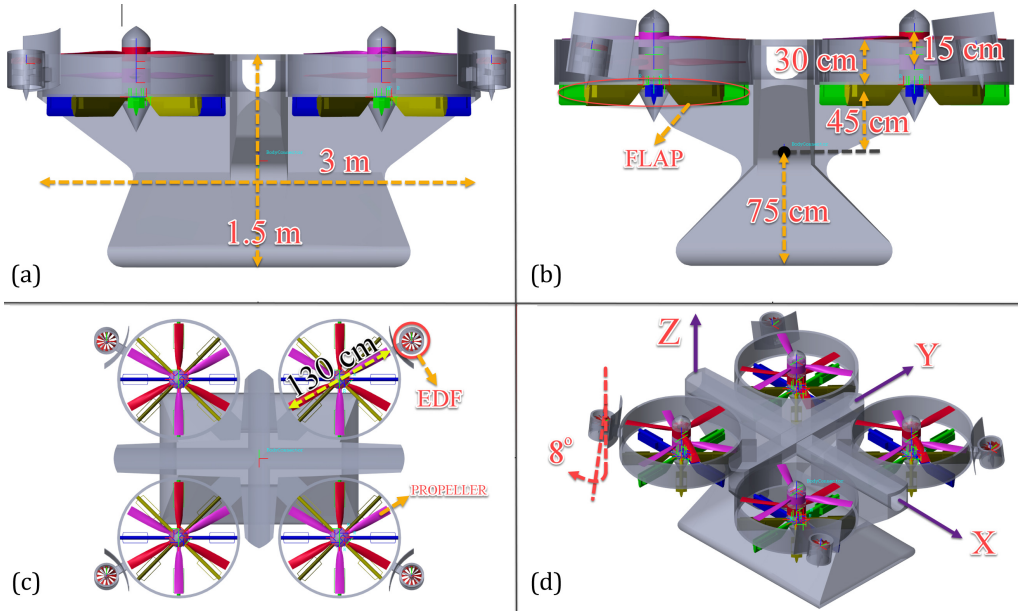

Fig. 1. A macroscopic schematic of the heavy DH. (a) side view; (b) toward or backward view; (c) up view; and (d) the 3D total vision of the DH.

virtual model by implementing unexpected random errors. A basic schematic of the DH is shown in Fig. 1. Various views of DH are revealed in this figure, including the vertical and horizontal dimensions (a); flap position, the center of mass (CoM), payload tank, and duct size (b); EDFs and four coaxial pairs of propellers (c); EDF angle of incidence, EDF wall, and *Body* frame (d). Inspiring from grand air-taxi *CityAirbus*. It is clear in Fig. 1(d) that the DH has four coaxial pairs of large propellers to lift principally; these eight propellers are augmented by four redundant EDFs to maintain the throttle safety margin in case of power-loss. Considering closed walls surrounding the EDF rotors, the vorticity throughout their ducts is semi-zero, producing an unimportant yawing moment. To compensate for this small magnitude, EDFs are installed with an incidence angle of 8°, and according to the experiments, normally, this angle is changeable up to 15° in case of high imbalance; however, DH has eight pairs of yaw flaps to maintain its stability; consequently, the inclination angle of EDFs is considered as 8°, which is the optimized angle, based on performed tests. While in Fig. 1(b), it is observed that CoM of the DH is $[0\ 0\ -0.45]^{\mathrm{T}}$m, the distance between CoM and bottom of the DH is 75 cm, and between the second propeller and the flap is 15 cm. In Fig. 1(c), the propeller diameter is 130 m and the EDF rotor diameter is 25 cm. Besides, the system has four 250 cc engines, with a total power output of 130 HP, which is equipped with a triple-redundant system. Considering the DH large body, all elements, even minuscule parameters have been under review. BTW, all equations are expressed in *Body* frame, supposing a standard 6DOF system. The transitional equations of motion could be rewritten as in Eq. (1). This equation states the total external force, F^t, acting on the drone

$$\mathrm{F}^t = \dot{m}\mathrm{v} + m\dot{\mathrm{v}} = F_x\hat{i} + F_y\hat{j} + F_z\hat{k}, \tag{1}$$

where v is the absolute velocity of the CoM. The first term of this equation states the mass ejection of the drone, which in the DH case is zero. Meanwhile, since the size of DH compared to the gravitational field is quite diminutive, the center of gravity (CoG) and CoM of the drone could be equal here. Extending the second term, the equation is as follows:

$$\begin{aligned}\dot{\mathrm{v}} &= \dot{\mathrm{v}}_r + \mathrm{w}\mathrm{v}\\ &= (\dot{\mathrm{u}} + wq - vr)\hat{i} + (\dot{\mathrm{v}} + ur - wp)\hat{j}\\ &\quad + (\dot{\mathrm{w}} + vp - uq)\hat{k},\end{aligned} \tag{2}$$

where ω is the absolute angular (rotational) velocity of the drone, $\dot{v}$ and $\dot{\mathrm{v}}_r$ are absolute and relative accelerations of CoM, respectively. To summarize, gravitational, centrifugal, aerodynamic, rotors, and flaps forces and moments are expressed in the following equation, as is mentioned in [1]:

$$\begin{aligned}\mathrm{F}^t &= \mathrm{F}_{\mathrm{grav}} + \mathrm{F}_{\mathrm{fuse}} + \mathrm{F}_{\mathrm{prop}} + \mathrm{F}_{\mathrm{duct}} + \mathrm{F}_{\mathrm{edf}} + \mathrm{F}_{\mathrm{flap}},\\ \mathrm{M}^t &= \mathrm{M}_{\mathrm{gyro}} + \mathrm{M}_{\mathrm{prop}} + \mathrm{M}_{\mathrm{duct}} + \mathrm{M}_{\mathrm{edf}} + \mathrm{M}_{\mathrm{flap}},\end{aligned} \tag{3}$$

where $\mathrm{F}_{\mathrm{grav}}$ is the gravity force affecting on the drone. Thereafter, all aforementioned forces and moments are described in six subcategories to show the effect of each parameter, i.e. gravitational force; aerodynamic forces; propeller force; duct force; flap force; and EDF force.

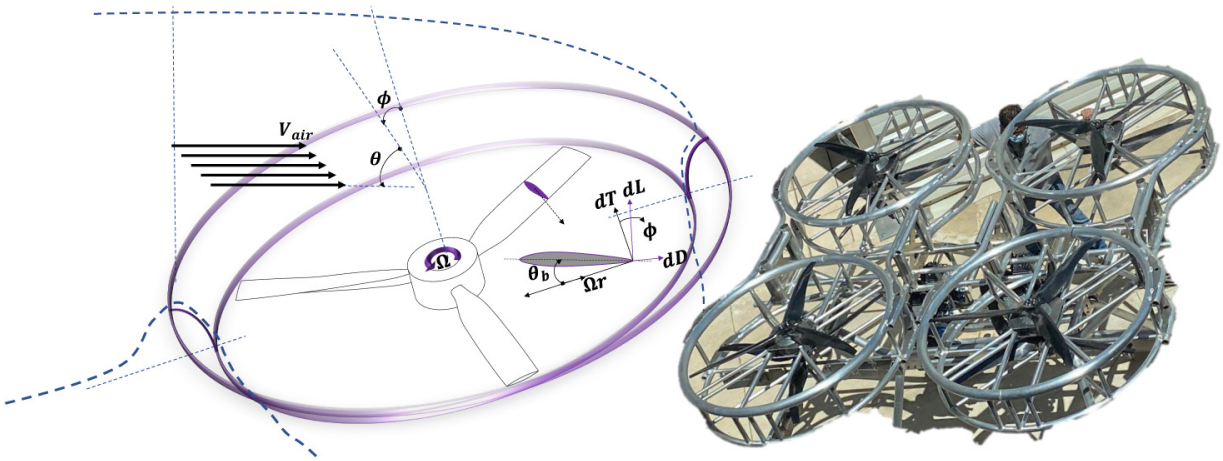

Fig. 2. Schematic of free-stream entering to the duct while inclined, where the real coaxial model is demonstrated.

2.1. *Gravitational force and gyroscopic moment*

Supposing the moving drone with θ angle toward the N-axis, ϕ angle toward E-axis, and ψ angle toward the D-axis, the third one does not affect on the gravitational force, then the equation is as follows:

$$\begin{aligned} \mathrm{F}_{\mathrm{grav}} &= \begin{bmatrix} -mg\sin\theta \\ mg\cos\theta\sin\phi \\ mg\cos\theta\cos\theta \end{bmatrix}, \\ \mathrm{M}_{\mathrm{gyro}} &= NJ\omega \begin{bmatrix} -q \\ p \\ 0 \end{bmatrix}. \end{aligned} \tag{4}$$

Related to the gyroscopic terms, N is the number of the propellers, J is the rotor inertia, p and q are angular rates of the propeller [1,5], regardless of aggressive behavior, this equation is supposed when the angular rates are semi-constant.

2.2. *Fuselage forces*

As a quadcopter, various components like fuselage, ducts, propellers, flaps, etc. produce reaction forces against the air passing throughout. Hereupon, drag force derived from the fuselage will be expressed through the following equation, as mentioned in [4,11]:

$$\mathrm{F}_{\mathrm{fuse}} = -0.5\rho \begin{bmatrix} C_{D,x}u|u|A_{\mathrm{side}} \\ C_{D,y}v|v|A_{\mathrm{side}} \\ C_{D,z}w|w|A_{\mathrm{top}} \end{bmatrix}, \tag{5}$$

where C_D is the drag coefficient of the fuselage, A_{side} is the cross area of the drone (here, regarding the symmetrical shape, both sides equal), and A_{top} is the top area of the drone.

2.3. *Propeller forces and moments*

The propeller is the principal thrust generator of the DH, entering free-stream air to the duct creating a boundary layer of inlet having a semi-circular shape [17]. If each propeller revolves with an angular velocity, the blade pitch θ_b, and the blade incidence angle ϕ_b, as shown in Fig. 2, this could be expressed as [8,9]. To calculate the thrust force generated by each propeller, the equation is as follows:

$$\mathrm{F}_{\mathrm{prop}} = 0.5\rho A_r b\Omega^2 \begin{bmatrix} C_{D,b}\sin\alpha_b\sin\theta_b \\ -C_{D,b}\sin\alpha_b\sin\theta_b \\ C_{L,b}\cos\alpha_b\cos\theta_b \end{bmatrix}, \tag{6}$$

where Ω is the rotor angular velocity, b is the thrust factor of the propeller, and $C_{D,b}$ and $C_{L,b}$ are the drag and the lift coefficients of the propeller blades, and the A_r is the area of the rotor plane. Normally, θ_b and α_b are considered zero because of their small values.

2.4. *Duct forces and moments*

The propeller duct functions as an augmentative lifter when its lips are curved by aerodynamic extension. In addition, the closed walls of the duct to propellers, the fewer tip losses associated with free-air propellers. Due to ducts' inclination during the flight, they react to the air, and consequently, a momentum drag will be generated. When there is no crosswind (static condition), the momentum drag equals zero, since the stream enters the duct symmetrically; nonetheless, during movement, crosswind

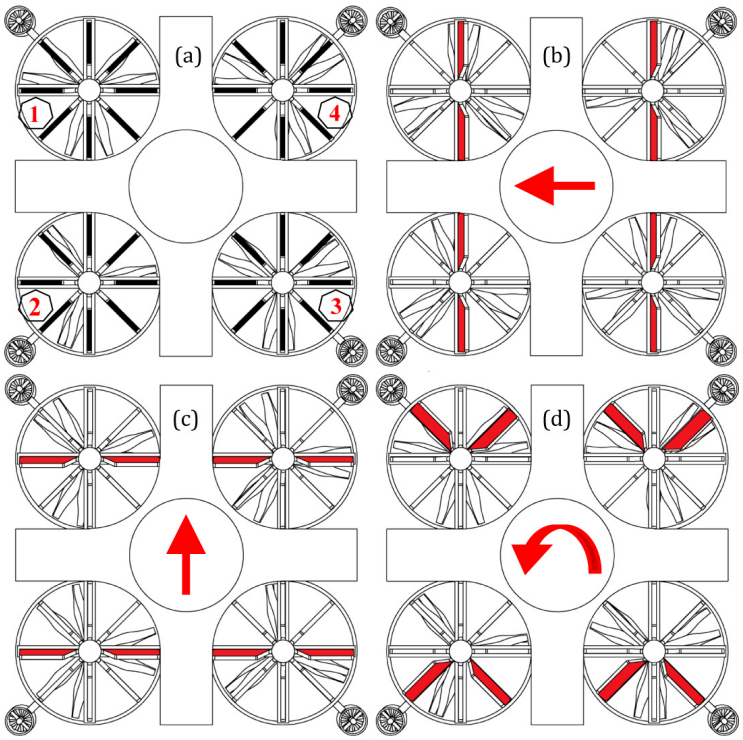

Fig. 3. Distribution of flaps movement; (a) hover mode without flapping, (b) four pairs of roll flaps are used to move toward *y*-axis, (c) four pairs of pitch flaps are used to move toward *x*-axis, (d) four pairs of psi flaps are used to rotate around *z*-axis.

enters asymmetrically [2,12]. Approximately, it could be given by

$$\mathrm{F}_{\mathrm{duct}} = \mathrm{D}_m + \mathrm{K}_{\mathrm{aug}}\mathrm{F}_{\mathrm{prop}} = 0.5\rho C_d \begin{bmatrix} A_e V_{i,x}|V_{i,x}| \\ A_e V_{i,y}|V_{i,y}| \\ A_r K_{\mathrm{aug}} V_r|V_r| \end{bmatrix}, \quad (7)$$

$$\mathrm{M}_{\mathrm{duct}} = \begin{bmatrix} \mathrm{F}_{\mathrm{duct},y} r \\ \mathrm{F}_{\mathrm{duct},x} r \\ \mathrm{F}_{\mathrm{duct},z} l_d \end{bmatrix},$$

where $\mathrm{K}_{\mathrm{aug}}$ is the augmentation factor of the duct helping propellers to trigger thrust, C_d is the duct moment coefficient which is a proportionality constant, in which the moment is related to the dynamic pressure due to cross-wind [1]. V_i is the inlet air velocity, r is the duct exit radii, l_d is the diagonal distance between the center of pressure (CoP) of the duct to CoG of the drone, and V_r, A_r, V_e, and A_e are the rotor plane and duct exit velocities and areas, respectively. Consider mass flow rate through the

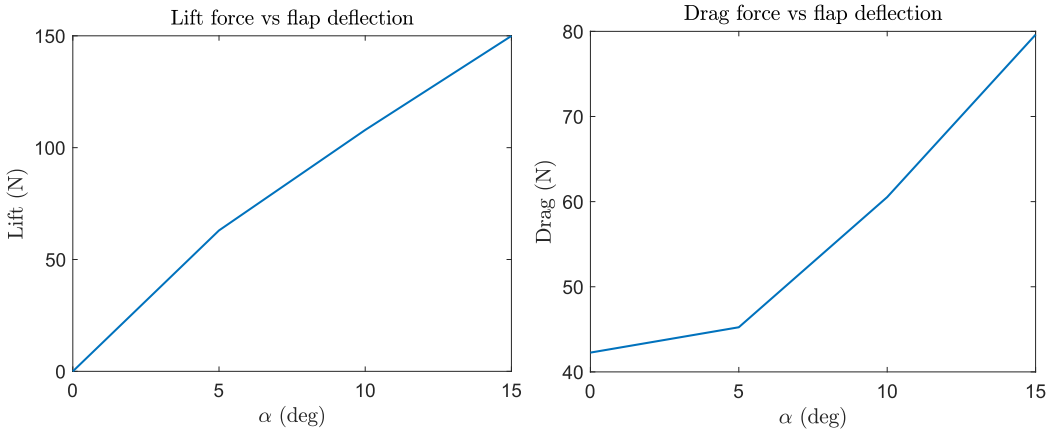

Fig. 4. Comparison of Lift and Drag forces versus increment of flap deflection angle.

duct [8,12,15]. In order to calculate the mass flow rate through the duct ($\dot{m}_d$), the following equation is used [3]:

$$\dot{m}_d = \rho A_i V_i = \rho A_e V_e. \tag{8}$$

2.5. *Flap forces and moments*

Regardless of incident angle or direction of installment, a flap can produce forces and moments in all coordinate axis [15]. Usually, flying drones use flaps to make the system more stable, preventing out-of-range moments; nevertheless, they have a standard form, hence for heavy drones, controlling by flaps is a big problem. That is why in grand systems, most flaps are employed as redundant components but not principles. The distribution of flaps movement is shown in Fig. 3, displaying the drone movement control to the right, left, upward, and backward.

In addition to the drone movement control, determining the calculation of a roll controller flap could be expressed as in Eq. (9), clarifying the roll flap force (F_{rf}) and the moment (M_{rf}) produced.

$$L = 0.5\rho V_e^2 A_e C_l,$$

$$D = 0.5\rho V_e^2 A_e C_d,$$

$$F_{rf} = \begin{bmatrix} 0 \\ L\cos\gamma - D\sin\gamma \\ L\sin\gamma + D\cos\gamma \end{bmatrix},$$

$$M_{rf} = \begin{bmatrix} M_x \\ M_y \\ M_z \end{bmatrix} = \begin{bmatrix} \pm F_{rf,z} dy_i - F_{rf,y} dz_i \\ \pm F_{rf,z} dx_i \\ \pm F_{rf,y} dx_i \end{bmatrix}, \tag{9}$$

Noting that L and D are the lift and drag forces generated by the flaps, γ is the deflection angle of each flap related to the vertical axis. During the flight, if $\gamma = 0$ no lift or drag is produced, and the more deflection angle is applied, the more lift is brought about. Meanwhile, the drag force is small enough. The research experiments demonstrate that for γ angles more than 18°, the increment rate of the drag force is more than lift, regardless of interference among flaps movements, and due to this fact result, it is observed that the best deflection angle domain is $0° \leq \gamma \leq 10°$, as presented in Fig. 4, which shows an increment of aerodynamic forces based on flap deflection angle when it rotates from 0° to 10°.

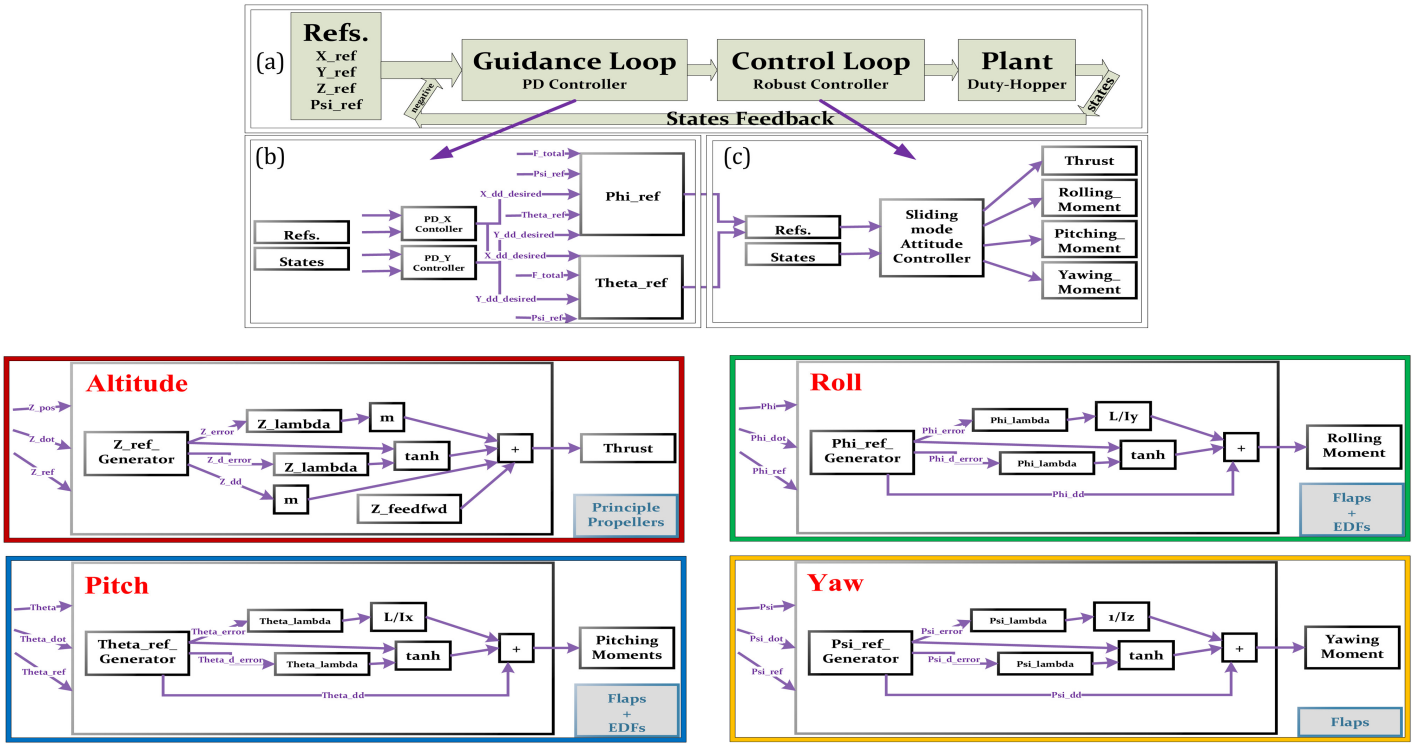

Fig. 5. A full schematic diagram of the guidance and controller loop to be simulated. Noticeably about the four squares below; thrust is produced by the main four pairs of propellers, rolling moment and pitching moment by flaps and in case of emergency aimed by EDFs, and yawing moment by flaps only. As described in Sec. 2, EDFs do not produce any magnificent yawing moment, especially here, they are installed inclined to cancel out each other.

Also, regarding to a pitch controller flap, Eq. (10) is given, presenting pitch flap force (F_{pf}) and its moment (M_{pf})

$$\begin{aligned} F_{pf} &= \begin{bmatrix} L\cos\gamma - D\sin\gamma \\ 0 \\ L\sin\gamma + D\cos\gamma \end{bmatrix}, \\ M_{pf} &= \begin{bmatrix} M_x \\ M_y \\ M_z \end{bmatrix} = \begin{bmatrix} \pm F_{pf,z} dy_i \\ \pm F_{pf,z} dx_i - F_{pf,x} dz_i \\ \pm F_{pf,y} dy_i \end{bmatrix}. \end{aligned} \tag{10}$$

Finally, for a determination of a yaw controller flap, the following equation is given, determining yaw flap force (F_{yf}) and its moment (M_{yf}):

$$\begin{aligned} F_{yf} &= \begin{bmatrix} \sqrt{2}/2(L\cos\gamma - D\sin\gamma) \\ \sqrt{2}/2(L\cos\gamma - D\sin\gamma) \\ L\sin\gamma + D\cos\gamma \end{bmatrix}, \\ M_{yf} &= \begin{bmatrix} M_x \\ M_y \\ M_z \end{bmatrix} = \begin{bmatrix} \pm(F_{yf,z} dy_i - F_{yf,y} dz_i) \\ \pm(F_{yf,z} dx_i - F_{yf,x} dz_i) \\ F_{yf,x} dy_i \pm F_{yf,y} dx_i \end{bmatrix}, \end{aligned} \tag{11}$$

where in Eqs. (9), (10), and (11), the sign $\pm$ is observed alternatively, based on the nomination model.

2.6. *EDF forces and moments*

Like flaps, EDFs also are useful to make the drone more balanced. A normal formulation of an EDF rotor is likewise as propellers, but without considering lateral forces to conclude a drag or yawing moment. Instead, it produces a pure thrust with a much higher angular velocity rather than normal propeller engines. The EDF thrust equation can be stated as

$$\begin{aligned} \omega &= \sqrt{V^2 + (\pi d_r N)^2}, \\ \beta &= \arctan V/\pi d_r N, \\ F_{\text{EDF}} &= 0.5\rho A_r b\omega^2 \begin{bmatrix} C_l\sin\beta + C_d\cos\beta \\ 0 \\ C_l\cos\beta - C_d\sin\beta \end{bmatrix}, \end{aligned} \tag{12}$$

where A_r is the surface area of the rotor plane, V is the blade axial velocity, N is the blade tangential velocity, β is the pitch angle of the blade, b is the thrust factor of the EDF rotors, and ω is the angular velocity of the rotor.

3. Implemented Scenario

Simulation tests, using MATLAB and practical tests of the DH model, are designed at Drone Hopepr to compare the data obtained. Through the scenario, a detailed schematic diagram system of the guidance and controller loops was designed, using Simulink and Simscape, as shown in Fig. 5. The simulation process was conducted in two steps, 3D modeling and compiling in aerodynamic and mechanical software (SW). First, during virtual reconstruction, each component is designed in Soliworks SW. Overall, there were more than 340 parts such as fuselage, propeller, EDFs and flaps. Every component is designed in detail to guide its actual model, and then this process is continued directly to prepare the simulation model. The DH complete detailed

Table 1. DH detailed properties.

Part	Parameter	Range	Dimension
Fuselage	Mass	300	Kg
	Height	1.5	m
	Length/Width	3	m
	I_{xx}	337.32	Kg.m^2
	I_{yy}	337.32	Kg.m^2
	I_{zz}	466.84	Kg.m^2
Propeller	Number	4-Coax	—
	Number of Blades	3	—
	Nominal Rotor Rev.	1300	rpm
	Blade Radii	65	cm
	Blade Tip Chord	10	cm
	Blade Tip Angle	7	deg
	Thrust Factor [14]	2.15e-2	N · m^2
Propeller Servo	Av. Damping Coeff.	0.05	N · m · s/deg
Propeller Duct	Number	4	cm
	Length	30	cm
	Outer Diameter	133	cm
	Inner Hub Diameter	155	cm
	Arc Radii at Tip	7	cm
	Av. Inlet air Velocity	135	m/s
	Av. Exit air Velocity	63.56	m/s
EDF	Number	4	—
	Number of Blades	12	—
	Nominal Motor Rev.	29000	rpm
	Blade Radii	12	cm
	Blade Chord	3.1	cm
	Blade Pitch Angle	45	deg
	Blade twist Angle	33	deg
	Thrust Factor	5.16e-6	N · m^2
EDF Servo	Av. Damping Coeff.	0.002	N · m · s/deg
EDF Duct	Number	4	cm
	Diameter	25	cm
	Arc Radii at Tip	1.6	cm
Flap	Number	32	—
	Number per Prop	8	—
	Height	14	cm
	Length	53	cm
	Av. Width	8	cm
	Maximum Angle	$\pm$ 15	deg
Flap Servo	Av. Damping Coeff.	0.1	N · m · s/deg

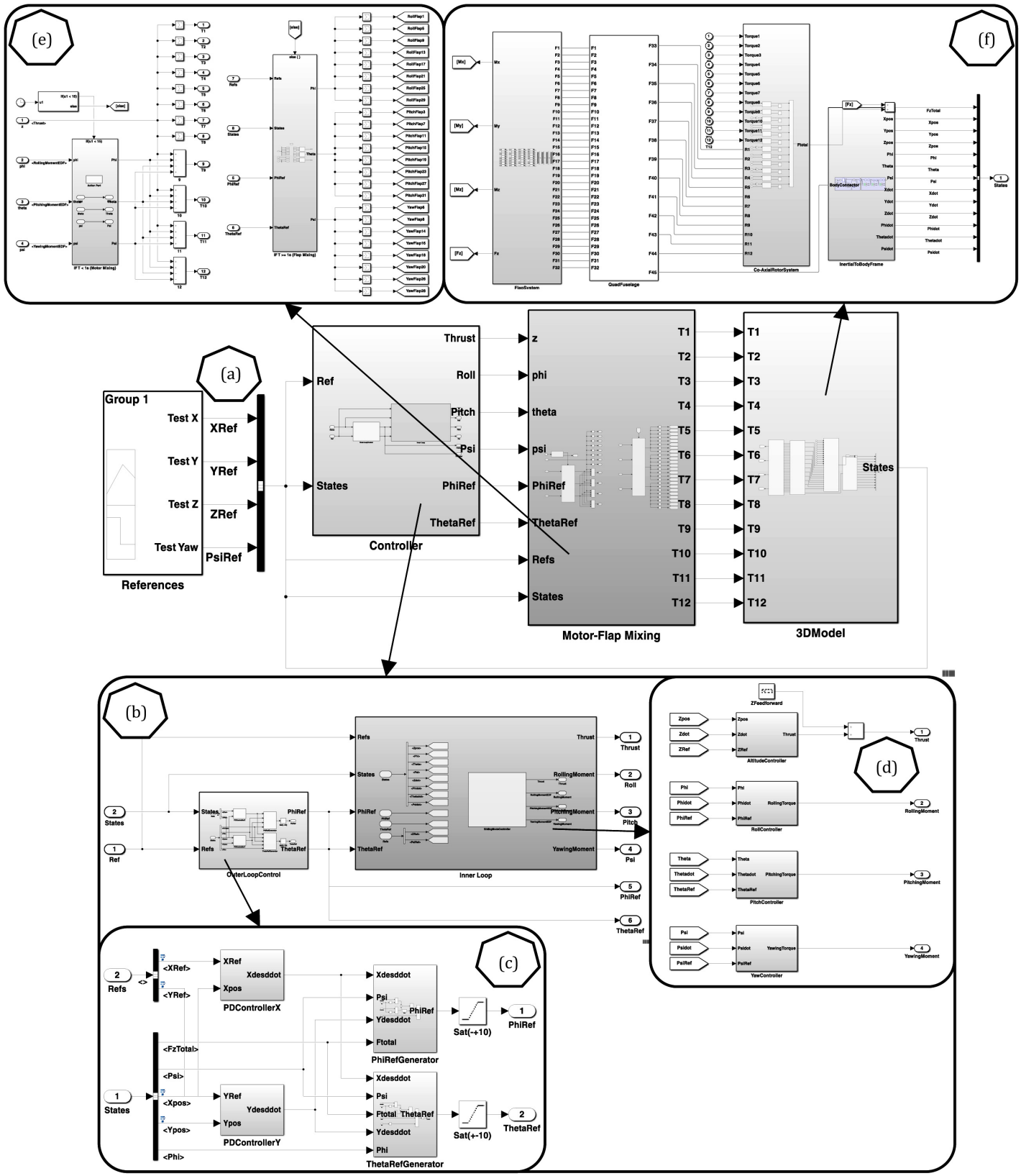

Fig. 6. A macroscopic schematic of the heavy DH simulation, using MATLAB Simulink.

properties are brought in Table 1. During the simulation, these magnitudes are changed several times to be optimized, and eventually, an accurate model is built. Meanwhile, to make the simulation appears realistic, various random noises are implemented, whether in local parts or from external phenomena, like internal errors in joints and wind disturbance models.

Second, ANSYS-Fluent and Simulink, as shown in Fig. 5, are used to analyze aerodynamic forces and moments, and DH behavior against disturbance. Simulink is a fully applicable mechanical platform to simulate forces and moments of objects. Here, the goal is to simulate the effective parts as a plant. Meanwhile, simulations of the DH in ANSYS-Fluent were done under the following setup, viscous model k-omega, transient (as the principle propellers are rotating), defining the cell zones materials (air for the enclosure and Carbon for the aircraft parts) and the moving parts rotating axis [10]. The boundary conditions were also set for the inlet and outlet. Once the solution was obtained, the parameter Flap angle, previously created in the geometry editor SW, was varied in different design points to obtain the lift and drag forces on the flaps. Figure 5(a) demonstrates the overall configuration of the loops. Starting by denoting the four principle references (x_{ref}, y_{ref}, z_{ref}, and ψ_{ref}) which all inter into guidance loop (as the high level controller) and the results are generated ϕ_{des} and θ_{des} as indirect integrator inputs for the robust controller loop (as the low level controller). Finally, the controller outputs are applied to the plant besides feedback to complete the control diagram. Figure 5(b) presents the guidance part, containing two PD controllers. Based on this research, using a PD controller to generate attitude references values is optimized compared to when utilized PID; that is, using I brings about latency in the transient response. Equations used in this loop could be found in [6]. Furthermore, Fig. 5(c) shows the desired attitude parameters entering

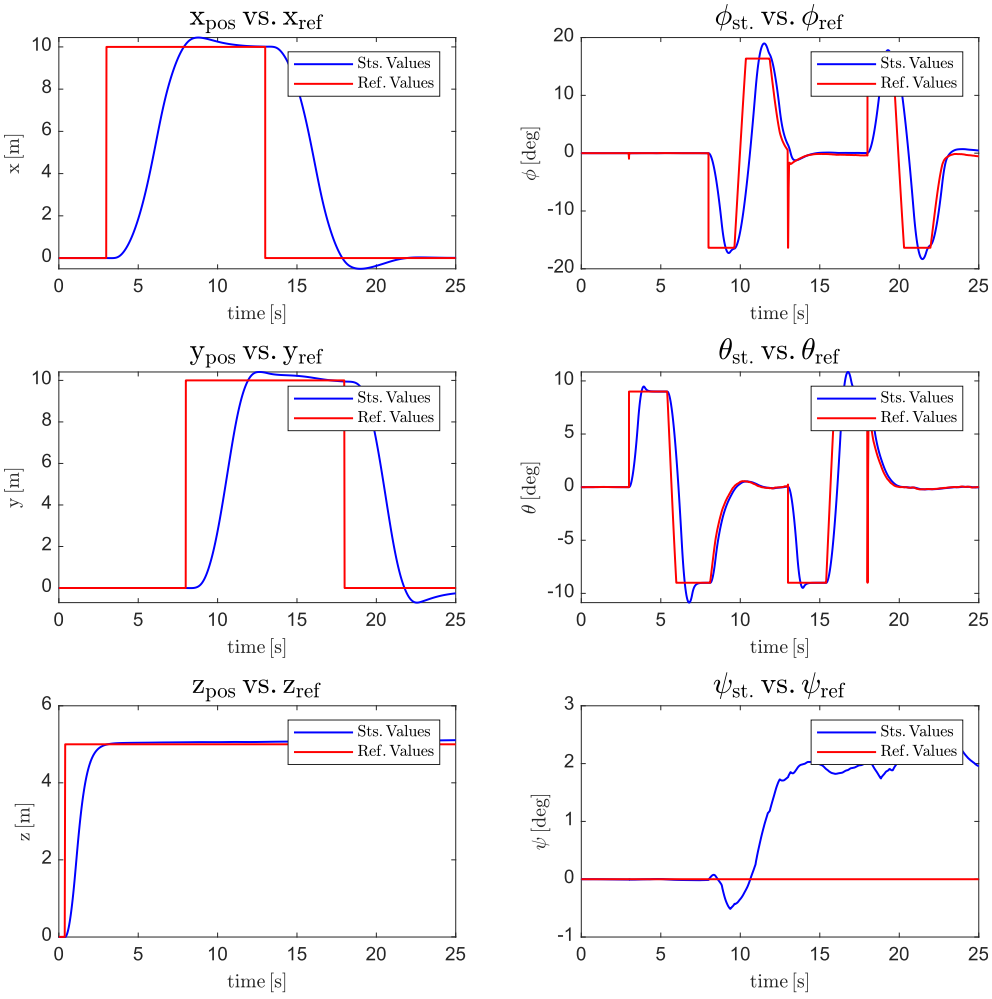

Fig. 7. Comparison of the drone state and reference positions and attitude angles, when $X_{\text{ref}} = 6$ m, $Y_{\text{ref}} = 6$ m, and $Z_{\text{ref}} = 5$ m and both flaps and EDFs are utilized.

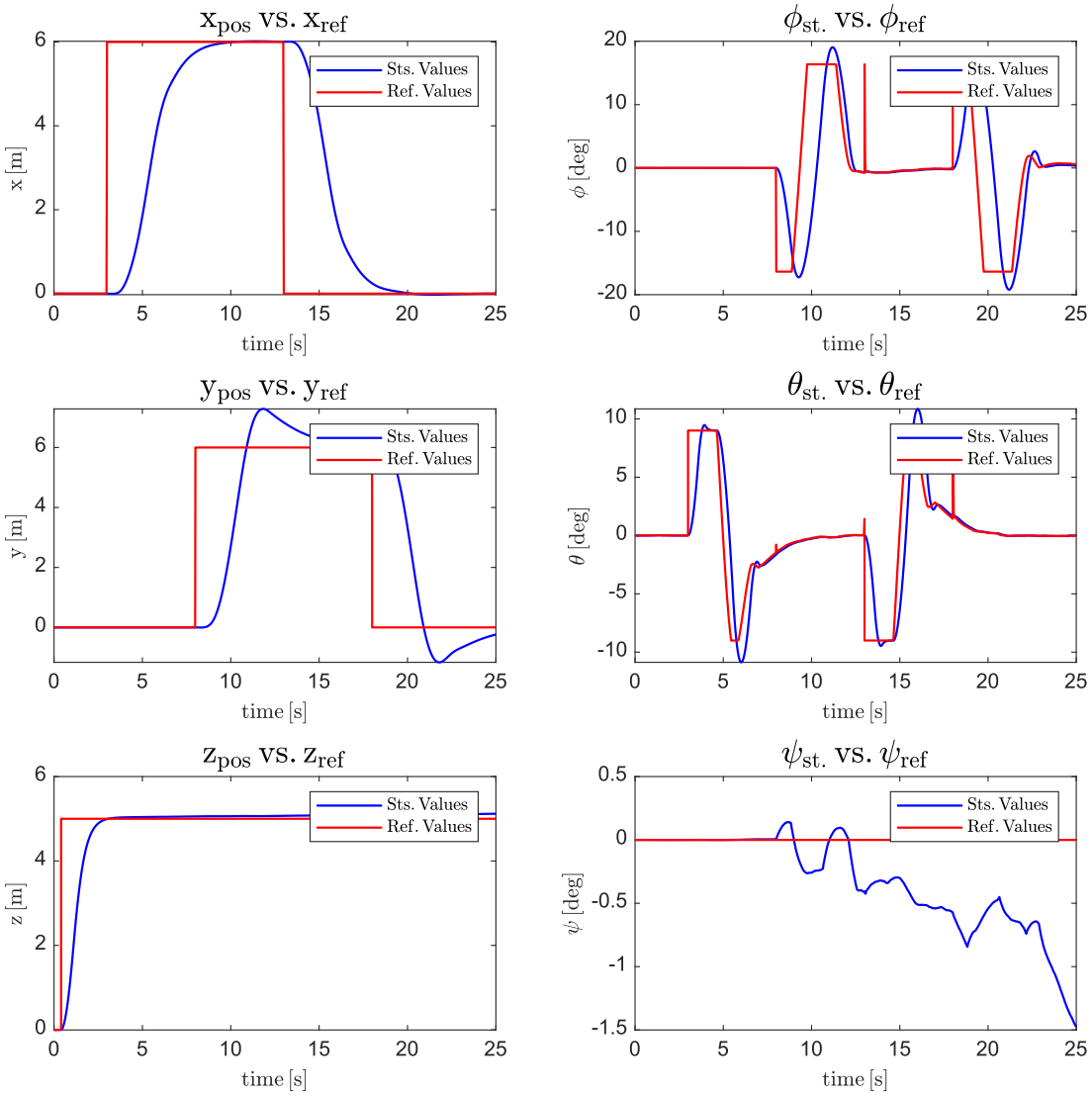

Fig. 8. Comparison of the drone state and reference positions and attitude angles, when $X_{ref} = 6$ m, $Y_{ref} = 6$ m, and $Z_{ref} = 5$ m and only EDFs are utilized.

into a low-level controller, denoting sliding mode is the robust method used in this work, then, all the attitude controller loops (including altitude loop) are mentioned and described below at Fig. 5(Altitude), 5(Roll), 5(Pitch), and 5(Yaw), which display the desired values computed by a reference generator (RG) box to generate saturated $\ddot{z}_{des}$, $\dot{z}_{des}$, Z_{des}, $\ddot{\phi}_{des}$, $\dot{\phi}_{des}$, ϕ_{des}, $\ddot{\theta}_{des}$, $\dot{\theta}_{des}$, θ_{des}, $\ddot{\psi}_{des}$, $\dot{\psi}_{des}$, and ψ_{des} parameters. The aforementioned RG is a second-order system, which could be expressed as

$$G(s) = \frac{1}{s^2 + 2\xi\omega s + \omega^2}. \tag{13}$$

To continue, the sliding mode algorithm is deployed, this method could be formulated as in Eqs. (14), which concludes in thrust force (U_1), rolling torque (U_2), pitching torque (U_3), and yawing torque (U_4)

$$\begin{cases} \ddot{x}_d = -\lambda \dot{e}_x - K\tanh(S_x), \\ \ddot{y}_d = -\lambda \dot{e}_y - K\tanh(S_y), \\ U_1 = m(\ddot{z}_d - \lambda \dot{e}_z) - K\tanh(S_z), \\ U_2 = \dfrac{I_x}{l}(\ddot{\phi}_d - \lambda \dot{e}_\phi) - K\tanh(S_\phi), \\ U_3 = \dfrac{I_y}{l}(\ddot{\theta}_d - \lambda \dot{e}_\theta) - K\tanh(S_\theta), \\ U_4 = I_z(\ddot{\psi}_d - \lambda \dot{e}_\psi) - K\tanh(S_\psi). \end{cases} \tag{14}$$

Furthermore, in Fig. 5, where λ values are tunable like PID parameters, e_i is the difference between each value and

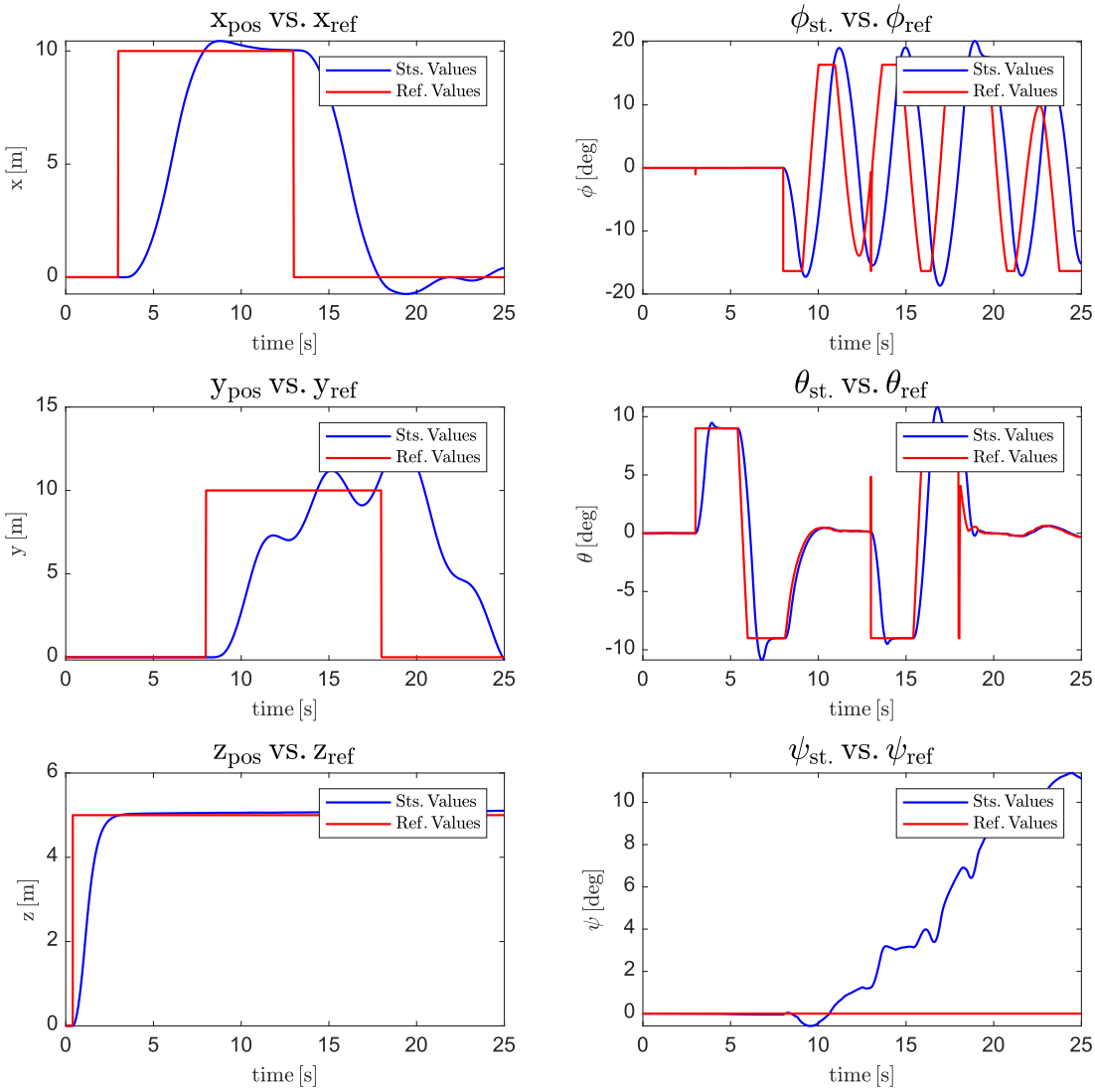

Fig. 9. Comparison of the drone state and reference positions and attitude angles, when $X_{ref} = 6$ m, $Y_{ref} = 6$ m, and $Z_{ref} = 5$ m and only flaps are utilized.

its reference, l is the length of the drone, K refers to a discontinuous component against system noises, which is calculated with try and error method; i.e. if it is more than a determined magnitude, the system will be stable. This is derived from the fact that how far negative is the Lyapunov function derivative, it will converge to a value more negative and so will be stable faster. In addition, instead of sign, we use the tanh function to make the chattering of the switching surface more smooth. As displayed in Fig. 5(d) and Eqs. (14), the output is a summation among position, velocity, and acceleration, where velocity is weighting element compared to others; consequently, to tune the controller, a higher amount is required to filter the velocity when goes out the integration. Likewise, Figs. 5(e), 5(f), and 5(g) show the attitude controller, denoting that yawing torque is only produced by flaps; however, the roll and pitch moments could be generated using both. Figure 6(a) demonstrates the total configuration of the simulator, all of the main reference values are generated, using a signal producer; then controller part which is distributed into Fig. 6(b), regarded as the whole control loop. Considering higher level and lower level, once $\ddot{x}_{des}$ and $\ddot{y}_{des}$ are brought up, as shown in Fig. 6(c), by a PD controller to generate ϕ_{des} and θ_{des} [6], then entering reference and state magnitudes into the inner loop, the sliding algorithm is conducted to result thrust force and circular moments, as presented in Fig. 6(c). To continue, Fig. 6(e) displays the Motor-Flap Mixing part, which is the configuration of controller outputs to be legible for engines and flaps. As described in Fig. 5, the principle propellers are only in charge of generating lift

force, and for attitude, flaps and EDFs are employed. Finally, Fig. 6(f) demonstrates the 3D model of SimScape, which is imported from the previous approximated model in Solidworks. Despite the movements and rotations defined in modeler SW, here in counterpart, they are translated to *transform joints* and *revolut joints*, respectively, then a full 6DoF model is simulated by rotations to connect the *Body* and *Inertial* frames; therefore, all forces and moments are transformed. Moreover, a full model of 32 flaps, 8 EDFs, and the state feedback loop are developed in this segment.

4. Results and Analysis

Hereupon, some of the graph results are brought. Considering the mass is an important clue in such a heavy drone, then realize that it is impossible to tune a controller acting in a second. Meanwhile, through Fig. 5, it is cleared that the position and attitude variables are dependent, since the position values are issued by the reference block, and then through the guidance loop, attitude desired values (ϕ_{des} and θ_{des}) are computed. Despite a hasten reaction of small drones, the DH behavior is far slower. Figure 7 shows the comparison of the state and reference values of attitude angles, ϕ, θ, and ψ, when EDfs and flaps are working simultaneously. The minuscule yawing rotation is due to the unwanted moments affected on the drone, which is generated by increasing the damping coefficient of flap servos to accelerate and decelerate the yaw flaps abruptly. Figure 8 shows the comparison of the state and reference values of position, x, y, and z, when no flap functions and the drone is controlled only by EDFs. Supposing the command of the vertical axis is to go up to 5 m, and 6 m for the lateral values; hence, as described before, the DH acts latent but with less than 10% error is acceptable in graphs. Notwithstanding, the controller performance is semi-valuable using EDFs, controlling only by flaps makes the system highly delayed. This is due to the low power of flaps in such a grand system. Results in Fig. 9 demonstrate the impact of the flaps controller when no EDF is employed.

5. Conclusion

In short, during this research, once the system was designated to be controlled only by flaps, then only by EDFs, and finally, equipping both, concurrently. According to the results, it was observed that using only flaps makes DH suffer from latency as shown in Fig. 9. To the lower extent, when only EDFs work, the same phenomenon was perceived. While equipping both flaps and EDFs makes the system acts agile, adequately, to be valuable in attitude control stability. Therefore, this research recommends using both flaps and EDFs in the control system. Moreover, the huge benefit of using such a system is controlling the attitude, using flaps and EDFs, and increasing the flight time endurance by using gas engines.

Acknowledgments

This project is pre-designed by the innovation group of Drone-Hopper company and implemented after a long-term simulation process in both propulsion and flight dynamics. We are thankful to all members who helped, especially Sebastián Álamo López, in parts of aerodynamics and flap controller.

References

[1] E. N. Johnson and M. A. Turbe, Modeling, control, and flight testing of a small ducted fan aircraft, *J. Guidance Control Dynam.* **29** (2006) 769–779.
[2] W. E. Graf, Effects of duct lip shaping and various control devices on the hover and forward flight performance of ducted fan UAVs, MS thesis, College of Aerospace Eng., Virginia Polytechnic State Uni., Virginia (2005).
[3] M. Speck, J. Buchholz and M. Sellier, A mathematical model of a twin ducted-fan vertical takeoff and landing jetpack, *J. Aerosp. Eng.* **228**(10) (2013) 1831–1844.
[4] J. Jeong, S. Kim and J. Suk, Control performance analysis on the variable configuration of ducted-fan flight array, *J. Aeronaut. Space Sci.* **21** (2019) 524–537.
[5] W. Fan, C. Xiang and B. Xu, Modelling, attitude controller design and flight experiments of a novel micro-ducted-fan aircraft, *J. Adv. Mech. Eng.* **10**(3) (2018) 1–16.
[6] M. S. Ale Isaac, S. H. Mirtajadini and A. Naghash, Control and guidance of an autonomous quad-rotor landing phase on a moving platform, in *IMAV Annual Conf. of Autonomous Vehicles* (Madrid, 2019).
[7] L. Boggero, S. Corpino, A. D. Martin, G. Evangelista, M. Fioriti and M. Sorli, A virtual test bench of a parallel hybrid propulsion system for UAVs, *Aerospace, J. Aerosp.* **6** (2019) 77.
[8] A. R. S. Bramwell, *Bramwell's Helicopter Dynamics*, 2nd edn. (Butterworth-Heinenmann, 2001).
[9] D. Langkamp and W. J. Crowther, The role of collective pitch in multi rotor UAV aerodynamics, *36th European Rotorcraft Forum*, Vol. 1 (UK, 2010), pp. 238–245.
[10] W. Graf, J. Fleming and W. Ng, Improving ducted fan UAV aerodynamics in forward flight, in *46th AIAA Aerospace Sciences Meeting and Exhibition* (Nevada, 2008), pp. 1–11.
[11] M. A. Stamate, A. F. Nicolescu and C. Pupaza, Mathematical model of a multi-rotor drone prototype and calculation algorithm for motor selection, *J. Manufact. Syst.* **11** (2017) 119–128.
[12] C. Xiang, W. Fan, H. Liu, B. Xu and N. Huang, Fan vehicle with tilting system, in *Int. Conf. on Unmanned Aircraft Systems* (Colorado, 2015), pp. 1196–1204.
[13] S. Jafari, A. Bouchareb and T. Nikolaidis, Thermal performance evaluation in gas turbine aero engines accessory gearbox, *Int. J. Turbomach., Propul. Power* **5** (2020) 21.

[14] P. Pounds, R. Mahony and P. Corke, Modelling and control of a large quadcopter robot, *J. Control Eng. Pract.* **18** (2010) 691–699.
[15] Z. Wang, Z. Liu, N. Fan and M. Guo, Flight dynamics modeling of a small ducted fan aerial vehicle based on parameter identification, *Chin. J. Aeronaut.* **6** (2013) 1439–1448.
[16] J. Y. Hung and L. F. Gonzalez, On parallel hybrid-electric propulsion system for unmanned aerial vehicles, *Prog. Aerosp. Sci.* **51** (2012) 1–17.
[17] A. S. Sanca, P. J. Alsina and J. De Jesus, F. Cerqueira, Dynamic modeling with nonlinear inputs and backstepping control for a hexarotor micro-aerial vehicle, in *Proc. Latin American Robotics Symp. and Intelligent Robotics Meeting (LARS)* (Brazil, 2010), pp. 36–42.
[18] E. Fresk and G. Nikolakopoulos, Experimental model derivation and control of a variable pitch propeller equipped quadcopter, in *IEEE Conf. Control Applications (CCA)* (France, 2014), pp. 723–729.
[19] B. Wang and Y. Zhang, Adaptive sliding mode fault-tolerant control for an unmanned aerial vehicle, *J. Unmanned Syst.* **5**(4) (2017) 209–221.
[20] E. Altuğ and A. Türkmen, A Novel mini jet engine powered unmanned aerial vehicle: Modeling and control, Journal of Unmanned Systems, *J. Unmanned Syst.* **1024** (2021) 012072.
[21] Y. Xie, X. Zhang, L. Jiang, J. Meng, G. Li and S. Wang, Sliding-mode disturbance observer-based control for fractional-order system with unknown disturbances, *J. Unmanned Syst.* **8**(1) (2020) 1–10.
[22] Y. Jin, Y. Qian, Y. Zhang and W. Zhuge, Modeling of ducted-fan and motor in an electric aircraft and a preliminary integrated design, *SAE Int. J. Aerosp.* **11**(2) (2018) 115–126.
[23] C. L. Bowman, J. L. Felder and T. V. Marien, Turbo-and hybrid-electrified aircraft propulsion concepts for commercial transport, in *Proc. AIAA/IEEE Electric Aircraft Technologies Symp.* (USA, 2018).
[24] S. Sahoo, X. Zhao and K. Kyprianidis, A review of concepts, benefits, and challenges for future electrical propulsion-based aircraft, *J. Aerosp.* **7**(4) (2020) 44.
[25] G. M. Bravo, N. Praliyev and Á Veress, Performance analysis of hybrid electric and distributed propulsion system applied on a light aircraft, *J. Energy* **214** (2021) 118823.
[26] A. Savvaris, Y. Xie, L. Wang, S. Wang and A. Tsourdos, Control and optimisation of hybrid electric propulsion system for light aircraft, *J. Eng.* (2018) 478–483.
[27] J. P. Ruscio, J. Jezegou, E. Benard, A. Gomez Pacheco, P. Laonet and R. A. Castilla, Hybrid electric distributed propulsion overall aircraft design process and models for general aviation (FAST GA), *IOP Conf. Ser.: Mater. Sci. Eng.* (2021).
[28] R. Capata, L. Marino and E. Sciubba, A hybrid propulsion system for a high-endurance UAV: Configuration selection, aerodynamic study, and gas turbine bench tests, *J. Unmanned Vehicle Syst.* **2** (2014) 16–35.

Mohammad Sadeq Ale Isaac is a robotic/aerospace Ph.D. student at the Polytechnic University of Madrid (UPM), Spain, and working as a control engineer at Drone Hopper Company, Madrid, Spain. He has been awarded his master's from Polytechnic University of Tehran (Amirkabir) in aerospace engineering, specializing in flight dynamics and control. His thesis is titled, "The autonomous landing of a drone on a chaotic moving platform". He mainly works on the nonlinear control field concentrated on flying drones.

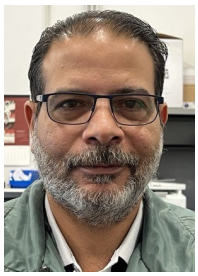

Ahmed Refaat Ragab is a postdoctoral researcher at the University of Carlos III of Madrid (UC3M), Spain, and Drone Hopper Company, Madrid, Spain. He was a lecturer at October 6 University (O6U), Egypt. He graduated from Air Defense College, Alexandria, Egypt. His field of interest is Unmanned Aerial Systems.

Marco Andres Luna is a Ph.D. student at the Polytechnic University of Madrid (UPM), Spain and a software engineer at Drone Hopper Company, Madrid, Spain. He obtained his B.Sc. in automation and control engineering from Universidad de las Fuerzas Armadas ESPE, Ecuador, and his master's in automatic and robotics from the Polytechnic University of Madrid, Spain. His thesis' title was "3D location system for aircraft inspection by UAVs".

Pablo Flores Peña is an aeronautical engineer. He is the CEO and CTO of Drone Hopper Company, Madrid, Spain. He created the research center at Drone Hopper Company, Madrid, Spain. He also obtained a Master in Business Administration (MBA) at International Entrepreneurship (IE) Business School, Madrid, Spain. Previously, he was a chief engineer at Airbus Company, Spain, for more than 15 years.

Pascual Campoy Cervera is a professor at the Higher Technical School of Industrial Engineers of the Polytechnic University of Madrid (UPM), Spain. He is the head of the research group "Vision for Unmanned Aerial Vehicles (UAVs)" of the Department of Automation, Electrical Engineering and Electronics and Industrial Informatics, UPM. He belongs to the Center for Automation and Robotics, a joint research center of the UPM with the Superior Council of Scientific Investigations (CSIC). The objective of his research group is to provide unmanned systems with greater autonomy through the use of computer vision techniques.

9.2 Publication Ad

Ale Isaac, M.S., Luna, M.A., Ragab, A.R., Ale Eshagh Khoeini, M.M., Kalra, R., Campoy, P., Flores Peña, P. and Molina, M. (2022). *Medium-Scale UAVs: A Practical Control System Considering Aerodynamics Analysis.* Drones, 6(9), p.244, doi:10.3390/drones6090244.

drones

MDPI

Article

Medium-Scale UAVs: A Practical Control System Considering Aerodynamics Analysis

Mohammad Sadeq Ale Isaac [1,2,†], Marco Andrés Luna [1,3,†], Ahmed Refaat Ragab [3,4,5,†], Mohammad Mehdi Ale Eshagh Khoeini [6,†], Rupal Kalra [3,7,†], Pascual Campoy [1,†], Pablo Flores Peña [3,6,†] and Martin Molina [8,*,†]

1 Computer Vision and Aerial Robotics Group, Centre for Automation and Robotics (C.A.R.), Universidad Politécnica de Madrid (U.P.M.-CSIC), 28006 Madrid, Spain
2 Wake Engineering Company, 28906 Getafe, Spain
3 Drone-Hopper Company, 28919 Leganés, Spain
4 Department of Network, Faculty of Information Systems and Computer Science, October 6 University, Giza 12511, Egypt
5 Department of Electrical Engineering, University Carlos III of Madrid, 28919 Leganés, Spain
6 Department of Business Administration, Istanbul Aydin University, 34295 Istanbul, Turkey
7 Department of Aerospace Engineering, Universidad Politécnica de Madrid, 28040 Madrid, Spain
8 Department of Artificial Intelligence, Universidad Politécnica de Madrid, 28040 Madrid, Spain
* Correspondence: martin.molina@upm.es
† These authors contributed equally to this work.

Abstract: Unmanned aerial vehicles (UAVs) have drawn significant attention from researchers over the last decade due to their wide range of possible uses. Carrying massive payloads concurrent with light UAVs has broadened the aeronautics context, which is feasible using powerful engines; however, it faces several practical control dilemmas. This paper introduces a medium-scale hexacopter, called the Fan Hopper, alimenting Electric Ducted Fan (EDF) engines to investigate the optimum control possibilities for a fully autonomous mission carrying a heavy payload, even of liquid materials, considering calculations of higher orders. Conducting proper aerodynamic simulations, the model is designed, developed, and tested through robotic Gazebo simulation software to ensure proper functionality. Correspondingly, an Ardupilot open source autopilot is employed and enhanced by a model reference adaptive controller (MRAC) for the attitude loop to stabilize the system in case of an EDF failure and adapt the system coefficients when the fluid payload is released. Obtained results reveal less than a 5% error in comparison to desired values. This research reveals that tuned EDFs function dramatically for large payloads; meanwhile, thermal engines could be substituted to maintain much more flight endurance.

Keywords: medium-scale UAV; adaptive control; motor failure; payload carriage

Citation: Ale Isaac, M.S.; Luna, M.A.; Ragab, A.R.; Ale Eshagh Khoeini, M.M.; Kalra, R.; Campoy, P.; Flores Peña, P.; Molina, M. Medium-Scale UAVs: A Practical Control System Considering Aerodynamics Analysis. *Drones* **2022**, *6*, 244. https://doi.org/10.3390/drones6090244

Academic Editor: Bo Cheng

Received: 14 August 2022
Accepted: 23 August 2022
Published: 6 September 2022

1. Introduction

Several research studies have been conducted to classify UAVs regarding their size, which finally, drive on micro, small, medium, and large scale platforms [1–4]. According to the mentioned categories, micro-scale and small-scale UAVs are those less than 25 kg, large-scale UAVs are more than 500 kg, and medium-scale UAVs are classified with less than 500 kg of gross takeoff weight, containing payloads up to 200 kg weight [1], which are currently spread in abundant applications, namely firefighting, irrigation, camera carriage, emergency and rescue, etc. Designing beneficial aerial systems requires high stability and safe flights. The former needs potent engines that work with tuned controllers, and the latter requires enclosed platforms and auxiliary actuator units to protect the structure and components and satisfy the standard control requirements. Moreover, to satisfy the mentioned applications, heavier payloads will aim to perform optimized missions at lower time stamps. Consequently, these drones necessitate quite a lot of power to carry out heavy

payload missions, and the EDFs generate this energy adequately, supplying electrical batteries but with lower autonomy than thermal resources. This comes from rechargeable batteries having a current useful energy density of around 120 Wh/kg, compared to 12,000 Wh/kg for fossil fuels; in other words, 1 kg of gasoline is equivalent to 25 to 30 kg of batteries [5]. In counterpart, due to thermal engines' drawbacks in emitting nitrogen oxide and carbon oxide (NOx and CO_2) elements, mechanical uncertainties of many components required for propulsive systems, slower reactions, and wasting a significant volume of fuel, they are not highly efficient. Therefore, the dispute between the weight of the batteries and their sufficient energy leads to the use of electrical power sources.

On the other hand, powerful electrical engines that maintain higher thrusts for longer are practically targeted for heavy payloads, as mentioned in [6,7]. Performing the mentioned factors necessitates engines with the minimum energy waste that could be found in EDF types. Furthermore, another novel manner for low energy consumption is mentioned in [8], as the authors proposed dynamic energy saving for heavy drones in a swarm mission, concurrently optimizing the time and distance. Aerodynamically, tight ducted fans facilitate the actuators' function by reducing the blades' tip losses, which results in decrements in undesired yaw moments and produces more efficient thrust than convectional propellers of similar diameters [9–11]. Moreover, ducts protect the propellers, operate more efficiently at high airspeeds, reduce the blade tip speed and vorticity to be quieter, and produce higher static thrust than free propellers of the same size [12,13]. In contrast, ducted fans have instabilities, especially when leaving the near ground space [12], in transient mode between hover and forward flight, and when exposed to a wind gust, by reacting with a nose-up pitching moment [14]. The latter happens at a higher angle of attack (AoA), in which the duct produces aerodynamic drag [15]. Overall, the potential benefits outweigh the disadvantages, and the ducted fan geometry was pursued in this research, since concatenating six ducts symmetrically moves the center of mass (CoM) to the midpoint of the structure and eliminates static instabilities, as shown further in Figure 1. Several models are studied to overcome structural complexities, namely high vibration of the fuselage during flight and instabilities coming from the heavy payload, especially when it contains liquid, which produce extra forces and moments on the body system, where they might increase the system degrees of freedom (described further in Section 2). Through this research, a brief aerodynamic analysis is stated to show the weak and robust points of EDF design.

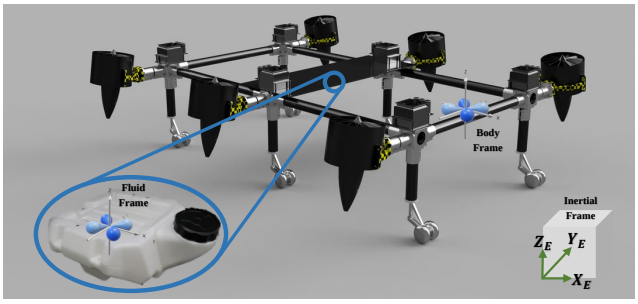

Figure 1. Demonstration of different coordinate systems, *Body* frame, *Fluid* frame, and the *Inertial* frame.

In comparison to traditional PID controllers, nonlinear techniques that conquer abrupt instabilities such as motor failure and payload release converge to stability faster, and among them, adaptive methods perform better tracking [16,17]. Accordingly, the authors of [18] presented an adaptive sliding mode controller (ASMC) augmented by a control allocation scheme to examine the benefits of the controller for a hexacopter platform, which resulted in better tracking against drastic faults through simulation in comparison to SMC; however, this work is limited to the simulation. Likewise, in [19], the authors concentrated on an adaptive neural PID controller, using an identification method for a discrete-time system to be developed in the real world. Furthermore, they compared the designed model

with static PID, and the one advanced with an extended Kalman filter (EKF) for better tracking adaptation. In addition, the authors of [20] studied a fuzzy adaptive fixed-time sliding mode controller (FAFSMC) on two and three-link manipulators as systems with high degrees of uncertainty. Then they affirmed the benefits of FAFSMC against non-fuzzy mode and non-fixed-time observers, concluding faster convergence in FAFSMC due to the fuzzy logic and the online estimators. Nonetheless, this work was also carried out on a simulation platform. The controller proposed in this paper is empowered by an adaptive reference model system, which proves asymptotic stability in a practical case utilizing a suitable Lyapunov candidate.

Additionally, considering a huge fuel tank as the payload requires complete mathematical modeling and then a controller law, leading the system to stability. During this research, a 35 kg hexacopter called Fan Hopper was modeled, designed, built, and flown. For the first design, a comprehensive aerodynamics analysis was conducted to determine the strength and weaknesses of the conceptual model and to investigate the controllability of such a model using turbofan engines. This paper is organized into nine sections, as follows; Section 2 describes medium-scale multicopters, the novel designed model, and aerodynamics considerations; Section 3 discusses a time-varying dynamic system of a multicopter; Section 4 describes the control algorithm implemented; Section 5 examines the results obtained from the simulation; Section 6 describes the hardware system and components utilized; Section 7 displays the results obtained for practical tests; Section 8 compares virtual and real results.

2. Medium-Scale Multicopters

Among medium-scale UAVs, multicopters have recently been more popular than other types because of their easy configuration, multifunctional usage, static stability, and vertical takeoff and landing (VTOL) [21,22]. Among multicopters, hexacopters offer more power, efficiency, and stability. Additionally, Hexa-kinds can handle the flight effectively enough to land safely in the case of failure and can carry greater payloads [21]. According to this research, a quadratic Hexa configuration is a better solution to manage heavy payloads and failure modes than a circular one, discussed further in Section 3. Further, the innovative configuration considered for this research is introduced.

2.1. Fan Hopper, a Novel Design for Medium-Scale Hexacopters

The multirotor under investigation through this research is called Fan Hopper; this platform has several complexities, from mechanical design to control algorithms, practical flight tests, and aerodynamic amendments. As shown in Figure 2, the drone has six EFDs installed inclined, varying the incident angle from 0° (vertical) to 22°, to maintain both thrust and cancel the yaw moment produced by each engine. This phenomenon occurs when all rotors rotate in the same direction, as in our investigation. Considering the geometry of EDFs, the yaw moment produced by each engine is minuscule but not zero; therefore, installing motors with an incident angle is an ingenious solution to control this small amount. The system is led by an open source autopilot (Pixhawk Cube), which allows development of the guidance loop (upper controller loop) using special plugins, which are described further in Section 4. Furthermore, the system contains a fluid payload tank under its CoG up to 20 kg weight that is dynamically modeled in Section 3.

(**a**)

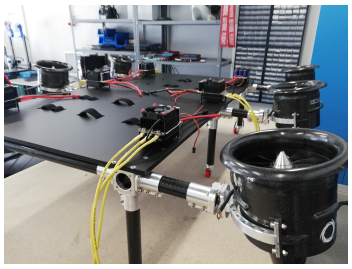

(**b**)

Figure 2. A brief schematic of Fan Hopper's designed model; (**a**) the configuration with components installed as a whole; (**b**) the incident angle of the ducted fan.

2.2. Aerodynamics Considerations

Considering EDFs to lift the drone, several investigations were conducted, including an optimized aerodynamic configuration briefly approached as follows:

- Firstly, a single rotor with a 1 m diameter, 5 m/s inlet air velocity, and 300 rad/s rotor tangential velocity was considered. Obviously, due to the self-feeding toroidal vortex, asymmetry of the streamline aft and forward of the duct (triggered by the velocity of the rotor), high pressure down the rotor, disperse the droplets, as shown in Figure 3a, and the backflow area of the efficiency faced reduction; meanwhile, a huge stream rotation was observed, as shown in Figure 3b.

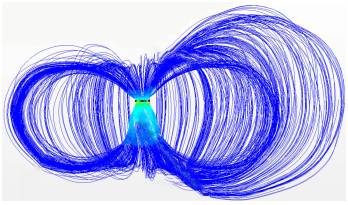

(**a**)

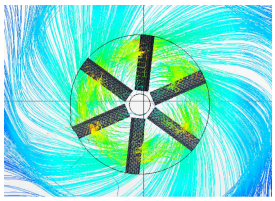

(**b**)

Figure 3. Analysis of a single propeller; (**a**) asymmetry streamlines around the rotor; (**b**) the stream rotation.

- Secondly, the stator was added to eliminate the stream rotation, as shown in Figure 4a; this added a shrouded design which led the stream downwards and avoided vortex formation much better, as well as the backflow area; however, convergence of the stream was still complicated. As shown in Figure 4b, the droplet distribution was unrealistic due to lack of an actual injector. Additionally, the multiphase observed was adequate but complicated to match the transient approach.
- Thirdly, multiple ducts are concatenated to compensate for the instabilities in the transient mode and investigate the interaction between the ducts and the ground effects. Additionally, the propeller design was improved to give a realistic downstream, as shown in Figure 5a. Moreover, considering the airspeed as $v_a = 5$ m/s, the blade tangential tip speed as $\omega_t = 25$ rad/s, and the propeller diameter as $d_p = 1$ m, Equation (1) could be solved as follows:

$$TSR = \frac{\omega_t R}{v_a} = \frac{25 \frac{rad}{s} * \frac{3.14}{2\pi} \frac{m}{rad}}{5 \frac{m}{s}} = 2.5 \quad (1)$$

where TSR represents the tip speed ratio that equals 2.5, which is sufficient for a propeller of 5–6 blades. In addition, the total thrust diagram of different rotors was evaluated, which went up to 2700 N at the steady-state level; also, the medium mass flow reached 90 kg/s. Meanwhile, the absence of a multiphase model gave a better convergence, the downwash was realistic without the presence of backflow, and droplet ground impingement was corrected, as shown in Figure 5c. Furthermore, according to the table in Figure 5b, *rotor 12* and *rotor 22* had higher downforce than others, which overall stated the improved configuration of multiple rotors rather than a single one. The different rotor behaviors suggest a distinct injector strategy that even influences the UAV control.

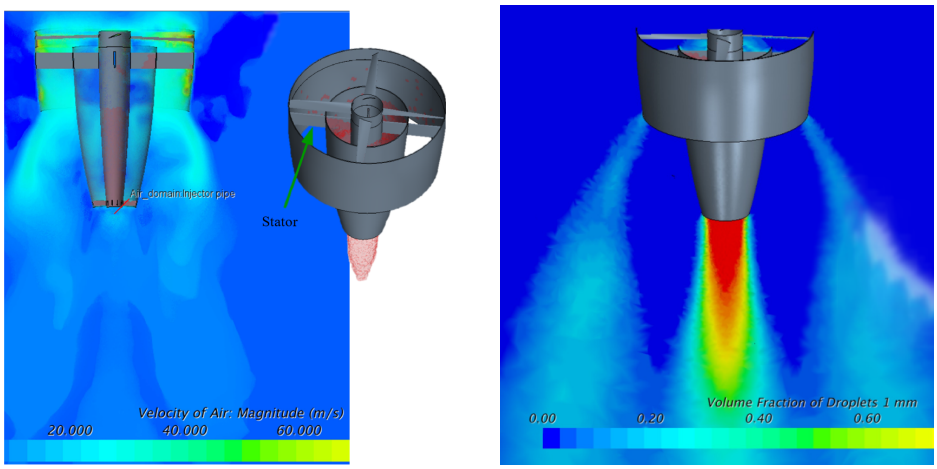

(**a**) (**b**)

Figure 4. Analysis of a single propeller; (**a**) the rotor and shroud; (**b**) unrealistic droplet distribution due to no real injector.

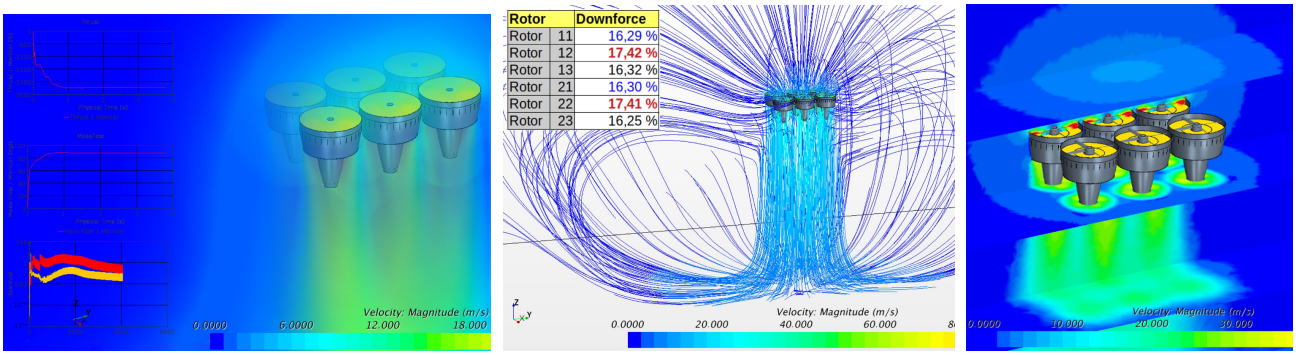

(**a**) (**b**) (**c**)

Figure 5. Analysisof 6 propeller engines; (**a**) (upper-left part) rotor thrust; (right part) mass flow of the stream passing through the engines; (**b**) streamlines around the model; (**c**) absence of multiphase model gave better convergence.

- Finally, regarding the volume fraction of vapors (H_2O) exhausted from the tube, as shown in Figure 6, numerous iterations were carried out, multiple injector models were developed, excellent results were obtained due to several multiphase calculations, different droplet sizes were evaluated, and the ground impregnation was improved.

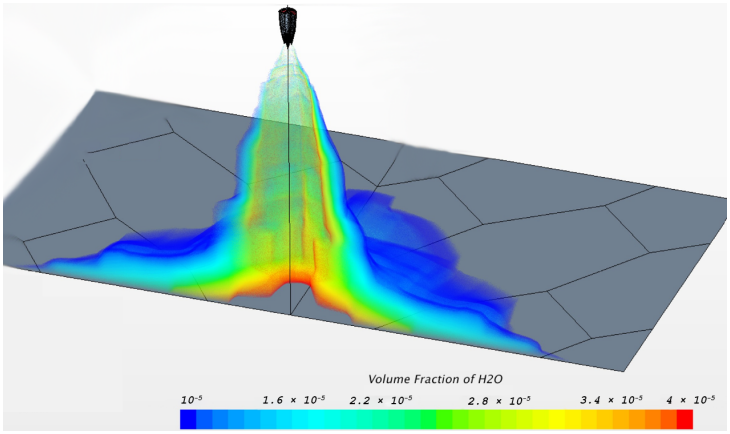

Figure 6. Injectorsdeployed to make the droplet distribution realistic; the color distribution relates to the H_2O volume fraction.

3. Hexacopter Time-Varying Dynamics

Regardless of general dynamics, substantial equations of conventional multirotors have been described several times through research works such as [23–25]; considering a fluid payload under the center of mass (CoM) of the UAV, the moving fluid generates a considerable sloshing effect [26]; depending on the repository shape, baffle balls, and baffle walls, for the same amount of fluid, the displacement of the center of gravity (CoG) of the fluid causes less slosh height with a baffle wall and even less in the presence of a baffled ball inside the tank. Meanwhile, among several types of tank shapes, hexagonal geometry functions more appropriately than circular or rectangular geometry. Therefore, in this research, a hexagonal box is utilized with a baffled ball inside using an optimized configuration.

Furthermore, to determine an acceptable solution for the sloshing problem, assuming Newtonian viscous incompressible flow and constant density, the results of a computational investigation of a similar case are employed [27]. Regardless of the fluid movements during the flight, the fluid mass matrix is constant, which leads the centrifugal and Coriolis forces to zero, so that for an element, this could be rewritten as in Equation (2).

$$M_e = \int_{V_e} \rho_e S_e^T S_e \, \mathrm{d}V_e \tag{2}$$

where, ρ_e and V_e are the density and volume of the fluid element, S_e is the matrix of element shape function, and $*^T$ states the transposition of that matrix. Then, the total force of the fluid could be proposed as a summation of its inertia force, body force, inertial elastic forces (viscous force and stress force), surface traction force, and penalty force due to the incompressibility assumption, as elaborated in [27–29], and summarized in Equation (3).

$$F_T = \int_{V_e} F_{l,e}^T S_e \delta e_e \, \mathrm{d}V_e + \int_{A_e} N_e^T \mu_{e1} S_e \, \mathrm{d}A_e - \int_{V_e} \mu \delta J_e J_e^{-1} \, \mathrm{d}V_e - \int_{V_e} (\rho_e a)^T S_e \delta e_e \, \mathrm{d}V_e \tag{3}$$

where F_l is the body force vector of the fluid element, δe_e is the differential vector of the element nodal coordinate, N_e is the vector normal to the surface of the element, $\mu_e 1$ is the first stress tensor of Piola–Kirchhoff, μ is Cauchy symmetry stress tensor, a is the acceleration vector of the fluid element, J_e is the matrix of position gradients vector of the fluid element, $J_e = \begin{pmatrix} r_x & r_y & r_z \end{pmatrix}$, and the determinant of this matrix equals one, and a is the acceleration vector of the fluid element.

Equations (2) and (3) are according to the final element (FE) absolute nodal coordinate formulation (ANCF), considering the continuity of the fluid element interface inside the tank and based on the Eulerian approach. Moreover, the nonlinearities of the tank fluid were negligible because of the lower velocity domain of a medium-scale multicopter; for high velocities and maneuvers causing severe movements, however, the fluid elements

could be described as eight nodal bricks, each one interpreted into a polynomial function of 32 coefficients, and consequently, the fluid element system could have 96DoF, as mentioned in [27], which should be linearized for a whole dynamical system. Considering the time-varying inertia effect of the fluid tank, the translational motion equation of the drone as a whole is driven by Equation (4). All the equations relate to the body coordinate, following the north-east-down (NED) coordinates with reversed *Z axis*, as shown in Figure 1. Then, to reduce the negativity of coefficients, *Z axis* of the *Body* frame was chosen to be reversed regarding the NED system.

$$\dot{r}_e = R_{eb}^T V_b + w_e \times r_e \tag{4}$$

where $\dot{r}_e$ denotes the CoM position vector derivative in the *Inertial* frame, R_{eb} is the rotation matrix from *Inertial* to frame *Body* frame, described in [25,27], V_b is the CoM relative velocity in *Body* frame, and $w_e \times r_e$ is the air absolute velocity at r_e. Then, the translational dynamics of the system are as follows in Equation (5), considering the Coriolis formulation of $\frac{d}{dt} V_b = \dot{V}_b + \omega_b \times V_b$.

$$F_b = \dot{V}_b m_f + \dot{m}_f V_b + R(\dot{m}_f - \omega_e)(w_e \times r_e) - (\omega_b + R\omega_e) \times V_b + Rg \tag{5}$$

where F_b is the total force impacting on *Body* frame, m_f is the fluid tank mass, $\dot{m}_f$ is the fluid-derived mass that is negligible for solid parts and considerable for the fuel part, ω_e and ω_b are the drone angular velocity in *Inertial* and *Body* frames, respectively, and g is the gravitational acceleration.

4. The Proposed Control Strategy

Considering the dynamics equations described through Section 2, a nonlinear controller is proposed to maintain the stability of the drone against the engine's failure. Among nonlinear methods, model reference adaptive control (MRAC) is a fine solution in the case of releasing payloads such as the Fan Hopper, since the total mass as an internal uncertainty is sustainably changing and the controller must adapt the parameters hastily. Then, to perform an agile reaction, the stability is established by a Lyapunov function to converge the model to the domain of attraction and stabilize the system. As shown in Figure 7, a brief schematic diagram of the adaptive controller is demonstrated regarding the inner loop. Differing from the reference and proposed model systems, an adaptive rule is defined to enter the state space, compute the position and velocity errors, and update the matrices as any internal error occurs. Multiplying the update matrix to the state model results in updated inputs for engines to be applied, then differing them to the errors obtained from the state space model concludes in EDF commands. Considering the state input vector of the system as X, it yields:

$$X = [\ x \quad \dot{x} \quad y \quad \dot{y} \quad z \quad \dot{z} \quad \phi \quad \dot{\phi} \quad \theta \quad \dot{\theta} \quad \psi \quad \dot{\psi}\ ]^T \tag{6}$$

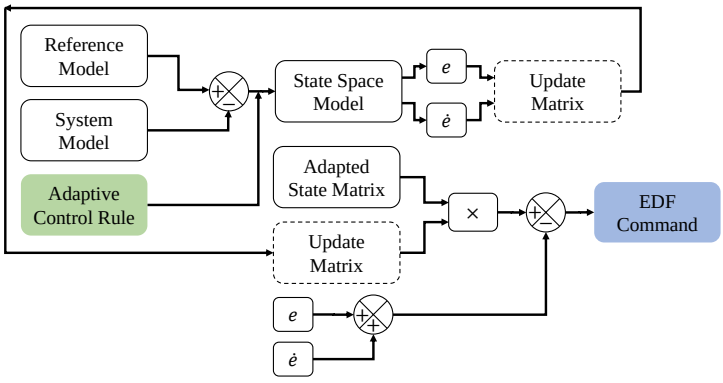

Figure 7. Diagram of implemented adaptive controller for attitude loop.

where the goal is to approximate the parameters of a model adapted to the main system, we express the reference model as a nonlinear second-order robot in state space as $G_m(s)$:

$$G_m(s) = \frac{w^2}{s^2 + 2\xi\omega s + \omega^2} \rightarrow\rightarrow \ddot{\chi}_m + \underbrace{2\xi\omega}_{m_1}\chi_m + \underbrace{\omega^2}_{m_2}\chi_m = \underbrace{\omega^2}_{n} u_c \tag{7}$$

where m_1, m_2, and, n are reference parameters, and u_c is the general controller input. Assuming $G(s)$ is a proposed second-order model to reduce the difference with the reference model, it gives

$$G(s) = \frac{1}{s(s+m)} \rightarrow \ddot{\chi} + m\dot{\chi} = u \tag{8}$$

where m is the parameter to be estimated when the adaptive model approaches the reference model. We determine the control rule for the second order system as follows:

$$u = \alpha_1 u_c - \alpha_2\dot{\chi} - \alpha_3\chi \tag{9}$$

Taking the mass uncertainty into account, it differs as the payload tank releases the fluid, which is computed by update values $\alpha_i, i = \{1,2,3\}$ for the adaptation law. Differentiating Equations (7) and (8)

$$\ddot{\chi} - \ddot{\chi}_m - m_1\dot{\chi}_m - m_2\chi_m = -(m+\alpha_2)\dot{\chi} - \alpha_3\chi + (\alpha_1 - n)u_c \tag{10}$$

Considering $e = \chi - \chi_m$, $\dot{e} = \dot{\chi} - \dot{\chi}_m$, $\ddot{e} = \ddot{\chi} - \ddot{\chi}_m$, and adding $m_1\dot{\chi} + m_2\chi$ to both sides of the equation,

$$\ddot{e} + m_1\dot{e} + m_2 e = -\underbrace{(m + \alpha_2 - m_1)}_{\beta_2}\dot{\chi} - \underbrace{(\alpha_3 - m_2)}_{\beta_3}\chi + \underbrace{(\alpha_1 - n)}_{\beta_1} u_c \tag{11}$$

where e denotes the error between the reference and adaptive values. Hence:

$$e = \frac{1}{s^2 + 2\xi\omega s + \omega^2}[\dot{\chi} \quad -\chi \quad u_c][\beta_2 \quad \beta_3 \quad \beta_1]^T \tag{12}$$

Obviously in Equation (12), the numerator and denominator difference degree is more than one; therefore, it is not strictly positive real (SPR), and Kalman Yakubovich's Lemma [30] is not usable, while it is solvable utilizing state space equations, as follows:

$$\begin{cases} \dot{X} = AX + BU \\ Y = CX + DU \end{cases} \tag{13}$$

$$A = \begin{bmatrix} O_{6\times6} & I_{6\times6} - a_2 \\ O_{6\times6} & -a_1 \end{bmatrix} = \begin{bmatrix} 0&0&0&0&0&0&1-\omega_\phi^2&0&0&0&0&0 \\ 0&0&0&0&0&0&0&1-\omega_\theta^2&0&0&0&0 \\ 0&0&0&0&0&0&0&0&1-\omega_\psi^2&0&0&0 \\ 0&0&0&0&0&0&0&0&0&1-\omega_{\dot{\phi}}^2&0&0 \\ 0&0&0&0&0&0&0&0&0&0&1-\omega_{\dot{\theta}}^2&0 \\ 0&0&0&0&0&0&0&0&0&0&0&1-\omega_{\dot{\psi}}^2 \\ 0&0&0&0&0&0&-2\xi_\phi\omega_\phi&0&0&0&0&0 \\ 0&0&0&0&0&0&0&-2\xi_\theta\omega_\theta&0&0&0&0 \\ 0&0&0&0&0&0&0&0&-2\xi_\psi\omega_\psi&0&0&0 \\ 0&0&0&0&0&0&0&0&0&-2\xi_{\dot{\phi}}\omega_{\dot{\phi}}&0&0 \\ 0&0&0&0&0&0&0&0&0&0&-2\xi_{\dot{\theta}}\omega_{\dot{\theta}}&0 \\ 0&0&0&0&0&0&0&0&0&0&0&-2\xi_{\dot{\psi}}\omega_{\dot{\psi}} \end{bmatrix} \tag{14}$$

$$B = \begin{bmatrix} 0&0&0&0&0&1/m&0&0&0&0&0&0 \\ 0&0&0&0&0&0&0&l/I_x&0&0&0&0 \\ 0&0&0&0&0&0&0&0&l/I_y&0&0&0 \\ 0&0&0&0&0&0&0&0&0&0&1/I_z \end{bmatrix}^T, C = [0 \cdots_4 0\ 1 \cdots_4 1]_{1\times12}, D = O_{12\times4} \tag{15}$$

where, $A \in \mathbb{R}^{12\times12}$ denotes the state coefficients matrix generalized of Jacobian matrix, $B \in \mathbb{R}^{12\times4}$ expresses the controller inputs to state matrix, $U \in \mathbb{R}^4$ is the controller inputs vector, $C \in \mathbb{R}^{1\times i}$ is the state-to-output matrix depending on j demands, which are $\phi, \theta, \psi, \dot{\phi}, \dot{\theta}, \dot{\psi}$ for this research, $D \in \mathbb{R}^{12\times4}$ is the static gain matrix, which represents the output-to-input ratio, ξ_i and $\omega_i, i = \{\phi, \theta, \psi, \dot{\phi}, \dot{\theta}, \dot{\psi}\}$ are calculated iterating the simulation numerous times. Additionally, the parameters in the B matrix are linearized fast dynamics of the hexacopter, coming from $\Delta U_1 = m\ddot{z}$, $U_2 = I_x\ddot{\phi}$, $U_3 = I_y\ddot{\theta}$, $U_4 = I_z\ddot{\psi}$, in which the m refers to the whole drone mass, containing m_f mentioned in Equation (5). Determining the errors in state space, it gives

$$\begin{bmatrix} \dot{e} \\ \ddot{e} \end{bmatrix} = A\begin{bmatrix} e \\ \dot{e} \end{bmatrix} + B[-\dot{\chi} \quad -\chi \quad u_c][\beta_2 \quad \beta_3 \quad \beta_1]^T \tag{16}$$

To obtain the update matrix for attitude values and rates, $F \in \mathbb{R}^{6\times6}$ and $P \in \mathbb{R}^{6\times6}$ are defined as diagonal positive definite (DPD) matrices. The former contains $f_i, i = \{f_\phi, f_\theta, f_\psi, f_{\dot{\phi}}, f_{\dot{\theta}}, f_{\dot{\psi}}\}$ as diagonal elements equal to eigenvalues, and the latter satisfies the condition $A^TP + PA = -I$, in which I is the identity 6×6 matrix. Thus, solving Equation (16) and the latter criterion [31,32], the update matrix yields:

$$[\dot{\beta}_2 \quad \dot{\beta}_3 \quad \dot{\beta}_1]^T = -F[-\dot{\chi} \quad -\chi \quad u_c]^T B^T P\begin{bmatrix} \dot{e} \\ \ddot{e} \end{bmatrix} \tag{17}$$

On the other hand, in terms of stability, a positive definite function (PDF) is proposed as a Lyapunov candidate, and its derivative must be demonstrated to be negative definite.

$$V = \frac{1}{2}e^TPe + \beta^TF\beta \tag{18}$$

where V denotes the Lyapunov function, e is the aforementioned error term of $\mathbb{R}^6$ (refers to Equation (11)), and β is the update matrix defined previously. Meanwhile, F appeared as a matrix and functions as a dot product due to being diagonal between two vectors; consequently, both terms result in $[\cdots]_{1\times6}[\cdots]_{6\times6}[\cdots]_{6\times1} = N_{1\times1}$ dimension. Then, the derivative of the Lyapunov candidate simplifies as follows:

$$\begin{aligned}
&\dot{V} = \tfrac{1}{2}(\dot{e}^TPe + e^TP\dot{e}) + \dot{\beta}^TF\beta + \beta^TF\dot{\beta} \\
&\rightarrow \dot{V} = \tfrac{1}{2}((\dot{x} - \dot{x}_m)^TPe + e^TP(\dot{x} - \dot{x}_m)) + 2F\beta^T\dot{\beta} \\
&\rightarrow \dot{V} = \tfrac{1}{2}((A_me + \underbrace{\cdots}_{\zeta\beta})^TPe + e^TP(A_me + \zeta\beta)) + 2F\beta^T\dot{\beta} \\
&\rightarrow \dot{V} = \tfrac{1}{2}e^T(\underbrace{(A_m^TP + pA_m)}_{-I,\,(19)})e + \underbrace{\beta^T\zeta^TPe}_{\Delta} + \underbrace{e^TP\zeta\beta)}_{\Delta^T} + 2F\beta^T\dot{\beta} \\
&\rightarrow \dot{V} = \underbrace{-\frac{1}{2}e^TIe}_{ND} + \tfrac{1}{2}\beta^T\underbrace{(Pe + e^TP\zeta\beta + 4F\beta^T\dot{\beta})}_{to\ be\ equal\ 0}
\end{aligned} \tag{19}$$

where A_m is the Jacobian matrix of the reference model, and ζ is a synoptic notation of update matrix products. The first term of the simplified derivative function is ND; regarding the second term, the assumption is that $\beta^T = 0$ is not acceptable, and only $Pe + e^TP\zeta\beta + 4F\beta^T\dot{\beta}$ must equal zero to satisfy the definite negativeness of the term.

5. Simulation Results

Through this research, a complete virtual model of the Fan Hopper was designed to apply the controller algorithm to a 3D model and prevent multiple failures in the real world. Meanwhile, several random noises were imported, including the fluid release and a motor failure that examined the controller's functionality to update adaptive parameters. The simulation was carried out employing the open dynamic engine (ODE) of Gazebo. Thanks to the asset loading and unloading feature, Gazebo makes the simulation drive realistic. Concurrently, it can connect to the robotic operating system (ROS), which handles the movements, orientation, various sensors, and the control algorithm. Preparing for the simulation, all the cad models (refer to Section 6.1) were exported to **.urdf* format, using the ROS-URDF library (accessed on 3 July 2022), in order to prepare the mathematical for the simulation, as shown in Algorithm 1.

Algorithm 1 FanHopper URDF Configuration.

Require: geometric params.
Ensure: the mathematical model

$< robot\ name\ space ='' FanHopper'' >$
  $< linkname ='' \textbf{\textit{fuselage}}'' >$
    $< inertial > \cdots < origin >, < mass >, and\ < inertia > \cdots < /inertial >$
    $< visual > \cdots < origin >, < geometry >, and\ < material > \cdots < /visual >$
    $< collision > \cdots < origin > and < material > \cdots < /collision >$
  $< /link >$
  $< \textbf{\textit{propellers}}\ joint >$
    $< origin >< parent >, < child >, < axis >, < dynamic >, and\ < limit >$
  $< /joint >$ ▷ six propellers
  $< gazebo\ reference ='' \textbf{\textit{sensors}}''\ joint >$
    $< type > and < plugin$
  $< /gazebo >$ ▷ IMU, forces, moments, and camera controllers
$< /robot >$

As described in Algorithm 1, two hierarchies were applied; the *base link*, which is mentioned as *fuselage*, and *propellers*, which are dependent joints to the root. Then, all sensors used to communicate with ROS are at the same level defined as *reference*. Connecting the simulation with an adaptive algorithm elaborated in *python*, sensor data were subscribed to, and control regulations were applied by the ROS publishers. Several results were obtained by enhancing the controller algorithm, which briefly includes engine failure during the flight. As shown in Figure 8b, a semi-sine wave trajectory was simulated to examine the adaptive controller during a 5 min period. Accordingly, the purple lines highlight the control inputs and the blue lines correspond to the actual behavior of the system. Upon starting the mission, the drone lifted off to a 2.5 m altitude and followed the horizontal trajectory with less than 1% error, as shown in Figure 8a,d,g. Though after 2.7 min, one of the EDFs failed, the drone maintained stability, as shown in Figure 8b,c,e,f, and the only visible error appeared in the yaw angle, as shown in Figure 8h,i, which is even about 5° that could be neglected.

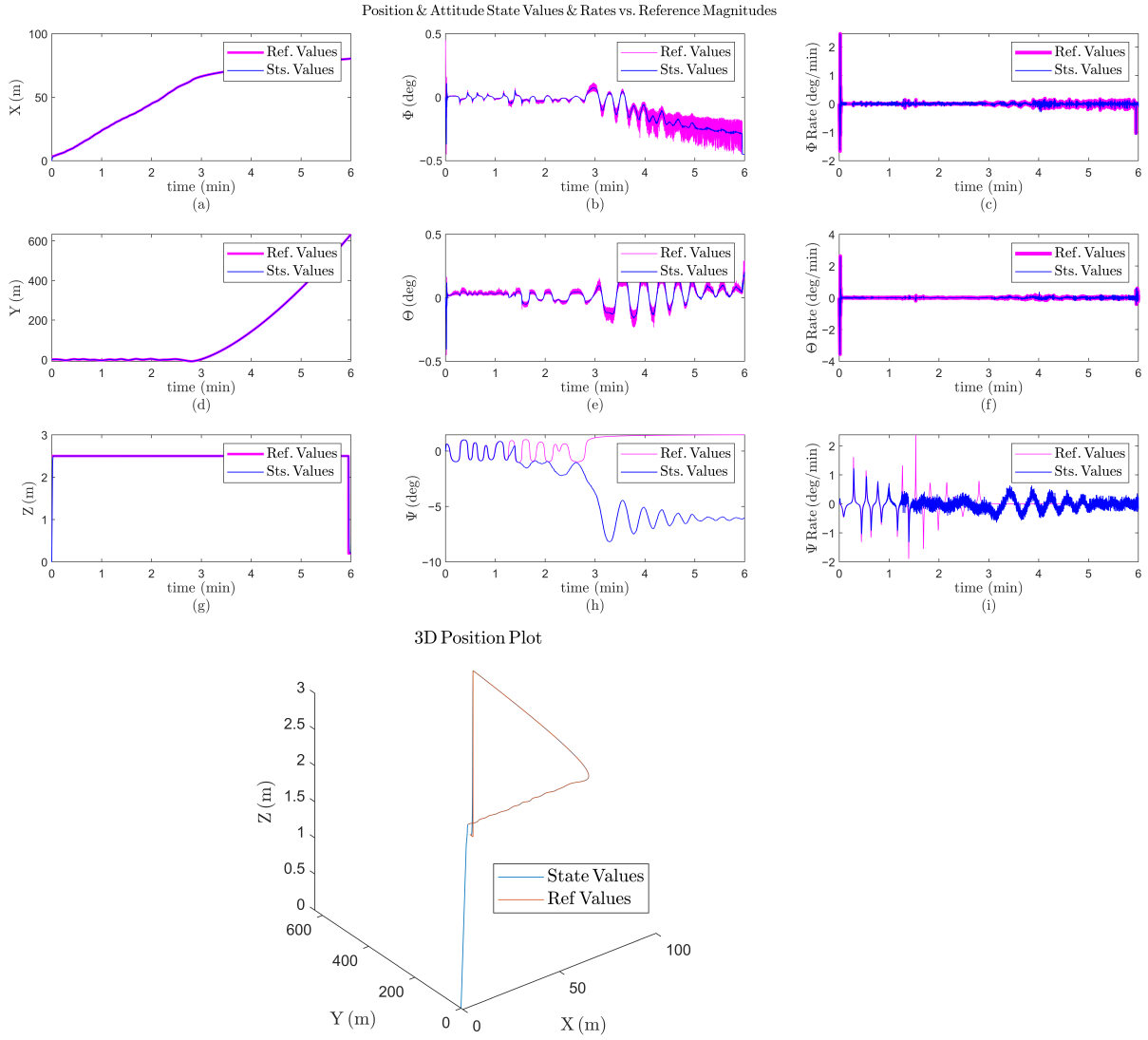

Figure 8. Simulation results when an EDF fails during 5 min; (**a**) the horizontal (x) position variation versus time; (**b**) the roll (ϕ) angle variation versus time; (**c**) the roll rate ($\dot{\phi}$) variation versus time; (**d**) the horizontal (y) position variation versus time; (**e**) the pitch (θ) angle variation versus time; (**f**) the pitch rate ($\dot{\theta}$) variation versus time; (**g**) the vertical (z) position variation versus time; (**h**) the yaw (ψ) angle variation versus time; (**i**) the yaw rate ($\dot{\psi}$) variation versus time.

6. Hardware Design

The design process followed in this research consists of three main steps: preliminary model design, assembly of the components, and mechanical and electrical integration. Then, multiple components are reviewed, redesigned, and reconstructed to guarantee a safe flight. Among possibilities for a hexacopter frame, a rectangular platform was chosen since a heavy payload shall be carried; when this was added to the electrical power system, which exceeded five kg in weight, it made the configuration rectangular. Additionally, as described in the Section 2.1, ducts that generated yaw moments were canceled out thanks to the quadratic frame.

6.1. Model Design and Assembly

Briefly, each component was designed in Microsoft Fusion, as shown in Figure 9. The drone fuselage has 97 cm width, 40 cm height with open wheels, is and 1090 cm

long, containing inclined EDFs installed, as shown in Figure 9a,b,d. The fluid tank was installed under the CoM of the drone. For instance, several component models are drawn in Figure 9e–g, including the novel designed connectors function to adjust the install angle of EDF that functions as a thrust vector, configurable between 0° and 22°. In addition, Figure 10 demonstrates the differentiation of the thrust and yawing torque of a Fan Hopper's EDF, respectively, and in a period of 30 s, based on the variation of the installment angle from 0° and 22°. Observing the diagram, the most optimized line belongs to the one with more thrust and less torque to cancel. Furthermore, the highest and lowest thrust happened at 15° and 20°, respectively; however, the absolute torque magnitude increased alongside the angle. Additionally, regarding the effective thrust timestamp during seconds 16 and 23, the thrust maximum difference amount was $\leq$100 N, and for torque, it was $\leq$0.05 N.m. The former amount is considerable and weighted the latter, since the torque was canceled out further by other EDFs in the Hexa configuration. Hence, considering detailed values, the optimized incident angle domain was chosen between 8° and 11° to perform the practical tests. In addition, Figure 10b displays the EDF vibration increasing as the installment angle raises, which is exempted near to 15°, which was related to a higher thrust. Therefore, this diagram again confirms the chosen domain in terms of vibrations.

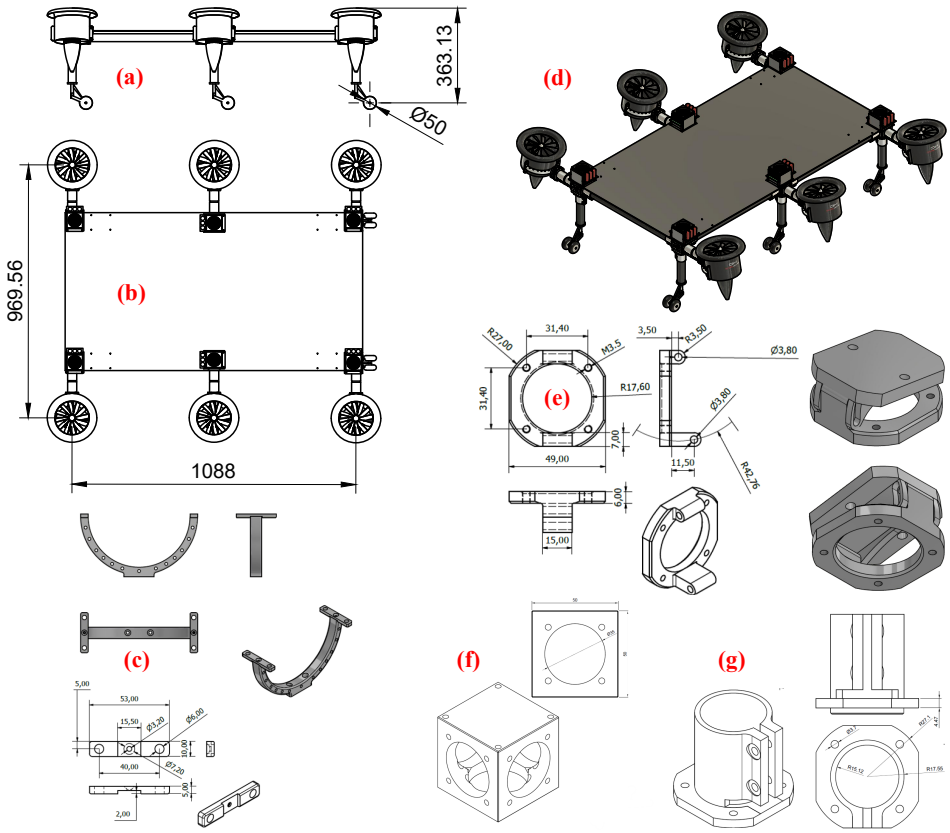

Figure 9. The CAD models of the Fan Hopper; (**a**) side elevation of the CAD model; (**b**) top view of the CAD model; (**c**) engine arm connectors; (**d**) a 3D view of the CAD model; (**e**) incident angle adjusters for duct engines; (**f**) the conjunction main connector; (**g**) body to duct arm connectors.

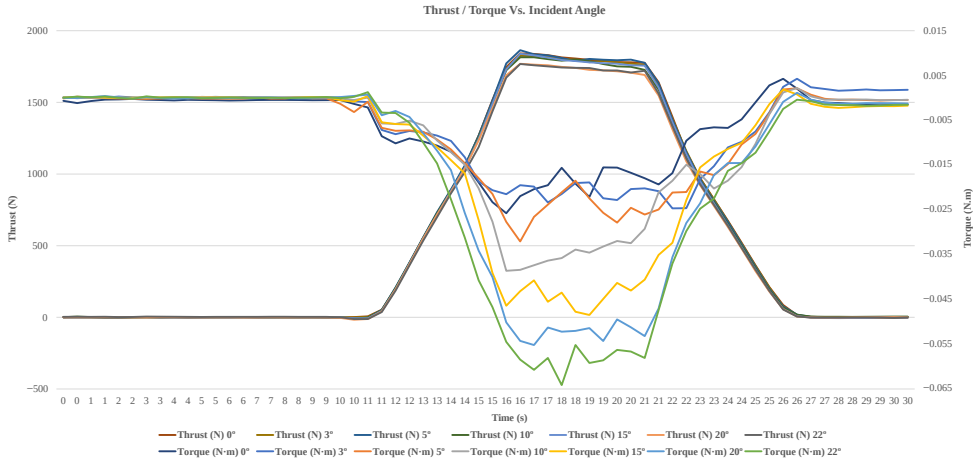

(**a**)

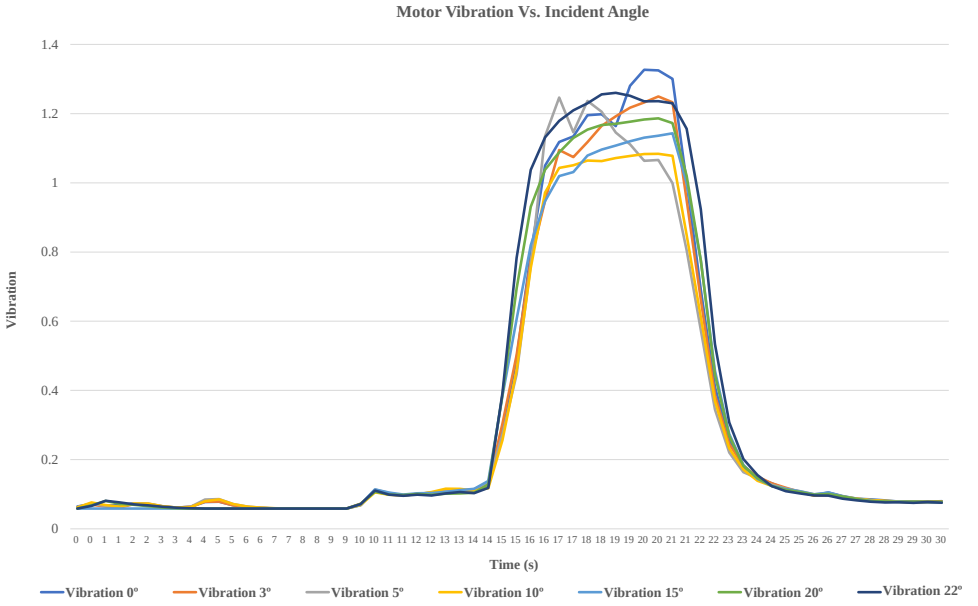

(**b**)

Figure 10. Diagram of an EDF data versus incident angles (0°–22°) during 30 s; (**a**) diagram of EDF thrust and yawing torque, (**left bar**) thrust values, (**right bar**) torque values; (**b**) the expressed vibration impact of distinct incident angles on the duct.

6.2. System Integration

Following the assembly, concatenated components as a whole are shown in Figure 9d,b, and the corresponding actual model is displayed in Figure 11f. Thanks to adjustable joints and landing bases, EDFs could be installed closer to the base link, and the landing basis varies according to the fluid tank dimension, as elaborated in Figure 12. Additionally, the initial characteristics of the Fan Hopper are stated in Table 1. Based on the aerodynamic analysis reviewed in Section 2.2, a suitable EDF configuration was selected for the Fan Hopper to facilitate a large payload; each SCHUBELER HST engine lifts to 10 kg weight and enhances the stator aerodynamics, with its efficiency maximized to 70%.

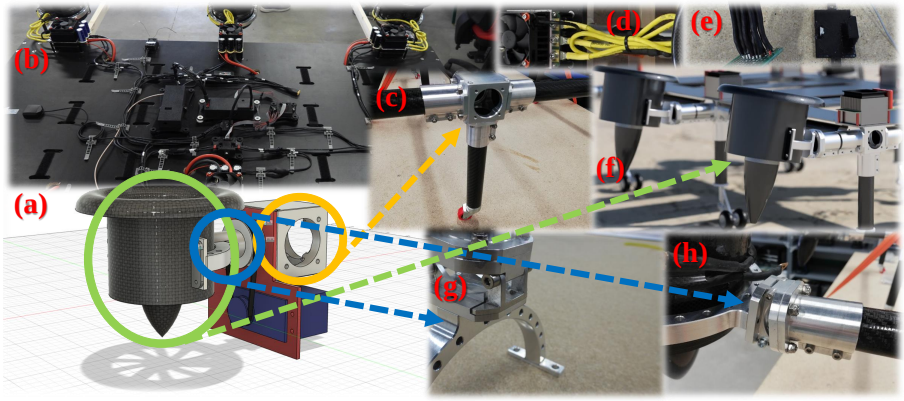

Figure 11. Assembled model of the Fan Hopper; (**a**) the EDF model connected to the joints, modifiable by the rubber band; (**b**) the base link, containing AP, connectors, antenna, fan, joints, wires, etc.; (**c**) the aluminum joint for the landing gear and motor arm; (**d**) the ESC cooler; (**e**) power distribution board; (**f**) the EDF system; (**g**) the duct holder; (**h**) the configurable duct joint to the arm.

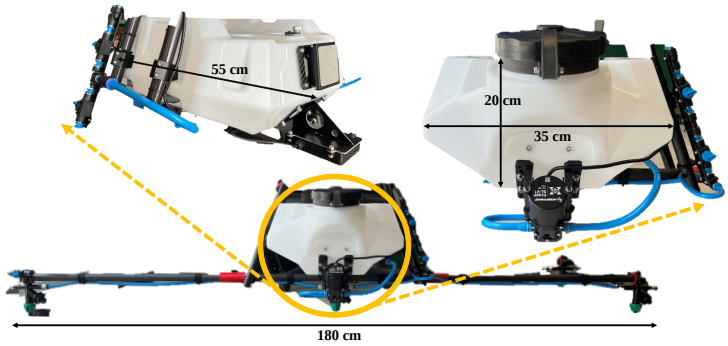

Figure 12. the integrated fluid tank schematic of the Fan Hopper; electrical components, valves, and tubes could be seen precisely on the left and right sides.

Table 1. Initial characteristics of the of the Fan Hopper.

Parameter	Description	Weight (kg)
AP	Pixhawk Standard Set Cube Orange + ADS-B	0.32
EDF	SCHUBELER, *DS-98-DIA* HST	1330 × 6
GCS	modified QGroundControl, using *Qt*15.5.2	-
ESC & Fan		0.52 × 6
Battery	Quantum 5000 mAh	2.215 × 6
Base link	Wood and flexible materials	5
Cabling	-	1
Fluid tank	Containing the spray system and the regulator	3
	TOTAL empty weight	35

Regarding the Section 2, the motor mixing configuration is described in Table 2. The numeration direction of the EDFs is counter clockwise, and central EDFs (2, 5) do not collaborate for pitch and yaw moments.

Table 2. Motor mixing configuration of the Fan Hopper.

EDF	Roll Moment	Pitch Moment	Yaw Moment	Configuration
R1	0.5	−1	0.5	
R2	0.5	0	0	1 ↺ —— ↻ 6
R3	0.5	1	−0.5	2 ↻ —— ↺ 5
R4	−0.5	1	0.5	3 ↺ —— ↻ 4
R5	−0.5	0	0	
R6	−0.5	−1	−0.5	

7. Practical Results

Several analyses were conducted to ensure the components' functionality and safety issues, including EDF, ground and balance, and flight tests. As shown in Figure 13, multiple balance tests were performed, once with two payload packages, each one weighing 5 kg, and then with four packages in symmetric order. Moreover, the total Fan Hopper weight is 35.4 kg, and the wooden ballast stabilizer below the drone has a 4 kg weight. During the first flight, numerous vibrations were observed in the base link, which decreased significantly using the adaptive method described in Section 4 by tuning the update matrix parameters. Meanwhile, several modifications were applied to the base link to make it more flexible against undesired vibrations. Previously, a complete practice was performed using the default parameters of the AP (Pixhawk) to affirm MRAC estimated values. In addition, results of two flight tests with altitudes higher than 5 m are shown, once with random low noises and then, with higher noises applied by the pilot.

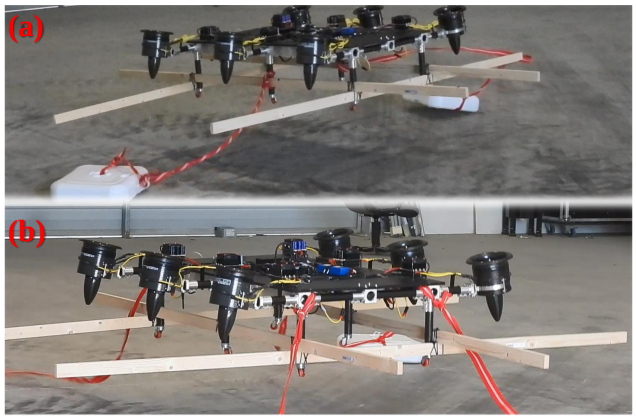

Figure 13. Ground tests made to assure the stability of Fan Hopper, and examine the lifting power; (**a**) lifting two payloads of 5 kg; (**b**) lifting four payloads of 5 kg.

The analytical results of a balance test are shown in Figure 14. This test was conducted near the ground with varying altitudes up to 1.5 m with different payload weights. Moreover, the flight was carried out with a copilot, i.e., piloting manually saturated by AP limitations to test its reactions. Meanwhile, the payload was separated by a rope further from the fuselage to prevent any accidents. During the test, in the time interval between 6 s to 7.5 s, the pilot applied 15° roll and pitch commands simultaneously with a random yaw command, which is demonstrated in Figure 14a–c. Although there was an alteration in attitude angles, the controller compensated the stability rapidly in less than 2 s, with minor errors.

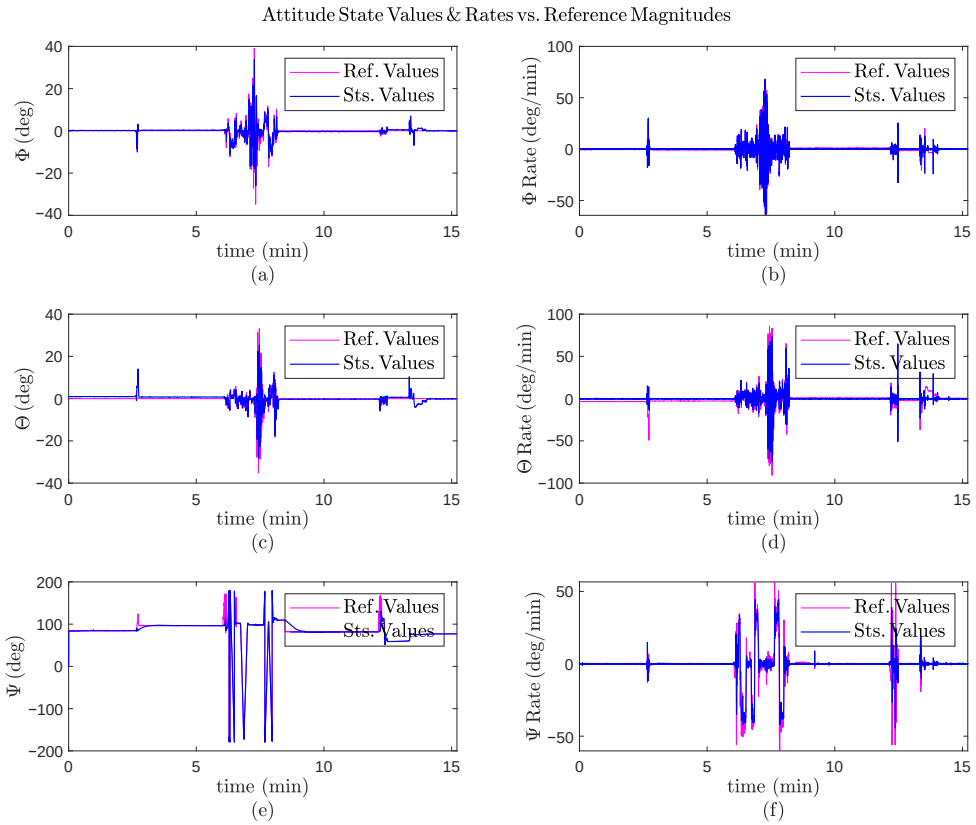

Figure 14. Balance test results near the ground during 15 min; (**a**) the roll (ϕ) angle variation versus time; (**b**) the pitch (θ) angle variation versus time; (**c**) the yaw (ψ) angle variation versus time; (**d**) the roll rate ($\dot{\phi}$) variation versus time; (**e**) the pitch rate ($\dot{\theta}$) variation versus time; (**f**) the yaw rate ($\dot{\psi}$) variation versus time.

Multiple flight tests at higher altitudes were conducted after configuring the ground tests and tuning the PID parameters to ensure the controllability of the FanHopper. The first results relate to a flight test during 18 min, containing a sudden pilot disturbance after passing 7.5 min, in which the attitude controller had an undershoot reaction due to saturating inputs, as shown in Figure 15a. The stability was regained in less than 10 s, since the deviation was canceled by a cascade approach, eliminating errors by regulating both the roll angle and its rate, as shown in Figure 15b. Likewise, unexpected phenomena were applied to the pitch and yaw angles that were damped rapidly after 7.5 min, 9.5 min, and 13 min.

Finally, the last results contain high disturbances leading to instability; however, they were damped with adequate haste. As shown in Figure 16, after 10 min, all attitude angles were altered simultaneously, as 10° for roll, 8° for pitch, and up to −200° for yaw, but were regulated in less than 2 s. At 15 min, one of the EDFs was unplugged from the system, which triggered a negligible transient error (less than 1°) to the pitch angle.

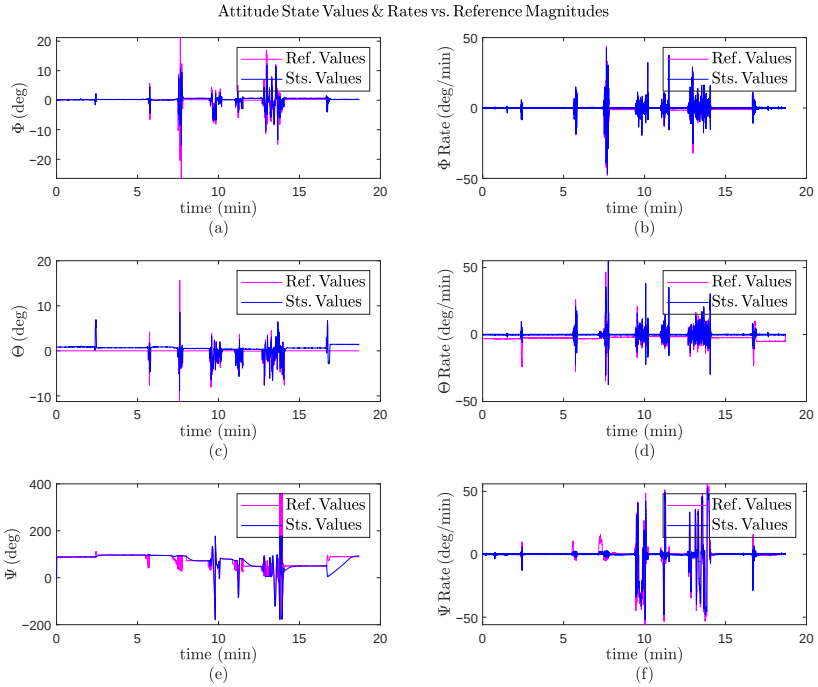

Figure 15. Practical results with intermediate disturbance, during 18 min; (**a**) the roll (ϕ) angle variation versus time; (**b**) the pitch (θ) angle variation versus time; (**c**) the yaw (ψ) angle variation versus time; (**d**) the roll rate ($\dot{\phi}$) variation versus time; (**e**) the pitch rate ($\dot{\theta}$) variation versus time; (**f**) the yaw rate ($\dot{\psi}$) variation versus time.

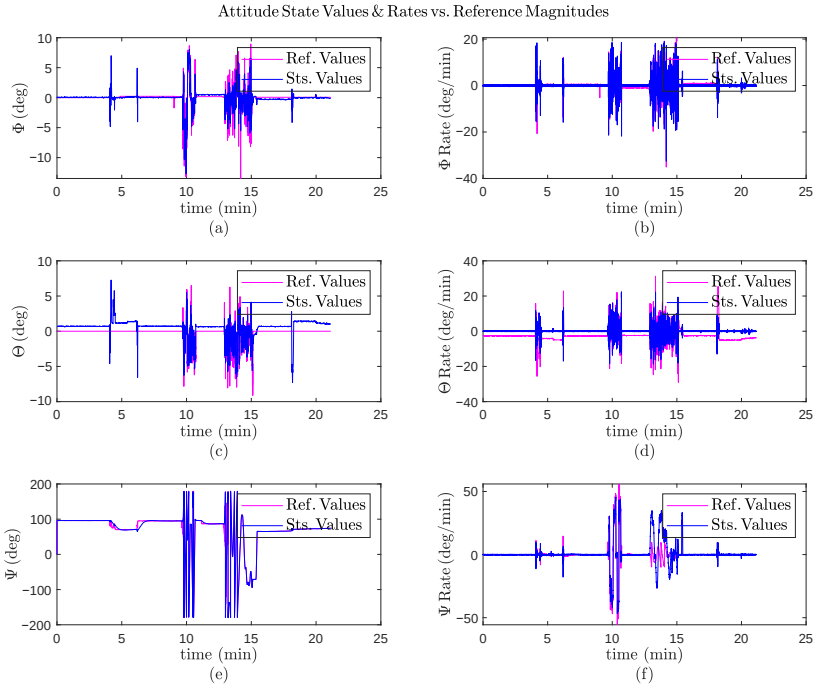

Figure 16. Practical results with an EDF failure, during 22 min; (**a**) the roll (ϕ) angle variation versus time; (**b**) the pitch (θ) angle variation versus time; (**c**) the yaw (ψ) angle variation versus time; (**d**) the roll rate ($\dot{\phi}$) variation versus time; (**e**) the pitch rate ($\dot{\theta}$) variation versus time; (**f**) the yaw rate ($\dot{\psi}$) variation versus time.

8. Discussion and Conclusions

This paper concentrated on the attitude control system of a medium-scale hexacopter powered by EDFs employing an MRAC algorithm with proven asymptotic stability by introducing an appropriate Lyapunov candidate. During the investigation, complete aerodynamic modeling was performed to choose suitable ducted fans and prevent the fluid injection system from making the UAV unstable. Furthermore, the controller's performance was examined through the Gazebo dynamic space simulation, estimating the controller's initial parameters and maintaining the safety of the practical tests. According to the results obtained from simulation and practice, the attitude regulator functions are adequately acceptable, with errors of less than 5% in most cases. Additionally, an EDF failure was applied to the system in both spaces, but the controller quickly brought everything back to stability. This research revealed the possibility of controlling a rectangular hexacopter when powerful engines are mounted to the system, and even if one of the motors fails, the flight can be recovered.

Author Contributions: Conceptualization, M.S.A.I., M.A.L., M.M.A.E.K., R.K., A.R.R., P.C., P.F.P. and M.M.; data curation, M.S.A.I. and M.A.L.; formal analysis, M.S.A.I., M.A.L., A.R.R. and M.M.A.E.K.; funding acquisition, P.F.; investigation, M.S.A.I., M.A.L., A.R.R., P.C., P.F.P. and M.M.; methodology, M.S.A.I., M.A.L., A.R.R., M.M.A.A, R.K., P.C. and M.M.; project administration, M.M.A.E.K., R.K., P.C., P.F.P. and M.M.; resources, P.C. and P.F.; software, M.S.A.I. and M.A.L.; supervision, A.R.R., P.C., P.F.P. and M.M.; validation, M.S.A.I., M.A.L., A.R.R., M.M.A.E.K., R.K., P.C., P.F.P. and M.M.; visualization, M.S.A.I. and M.A.L.; writing—original draft, M.S.A.I., M.A.L. and A.R.R.; writing—review and editing, A.R.R., P.C., and M.M. All authors have read and agreed to the published version of the manuscript.

Funding: This research was supported by the European Commission-funded program FASTER, under H2020 Grant Agreement 833507 and partially funded by the Community of Madrid through the project REF: IND2020/IND-17478 "Ayudas para la realización de Doctorados Industriales", specially regarding the work of the second and sixth authors. This work has also been supported by the project COMCISE RTI2018-100847-B-C21, funded by the Spanish Ministry of Science, Innovation and Universities (MCIU/AEI/FEDER, UE).

Institutional Review Board Statement: Not applicable.

Informed Consent Statement: Not applicable.

Data Availability Statement: Not available.

Acknowledgments: We are so thankful to the Drone Hopper company for supporting the project, the Carlos III University for providing the hanger and academic space to investigate, Adrian Revuelta for designing the exact models and assemblies, Antonio Buendia Ruiz for sharing precious experiences regarding the ducted fan analysis and documentation, and also the Flow Engineering Company for a deep aerodynamic analysis of the EDFs.

Conflicts of Interest: The authors declare no conflict of interest.

Abbreviations

The following abbreviations are used in this manuscript:

AoA	Angle of attack.
ANCF	Absolute nodal coordinate formulation.
AP	Autopilot.
CoG	Center of gravity.
CoM	Center of mass.
ECEF	Earth centered Earth fixed frame.
EDF	Electric ducted fan.
EKF	Extended Kalman filter.
ESC	Electrical speed controller.

FAFSMC	Fuzzy adaptive fixed-time sliding mode controller.
FE	Final element.
MRAC	Model reference adaptive controller.
NED	North east down.
SPR	Strictly positive real.
TSR	Tip speed ratio.
VTOL	Vertical takeoff and landing.

References

1. Fahlstrom, P.G.; Gleason, T.J.; Sadraey, M.H. *Introduction to UAV Systems*; John Wiley & Sons: Hoboken, NJ, USA, 2022.
2. Crouch, C.C. *Integration of Mini-UAVs at the Tactical Operations Level: Implications of Operations, Implementation, and Information Sharing*; Technical Report; Naval Postgraduate School: Monterey, CA, USA, 2005.
3. Watts, A.C.; Ambrosia, V.G.; Hinkley, E.A. Unmanned aircraft systems in remote sensing and scientific research: Classification and considerations of use. *Remote Sens.* **2012**, *4*, 1671–1692. [CrossRef]
4. DeSmidt, H. *Conceptual Design: Optimization of Medium Scale Unmanned Aerial Vehicle Propulsion System*; Technical Report; University of Tennessee: Knoxville, TN, USA, 2020.
5. Donateo, T.; Ficarella, A.; Spedicato, L.; Arista, A.; Ferraro, M. A new approach to calculating endurance in electric flight and comparing fuel cells and batteries. *Appl. Energy* **2017**, *187*, 807–819. [CrossRef]
6. Achtelik, M.; Doth, K.M.; Gurdan, D.; Stumpf, J. Design of a multi rotor MAV with regard to efficiency, dynamics and redundancy. In Proceedings of the AIAA Guidance, Navigation, and Control Conference, Minneapolis, MN, USA, 13–16 August 2012; p. 4779.
7. Vu, N.A.; Dang, D.K.; Le Dinh, T. Electric propulsion system sizing methodology for an agriculture multicopter. *Aerosp. Sci. Technol.* **2019**, *90*, 314–326. [CrossRef]
8. Luna, M.A.; Ale Isaac, M.S.; Ragab, A.R.; Campoy, P.; Flores Peña, P.; Molina, M. Fast Multi-UAV Path Planning for Optimal Area Coverage in Aerial Sensing Applications. *Sensors* **2022**, *22*, 2297. [CrossRef] [PubMed]
9. Li, Y.; Yonezawa, K.; Liu, H. Effect of Ducted Multi-Propeller Configuration on Aerodynamic Performance in Quadrotor Drone. *Drones* **2021**, *5*, 101. [CrossRef]
10. Miwa, M.; Uemura, S.; Ishihara, Y.; Imamura, A.; Shim, J.h.; Ioi, K. Evaluation of quad ducted-fan helicopter. *Int. J. Intell. Unmanned Syst.* **2013**, *2*, 187–198. [CrossRef]
11. Moaad, Y.; Alaaeddine, J.; Jawad, K.; Tarik, B.; Lekman, B.; Hamza, J.; Patrick, H. Design and optimization of a ducted fan VTOL MAV controlled by Electric Ducted Fans. In Proceedings of the 8th European Conference for Aeronautics and Space Sciences, Madrid, Spain, 1–4 July 2019; pp. 1–4.
12. Chen, C.; Dong, T.; Fu, W.; Liu, N. On dynamic characteristics and stability analysis of the ducted fan unmanned aerial vehicles. *Int. J. Adv. Robot. Syst.* **2019**, *16*, 1729881419867018. [CrossRef]
13. Jin, Y.; Qian, Y.; Zhang, Y.; Zhuge, W. Modeling of ducted-fan and motor in an electric aircraft and a preliminary integrated design. *SAE Int. J. Aerosp.* **2018**, *11*, 115–126. [CrossRef]
14. Ohanian, O.J. Ducted Fan Aerodynamics and Modeling, with Applications of Steady and Synthetic Jet Flow Control. Ph.D. Thesis, Virginia Tech, Blacksburg, VA, USA, 2011.
15. Longbottom, J. Investigation into the Reduction of the Drag Area of a Paramotor. Bachelor's Thesis, University of New South Wales, Sydney, Australia, 2006.
16. Zuo, X.; Liu, J.W.; Wang, X.; Liang, H.Q. Adaptive PID and model reference adaptive control switch controller for nonlinear hydraulic actuator. *Math. Probl. Eng.* **2017**, *2017*, 6970146. [CrossRef]
17. Gai, H.; Li, X.; Jiao, F.; Cheng, X.; Yang, X.; Zheng, G. Application of a New Model Reference Adaptive Control Based on PID Control in CNC Machine Tools. *Machines* **2021**, *9*, 274. [CrossRef]
18. Nguyen, N.P.; Xuan Mung, N.; Ha, L.N.N.T.; Hong, S.K. Fault-Tolerant Control for Hexacopter UAV Using Adaptive Algorithm with Severe Faults. *Aerospace* **2022**, *9*, 304. [CrossRef]
19. Rosales, C.; Soria, C.M.; Rossomando, F.G. Identification and adaptive PID Control of a hexacopter UAV based on neural networks. *Int. J. Adapt. Control Signal Process.* **2019**, *33*, 74–91. [CrossRef]
20. Abadi, A.S.S.; Hosseinabadi, P.A.; Mekhilef, S. Fuzzy adaptive fixed-time sliding mode control with state observer for a class of high-order mismatched uncertain systems. *Int. J. Control. Autom. Syst.* **2020**, *18*, 2492–2508. [CrossRef]
21. Bartsch, R.; Coyne, J.; Gray, K. *Drones in Society: Exploring the Strange New World of Unmanned Aircraft*; Routledge: Oxfordshire, UK, 2016.
22. Ranasinghe, K.; Bijjahalli, S.; Gardi, A.; Sabatini, R. Intelligent Health and Mission Management for Multicopter UAS Integrity Assurance. In Proceedings of the 2021 IEEE/AIAA 40th Digital Avionics Systems Conference (DASC), San Antonio, TX, USA, 3–7 October 2021; pp. 1–9.
23. Ragab, A.R.; Isaac, M.S.A.; Luna, M.A.; Flores Peña, P. WILD HOPPER Prototype for Forest Firefighting. *Int. J. Online Biomed. Eng.* **2021**, *17*, 148–168. [CrossRef]
24. Bresciani, T. Modelling, Identification and Control of a Quadrotor Helicopter. Master's Thesis, Lund University, Lund, Sweden, 2008.

25. Isaac, M.S.A.; Ragab, A.R.; Garcés, E.C.; Luna, M.A.; Peña, P.F.; Cervera, P.C. Mathematical Modeling and Designing a Heavy Hybrid-Electric Quadcopter, Controlled by Flaps. In Proceedings of the International Conference of Autonomous Systems (IEEE ICAS), Montreal, QC, Canada, 11–13 August 2021.
26. Ahmed, S.; Xin, H.; Faheem, M.; Qiu, B. Stability Analysis of a Sprayer UAV with a Liquid Tank with Different Outer Shapes and Inner Structures. *Agriculture* **2022**, *12*, 379. [CrossRef]
27. Wang, H.; Dong, X.; Xue, J.; Liu, J.; Wang, J. Modeling and simulation of a time-varying inertia aircraft in aerial refueling. *Chin. J. Aeronaut.* **2016**, *29*, 335–345. [CrossRef]
28. Spencer, A.J.M. *Continuum Mechanics*; Courier Corporation: Chelmsford, MA, USA, 2004.
29. Shabana, A.A. *Computational Continuum Mechanics*; John Wiley & Sons: Hoboken, NJ, USA, 2018.
30. Andrievsky, B.R.; Churilov, A.N.; Fradkov, A.L. Feedback Kalman-Yakubovich lemma and its applications to adaptive control. In Proceedings of the 35th IEEE Conference on Decision and Control, Kobe, Japan, 13 December 1996; Volume 4, pp. 4537–4542.
31. Dydek, Z.T.; Annaswamy, A.M.; Lavretsky, E. Adaptive control of quadrotor UAVs: A design trade study with flight evaluations. *IEEE Trans. Control Syst. Technol.* **2012**, *21*, 1400–1406. [CrossRef]
32. Murray, R.M.; Li, Z.; Sastry, S.S. *A Mathematical Introduction to Robotic Manipulation*; CRC Press: Boca Raton, FL, USA, 2017.

9.3 Publication II

Ale Isaac, M.S., Ragab, A.R., Luna, M.A., Ale Eshagh Khoeini, M.M. and Campoy, P. (2023). *Thrust Vectoring Control for Heavy UAVs, Employing a Redundant Communication System.* Sensors, 23(12), p.5561, doi:10.3390/s23125561.

sensors

MDPI

Article

Thrust Vectoring Control for Heavy UAVs, Employing a Redundant Communication System

Mohammad Sadeq Ale Isaac [1,2], Ahmed Refaat Ragab [3,4,5], Marco Andrés Luna [1,6], Mohammad Mehdi Ale Eshagh Khoeini [7] and Pascual Campoy [1]*

[1] Computer Vision and Aerial Robotics Group, Centre for Automation and Robotics (CAR), Universidad Politécnica de Madrid (UPM-CSIC), 28006 Madrid, Spain; mo.aleisaackhoueini@upm.es (M.S.A.I.); marco.lunaa@alumnos.upm.es (M.A.L.)
[2] Wake Engineering Company, 28906 Getafe, Spain
[3] Department of Network, Faculty of Information Systems and Computer Science, October 6 University, Giza 12511, Egypt; ahmed.refaat.csis@o6u.edu.eg (A.R.R.)
[4] Department of Electrical Engineering, University Carlos III of Madrid, 28919 Leganés, Spain
[5] Drone-Hopper Company, 28919 Leganés, Spain
[6] Ahyres Company, 28905 Getafe, Spain
[7] Department of Business Administration, Istanbul Aydin University, Istanbul 34295, Turkey; mehdy.al@gmail.com (M.M.A.E.K.)
* Correspondence: pascual.campoy@upm.es (P.C.)

Abstract: Recently, various research studies have been developed to address communication sensors for Unmanned Aerial Systems (UASs). In particular, when pondering control difficulties, communication is a crucial component. To this end, strengthening a control algorithm with redundant linking sensors ensures the overall system works accurately, even if some components fail. This paper proposes a novel approach to integrate several sensors and actuators for a heavy Unmanned Aerial Vehicle (UAV). Additionally, a cutting-edge Robust Thrust Vectoring Control (RTVC) technique is designed to control various communicative modules during a flying mission and converge the attitude system to stability. The results of the study demonstrate that even though RTVC is not frequently utilized, it works as well as cascade PID controllers, particularly for multi-rotors with mounted flaps, and could be perfectly functional in UAVs powered by thermal engines to increase the autonomy since the propellers cannot be used as controller surfaces.

Keywords: sliding mode; thrust vectoring control; UAV; sommunication

Citation: Ale Isaac, M.S.; Ragab, A.R.; Luna, M.A.; Ale Eshagh Khoein, M. M.; Campoy P. Thrust Vectoring Control for Heavy UAVs, Employing a Redundant Communication System. *Sensors* **2023**, *1*, 0. https://doi.org/

Received: 7 May 2023
Revised: 31 May 2023
Accepted: 9 June 2023
Published:

1. Introduction

If you are far away from your enemy, make him believe that you are near. This was written by Sun Tzu, about 2500 years ago [1]. It seems that this phrase was a precursor to the subject of unmanned aerial vehicles (UAV), a technical system combining several layers to make a flying platform, from communication to control and structural systems. UAVs are almost known as aircraft without a pilot onboard, and they have become increasingly dominant due to their wide usage as remote-controlled vehicles in different fields, such as the military, firefighting, logistics, and agriculture. The abbreviation has been changed to become unmanned aerial system (UAS), to show that such a system does not only depends upon the aircraft itself, but it depends upon several important issues such as the ground control station (GCS), Communication systems with complexity, and the computing system. UAVs have several classifications based on flight endurance, weight, flying application, altitude, flight range, and the structural type [2], which, amongst the weight and endurance, are sub-objectives of this research. According to the European Union aviation safety agency (EASA) regulations for civil UASs open category, four general types are considered

regarding the weight classification: Class A1 (less than 900 g), Class A2 (less than 4 kg), Class A3 (less than 25 kg), and for weights greater than 25 kg, other categories are observed that are based on some operational restrictions. Both piloting requirements and flying zones are considered [3]. In counterpart, according to the AP-3.3.7 mission qualifications of the global NATO-STANAG 4670 UAS category, they are divided into nanoscale (less than 250 g), microscale (less than 2 kg), small scale (less than 25 kg), medium scale (less than 150 kg), and large scales (more than 150 kg) [2,4]. Among the latter classification, the heavier the UAV, the more cargo payload benefits from a longer range in a single load. The medium scales are limited to a lower flight endurance and payload carriage. Therefore, many recent contexts are concentrated on heavy-lifter UAVs to improve the control and communication system for such platforms. Likewise, this research investigates a large-scale UAV of 200 kg weight, which contains several communication and control layers to maintain the safety of the flight. Meanwhile, the payload system is a releasable low-density liquid that complicates the system's dynamic.

Heavy UAVs consist of many components, in which the most crucial ones function as a communication system that is not only in charge of internal commands transmission but also external UAVs, which can be seen as ad hoc nodes, concatenating in a subcategory of the ad hoc network called the flying ad hoc network (FANET) [4]. Several novel technologies are proposed: infrastructure-based network (IBN), wireless sensor network (WSN), wireless mesh network (WMN), and flying ad hoc network (FANET) [5,6]. Of these, cellular assistant UAV communication is a novel technology handled by multi-aerial nodes [2,7,8]. The objective of this technology is to utilize the maximum 5G and beyond network quality supported by air-to-air and ground-to-air access points to maintain robustness in the presence of disturbance. Behjati et al. [9] represented several machine learning-based visual line of sight (VLoS) models to estimate the reference signal power and quality according to various mathematical methods. They found that the quality depends heavily upon the distance of the UAV and the GCS, and the flight altitude which leads to the elevation angle. The nonlinear models conquer the linear ones due to their highly accurate prediction. Meanwhile, the authors of [10] proposed a novel MANET protocol called UAV-to-UAV (U2U) plus UAV-to-Infrastructure (U2I) communication and outlined its benefits equipped with WSN and a linear sensor network (LSN) as data collectors, regarding the latency. They implemented a dynamic system to change the communication layers via relays, considering various ratios based on the strength of every node to be exchanged; then compared the average delay, service time, and delivery ratios of several topologies. They claimed the LSNs link to each other with minimum delay when the packets are transmitted in a queue, ordered by a lesser generation time; however, their work did not include any piratical scenarios.

In this research, a newly released U2I communication system is integrated into a WSN topology and is easily installed but responds with significantly less latency, even when transmitting high-quality videos to the ground control station (GCS). In this submission, the UAV's weight and payload type saliently impact the communications utilized, so that in a mini UAV, the communication links are significantly limited, while the danger is also negligible. In contrast, in a large case, communication is critical and if the payload material is a liquid, even more special sensors, such as thermal and chemical pressure sensors, will be needed.

On the other hand, the control system provides several challenges related to stabilizing heavy UAVs, especially when conventional solutions are not effective. Nowadays, electrical UAVs mostly work accurately and have been improved a dozen times; however, they suffer from low flight endurance, and if electrical motors are substituted by thermal engines, the controller surfaces would be changed due to the limits of thermal systems. The authors have previously discussed the limitations and solutions proposed in [11,12]. In this paper, a novel approach is put forth that, despite its rarity in the history of aeronautics, if constructed properly, may stabilize an unmanned aerial vehicle (UAV) for a long period, even in the presence of wind disturbances. More literature reviews could be found in authors' previous

works [11–16]. Briefly, the control strategy presented in this paper—thrust vectoring using flap vanes—offers various advantages over other strategies, including simplicity of servo installation and reduction in the mechanical complexities compared to those of collective pitch propellers because they have fewer movable components; more dynamic stability in attitude control, rather than rotatable hinges or ducts; more efficiency in lift generation based on flap design, as opposed to collective pitch props, which also offer faster response times, and when adjusting the flow direction and magnitude, allows for rapid changes in thrust vectoring, which can be advantageous for applications requiring agile flight control [17]; and finally, properly designed flap vanes can contribute to noise reduction. By controlling the flow patterns and reducing turbulence, flap vanes can help mitigate noise emissions, making them suitable for applications where noise reduction is a critical factor [18].

This paper is organized into five sections, as follows; Section Two discusses UAV communication subsystems; Section Three denotes the dynamic model and control; Section Four compares results, and finally, Section Five concludes the paper.

2. UAV Communication Subsystems

In particular, this paper represents a complete UAV system consisting of various components controlled by the autopilot (AP). The majority of connections are direct and in minor sub-components such as the cameras and lasers, an onboard computer processes the image data and collaborates with the AP in a lower level, as shown in Figure 1. This is elaborated further in Figure 2. Meanwhile, the positioning data are enhanced by the global navigation satellite system (GNSS). Moreover, the power management Unit (PMU) supplies the energy for all subsystems, which not only regulates the thermal energy to two main outputs of 12 V and 24 V but also feeds the power system. This includes the engine control unit (ECU), three internal combustion motors, and an engine monitor to demonstrate and regulate the power system in case of danger, as shown in Figure 1. Furthermore, the UAV is empowered with a redundant radio system. Principally, the command and control radio leads all the communication levels regarding internal subsystems and outperforms the U2I communication, which is further described in Figure 3. Meanwhile, in case of no functionality, the backup radio compensates the essential subsystems to follow up the last waypoints stored in the buffer to return to land in safe mode. The UAV benefits from various advantages of such redundancy, including more reliability and fault tolerance when the principal radio fails, and the second one transmits only critical telemetry to the GCS and vice versa. Additionally, when the primary communication channel experiences problems, the redundant system helps isolate and identify the source of the issue, which facilitates timely maintenance and repairs, reducing downtime and improving overall system availability. In particular, the safety package consists of a flight termination system (FTS) used to manage the whole UAV system in an emergency case, which is simplified to an electrical board that receives and stores the last flight mode and important logs with high frequency. The designed UAV in this paper has a redundant power system, comprising thermal and electrical thrusters. Electric ducted fans (EDFs) that are much smaller only maintain stability during an emergency landing and are inactive when conditions are normal so as not to impact the inlet air stream during the flight, as shown in Figure 3. In emergency circumstances, the FTS automatically activates between six to eleven seconds (to be chosen by the GCS pilots) after the PMU output power faces a sudden decrement and transfers the supply power to batteries located next to the thermal engines, which are adequate for an agile landing. Further, the system is detailed in several subsections, the AP and digital system, the power system, the safety system, and the communication package.

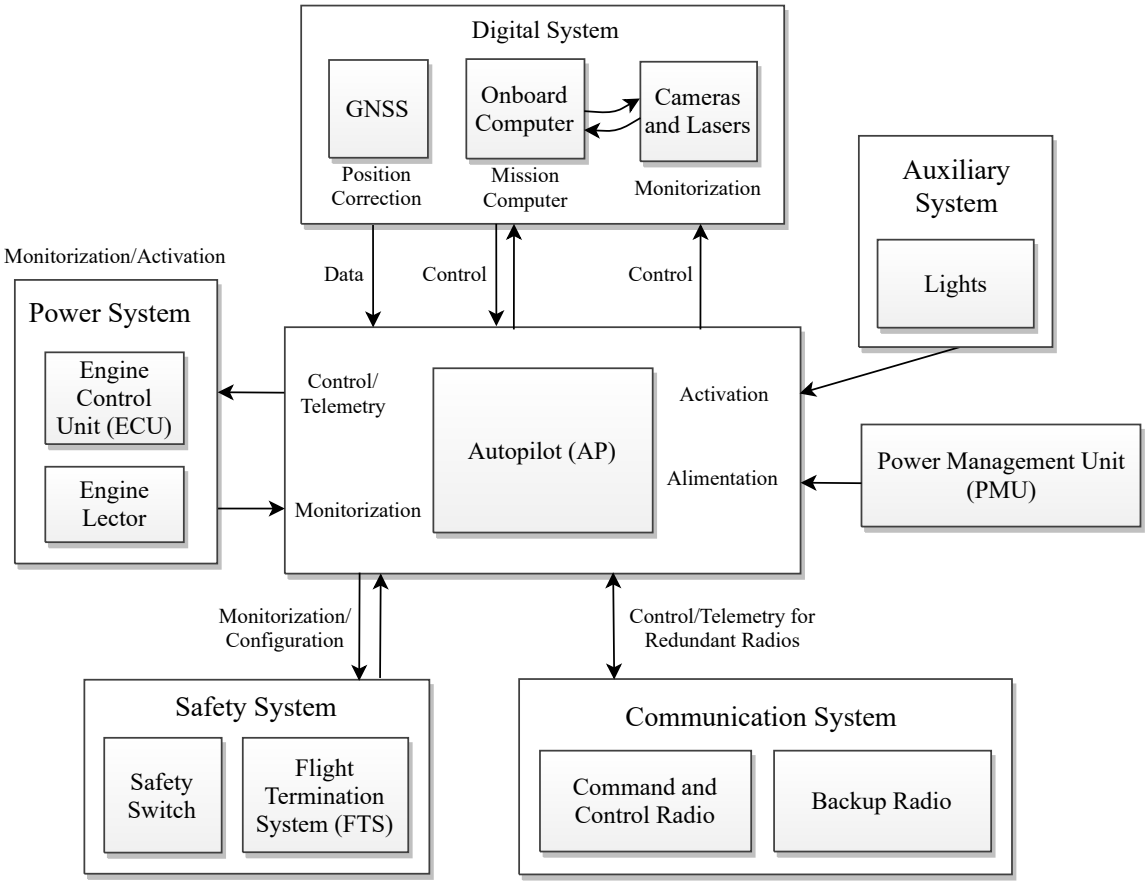

Figure 1. The overall schematic of the UAV system.

2.1. Autopilot (AP) and Digital Systems

The AP configuration system is made up of several layers that receive the actual state traumas of each component equipped with a real-time operating system (RTOS), which analyzes the data in hierarchical series and prohibits the non-critical processes from interfering with the principal functions and performing adequate safety. Moreover, the powerful NXP-based microcontroller board is equipped with a double CPU configuration to parallelize the data logging and calculation process. Meanwhile, the high-level reference data are outputted by the guidance loop that includes a flight navigation system corrected by several references, then, the low-level orientations and estimations are provided by the attitude and heading reference system (AHRS). This imports the position desired values and desired attitude angles and generates the necessary moments for the dynamics system of the UAV, which are later saturated for the actuators. Meanwhile, the controller SW loops are divided into two modes. The guidance corrections are constantly impacting the input reference values in a closed-loop system to regulate the desired outputs. In addition, the digital system contains a Jetson Xavier (https://developer.nvidia.com/embedded/learn/get-started-jetson-xavier-nx-devkit, accessed on 02/05/2023) onboard flight computer to control and analyze the camera output and stream the video in the multi-cast mode for ground observers. Meanwhile, the flight computer is connected directly to the AP, and some of the less important commands, such as navigation enhancement achieved by processing an Extended Kalman Filter (EKF) algorithm, utilizing an additional IMU to compare the data with the AP IMU and recording auxiliary telemetry.

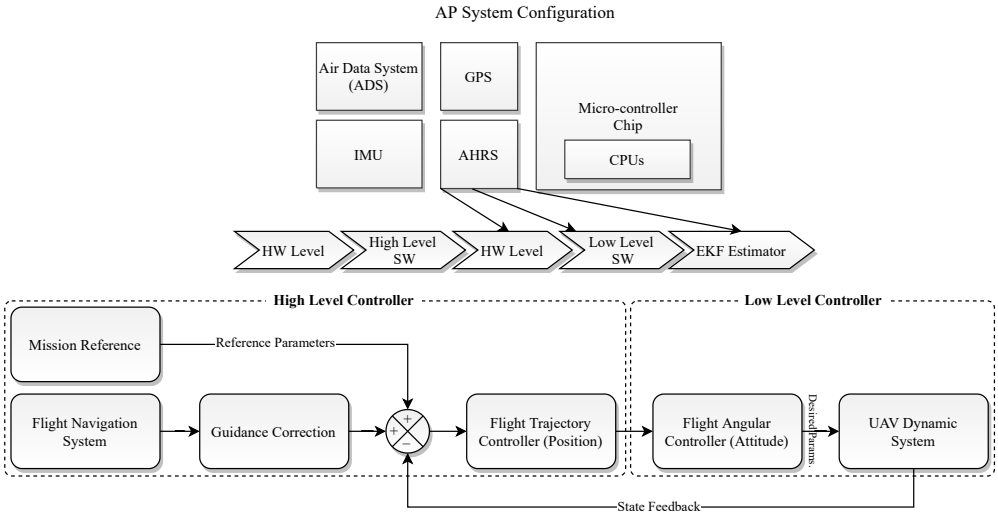

Figure 2. The AP infrastructure and its sub-components.

2.2. Communication System

As mentioned in the introduction, the UAV is empowered by a duplicate communication system in which the principal command and control radio leads the critical commands between the autopilot and other subsystems. Explicitly, two types of communication are considered: an internal communication system and external communication with the GCS (U2I). The internal commands are transmitted by a standard RS-485 serial interface facilitated through an internal switch to receive/send the data with the least latency (less than 5 ms) and to secure the communication system. All the auxiliary connections—namely, video streaming, the onboard computer commands, and the lights—are transmitted through a separate line. Regarding the U2I communication, two antennas are installed on the UAS, as shown in Figure 3, once an omnidirectional antenna plate is utilized for distances lesser than 10 km, which is highly powerful for flights bounded in small areas, but lacks the performance to handle all the data for longer distances. Then, a yagi antenna is installed for distances longer than 10 km.

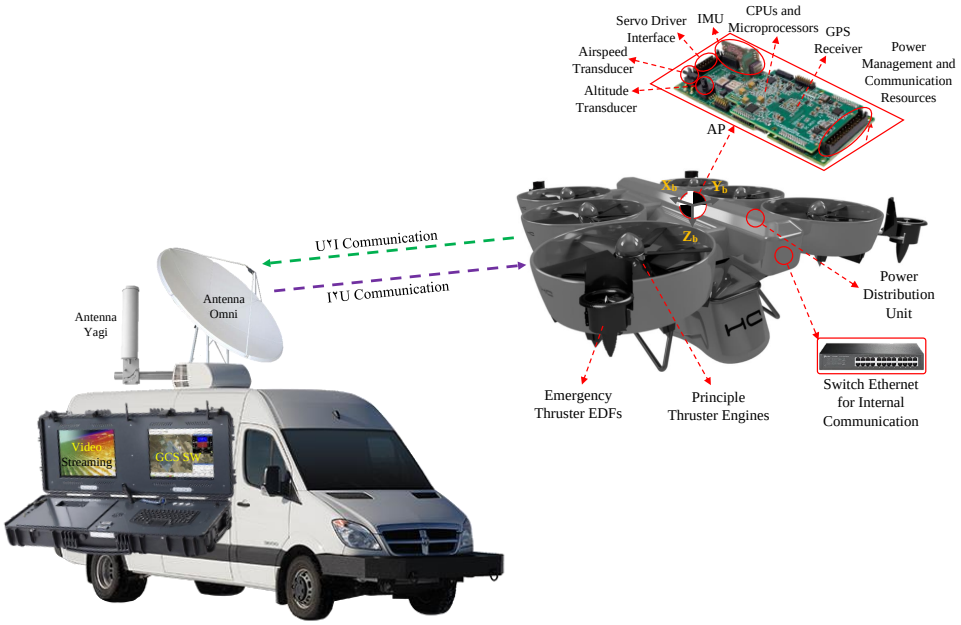

Figure 3. The UAS infrastructure and the communication system.

3. Dynamic System and Control

In order to ensure successful missions for heavy UAVs, the performance of various components and dynamic systems necessitates optimization of the overall reaction to commands, in which minimizing error time is one of the most crucial optimization criteria, i.e., reaching zero error in the higher controller loop and all of its derivatives as quickly as possible. Among the various possibilities, the vertical thermal thrusters regulate the altitude with the least error, benefiting a long flight; however, regarding the horizontal flight, the system suffers in terms of efficiency due to the latent response of motors when the speed controller unit (ECU) commands distinct spin rates in small time intervals. Therefore, one of the most efficient solutions presented is thrust vectoring control (TVC) [19], which aims for both the optimal time and the least error. Typically, TVC consists of sensors and actuators. The sensors provide information on the UAV's attitude and motion, while the actuators adjust the flaps' deflection angle in response to the control signals generated by the autopilot. In particular, in the case of a multi-rotor, the system could be thought of as a multi-ducted-fan (MDF), in which each duct contains a set of lateral and longitudinal flaps corresponding to a servo (the number of flap vanes could vary depending on the design, but the less servos control employed, the less functional issues and AP limitations). In this section, two studies are conducted, focusing on aerodynamic analysis and dynamic stability.

3.1. Aerodynamics Analysis

Optimizing the structure according to aerodynamics principles, TVC performance mostly depends on duct design and outlet duct section; the larger diameter of the outlet section, the greater the lift production and the lower the energy consumption [19], as shown in the form of continuity in Equation (1).

$$\begin{gathered} \rho A_r v_r = \rho A_e v_e \rightarrow v_e = \frac{A_r v_r}{A_e} \\ S_{r,e} = \frac{1}{4}\pi(D_{r,e}^2 - D_s^2) \rightarrow \beta_d = \frac{S_e}{S_r} \end{gathered} \tag{1}$$

where, $\{\}_{r,e}$ refers to the rotor and exhaust prefixes, respectively, A is the section area, S is the air inlet area, which is extracted from the central spinner area, D is the section diameter, v is the airflow velocity, and β_d is duct sectional efficiency. This is experimented with by expanding the exhaust duct area up to 1.7 times. The efficiency is advanced up to 1.3 times [19]. This phenomenon is also observable with flap presence, while the thruster flap vanes intrigue a product drag force that decreases the total thrust.

In addition, the blade profile leads the inlet air impacts directly on the thrust and the power consumption [20]. As shown in Figure 4, during an aerodynamic analysis with a spinning velocity up to 5000 RPM, it was proven that the higher the pitch angle at the blade tip, the more thrust is produced and more power is consumed, referring to the table in Figure 4. Likewise, the pressure drop cowling is doubled when a tip angle is implied. Additionally, the propeller after pressure (prop. aft. pressure) is merely higher with the tip angle, which demonstrates an overall better performance with the tip angle.

	Without Tip Angle	*With Tip Angle*
Thrust Cowling (N)	-542	-932.767
Power Consumption Fan (W)	30074	62603
Pressure Drop Cowling (Pa)	78	195

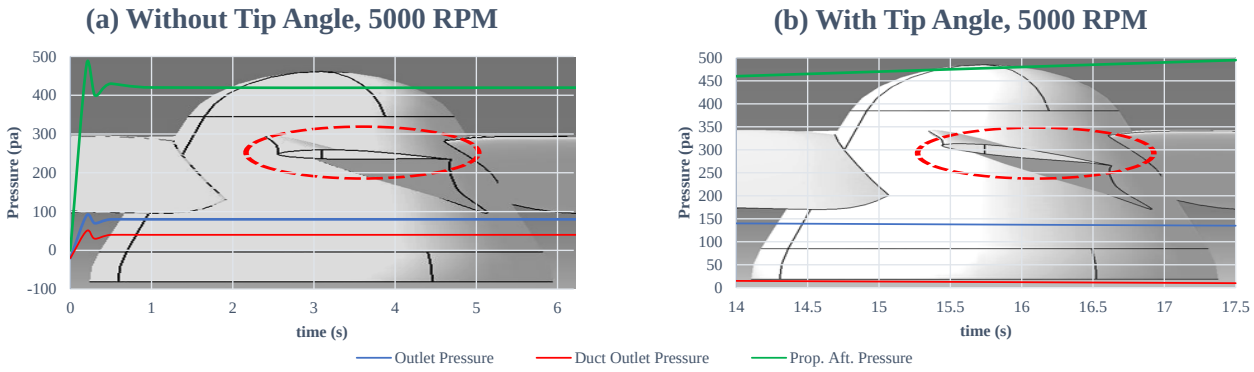

Figure 4. Effects of the blade tip angle on the thrust generation and power consumption.

Furthermore, to have a better thrust, the number of blades has an outstanding effect. To investigate the importance of this and find a suitable blade number, four different types are studied, with 5, 8, 16, and 32 blades, as shown in Figures 5, and 6. during the test, the spinning velocity grew up to 6500 RPM, in which, variables of thrust cowling, pressure consumption, pressure drop cowling, outlet pressure, duct outlet pressure, and the prop. aft. pressure were observed. As shown in the four plots in Figure 5, the more blades installed, the more thrust and power consumption are obtained, while the duct outlet pressure is approximately equal for the propeller with 8 and 32 blades, the two others are lesser which means also a lesser efficiency. This also could be observed in the prop. aft. pressure, which is way higher in the propeller with 8 blades. Additionally, as is shown in the middle table in Figure 5, the thrust cowling arises as the blade number increases, but also accompanies an increment in the power consumption. Therefore, comparing all increments of thrust, power consumption, and pressure drop, in which the first one is desirable and two letters are unwanted, a configuration with eight blades has the best performance that also benefits from the continuous stream at the duct exit, as shown in Figure 5. To understand the numerical data shown in Figures 4 and 5, they are clarified in distinct plots shown in Figure 6.

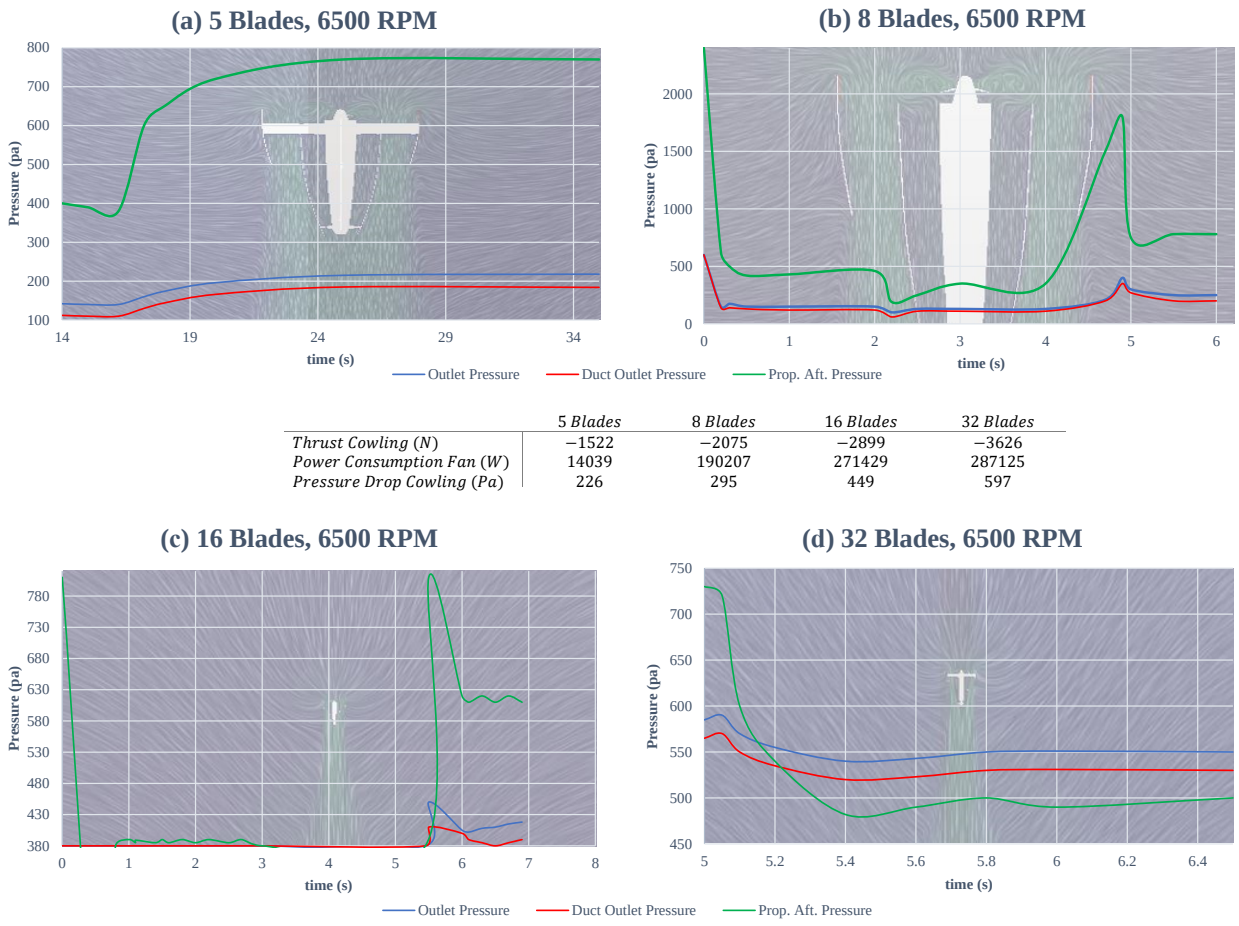

	5 *Blades*	8 *Blades*	16 *Blades*	32 *Blades*
Thrust Cowling (N)	−1522	−2075	−2899	−3626
Power Consumption Fan (W)	14039	190207	271429	287125
Pressure Drop Cowling (Pa)	226	295	449	597

Figure 5. Effects of the blade numbers on the thrust generation and power consumption.

As shown in Figure 6, to observe the best performance among four different types of propellers, four main elements are considered: power, pressure drop, thrust, and the power-to-weight ratio. The power required by the propellers is directly proportional to their thrust, so more power results in higher performance. Conversely, decreasing power reduces the propeller's thrust output. Likewise, increasing thrust is desirable as it enables the multi-ducted fan to lift heavier loads. Then, the power-to-weight ratio represents the amount of power generated by the propeller relative to its weight, in which a higher one indicates greater efficiency and performance. Finally, pressure drop refers to the decrease in air pressure across the propeller as it generates thrust, and a moderate pressure drop is desirable for efficient operation, while an excessive one can indicate an inefficient design. In summary, the only plot that demonstrates a lesser decrement in the pressure drop, although the higher increment in the thrust is the one belonging to the propeller with eight blades. Additionally, in cases of generated thrust, 8 blades and 32 blades functioned better, suggesting that the eight-blade model is best.

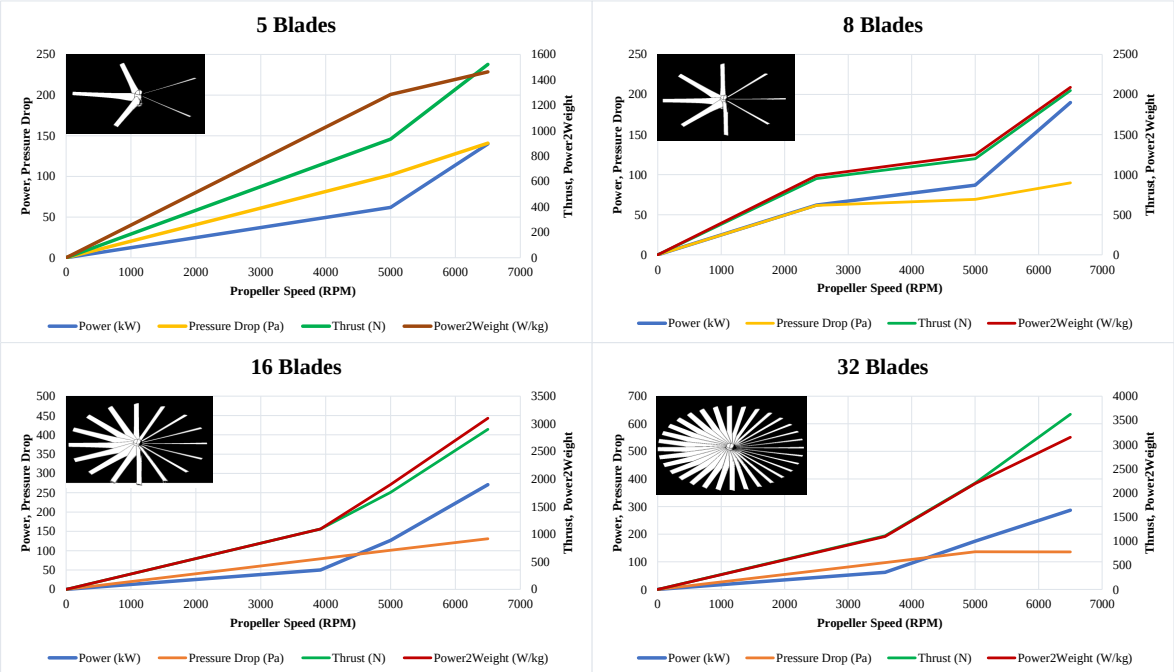

Figure 6. Comparison of the impact of blade number on the power, pressure drop, thrust, and power-to-weight ratio.

According to several experiments [21–23], to achieve more benefits of flap vanes and less production drag, the CoM of the UAV is considered above the rotor section, i.e., the more distance between flap vanes, the more lift forces generated. Therefore, the aerodynamic forces generated by the vanes are described as follows,

$$\begin{aligned} Lift_f &= \tfrac{1}{2}\rho v^2 C_l A_f \\ Drag_f &= \tfrac{1}{2}\rho v^2 C_d A_f \end{aligned} \tag{2}$$

where C_l and Cd are the lift and drag coefficients of the flap vane, and A_f is the effective area toward the aerodynamic forces.

Furthermore, several clues are considered for the flap vanes, since all the vanes are installed at the duct outlet, as shown in Figure 7. Importantly, the longer duct, the higher velocity at the exit; however, it changes the CoM downward, which leads to a reduction in the dynamic stability of the whole system. Therefore, weighting these two factors, a medium height is chosen for the ducts based on experimental analysis. Generally, there are no universal geometry rules for the height of the flap vanes compared to the duct height. This depends on several elements, including the desired thrust vectoring capability, control authority, and aerodynamic performance. Therefore, the height of the flaps or vanes could be determined through aerodynamic analysis, computational fluid dynamics (CFD) simulations, or empirical testing [24]. The objective is to achieve the desired flow control and vectoring characteristics while minimizing flow separation, drag, vane-to-duct proximity, and noise production. In this paper, the height of the flaps is considered as 70% of the ducts to maintain the effectively interact with the flow passing through the duct, improving the lift force generation and controlling the overpassing of the drag forces. Meanwhile, the geometry of the flaps is considered NACA-0015 and their deflection angle is limited to 15°, referring to a previous experiment [12].

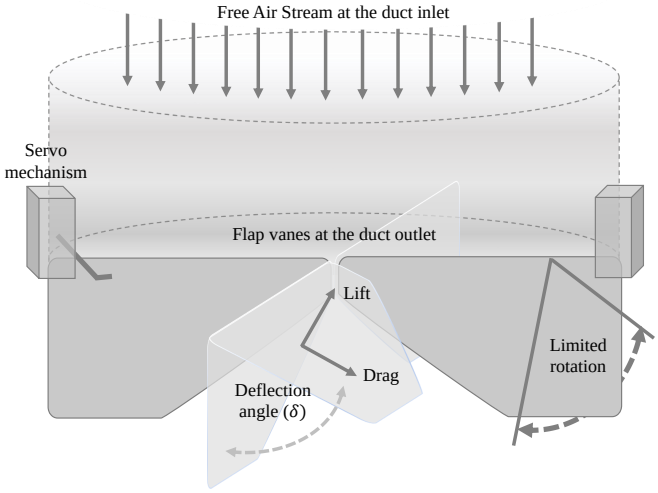

Figure 7. A simple schematic of the duct and the flap vanes installed at the exhaust.

3.2. Control Strategy

A brief equation set of a robust sliding mode TVC is presented in this section for UAV multirotor systems. Generally, hexagonal cases are equipped with more motors and propellers that provide more redundancy and improve control in the case of a motor failure. Thus, hexacopters are thus a well-liked option for heavy-lift applications [25–27]. As mentioned in the introduction, the solution provided in this paper involves installing flap vanes at the engine exhaust, which leads to employing a ducted-fan application. Considering mentioned clues, and the position reference objective for the system, the system's primary state matrix contains $x, y, z, \phi, \theta, \psi$, and their derivatives. Addressing the servos connected to the flap vanes, the whole attitude controller is upon their movements, so if every duct has four flaps at the exit, then four deflection angles per duct will be added to the system's states, which complicates the process. Simplifying the problem, all the desired movements and turns could be summarized into the combination of all ducts, therefore, two flap vanes per duct will be sufficient for easiness in both mechanical and computational processes, which concludes 2 extra angles per duct and overall yields 12 deflection angles as additional states, $\delta_{11}, \delta_{12}, \delta_{21}, \delta_{22}, \delta_{31}, \delta_{32}, \delta_{41}, \delta_{42}, \delta_{51}, \delta_{61}, \delta_{61}, \delta_{62}$ that in δ_{ij}, i represents the duct number and $j \in 1, 2$ demonstrates the latitudinal or longitudinal mode of the vanes, respectively. Thus, knowing the actual and desired states of the drone, two principal modes are considered: a vertical and attitude controller, which leads to the planar controller. Among several sliding modes (SMs) design approaches, including pole placement, Lyapunov-based, optimal control-based, and model predictive methods, we chose a Lyapunov candidate that converges to zero and in a finite time and maintains there. To this end, a suitable sliding surface is defined, containing all attitude variables, which yields;

$$S = \frac{sin(\psi_d - \psi)cos(\theta_d - \theta)cos(\phi_d - \phi) - cos(\psi_d - \psi)sin(\theta_d - \theta)}{cos(\delta_{f,d} - \delta_f)} \tag{3}$$

where, ϕ, θ, ψ are roll, pitch, and yaw angles, respectively, δ_f is the flap vane's deflection angle, and the $\{\}_d$ is the desired value. Conditioning the Lyapunov candidate to be positive–definite, radially bounded, and decreasing along the sliding surface, the function and its derivative of $V(s)$ with respect to time are as follows,

$$\begin{gathered} V(s) = \tfrac{1}{2} S^2 P S \\ \rightarrow dV(s)/dt = \tfrac{1}{2} P(2SdS/dtS + S^2 dS/dt) \end{gathered} \tag{4}$$

where P is a positive–definite matrix, and $dV(s)/dt$ must be always negative to ensure that during the sliding mode, the system is always in a neighborhood of the sliding surface and will converge to the desired state despite any disturbances or uncertainties in the system.

SMC law is defined as $dS/dt = u = -k_1 Sign(S) + k_2 \tanh(k_3 S)$, in which $k_i, i \in 1,2,3$ are constants that determine the rate of convergence to the sliding surface and are obtained through the controller design process. Thus, based on the sliding surface (S),

$$\begin{array}{c} dV(s)/dt = \frac{1}{2}P(2S(-k_1 Sign(S) + k_2 \tanh(k_3 S))S + S^2(-k_1 Sign(S) + k_2 \tanh(k_3 S))) \\ \rightarrow dV(s)/dt = PS^2(k_2 \tanh(k_3 S) - k_1|S|) \end{array} \quad (5)$$

Where $dV(s)/dt$ will be negative whenever $k_2 \tanh(k_3 S) < k_1|S|$, since $\tanh(k_3 S)$ is bounded in $(-1,1)$, and P and the constants $k1, k2, k3$ are all positive. This means that $dV(s)/dt$ is negative for all non-zero values of S when $k_1 > k_2$ and $k_3 < 1$. Therefore, it is proven that $dV(s)/dt$ is always negative and the system converges to a stable equilibrium point, and the control law given by $u = -k_1 Sign(S) - k_2 \tanh(k_3 S)$ guarantees the stability of the closed-loop system. Finally, substituting the earlier expression of S,

$$\begin{array}{c} dV(s)/dt = [(S(e_\psi)C(e_\theta)C(e_\phi) - C(e_\psi)S(e_\theta))/C(e_{\delta_f})]^2 * \\ \frac{P[C(\delta_{f,d})C(\phi_d)C(\delta_f)C(\phi)+S(\delta_{f,d})S(\phi_d)S(\delta_f)S(\phi)+C(\delta_{f,d})S(\theta_d)C(\delta_f)S(\theta)+S(\delta_{f,d})C(\theta_d)S(\delta_f)C(\theta)]}{S(e_\psi)C(e_\theta)C(e_\phi)C(\delta_{f,d})C(\delta_f)C(\phi)+S(\delta_{f,d})S(\phi_d)S(\delta_f)S(\phi)+C(\delta_{f,d})S(\theta_d)C(\delta_f)S(\theta)} \end{array} \quad (6)$$

where $S() \cong sin()$, $C() \cong \cos()$, and e refer to the difference between the desired and actual value. Hence, considering the control law, the attitude controller with respect to the flaps vanes' deflection angle could be rewritten as

$$\begin{array}{c} U_{roll} = I_x(\ddot{\delta}_{f,d} - k_1\dot{e}_\phi) - k_1 \tanh(k_3 S) \\ U_{pitch} = I_y(\ddot{\delta}_{f,d} - k_2\dot{e}_\theta) - k_1 \tanh(k_3 S) \\ U_{yaw} = I_z(\ddot{\delta}_{f,d} - k_3\dot{e}_\psi) - k_2 \tanh(k_1 S) \end{array} \quad (7)$$

where the constants $k_i, i \in 1,2,3$ will be obtained via trial and error during the implementation, and I demonstrates the inertial moment. The Equation (7) states the attitude controller that leads to the position controller.

4. Results

Affirming the TVC algorithm proposed through the control design section, a complete platform is modeled in SolidWorks (https://www.solidworks.com/, accessed on 01/21/2023) and exported to the Gazebo (https://gazebosim.org/, accessed on 02/05/2023) dynamic environment to observe the results, in which several platforms and trajectories were tested to optimize and tune the controller gains. Meanwhile, since the control objective in this research is to stabilize a smooth movement without harsh maneuvers, the best trajectories were ones with a few sharp turns. However, these trajectories are still too long to observe the thermal engines' performance. Hereupon, two routes are suggested in a 300×300 m^2 area, once a circular route and then a rectangular one to be compared thereafter, where both plans are smoothed in corners. Meanwhile, in the first two plots, a realistic simulation is performed to observe the performance of the controller in the long run. The wind noise equation applied to the system is assumed to be a zero mean with a normal distribution (Gaussian), and a differential variance to be integrated with the controller input matrix, as shown in Equation (8),

$$\begin{array}{c} U_t = U_c + N_t \\ N_t = \int_{-\pi}^{\pi} v(cos(\theta) + sin(\theta))\, d\theta \end{array} \quad (8)$$

where the total controller input matrix (U_t) can be determined by the primary controller input (U_c) and the noise function (N_t) based on the constant velocity and the pitch angle of the drone.

In Figure 8, a semicircular route is projected in the horizontal plane, where the desired values are highlighted with the red line, and the actual UAV movements are in blue. The flight plan constantly maintains a 5 m altitude, so the vertical Z axis is not considered. Starting from the waypoint $(0,0)$, the heavy UAV moves with a constant velocity of 5 m/s.

It moves smoothly along the reference trajectory, containing a random noise applied to the controller to examine the performance in the long run as a steady state mode.

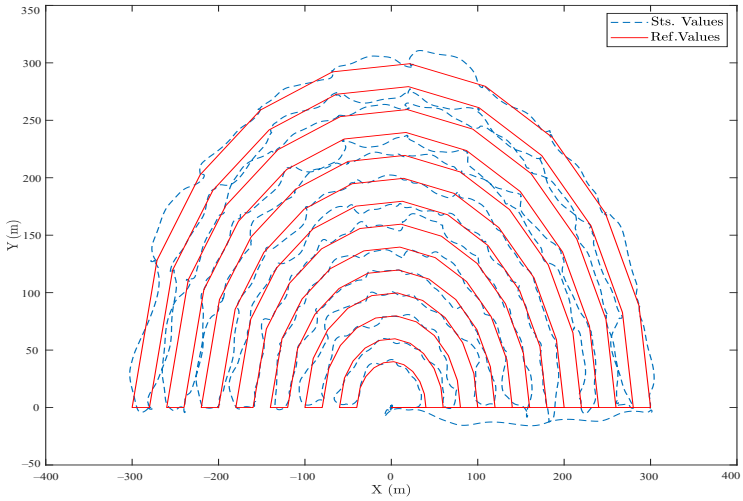

Figure 8. (Realistic Simulation). The horizontal projection of the reference and actual trajectory in the presence of a random wind disturbance and a semi-circular area.

Likewise, as shown in Figure 9, a rectangular trajectory with more direct and longer routes was planned in the presence of a random wind disturbance, and the controller performed better because of lesser radial lines through the trajectory. In both cases, the steady-state error was less than 4%, which proves the efficiency of the SMC presented.

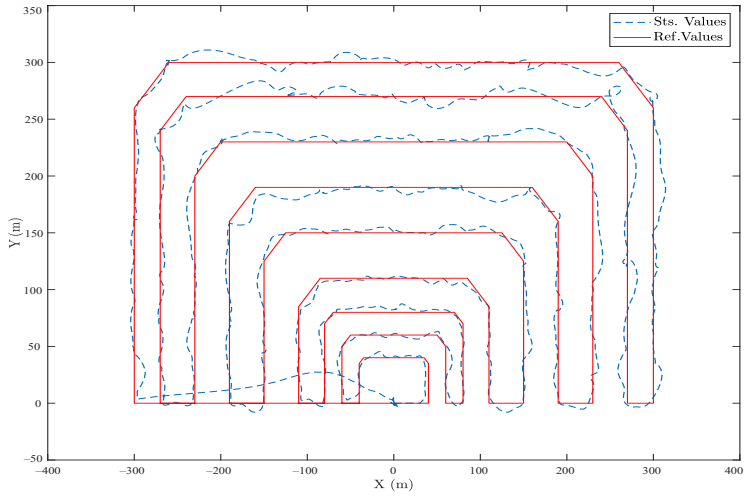

Figure 9. (Realistic Simulation). The horizontal projection of the reference and actual trajectory in the presence of a random wind disturbance and a rectangular area.

Comparing these results to ones obtained by a well-tuned cascade PID controller and in a fully electrical hexacopter that uses propellers as the controller surfaces for attitude, the results are shown in Figures 10 and 11, in which the overall steady-state error is less than 2%. However, in sharp points and during turns, the SMC functioned better. To be precise, the main difference between the two controllers is the use of flap vanes as the controller surfaces, as shown in Figures 8, and 9, which facilitates employing the thermal engines to have a way longer flight autonomy. However, this caused various uncertainties simulated by random noises, as observed in the figures.

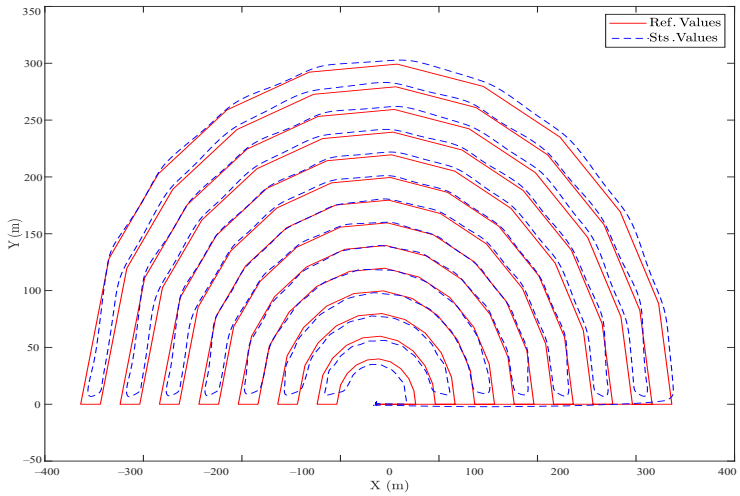

Figure 10. (Ideal Simulation). The horizontal projection of the reference and actual trajectory, in a semi-circular area, which is controlled by a cascade PID controller.

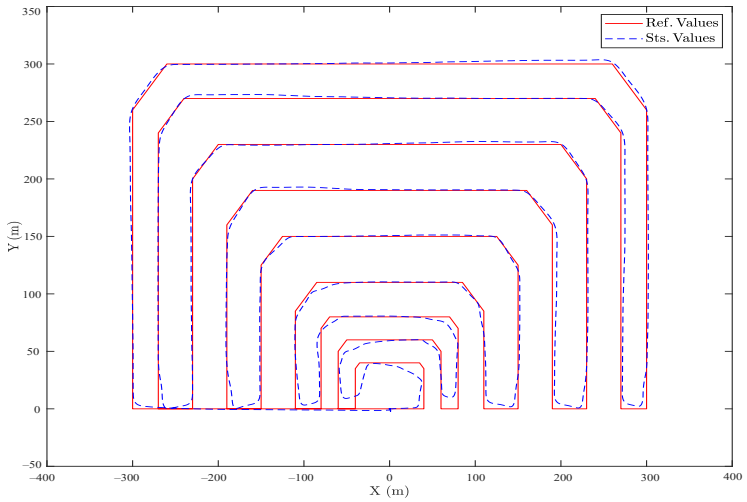

Figure 11. (Ideal Simulation). The horizontal projection of the reference and actual trajectory, in a rectangular area, which is controlled by a cascade PID controller.

5. Conclusions and Future Work

This research addresses theoretical and practical controller platforms, offering novel solutions to the vital control issues that arise when combined with communication problems in the case of multi-UAVs for remote sensing operations. In particular, a multi-ducted fan (MDF) is designed based on several considerations, including long flight endurance and transporting heavy payloads, and to maintain more stability, a hexa-duct casing is developed. Then, utilizing the aerodynamics results, a suitable duct geometry concentrating on the exhaust area is exploited to optimize the number of blades in each propeller, which leads to better performance. The presented system is powered by thermal and redundant electrical engines, in which the thermal ones generate the required thrust during the flight, and the electrical ducted fans (EDFs) survive the MDF in case of emergency. Furthermore, in order to overcome the uncertainties of the thermal thrusters, a novel robust controller based on thrust vectoring control (TVC) is presented. The results demonstrate an acceptable performance for long-range flights when compared to a tuned cascade PID performance for an ideal case, but improving the TVC's theory and practical application is required for the design of industrial platforms. Meanwhile, a redundant communication system is

carried out to support flights with medium and long ranges. Future works will include the analysis of the sensors and the useful outcomes of the enhanced system.

Author Contributions: Conceptualization, M.S.A.I., A.R.R., M.A.L., M.M.A.E.K. and P.C.; Formal analysis, M.S.A.I., A.R.R., M.A.L., M.M.A.E.K. and P.C.; Funding acquisition, P.F.P. and A.R.R.; Investigation, M.S.A.I., A.R.R., M.A.L., M.M.A.E.K. and P.C.; Methodology, M.S.A.I., A.R.R., M.A.L., M.M.A.E.K. and P.C.; Project administration, A.R.R. and P.C.; Software, M.S.A.I., M.A.L. and M.M.A.E.K.; Supervision, A.R.R. and P.C.; Writing—original draft, M.S.A.I.; Writing—review and editing, M.S.A.I. and A.R.R. All authors have read and agreed to the published version of the manuscript.

Funding: This research was supported by the European Commission-funded program WILDHOPPER, under H2020 Grant Agreement 880642.

Institutional Review Board Statement: Not applicable.

Informed Consent Statement: Not applicable.

Data Availability Statement: Simulation recorded videos could be found in (https://shorturl.at/uEY47).

Acknowledgments: We would like to thank the University of Carlos III, campus Leganes, Madrid, for performing laboratories and hangers through our research. We would also like to thank our colleagues at Drone Hopper for their support during the project. This work was conducted to complete the doctoral project of Mohammad Sadeq Ale Isaac, with the support of Professor Pascual Campoy and Ahmed Refaat Ragab.

Conflicts of Interest: The authors declare no conflicts of interest.

Abbreviations

The following abbreviations are used in this manuscript:

AP	Autopilot.
UAV	Unmanned Aerial Vehicle.
UAS	Unmanned Aerial System.
GCS	Ground Control Station.
SMC	Sliding Mode Controller.
TVC	Thrust Vectoring Control.
FANET	Flying ad hoc Network.
IBN	Infrastructure-Based Network.
WSN	Wireless Sensor Network.
WMN	Wireless Mesh Network.

References

1. Tzu, S. The art of war. In *Strategic Studies*; Routledge: Abingdon, UK, **2008**, 63–91.
2. Zeng, Y.; Zhang, R.; Lim, T.J. Throughput maximization for UAV-enabled mobile relaying systems. *IEEE Trans. Commun.* **2016**, *64*, 4983–4996.
3. NATO. *Minimum Training Requirements for Unmanned Aircraft Systems (UAS) Operators and Pilots*; Standardization Agreement 4670; NATO: Brussels, Belgium, 2019.
4. Castrillo, V.U.; Manco, A.; Pascarella, D.; Gigante, G. A Review of Counter-UAS Technologies for Cooperative Defensive Teams of Drones. *Drones* **2022**, *6*, 65.
5. Nawaz, H.; Ali, H.M.; Laghari, A.A. UAV communication networks issues: A review. *Arch. Comput. Methods Eng.* **2021**, *28*, 1349–1369.
6. Li, B.; Fei, Z.; Zhang, Y. UAV communications for 5G and beyond: Recent advances and future trends. *IEEE Internet Things J.* **2018**, *6*, 2241–2263.
7. Mozaffari, M. Wireless Communications and Networking with Unmanned Aerial Vehicles: Fundamentals, Deployment, and Optimization. Ph.D. Thesis, Virginia Tech, Blacksburg, VA, USA, 2018.
8. Li, B.; Fei, Z.; Dai, Y.; Zhang, Y. Secrecy-optimized resource allocation for UAV-assisted relaying networks. In Proceedings of the 2018 IEEE Global Communications Conference (GLOBECOM), Abu Dhabi, United Arab Emirates, 9–13 December 2018; IEEE: Piscataway, NJ, USA, 2018; pp. 1–6.
9. Behjati, M.; Zulkifley, M.A.; Alobaidy, H.A.; Nordin, R.; Abdullah, N.F. Reliable aerial mobile communications with RSRP & RSRQ prediction models for the Internet of Drones: A machine learning approach. *Sensors* **2022**, *22*, 5522.

10. Jawhar, I.; Mohamed, N.; Al-Jaroodi, J.; Agrawal, D.P.; Zhang, S. Communication and networking of UAV-based systems: Classification and associated architectures. *J. Netw. Comput. Appl.* **2017**, *84*, 93–108.
11. Isaac, M.S.A.; Ragab, A.R.; Garcés, E.C.; Luna, M.A.; Peña, P.F.; Cervera, P.C. Mathematical Modeling and Designing a Heavy Hybrid-Electric Quadcopter, Controlled by Flaps. *Unmanned Syst.* **2022**, *10*, 241–253.
12. Ale Isaac, M.S.; Luna, M.A.; Ragab, A.R.; Ale Eshagh Khoeini, M.M.; Kalra, R.; Campoy, P.; Flores Peña, P.; Molina, M. Medium-Scale UAVs: A Practical Control System Considering Aerodynamics Analysis. *Drones* **2022**, *6*, 244.
13. Luna, M.A.; Ale Isaac, M.S.; Ragab, A.R.; Campoy, P.; Flores Peña, P.; Molina, M. Fast Multi-UAV Path Planning for Optimal Area Coverage in Aerial Sensing Applications. *Sensors* **2022**, *22*, 2297.
14. Ragab, A.R.; Isaac, M.S.A.; Luna, M.A.; Flores Peña, P. WILD HOPPER Prototype for Forest Firefighting. *Int. J. Online Biomed. Eng.* **2021**, *17*.
15. Isaac, M.; Naghash, A.; Mirtajedini, S. Control and guidance of an autonomous quadrotor landing phase on a moving platform. In Proceedings of the IMAV Annual Conference of Autonomous Vehicles, Madrid, Spain, 1–4 October **2019**; Volume 29.
16. Peña, P.F.; Ragab, A.R.; Luna, M.A.; Isaac, M.S.A.; Campoy, P. WILD HOPPER: A heavy-duty UAV for day and night firefighting operations. *Heliyon* **2022**, *8*, e09588.
17. Miwa, M.; Shigematsu, Y.; Yamashita, T. Control of ducted fan flying object using thrust vectoring. *J. Syst. Des. Dyn.* **2012**, *6*, 322–334.
18. Zhao, Y.; Tian, Y.; Wan, Z. Aerodynamic Characteristics of a Ducted Fan Hovering and Transition in Ground Effect. *Aerospace* **2022**, *9*, 572.
19. Urban, D.; Kusmirek, S.; Socha, V.; Hanakova, L.; Hylmar, K.; Kraus, J. Effect of Electric Ducted Fans Structural Arrangement on Their Performance Characteristics. *Appl. Sci.* **2023**, *13*, 2787.
20. Eltayesh, A.; Castellani, F.; Burlando, M.; Hanna, M.B.; Huzayyin, A.; El-Batsh, H.M.; Becchetti, M. Experimental and numerical investigation of the effect of blade number on the aerodynamic performance of a small-scale horizontal axis wind turbine. *Alex. Eng. J.* **2021**, *60*, 3931–3944.
21. Jacobsen, E.B. Modelling and Control of Thrust Vectoring Mono-copter, *Master's Thesis in Control and Automation, Aalborg University.* **2021**. p. 89.
22. Abrego, A.I.; Bulaga, R.W.; Rutkowski, M. Performance study of a ducted fan system. In Proceedings of the American Helicopter Society Aerodynamics, Acoustics and Test and Evaluation Technical Specialists Meeting, San Francisco, CA, USA, 23–25 January **2002**.
23. Muehlebach, M.; D'Andrea, R. The flying platform–a testbed for ducted fan actuation and control design. *Mechatronics* **2017**, *42*, 52–68.
24. Vehi Perich, M.d. Ducted fan propulsion system study for ONAerospace eVTOL; *Bachelor's Thesis, Polytechnic University of Cataluyna.* February **2023**.
25. Sharma, P.; Atkins, E. Experimental investigation of tractor and pusher hexacopter performance. *J. of Aircraft.* **2019**, *56(5)*, 1920–1934.
26. Reddy, R.S.; Dash, S.K. Design and Analysis of a Hexacopter for Heavy Lift Applications. *Int. J. Eng. Res. Technol* **2014**, *3*, 1352–1357.
27. Manal Shaban, E.; Merzban, M.; AM Khalaf, A.; Fathy Aly Hamed, H. Comparison of various Control Techniques Applied to a Quadcopter. *J. of Advanced Engineering Trends* **2023**, *42(2)*, 233–244.

9.4 Publication III

Ale Isaac, M.S., Flores Peña, P., Luna, M.A., Ragab, A.R., and Campoy, P. (2024). *Sensing and Control Integration for Thrust Vectoring in Heavy UAVs: Real-World Implementation and Performance Analysis.* Unmanned Systems, 23(12), p.5561, doi:10.1142/S2301385025500396.

OPEN ACCESS
Unmanned Systems (2025)

DOI: 10.1142/S2301385025500396

UNMANNED SYSTEMS
https://www.worldscientific.com/worldscinet/us

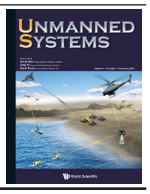

Sensing and Control Integration for Thrust Vectoring in Heavy UAVs: Real-World Implementation and Performance Analysis

Mohammad Sadeq Ale Isaac [*,¶], Pablo Flores Peña [†,§], Marco Andrés Luna [*], Ahmed Refaat Ragab [†,‡,§], Pascual Campoy [*,‖]

[*]*Computer Vision and Aerial Robotics Group, Centre for Automation and Robotics (CAR), Universidad Politécnica de Madrid (UPM-CSIC), 28006 Madrid, Spain*

[†]*Department of Electrical Engineering, University Carlos III of Madrid, 28919 Leganés, Spain*

[‡]*Department of Network, Faculty of Information Systems and Computer Science, October 6 University, Giza 12511, Egypt*

[§]*Drone-Hopper Company, 28919 Leganés, Spain*

Unmanned Aerial Vehicles (UAVs) have garnered significant attention among researchers due to their versatility in diverse missions and resilience in challenging conditions. However, electric UAVs often suffer from limited flight autonomy, necessitating the exploration of alternative power sources such as thermal engines. On the other hand, managing thermal engines introduces complexities and internal uncertainties into the system. In this paper, an Adaptive Robust attitude controller (ARAC) is proposed to address these challenges by drawing inspiration from helicopter solutions while minimizing mechanical intricacies. Specifically, the designed algorithm employs Thrust Vector Control (TVC) for an industrial heavy Multi-Ducted Fan (MDF), known for its superior static stability compared to conventional ducted fans. Subsequently, an integrated flap vanes system is positioned at the exhaust of the ducts for precise attitude control, effectively removing unwanted yaw moments associated with traditional propellers. This research builds on prior authors' works to establish a proper mathematical and aerodynamic model. Also, using former simulation results to conduct real flight experiments aimed at enhancing TVC functionality. The findings highlight the effectiveness of this approach for heavy UAV applications. It is worth noting that the practical value of this research lies in its potential to significantly extend flight autonomy supplied by thermal engines and improve the resilience of UAVs in challenging real-world missions. This is particularly achievable provided that the design of flap vanes aligns closely with the dimensions of the duct system, offering a promising solution to a critical engineering challenge in the field of UAV technology.

Keywords: Adaptive sliding mode control; thrust vector control; attitude control; servo flap sensing; heavy UAVs; multi-ducted fan.

Received 12 November 2023; Revised 1 April 2024; Accepted 1 April 2024; Published 4 June 2024. This paper was recommended for publication in its revised form by editorial board member, Swee King Phang.
Email Addresses: ¶*mo.aleisaackhoueini@upm.es*, ‖*pascual.campoy@upm.es*
‖ Corresponding author.

1. Introduction

During the 20th century, the concept of unmanned Aerial Vehicles (UAVs) or drones emerged as aircraft that operated without human pilots or crew members on board. Originally, UAV or Remotely Piloted Aerial Vehicles (RPAV) was coined and developed for military aviation, which became widely used to describe such aircraft. However, its application has since expanded beyond the military and into civilian domains. To encompass the complexities of the entire system, the terminology evolved from UAV to Unmanned Aerial System (UAS). The UAS concept incorporates not only the UAV itself but also the Ground Control Station (GCS), communication systems, and networking components [1]. The Federal Aviation Administration (FAA) and the United States Department of Defense (DOD) adopted the terms UAS and Remotely Piloted Aerial System (RPAS) in 2005 to outline their UAS roadmap until 2030 [2]. UAVs can be operated remotely through human piloting or can possess varying degrees of autonomy with the assistance of an Autopilot (AP), ranging from semi-autonomous to fully autonomous capabilities [3, 4].

Additionally, a Ducted Fan (DF) or Ducted Propeller (DP) refers to a mechanical fan or propeller installed inside a cylindrical duct or shroud. This configuration, as studied in the previous research [5, 6], allows for the enhancements to create a Multiple Ducted Fan (MDF) system. The MDF system incorporates a coherent geometry that optimizes the arrangement of DFs to generate the necessary thrust force during flying missions. Depending on their installation direction, DFs can function as longitudinal or vertical thrusters. To meet specific output requirements, DFs undergo optimizations based on factors such as inlet arc shape, duct wall length, and outlet-to-inlet area ratio. These considerations ensure the DFs are precisely designed for optimal performance and efficiency. The integration of DFs and the utilization of MDF systems contribute to advancements in aerospace engineering, enhancing thrust generation and maneuverability in various flight scenarios.

UAVs have garnered great attention from researchers thanks to their wide-ranging applications and exceptional performance capabilities. These versatile aircraft have found extensive utility in both civil and military domains, delivering groundbreaking solutions while minimizing risks for operators. In the civil sector, UAVs have proved invaluable in aerial photogrammetry and videography, cultivation analysis and crop monitoring, firefighting, search and rescue operations, infrastructure inspection, and environmental monitoring. In the military realm, they have diverse applications such as surveillance and reconnaissance, target acquisition and object tracking, battlefield support, and combat operations [7]. Furthermore, the emergence of Vertical Takeoff and Landing (VTOL) systems, particularly the promising MDFs, has added another dimension to their attractiveness, offering enhanced agility, stability, and versatility for a wide range of applications. Specifically, heavy clusters of UAVs are spread in myriad applications such as firefighting, large package delivery, agricultural protection, passenger transportation, communicative portable stations, and military patrol. Attending such beneficial aerial systems in the industry requires high stability and safe flights, especially in the case of human carriage. Meanwhile, to satisfy the mentioned applications, long-range and high-endurance platforms will be aimed; consequently, heavy drones necessitate quite a lot of power to serve long missions.

UAVs can be classified based on various factors and their extensive usage. These classifications include weight-based, mission-based, flight endurance or range-based, payload-based, and more. Among these, the weight and payload capacity of UAVs plays a significant role in their categorization. According to research in [8, 9], UAVs are categorized as micro, small, medium, and large-scale platforms. In the European Union aviation safety regulations, weight classifications are defined as Class A1 (less than 900 g), Class A2 (less than 4 kg), Class A3 (less than 25 kg), and additional categories for weights exceeding 25 kg. Similarly, the global NATO-STANAG 4670 UAS category classifies UAVs as nanoscale (less than 250 g), microscale (less than 2 kg), small scale (less than 25 kg), medium scale (less than 150 kg), and large scales (more than 150 kg) [10, 11]. Denoting that larger UAVs offer the advantage of carrying heavier payloads over longer distances, While mini-scale UAVs have considerable limitations in terms of flight endurance and payload capacity.

Improving a DF to MDF has several merits, including much more static and dynamic stability due to moving the COG toward a point in the middle of DFs and higher thrust power to carry heavier payloads. To this end, some research focused on controlling MDFs, as the study outlined in [12], researchers focused on a triangular EDF system, focusing on TVC as a critical stabilizing factor. Employing a linear cascade controller, they achieved stable hover performance with minimal disruptions, efficiently regulating angular rates at high frequencies. The controller was split into two components: an onboard gyroscope for real-time angular rate measurement and an offboard calculation module for position and attitude control. Communication with the PX4 autopilot ensured coordination. Notably, mounting the motor controller (YGE 90HV) at the exit nozzle provided cooling through airflow. However, this work primarily relied on controlled settings with motion capture, potentially limiting real-world applicability. Offline primary controller components posed vulnerability to delays or data loss due to connection issues. Battery reliance led to constrained operational times for energy-intensive DFs. While hover

stability was validated, further exploration of diverse flight maneuvers remains a promising avenue.

In a recent study [13], a comprehensive backstepping control approach was introduced, focusing on the trajectory tracking control of a multirotor. This control strategy addressed several intricate challenges, including cascade constraints, constrained actuator dynamics, and complex unknowns. It achieved robustness by integrating sliding mode and dynamics surface control techniques. The researchers decomposed the entire system into five cascade subsystems connected through intermediate nonlinearities. To deal with complex unknowns, they employed adaptive compensators, and through Lyapunov synthesis, they verified minimal errors. While this work provides valuable insights into control methodologies, its application has been primarily limited to simulations and electrical motors.

However, the study in [14] placed a strong emphasis on model predictive and robust model predictive algorithms in the context of DF applications, particularly when dealing with internal uncertainties and external disturbances. Their approach involved addressing a nonminimum phase nonlinear system dynamics and deploying a compound controller designed for both trajectory tracking and attitude control. Similarly, the research presented in [15] delved into the development of a TVC algorithm tailored for a tilt-rotor UAV, even in the presence of actuation constraints. Their simulation methodology prominently featured an infinity curve for applying maximum tilt angles to achieve precise objective tracking. Furthermore, the work in [16] showcased a novel integration of the backstepping technique and fast terminal sliding mode control to govern yaw and tilting angles. These angles were accurately estimated using a robust adaptive backstepping controller within the context of a position controller for path-tracking applications. It is important to note that, similar to previous studies, these investigations have primarily focused on electrical power supply and simulation results.

Whereas in distinct research [17], a comprehensive simulation methodology for a Tandem Ducted Fan (TDF) system is presented, encompassing intricate considerations of aerodynamic interactions and the mathematical underpinnings of flap vanes. This simulation was realized using MATLAB Simulink, offering a versatile and modular framework for TDF analysis. Delving into the intricacies of airflow dynamics within the duct, the study scrutinized the destabilizing effects on the nose-down pitching moment during the transition from edge-wise to axial flight modes at low velocities. By fine-tuning the deflection angle of the vanes, the researchers reported enhancements in transient behavior. This work contributes significantly to theoretical insights and aerodynamic investigations of MDFs, especially those akin to the Urban Aeronautics X-Hawk and the 29-inch UAV, which served as inspirational sources; however, its real-world applicability might necessitate further implementation beyond the confines of the simulation environment.

In recent studies, [14, 18–21], researchers have extensively explored enhancing the control strategies of Single Ducted Fans (SDFs) using Adaptive Model Predictive Control (AMPC) and an Adaptive Fault-Tolerant approach. The primary objective has been to elevate the performance of SDFs in both transient and cruise modes. The first study introduces a novel control mechanism designed for a specialized DF aerial robot, focusing on fault tolerance against partial actuator failure. This mechanism integrates an identified state-space model in the frequency domain, an adaptive loop coupled with an estimator, and a reconfigurable adjustment law. This combination allows for the estimation and compensation of varying degrees of failure. The effectiveness of the proposed algorithm is validated through both theoretical simulations and real-time flight experiments. The second study explores an AMPC strategy tailored for engine-driven DF lift systems. This approach utilizes a global network model, trained offline with data from a general mean value engine model for two-stroke aviation engines. The constructed network serves as an adaptive, robust, and efficient prediction model for model parameters. The efficiency of this approach is demonstrated through numerical simulations depicting a vertical take-off thrust preparation process for the DF lift system. While these studies demonstrate the controller's effectiveness in stabilizing drones during real flights, a significant challenge remains in dealing with the inherent dynamics and instability characteristic of single DFs. While, this paper addresses the stability issues by introducing a hexa model, co-located to work in conjunction with the SDF. The combined configuration is designed to compensate for both transient and cruise flight dynamics. Additionally, the proposed approach aims to enhance the payload capacity, a task challenging to achieve with single DFs alone.

In a related study, discussed in [22], researchers focused on an MDF flying object consisting of two EDFs connected by a vertical wooden bar. The unique feature of their design was the rotatable installation of the EDFs, functioning like a hinge to induce roll, pitch, and yaw rotations. Employing a PD controller initially, the system encountered a persistent steady-state error, prompting the integration of an integral term, which effectively mitigated this error. While the effort showcased valuable insights, the positioning of the battery and equipment on the wooden bar introduced an imbalance by shifting the COG to a higher point relative to the EDF plane. This configuration likely contributed to the observed steady-state error. Furthermore, the study highlighted a limitation in endurance, attributed to the low battery capacity not suitable for powering two EDFs.

However, in another research [23], the authors proposed a novel TDF for drones, featuring small EDFs and larger TDFs controlled by a robust static H_∞ output feedback technique. The controller effectively stabilizes and decouples body-frame velocities and yaw angle states, even in the presence of disturbances and EDF tilting. The study also addresses time delays caused by open-loop gain roll-off using system identification. However, the approach's applicability to industrial platforms is limited due to component disharmony and complexities associated with decoupling.

In a relevant study [24], a compact MDF was introduced, utilizing two DFs for vertical stabilization and two EDFs for attitude control. The study employed a structured multiloop feedback attitude controller based on H_∞ synthesis, encompassing a low-order attitude controller and multiloop feedback for cross-attitude decoupling and reference signal tracking. Controller parameter tuning was conducted using a nonsmooth optimization method. Although the approach demonstrates promise, further investigation is recommended to address significant uncertainties, disturbances, or actuator/sensor faults, as also asserted by the authors.

Moreover, the advancements in intelligent health management methods for complex mechanical gear systems in DFs can significantly enhance their operational reliability. The work done in [25, 26], which employs a digital twin-driven methodology for gear surface degradation assessment, provides valuable insights into predictive maintenance and real-time system assessment. The ability to automatically establish high-fidelity digital twin models that reflect dynamic responses is akin to the development of digital twins for DF systems, where real-time modeling can be crucial for precise attitude control and stability. The use of transfer learning and advanced signal processing methods, as explored in their research, can have parallels in the development of control algorithms, ensuring efficiency even in the presence of wear-related changes. Furthermore, their emphasis on the broader applicability of digital twin techniques in industrial practices aligns with enhancing DF control methods for heavy UAV applications.

On the other hand, to choose appropriate engines and meet power requirements, a delicate balance must be struck when selecting the engine and fuel type. As discussed in [27], combustion engines remain a popular choice for both commercial and private applications, despite their lower efficiency compared to more reliable electrical counterparts. Electric power supply units (PSUs) boast high density but are sensitive to water or vapor and exhibit limited recharge cycles, making them less suitable for large-scale flying drones. Hydrogen fuel cells (HFCs) offer renewable energy with remarkable endurance, producing 150 times the energy of Li-Po batteries in fixed-wing aircraft. However, their reliance on a rapid-response hydrogen setup limits their affordability. Uninterruptible power sources (UPS) via cable are effective for near-ground tests and emergency landings but impractical for long-range flights [28]. Considering the advantages and disadvantages of various power sources in terms of engine efficiencies, fossil fuels emerge as a concentrated and cost-effective choice, easily accessible and capable of providing substantial energy for extended flight durations. In contrast, a myriad of engine types can be considered, powered by chemical, electrical, and nuclear energy. These include heat engines, electrical engines, disk engines, nuclear propulsive, hybrid propulsive, jet propulsive, and ion propulsive engines [29]. Electric engines demonstrate rapid acceleration and operational efficiency but require a continuous power supply, making them unsuitable for prolonged flights. Heat engines encompass both internal and external combustion engines, featuring variations such as piston, rotary, jet, and ion engines. The piston engine, particularly in two- and four-stroke configurations, is conventional and distributed in Wankel, dual-fuel, and other setups. While these engines exhibit high power-to-weight ratios, they tend to be noisier than electric alternatives. Focusing on internal combustion engines, two- and four-stroke categories stand out. The latter, despite having a lower power-to-weight ratio than its counterpart, proves more compatible with heavy drones due to distinct lubrication setups that eliminate the oil-fuel mixture. This advantage allows four-stroke engines to operate effectively at higher altitudes. While they are slightly heavier due to additional moving components, their reliability and economic efficiency make them a preferable choice among various engine types. In conclusion, this paper has opted for an industrial internal combustion engine arrangement, employing three engines consecutively to drive the six propellers. Each pair of propellers is dedicated to a thermal engine, ensuring a continuous rotation to maintain equal thrust. This distribution is selected to address the inherent delay thermal engines face in responding to different rotation requirements compared to electrical engines. Despite this drawback, if all motors consistently receive the same command with a simultaneous and constant change, the delay becomes negligible. Moreover, the system incorporates an industrial Engine Control Unit (ECU) to effectively regulate the parameters of the engines.

Addressing thermal engine instabilities, this paper focuses on the control solution to achieve extended autonomy while regulating uncertainties, building upon the authors' previous research presented in [8, 9, 30]. In this section and prior research, a variety of control solutions for DF applications have been explored, encompassing nonlinear methods, [14–16, 24, 27, 31–33], linear approaches like Proportional-Integral-Derivative (PID) control (PID) or cascade PIDs [12, 17, 22, 34], feedback linearization [23], and linear–quadratic regulator [35]. However, it is

noteworthy that there have been limited industrial efforts directed toward real-flight implementations of TVC for heavy multi-UAVs. The scarcity of such initiatives can be attributed to the challenges of translating theoretical techniques into practical reliability due to the numerous unknown uncertainties inherent in real-world scenarios, leading the industry to rely heavily on conventional PID controllers. This paper addresses this gap by introducing a fine-tuned compound controller, previously deployed on smaller platforms like the Fan Hopper [8], and enhancing its performance against external nonlinearities.

Building upon the comparison results discussed in [8, 9, 30], this paper distinctly focuses on real-world experiments, culminating in a final simulation step with fine-tuned controller parameters, comparing the Adaptive Robust attitude controller (ARAC) results to one conducted by a well-tuned PID controller. The contributions of this paper can be summarized as follows:

Refinement of Mathematical Model: The mathematical model previously introduced in [30] for a similar drone application is refined and optimized specifically for heavy drone applications. This refinement contributes to a more accurate representation of the system dynamics.
Enhancement of Robust Controller: The robust controller presented in [9] undergoes improvement through parameter tuning for both stationary and real flights on an industrial autopilot application. Additionally, an adaptive component is integrated into the controller, enhancing system reliability against internal nonlinearities and external disturbances.
Real Flight Conduct: After meticulous parametric refinement of the adaptive controller introduced in [8], taking into account fluid payload uncertainties impacting the overall UAV mass, the modeled system was subjected to real flight experiments. This phase aimed to assess the controller's performance in practical scenarios and identify areas for further enhancement.

By concentrating on these three key aspects, this paper advances the field by addressing experimental challenges and refining the ARAC methodologies for enhanced performance in real-world applications. The term ARAC embodies the fusion of two distinct systems: the adaptive controller, comprehensively discussed in [8], and the robust controller, detailed in [9]. While the latter paper showcases the ability to maintain the stability of a medium-scale hexa DF system, particularly when carrying a liquid payload that introduces nonlinearities and additional degrees of freedom during maneuvers or release phases, the former paper focuses on reinforcing the controller system against external uncertainties, such as wind disturbances. This paper takes a step further by integrating these two algorithms, refining the controller parameters, and constructing a robust algorithm capable of mitigating both internal and external uncertainties. This amalgamation aims to enhance the overall performance of the ARAC, offering a practical solution to challenges posed by various operational conditions.

The proposed solution involves the implementation of an ARAC to actuate the servo flaps on the control surfaces, improving the regulation of the multi-ducted fan's attitude. To achieve this goal, the robust algorithm harnesses the power of Sliding Mode Control (SMC) to counteract wind disturbances effectively. While SMC is a well-established methodology, this research introduces vital adaptations and refinements specifically tailored to confront the unique challenges experienced in real-flight applications. This endeavor entails sophisticated modifications aimed at mitigating the inherent complexities associated with a system of this magnitude and nature. Moreover, the adaptive aspect of this approach plays a pivotal role in managing internal nonlinearities induced by combustion engines, effectively addressing issues like undesired vibrations that are, at times, inevitable in such engine operations. Additionally, the exploration of TVC within this framework is driven by the need to provide a stable attitude controller among a few possible solutions for UAVs supplied by thermal engines. While TVC is not a novel concept itself, this presents innovative strategies for applying TVC to achieve optimal attitude control, particularly using flap vanes.

2. Sensor Integration Review

This paper consolidates the outcomes of three prior research endeavors conducted by the authors, offering a concise review to elucidate the progression of work and the evolution of prototypes in each study. Commencing with an exploration into the domain of MDFs, our initial undertaking involved the meticulous construction of a scaled-down prototype. As an initial step towards delving into the realm of MDFs, a scaled-down prototype was meticulously crafted. This prototype served as a valuable tool for gaining deeper insights into the intricate dynamics of EDFs and exploring the realms of stability enhancement to optimize controller performance, as delineated in [8]. Thus, the meticulously tailored MDF, referred to as "FAN HOPPER" in this publication, boasts distinctive attributes, which are briefly enumerated in what follows:

FAN HOPPER: It embodies a 6DOF hexa MDF system, leveraging electric propulsion technology that emulates the operational characteristics of conventional thermal engines. This design choice provides an avenue to explore and address the inherent uncertainties reminiscent of thermal motors within this context. Rigorous aerodynamic analyses

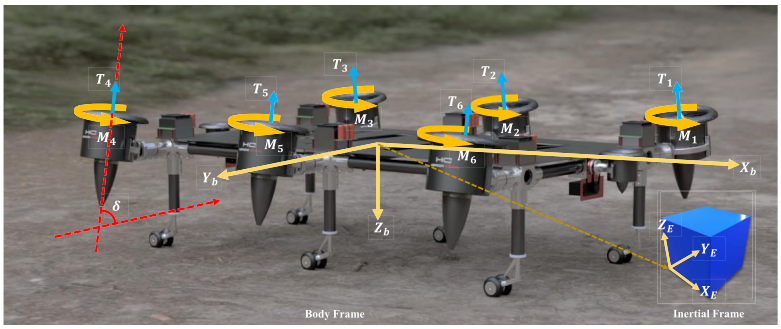

Fig. 1. The general coordinate system based on the FAN HOPPER prototype; T_i and M_i are thrusts and moments generated by the EDFs, δ is the Angel of Incidence (AOI) of EDFs according to experiment, $\{\}_b$ is the subscript for the body-fixed frame, and $\{\}_E$ is the subscript for the inertial frame.

were conducted, leading to significant enhancements across the entire platform. Notably, the innovative duct design yielded multiple benefits, including the attainment of a streamlined inlet and outlet airflow even at elevated horizontal velocities. Moreover, az remarkable reduction in undesired yaw moments, historically associated with instability in high-powered multi-rotor propellers, was observed. This achievement is particularly noteworthy as the constrained space between the duct wall and the rotor blades virtually eliminates yawing, thereby contributing to enhanced stability. Consequently, the consideration of rotor rotation direction becomes superfluous, and as illustrated in "Fig. 1", the EDFs exhibit uniform rotation due to their near-zero yawing moments. Furthermore, as depicted in the figure, empirical investigations led to the incorporation of an optimized Angle of Incidence (AOI), enhancing stabilization during yawing. This concept is further described in [8], providing a better insight into its implementation and impact.

In the next step, a significant milestone was achieved by developing a larger-scale prototype intended to be fitted with thermal engines, thereby advancing toward the ultimate objective. This design endeavor was fortified by meticulous modeling, expounded upon in [30], which furnished a comprehensive mathematical representation of the dynamic system governing the extensive MDF. Noteworthy traits of this UAV, dubbed "DUTY HOPPER," are briefly outlined as follows:

DUTY HOPPER: It is a 6DOF quad MDF system harnessing thermal propulsion technology through the integration of two longitudinally aligned motors. This configuration also boasts the capability to accommodate Lipo batteries for supplementary attitude stabilization. Detailed in [30], it marked the pioneering instance of laboratory modeling and design. Subsequently, to enhance controller performance, several tests were conducted, including the incorporation of diverse payloads (solid and liquid), culminating in the development of a standardized prototype. By utilizing thermal engines, this platform obviates the need for ESCs in the main ducts, instead adopting an ECU system to translate AP commands for propeller control and maintain a consistent angular velocity across all propellers using a simple PID for different RPM bounds, ensuring safe takeoff and landing. Attitude regulation is achieved via flap vanes, as depicted in

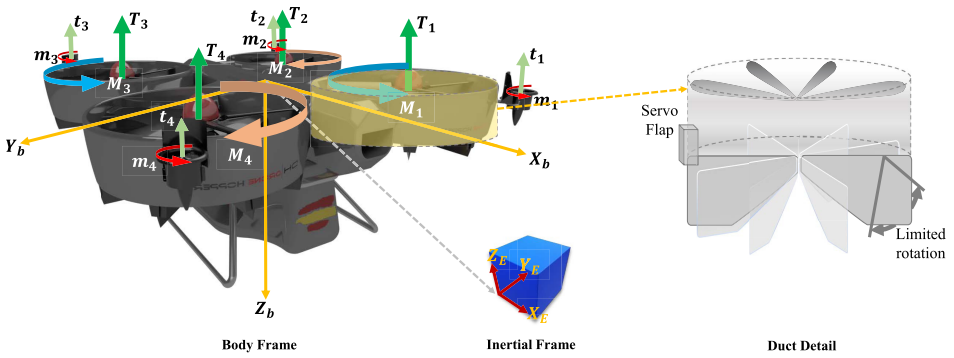

Fig. 2. The general coordinate system based on the DUTY HOPPER prototype; T_i and M_i are thrusts and moments generated by the main ducts, t_i and m_i are thrusts and moments generated by the EDFs, $\{\}_b$ is the subscript for the body-fixed frame, and $\{\}_E$ is the subscript for the inertial frame.

"Fig. 2", wherein commanded surge, sway, and heave movements are doubly derived to suitably control Euler angles ϕ, θ, and ψ. Furthermore, "Fig. 2" shows the configuration of each duct, the inlet airflow, and a schema of rotational flap vanes, which are unveiled in [9]. Notably, based on experimental findings, each flap's rotation is constrained within a $\pm 15^\circ$ range to avert mechanical interference with other flap rotations during both modeling and operational phases.

In the third stage, a synthesis of the preceding experiments led to the development of an advanced, larger-scale prototype tailored for integration with thermal engines. The comprehensive evolution encompassing enhanced modeling, refined control algorithms, and meticulous simulations culminated in [9]. This iteration witnessed significant advancements in power supply, safety measures, communication systems, auxiliary EDF concepts, and overall geometry. Aptly named "WILD HOPPER," this ultimate prototype encapsulates these refinements in a coherent design as follows.

WILD HOPPER: It is a hexa MDF platform featuring 6 DOF, equipped with six main ducts and four auxiliary EDFs for safety and emergencies, as elaborated in [9]. This prototype operates on two power sources: primary propellers are fueled by thermal energy, while EDFs are powered by Lipo batteries. The payload compartment can handle up to 60% of the total weight. The configuration, depicted in "Fig. 3", outlines forces, moments, rotations, movements, and frame connections between the **BFF** and **Inertial Frame**. The model has been extensively enhanced. Notable improvements include refining the aerodynamic model with blade tip angle adjustments and blade count optimization for superior thrust. The communication system received upgrades, incorporating redundancy for reliable short and long-distance links. Employing a TVC strategy, the control system employs geometrically enhanced flap vanes as control surfaces, evolved iteratively during the design.

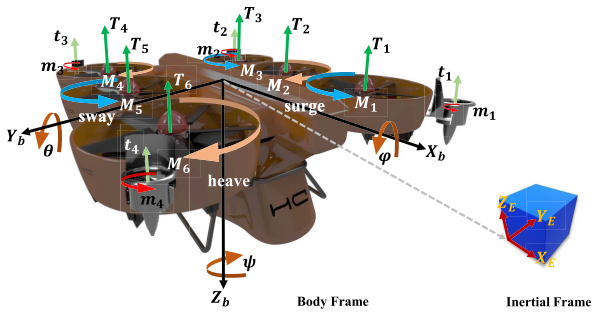

Fig. 3. The general coordinate system based on the final WILD HOPPER prototype; T_i and M_i are thrusts and moments generated by the main ducts, t_i and m_i are thrusts and moments generated by the EDFs, $\{\}_b$ is the subscript for the body-fixed frame, and $\{\}_E$ is the subscript for the inertial frame.

3. Methodology

The research methodology employed through this paper and previous works [8, 9, 30] can be classified as *Applied Research* [36], which differentiates the context from fundamental (basic) research in terms of purpose, context, and methods. Applied research aims to solve practical problems, whereas basic research seeks to study certain issues without immediate practical application. Specifically, the objective followed in this paper is to compound the control algorithms proposed in prior works and improve the controller parameters to provide a fine-tuned robust controller with optimized performance for a real industrial application. The key elements of this paper are elaborated as follows:

- **Purpose:** Solve the mathematical modeling and dynamics of heavy MDF UAVs while applying flap vanes to stabilize the attitude using Adaptive Sliding Mode Control (ASMC) and enhance the control issue by implementing TVC using flap vanes. In previous works, the focus was on solving the control issue defined previously in simulation and smaller prototypes for evaluating the controller's performance under motor failure and external noises.
- **Context:** The context of this paper is highly valuable due to the industry's long-standing need for easy-to-set-up UAVs that can carry heavy payloads for extended flight autonomy. This requirement is addressed in the aforementioned works, where a system is developed to supply thermal energy for extended flight autonomy and equipped with a controller that avoids mechanical complexities and is rational for such a system.
- **Methods:** The methods used in the whole work involve advanced control algorithms, particularly SMC, applied in a novel way to achieve TVC using flap vanes. The design is easily extendable for similar platforms, and the application of SMC offers the advantage of easy tuning compared to conventional PID controllers.

Furthermore, the methodology utilized in this paper is a combination of the system engineering method derived from the system engineering process organized in [37]. This process is abbreviated as "S.I.M.I.L.A.R." and encompasses the following steps: State the problem, Investigate alternatives, Model the system, Integrate solutions, Launch the system, Assess performance, and Reevaluate, which are shown in "Fig. 4":

4. Advanced Control Algorithm Integration for Attitude Stability

In Sec. 2, the three stages of development were reviewed and culminated in the creation of the final integrated model.

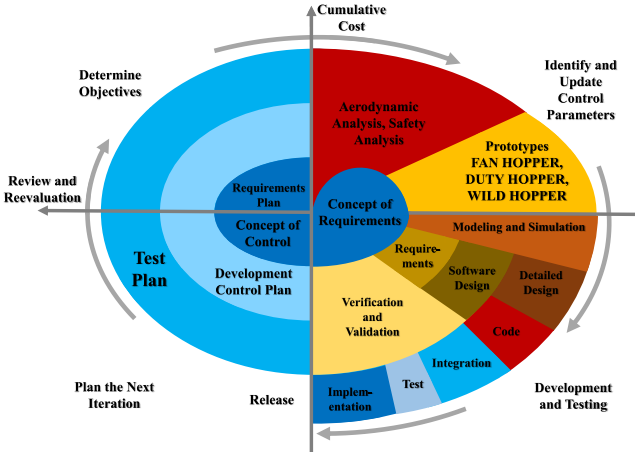

Fig. 4. Methodology approach model followed in this paper, according to the "S.I.M.I.L.A.R." [37], and the spiral procedure defined in [38].

This model integrates a complex control algorithm that merges Model Reference Adaptive Control (MRAC) and SMC methodologies, giving rise to an ASMC approach. By leveraging the MRAC algorithm outlined in a prior publication [8], along with the acquired parameters and the SMC parameters fine-tuned in this research, this novel approach has demonstrated remarkable efficiency in addressing the internal and external nonlinearities encountered during UAV operations. It utilizes a Lyapunov candidate to provide strong stability assurances, enhancing the overall stability and control of the UAV system. For ease of understanding, this section is divided into two parts: Enhanced dynamic model and advanced attitude controller.

4.1. *Enhanced dynamic model*

Given the 6DOF rigid body of an MDF as a complex Multi-Input Multi-Output (MIMO) system due to its nonlinear configuration, the governing equations can be derived from the Newton–Euler equation set. These equations are formulated with respect to either the **Body-Fixed Frame (BFF)** or **Earth-Fixed Frame (EFF)**, which are denoted as subscripts $\{\}_b$ and $\{\}_e$, respectively.

$$
\begin{aligned}
&\boldsymbol{v_b} = [u\ v\ w]^T,\\
&\boldsymbol{\omega_b} = [p\ q\ r]^T,\\
&\boldsymbol{I_b} = \begin{bmatrix} I_{xx} & 0 & 0\\ 0 & I_{yy} & 0\\ 0 & 0 & I_{zz}\end{bmatrix},\\
&\boldsymbol{F_b} = F_{\text{grav}} + F_{\text{fuse}} + F_{\text{prop}} + F_{\text{duct}} + F_{\text{edf}} + F_{\text{fv}},\\
&\boldsymbol{M_b} = M_{\text{gyro}} + M_{\text{prop}} + M_{\text{duct}} + M_{\text{edf}} + M_{\text{fv}},\\
&\dot{\boldsymbol{v}}_{\boldsymbol{b}} = -\boldsymbol{\omega_b} \times \boldsymbol{v_b} + \frac{1}{m_b}(\boldsymbol{F_b} + F_{\text{grav}}),\\
&\dot{\boldsymbol{\omega}}_{\boldsymbol{b}} = \boldsymbol{I_b^{-1}}(\boldsymbol{M_b} - \boldsymbol{\omega_b} \times \boldsymbol{I_b} \times \boldsymbol{\omega_b}),
\end{aligned}
\tag{1}
$$

it is worth noting the distinction between F_{prop} and F_{duct}, which may initially seem equal, but they serve distinct roles, and both contribute to force generation in the BFF. This distinction is as follows.

Propeller Thrust (F_{prop}): The primary thrust in a DF system originates from the propeller or fan itself. As the fan's blades rotate, they create an airflow that generates thrust by propelling the air in the opposite direction, by Newton's third law of motion. This thrust is the central driver of propulsion.

Duct Thrust (F_{duct}): The duct that surrounds the fan plays a critical role in optimizing the propeller's performance. By guiding and channeling the airflow generated by the fan, the duct minimizes air loss and enhances the system's overall efficiency. While the duct does not generate thrust in the same direct manner as the propeller, its design significantly influences the system's total thrust generation, which is elaborately discussed in [30].

Subsequently, translating the velocities and attitudes between the BFF and the Inertial frame yields:

$$
\begin{aligned}
&\boldsymbol{r} = [x\ y\ z]^T,\\
&\boldsymbol{\alpha} = [\phi\ \theta\ \psi]^T,\\
&\boldsymbol{C_{eb}} = \begin{bmatrix} c(\psi)c(\theta) & c(\psi)s(\theta)s(\phi) - s(\psi)c(\phi) & c(\psi)s(\theta)c(\phi) + s(\psi)s(\phi)\\ s(\psi)c(\theta) & s(\psi)s(\theta)s(\phi) + c(\psi)c(\phi) & s(\psi)s(\theta)c(\phi) - c(\psi)s(\phi)\\ -s(\theta) & c(\theta)s(\phi) & c(\theta)c(\phi)\end{bmatrix},\\
&\boldsymbol{v_e} = [\dot{x}\ \dot{y}\ \dot{z}]^T = \boldsymbol{C_{eb}}\boldsymbol{v_b},\\
&\dot{\boldsymbol{\alpha}} = \begin{bmatrix} 1 & s(\phi)t(\theta) & c(\phi)t(\theta)\\ 0 & c(\phi) & -s(\phi)\\ 0 & s(\phi)/c(\theta) & c(\phi)/c(\theta)\end{bmatrix}\boldsymbol{\omega_b},
\end{aligned}
\tag{2}
$$

In "Eqs. (2)", the symbol $\boldsymbol{r}$ represents the location vector observed in the EFF, while $\boldsymbol{C_{eb}}$ stands for the rotation matrix that corresponds to the airframe's yaw, pitch, and roll transformations from the Earth-Fixed Frame to the BFF. This pivotal matrix is known as the Direction Cosine Matrix (DCM). The functions $s()$, $c()$, and $t()$ signify the sine, cosine, and tangent functions, respectively. The symbol α refers to the Euler angles vector, while $\boldsymbol{v_e}$ represents the velocity vector in the EFF, which is equivalent to the velocity vector in the BFF after being multiplied by the rotation matrix. Additionally, the time derivatives of the Euler angles are determined by the angular velocity in the BFF and are multiplied by the rotational matrix to account for the transformation.

By substituting the moments into the Newton–Euler equation, the specified dynamic equations can be

determined. Further, the rotation dynamics equations can be obtained by considering the acceleration in EFF and the BFF, resulting in

$$
\begin{aligned}
\boldsymbol{F_b} &= [F_{b_x}\ F_{b_y}\ F_{b_z}]^T,\\
\boldsymbol{M_b} &= [M_{b_x}\ M_{b_y}\ M_{b_z}]^T,\\
\boldsymbol{F_{b_x}} &= m_b(\dot{u} + gs(\theta) + qw - rv),\\
\boldsymbol{F_{b_y}} &= m_b(\dot{v} - gc(\theta)c(\phi) + ru - pw),\\
\boldsymbol{F_{b_z}} &= \boldsymbol{F_b} - m_b(\dot{w} - gc(\theta)c(\phi) + pv - qu),\\
\boldsymbol{M_{b_x}} &= I_x\dot{p} + (I_z - I_y)qr - I_p\omega_p q,\\
\boldsymbol{M_{b_y}} &= I_y\dot{q} + (I_x - I_z)rp + I_p\omega_p p,\\
\boldsymbol{M_{b_z}} &= I_z\dot{r} + (I_y - I_x)pq + I_p\dot{\omega}_p - Q,\\
\rightarrow \dot{\boldsymbol{\omega}}_{\boldsymbol{b}} &= [\dot{p}\ \dot{q}\ \dot{r}]^T\\
&= \begin{pmatrix} ((I_y - I_z)qr + I_p\omega_p q + \boldsymbol{M_{b_x}})/I_x \\ ((I_z - I_x)rp - I_p\omega_p p + \boldsymbol{M_{b_y}})/I_y \\ ((I_x - I_y)pq - I_p\dot{\omega}_p + \boldsymbol{M_{b_z}} + Q)/I_z \end{pmatrix},\\
\rightarrow \dot{\boldsymbol{v}}_{\boldsymbol{b}} &= [\dot{u}\ \dot{v}\ \dot{w}]^T\\
&= \begin{pmatrix} \boldsymbol{F_{b_x}}/m_b - gs(\theta) + rv - qw \\ \boldsymbol{F_{b_y}}/m_b + gc(\theta)c(\phi) + pw - ru \\ (\boldsymbol{F_b} - \boldsymbol{F_{b_z}})/m_b + gc(\theta)c(\phi) + qu - pv \end{pmatrix}
\end{aligned}
\tag{3}
$$

Through "Eqs. (3)", the symbols I_p and ω_p refer to the inertia and angular rate of the propellers, respectively. Additionally, M_{b_x}, M_{b_y}, and M_{b_z} represent the moments along different axes in the BFF, while F_{b_x}, F_{b_y}, and F_{b_z} denote forces on the corresponding coordinate axes in the BFF. The term Q denotes the propeller's anti-torque, and g represents the gravitational acceleration.

Hence, as the analysis delves into the dynamic equation, it considers the presence of a duct, examining the aerodynamic interactions with it and the turning effects induced by the propeller, as illustrated in Fig. 5.

Figure 5 provides a visual representation of the various stages of the free airstream as it traverses through a duct. These stages encompass the upstream, propeller inlet, outlet, and downstream portions. Subscripts $\{\}_0$ correspond to the upstream airflow well before it enters the duct, $\{\}_i$ pertains to the inlet airflow, $\{\}_e$ signifies the exit or outlet airflow, and $\{\}_\infty$ represents the downstream airflow much further from the duct. Additionally, α, V, and A, respectively, denote the airflow angle, velocity, and planar area at each stage. Additionally, angles α_i and α_e, corresponding to the airflow angle within the duct inlet and the airflow angle at the outlet of the duct, respectively, can be determined as follows:

$$
\begin{aligned}
\boldsymbol{\alpha_i} &= \alpha_0 + k_i\left(\frac{\pi}{2} - \alpha_0\right),\\
\boldsymbol{\alpha_e} &= \alpha_0 + k_e\left(\frac{\pi}{2} - \alpha_0\right),\\
\boldsymbol{\alpha_\infty} &= \alpha_0 + k_\infty\left(\frac{\pi}{2} - \alpha_0\right),
\end{aligned}
\tag{4}
$$

In "Eqs. (4)", the terms k_i, k_e, and k_∞ correspond to flow turning efficiency factors influenced by the inlet propeller plane, the outlet plane, and the downstream region far from the duct. it is important to note that in various articles, notably [17, 39–42], a single airflow angle is commonly utilized for both α_e and α_∞. This approach simplifies the assumption or utilizes an average value for the angle of deflection at a specific downstream point, often situated far from the duct exit. This choice facilitates an understanding of aerodynamic behavior without delving into the intricacies of particular flow interactions. Now, based on the airflow angle at various stages, the velocities at the upstream,

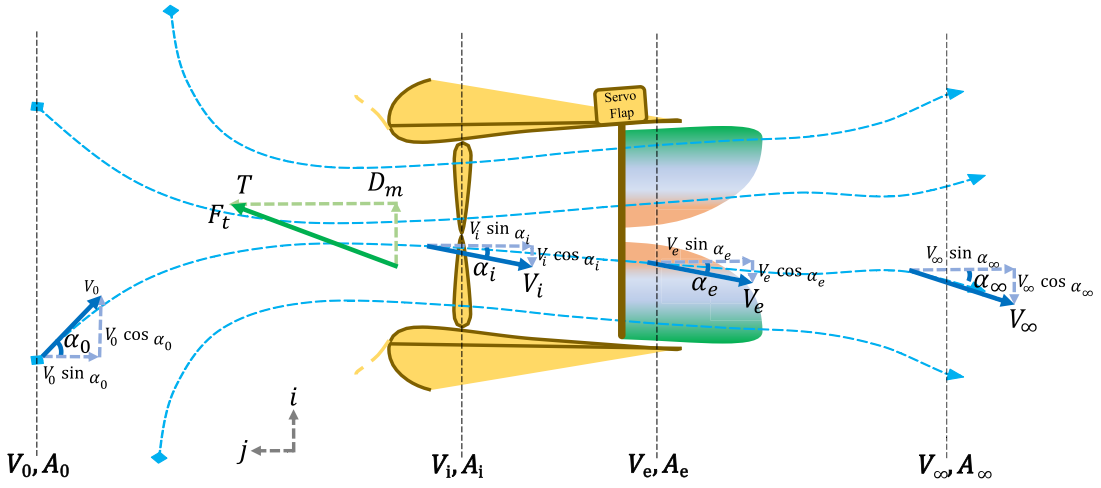

Fig. 5. Schematic of the free airstream passing through a duct, analyzed in four stages: upstream, propeller inlet, outlet, and downstream.

duct inlet, outlet, and downstream can be expressed as follows:

$$\begin{aligned}
\boldsymbol{V_0} &= V_0\cos(\alpha_0)i - V_0\sin(\alpha_0)j,\\
\boldsymbol{V_i} &= V_0\cos(\boldsymbol{\alpha_i})i - (V_0\sin(\boldsymbol{\alpha_i}) + v_i)j,\\
\boldsymbol{V_e} &= V_0\cos(\boldsymbol{\alpha_e})i - (V_0\sin(\boldsymbol{\alpha_e}) + v_e)j,\\
\boldsymbol{V_\infty} &= V_0\cos(\boldsymbol{\alpha_\infty})i - (V_0\sin(\boldsymbol{\alpha_\infty}) + v_\infty)j,
\end{aligned} \tag{5}$$

Using "Eqs. (5)", the terms v_i, v_e, and v_∞ represent the induced speeds caused by the airflow as it passes through the duct. Besides, the induced exit velocity is also well known as slipstream velocity [43]. These speeds are oriented vertically, in the same direction as the vertical axis. Furthermore, as shown in "Fig. 5", the total force vector generated by the duct system is denoted as F_t, which is assumed to comprise a vertical thrust component, T, and a horizontal momentum drag component, D_m. Specifically, T encompasses the combined thrust produced by both the propeller and the duct itself, leading to the equation:

$$\begin{aligned}
\boldsymbol{F}_{\text{duct}_t} &= D_m i + Tj,\\
\boldsymbol{T} &= F_{\text{prop}} + F_{\text{duct}} = F_{\text{prop}}(1 + k_{\text{aug}}).
\end{aligned} \tag{6}$$

In "Eq. (6)", the symbol k_{aug} denotes the Thrust Augmentation Factor (TAF), which signifies the influence of the duct's lift effect. A TAF value of 1 indicates that the total thrust generated is twice that of the propeller thrust alone. This rationale underscores the selection of the DF model, as it effectively enhances the overall system efficiency. Additionally, when taking into account the airflow mass rate, as well as the horizontal and vertical thrust forces, the following expressions are applicable:

$$\begin{aligned}
&\dot{m} = \rho A_i V_i,\\
&\boldsymbol{T} = \dot{\boldsymbol{m}}(\boldsymbol{V_e} - V_0),\\
&\xrightarrow{\text{Simplifying}} \boldsymbol{T} = \dot{\boldsymbol{m}}(\boldsymbol{V_\infty} - V_0),\\
&\xrightarrow{\text{Simplifying}} \boldsymbol{T} = \dot{\boldsymbol{m}}(\sin(\alpha_\infty) - \sin(\alpha_0))V_0 + v_\infty,\\
&\boldsymbol{D_m} = \dot{\boldsymbol{m}}(\cos(\alpha_0) - \cos(\alpha_e))V_0,\\
&\xrightarrow{\text{Simplifying}} \boldsymbol{D_m} = \dot{\boldsymbol{m}}(\cos(\alpha_0) - \cos(\alpha_\infty))V_0.
\end{aligned} \tag{7}$$

Equation (7) are obtained assuming the conservation of energy, momentum, and the mass flow rate from the inlet of the duct to the downstream. ρ is the density of the airstream, and for simplifying the $\alpha_e = \alpha_\infty$ and $V_e = V_\infty$. Finally, the whole force generated by the duct system is determined as follows:

$$\begin{aligned}
\boldsymbol{F}_{\text{duct}_t} = 2\rho A_i\left(\frac{1}{1+k_{\text{aug}}}(V_0\sin(\alpha_i) + v_i) - V_0\sin(\alpha_0)\right)\\
\sqrt{V_0^2 + 2V_0 v_i\sin(\alpha_i) + v_i^2}.
\end{aligned} \tag{8}$$

The total force denoted as $\boldsymbol{F}_{\text{duct}_t}$ in "Eq. (8)", can also be expressed and simplified in a vectorized manner as follows. Additionally, based on the equations detailed in (1) and described in [30], the remaining forces and moments acting on the BFF can be presented as follows:

$$\begin{aligned}
\boldsymbol{F}_{\text{grav}} &= \begin{bmatrix} -mg\sin\theta \\ mg\cos\theta\sin\phi \\ mg\cos\theta\cos\theta \end{bmatrix},\\
\boldsymbol{F}_{\text{fuse}} &= -0.5\rho\begin{bmatrix} C_{D_x}u_b|u_b|A_{\text{side}} \\ C_{D_y}v_b|v_b|A_{\text{side}} \\ C_{D_z}w_b|w_b|A_{\text{top}}, \end{bmatrix},\\
\boldsymbol{F}_{\text{prop}} &= 0.5\rho A_i b\Omega_p^2\begin{bmatrix} C_{D_{bl}}\sin\alpha_{bl}\sin\theta_{bl} \\ -C_{D_{bl}}\sin\alpha_{bl}\sin\theta_{bl} \\ C_{L_{bl}}\cos\alpha_{bl}\cos\theta_{bl} \end{bmatrix},\\
\boldsymbol{F}_{\text{duct}} &= D_m + K_{\text{aug}}F_{\text{prop}} = 0.5\rho C_{D_{\text{duct}}}\begin{bmatrix} A_e u_0|u_0| \\ A_e v_0|v_0| \\ A_i K_{\text{aug}} V_i|V_i| \end{bmatrix},\\
\boldsymbol{M}_{\text{gyro}} &= NJ\,\omega\begin{bmatrix} -q \\ p \\ 0 \end{bmatrix},\\
\boldsymbol{M}_{\text{duct}} &= \begin{bmatrix} F_{\text{duct}_y}r \\ F_{\text{duct}_x}r \\ F_{\text{duct}_z}l_d \end{bmatrix}
\end{aligned} \tag{9}$$

In "Eqs. (9)", specific parameters are defined as follows: N represents the number of propellers, J denotes the rotor inertia, while p and q correspond to the angular rates of the propellers discussed in [24, 44]. It is important to note that this equation is applicable when the angular rates are assumed to be semi-constant, irrespective of any aggressive flight behavior. Additionally, C_D stands for the drag coefficient of the fuselage, A_{side} represents the cross-sectional area of the drone, assuming symmetry on both sides and A_{top} denotes the top area of the MDF. The blade pitch is denoted as θ_{bl}, and the blade incidence angle is represented by α_{bl}, which in hover flight conditions, both θ_b and α_b are considered negligible due to their small values. The Ω_p corresponds to the propeller angular velocity, b is the thrust factor of the propeller, and $C_{D_{bl}}$ and $C_{L_{bl}}$ are the drag and lift coefficients of the propeller blades. The parameter $C_{D_{\text{duct}}}$ stands for the duct moment coefficient, serving as a proportionality constant that relates the moment to the dynamic pressure caused by crosswind effects, introduced in [44]. Referring to "Fig. 5", the variables V_0 represent the duct inlet air velocity, r corresponds to the duct exit radius, l_d is the diagonal distance between the Center of Pressure (COP) of the duct to the COG of the MDF, and finally, V_0, A_i, V_e, and A_e represent the rotor plane and duct exit velocities and areas, respectively.

As depicted in "Fig. 6", the "WILD HOPPER" platform utilizes a hexagonal geometry with a set of vanes positioned at the duct exits. This arrangement consists of 12 pairs of vanes strategically configured for optimal control and effective

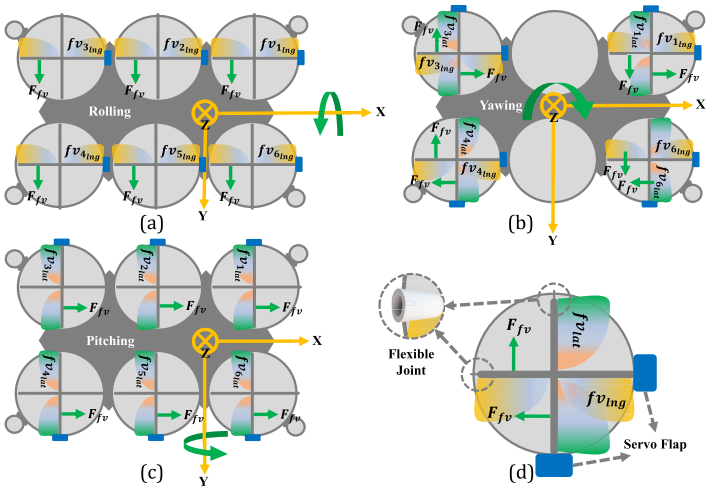

Fig. 6. Top-Down view schematic of 12 pairs of flap vanes on the "WILD HOPPER" prototype, strategically positioned at the duct outlets to generate specific moments: (a) Rolling moment, (b) Yawing moment, (c) Pitching moment. In (d), a detailed view of a single duct featuring two pairs of vanes is depicted.

functionality in influencing a sizeable payload. The term "pair" signifies that each duo of flap vanes is linked by a shaft and managed by a singular servo flap, efficiently rotating both vanes. This configuration offers several advantages: reduced mechanical complexity, simplified control and computation, error prevention, and enhanced moment generation. In this configuration, each duct has two lateral flap vanes, denoted as fv_{lat}, and two longitudinal flap vanes, labeled as fv_{lng}. In this context, the term fv signifies a flap vane, while F_{fv} symbolizes the force exerted by a flap vane oriented in the opposite direction of its corresponding azimuthal angle. This phenomenon is also clearly depicted in "Fig. 7". Additionally, the arrangement of each servo flap is illustrated in "Fig. 6(d)", showcasing the asymmetrical layout of the servo installations. The decision to employ two servo flaps instead of four is driven by efficiency, as it eliminates the need for disparate angle production and yields more harmonized force generation. This advantageous design choice is further emphasized in the magnified circle adjacent to the duct. A flexible joint is connected to the duct's wall at the other end of the servo bar, facilitating smooth rotation of the flaps bar under the influence of servo-generated moments.

Explicitly, considering the Wake Skew Angle (WSA) of the airflow, which correlates with α_i, α_e, and α_∞ as depicted in "Fig. 5". This entails:

$$\begin{aligned}\boldsymbol{\xi_i} &= \arctan\left(\frac{V_0\cos(\alpha_i)}{V_0\sin(\alpha_i)+v_i}\right),\\ \boldsymbol{\xi_e} &= \arctan\left(\frac{V_0\cos(\alpha_e)}{V_0\sin(\alpha_e)+v_e}\right),\\ \boldsymbol{\xi_\infty} &= \arctan\left(\frac{V_0\cos(\alpha_\infty)}{V_0\sin(\alpha_\infty)+v_\infty}\right).\end{aligned} \tag{10}$$

In "Eqs. (10)", the symbol ξ denotes the WSA, representing the angle that characterizes the skewness of the wake airflow. This angle quantifies the misalignment between the direction of the wake and the flight path of the drone. On the other hand, the high spinning of the propeller induces a drag force, resulting in a swirling motion of the flow. This effect introduces a swirl velocity into the flow, which can be described as follows:

$$\boldsymbol{\omega}_{\text{swirl}} = \frac{M_{\text{prop}}}{\frac{1}{2}\rho A_i V_i r_{\text{prop}}^2}. \tag{11}$$

In "Eq. (11)", M_{prop} represents the propeller torque, and r_{prop} is the radius of the propeller. The swirl velocity has a direct influence on the vertical component of the flap vanes' velocity. Taking into account the previously mentioned V_e in both horizontal and vertical directions, it yields:

$$\boldsymbol{V_e} = \begin{bmatrix} u_e \\ v_e \\ w_e \end{bmatrix} = \begin{bmatrix} V_e\sin(\alpha_e) \\ 0 \\ V_e\cos(\alpha_e) \end{bmatrix}. \tag{12}$$

In "Eqs. (12)", $\boldsymbol{u_e}$ and $\boldsymbol{w_e}$ represent the two components of the total outlet velocity, corresponding to the x and z axes, respectively. Introducing the flap vane velocity components in all three dimensions as V_{fv}, we arrive at the following set of equations:

$$\begin{aligned}\boldsymbol{V_{fv}} &= [u_{fv}\ v_{fv}\ w_{fv}]^T,\\ \boldsymbol{V_{fv}} &= \begin{bmatrix} 0 & 0 & -1 \\ -1 & 0 & 0 \\ 0 & 1 & 0 \end{bmatrix}\begin{bmatrix} \cos(\delta_{fv}) & -\sin(\delta_{fv}) & 0 \\ \sin(\delta_{fv}) & -\cos(\delta_{fv}) & 0 \\ 0 & 0 & 1 \end{bmatrix}\end{aligned}$$

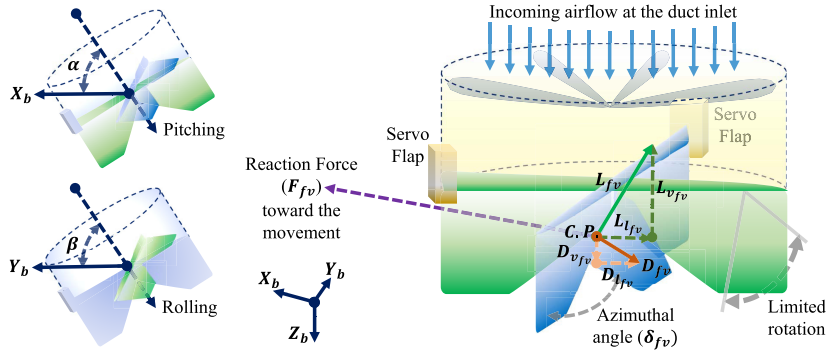

Fig. 7. Schematic of a duct with two pairs of flap vanes rotating, illustrating generated forces and reaction force.

$$\times \begin{bmatrix} \boldsymbol{u_e}\cos(\delta_{fv}) \\ \boldsymbol{u_e}\sin(\delta_{fv}) \\ -\boldsymbol{w_e} \end{bmatrix} + \begin{bmatrix} 0 \\ 0 \\ r\boldsymbol{\omega}_{\text{swirl}} \end{bmatrix},$$

$$\rightarrow \boldsymbol{V_{fv}} = \begin{bmatrix} \boldsymbol{u_e}\sin(\delta_{fv}) \\ -\boldsymbol{u_e}\cos(\delta_{fv}) \\ r\boldsymbol{\omega}_{\text{swirl}} - \boldsymbol{w_e} \end{bmatrix} \tag{13}$$

Equation (13) introduces three crucial variables: u_{fv}, v_{fv}, and w_{fv}, signifying the chordwise, spanwise, and normal constituents of the flap vane velocity. These variables derive their values from the influence of the outlet airstream exhaust emanating from the duct. The parameter δ_{fv}, equivalent to the vane's deflection angle or the widely acknowledged azimuthal angle ϕ, constitutes a pivotal aspect. This angle delineates the divergence between the vertical axis and the projection of the COP of the vane upon the horizontal plane. For an intricate depiction of the utilized flap vanes, refer to "Fig. 6". This illustrative diagram aptly showcases the three principal rotations imperative for generating roll, pitch, and yaw moments in the pursuit of optimal functionality.

Furthermore, the downwash angle induced by the duct is presented, which is usually negative due to the propeller that creates an airflow that is directed downward. It is also related to the lift force of the duct by the following expression:

$$\boldsymbol{\gamma_d} = \frac{\boldsymbol{F}_{\text{duct}}}{\dot{m}\boldsymbol{v}_e},$$

$$\boldsymbol{\gamma_d} = \begin{bmatrix} \gamma_{d_x} \\ \gamma_{d_y} \end{bmatrix} = \begin{bmatrix} \boldsymbol{F}_{\text{duct}}/(\rho\pi r^2((v_i - v_z)^2 + v_x^2)) \\ \boldsymbol{F_x}/(\rho\pi r^2((v_i - v_z)^2 + v_y^2)) \end{bmatrix},$$

$$\boldsymbol{V_{fv}} = \begin{bmatrix} u_{fv} \\ v_{fv} \\ w_{fv} \end{bmatrix} = \begin{bmatrix} u_{fv_p} & u_{fv_r} & u_{fv_y} \\ v_{fv_p} & v_{fv_r} & v_{fv_y} \\ w_{fv_p} & w_{fv_r} & w_{fv_y} \end{bmatrix},$$

$$\boldsymbol{\delta_{fv}} = \begin{pmatrix} \alpha_{fv} \\ \beta_{fv} \\ \epsilon_{fv} \end{pmatrix}$$

$$= \begin{pmatrix} \delta_{fv} + \arctan 2(-u_{fv_p} - v_{fv_p} l_{fv}, v_i - w_{fv_p}) \\ \quad - \gamma_{\boldsymbol{d_x}} - \delta_{fv} + \arctan 2(-v_{fv_r} - u_{fv_r} l_{fv}, v_i \\ \quad - w_{fv_r}) - \gamma_{\boldsymbol{d_y}} \\ \delta_{fv} + \arctan 2(-v_{fv_y} l_{fv}, v_i - w_{fv_y}) \end{pmatrix}. \tag{14}$$

In "Eq. (14)", the downwash angle (γ_d) is calculated based on the total duct thrust (as defined in "Eq. (8)", the mass airflow passing through the duct (refer to "Eq. (7)"), and the exit velocity. This equation unveils the significant impact of the downwash angle on the final azimuthal angle of the flap vanes. In practical scenarios, such as the "WILD HOPPER" platform with a wide-diameter exhaust, the downwash angle deviates from the ideal conditions considered during the design process. This deviation carries implications, particularly for large-scale systems. Considering the three rotational angle axes for the vane azimuthal angle, we have α_{fv} (longitudinal direction), β_{fv} (lateral direction), and ϵ_{fv} (vertical direction). To account for the entire body's angular velocity, induced velocity (v_i) at the flap vane neighborhood is factored in. Additionally, the distance between the Center of Gravity (COG) of the MDF and the Center of Pressure (COP) of the flap vane (or their aerodynamic center), represented as l_{fv}, plays a crucial role in these calculations. For a more detailed discussion on these aspects, refer to [44]. The velocity of the flap vanes is expressed in "Eqs. (14)" as a 3×3 matrix, delineating each element corresponding to pitch ($\{\}_{fv_p}$), roll ($\{\}_{fv_r}$), and yaw ($\{\}_{fv_y}$) flap vanes.

As depicted in "Fig. 7", the incoming airflow is directed into a duct as the MDF moves along the longitudinal X-axis. Positioned near the duct's outlet, the two servo flaps exert control on the exhaust airflow, prompting a reactive response from the flap vanes to the exiting airflow. In this dynamic, a pair of forces emerge L_{fv} and D_{fv}, signifying the creation of Lift and Drag forces for each set of vane pairs. An important consideration is the azimuthal angle, δ_{fv}, which is restricted within the $\pm 15^\circ$ range to prevent interference

with adjacent cross-linked vanes. This precaution safeguards against potential disruptions. Furthermore, "Fig. 7" demonstrates two potential deflections of the single duct. The deflection corresponding to longitudinal movement is denoted as α, while the angle associated with lateral movement is designated as β. Moreover, the derived force acting on the flap is central to defining the flap force equation set, which can be expressed as follows:

$$\begin{aligned}
\mathbf{L_{fv}} &= L_{l_{fv}} i + L_{v_{fv}} j = L_{fv} \cos(\delta_{fv}) i + L_{fv} \sin(\delta_{fv}) j, \\
\mathbf{D_{fv}} &= D_{l_{fv}} i + D_{v_{fv}} j = -D_{fv} \sin(\delta_{fv}) i + D_{fv} \cos(\delta_{fv})) j, \\
\mathbf{T_{fv}} &= L_{v_{fv}} i - D_{v_{fv}} j = \mathbf{L_{fv}} \sin(\delta_{fv}) - \mathbf{D_{fv}} \cos(\delta_{fv}), \\
\mathbf{F_{fv}} &= L_{l_{fv}} i + D_{l_{fv}} j = \mathbf{L_{fv}} \cos(\delta_{fv}) + \mathbf{D_{fv}} \sin(\delta_{fv}).
\end{aligned} \tag{15}$$

Equation (15) presents the breakdown of the lift force into distinct lateral and vertical components, denoted as $L_{l_{fv}}$ and $L_{v_{fv}}$, respectively. Similarly, the drag force is divided into lateral and vertical components, represented by $D_{l_{fv}}$ and $D_{v_{fv}}$ for a flap vane. The aggregate thrust force produced by the flap vane, denoted as T_{fv}, results from combining the vertical components of both lift and drag forces. In contrast, the lateral force generated by the flap, marked as F_{fv}, arises from the summation of both lateral components of lift and drag forces. This interesting observation reveals that the lateral components of the decomposed lift and drag forces act in parallel, enhancing the MDF's forward momentum with increased force.

4.2. *Advanced attitude controller*

Having thoroughly examined the dynamics and mathematical modeling of the MDF platform, this section, alongside the subsequent one, succinctly encapsulates the essence of the control algorithm put forth in previous publications. The aim is to provide a comprehensive overview of the equations presented in the publications while grasping the underlying hypotheses. The overall control schematic for both methods is depicted in "Fig. 8", encompassing several distinct packages as reference values presented x_r, y_r, z_r, and ψ_r; position controller, vertical controller, attitude controller, Electric Control Unit (ECU), Servo Flap Dynamics (SFD), EDF Motor Dynamics (EDF-MD), secondary attitude dynamics, attitude dynamics, position dynamics, and disturbances. In this paper, we delve into the intricacies of the attitude controller, a crucial component responsible for stabilizing the UAV during flight maneuvers, including rotations and turns that induce transitional movements. The control of these movements is achieved through dedicated controller surfaces strategically positioned at the duct exits. These surfaces modulate the exhaust air to generate the requisite lift force, thereby influencing the UAV's azimuthal angle. Furthermore, the vertical controller, while constituting a segment of the position controller, operates

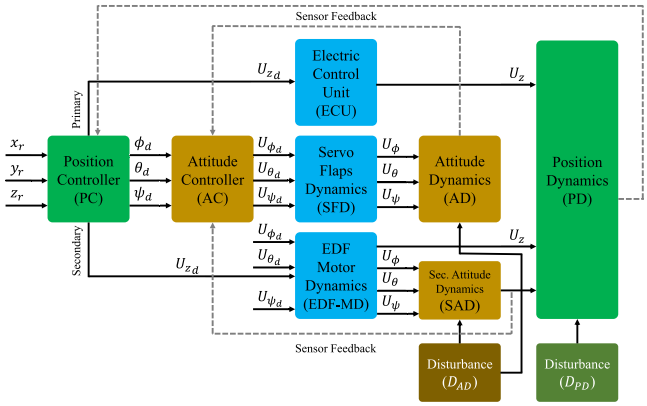

Fig. 8. Diagram illustrating the overarching control scheme implemented for precisely regulating the heavy hexa MDF system known as the "WILD HOPPER."

independently of attitude angles. Termed the "vertical controller," it plays a pivotal role in regulating the UAV's vertical movements. This section holds particular significance, representing a focal point in the authors' prior works, where it is expounded upon in greater detail in [8, 9].

Defining the state and input vectors, two approaches are evident: one based on the state values as followed in previous research, and the other aligned with state values utilized in studies concerning conventional DFs. In all scenarios, the input matrix remains consistent, as outlined below:

$$\begin{aligned}
\mathbf{X} &= [x\ \dot{x}\ y\ \dot{y}\ z\ \dot{z}\ \phi\ \dot{\phi}\ \theta\ \dot{\theta}\ \psi\ \dot{\psi}]^T, \\
\mathbf{X_{alt}} &= [u\ v\ w\ p\ q\ r\ \phi\ \theta\ \psi]^T, \\
\mathbf{U} &= [u_z\ u_\phi\ u_\theta\ u_\psi]^T.
\end{aligned} \tag{16}$$

In "Eq. (16)", $\mathbf{X_{alt}}$ corresponds to an alternative state matrix formulation as defined in other research works. In this section, the second model is considered to align the control framework with established DF standards in [40–42, 45] to present an ASMC strategy against an array of external disturbances, such as wind gusts, fluctuations in payload weight, and uncertainties in dynamics, which makes it particularly appealing. In the context of a state-space representation involving an nth-order derivative of the system's state vector, the determination of the sliding surface is expressed as

$$\begin{aligned}
&x^{(n)} = Ax + Bu + \delta(x) \rightarrow x^{(n)} = f(x) + u \\
&\rightarrow S = \left(\frac{d}{dt} + \lambda\right)^{(n-1)} (\dot{x} - \dot{x}_d) \rightarrow S = \left(\frac{d}{dt} + \lambda\right)^{(n-1)} e.
\end{aligned} \tag{17}$$

In "Eq. (17)", the symbol $\delta(x)$ denotes system uncertainties and nonlinearities encapsulated within the disturbance

function. It is assumed that δ remains within the bounds $\delta(x) < k$, where k is a positive constant representing the maximum anticipated disturbance magnitude. Additionally, the symbol λ represents the sliding surface gain or slope coefficient, determined based on the weighting of the uncertainties. The introduction of the sliding variable S serves to quantify the tracking error, e, that emerges between the desired trajectory X_d and the actual trajectory X of the system. The overarching objective is to drive the sliding variable S towards zero, thereby aligning the actual state values with the desired state. In this specific scenario where $n = 2$ and it corresponds to a straightforward MDF system,

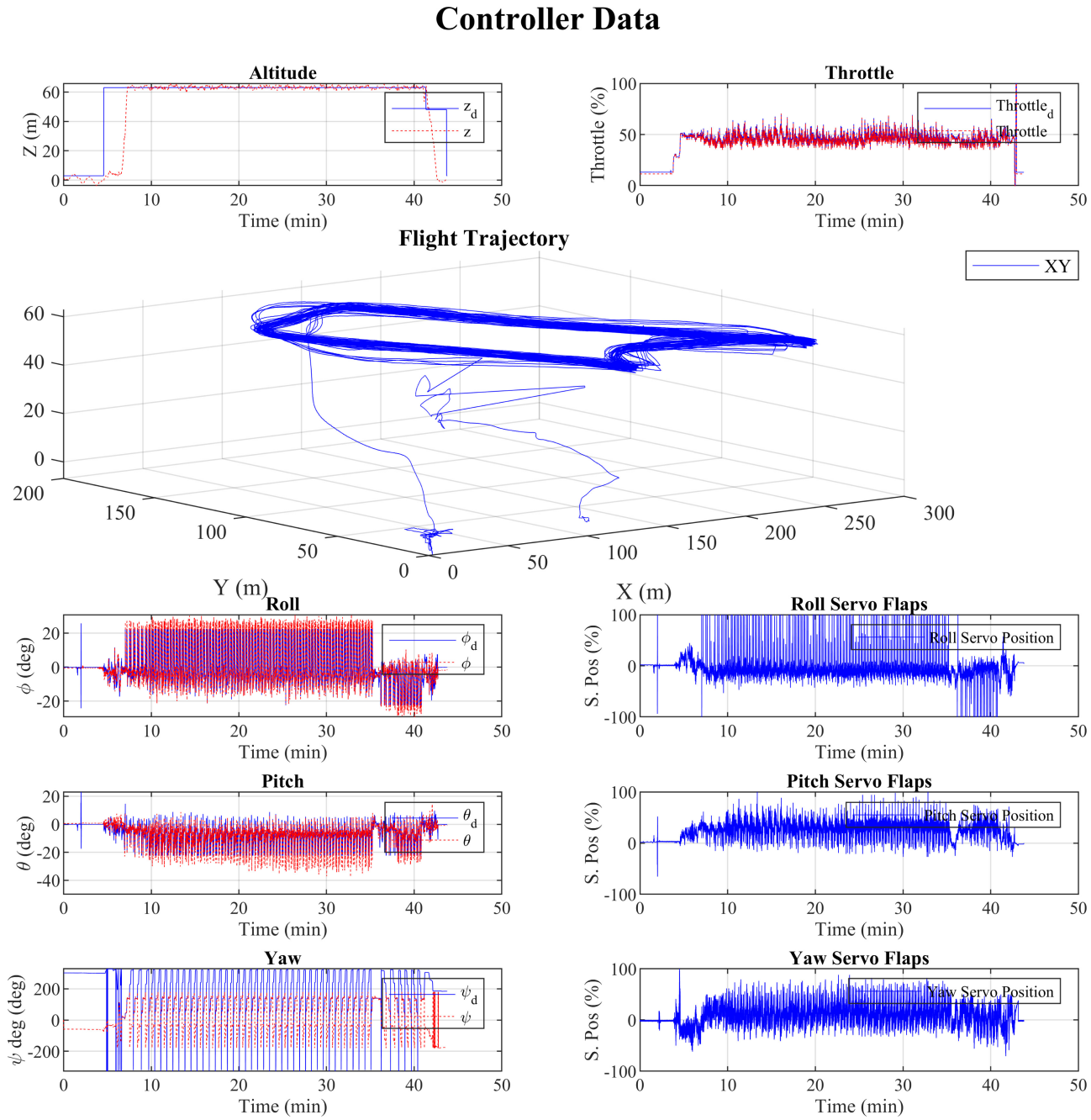

Fig. 9. Simulation: Attitude controller performance during a cruise flight, controlled by a cascade PID and utilizing flap vanes.

the formulation of the sliding surface is elaborated as follows:

$$S = \dot{e} + \lambda e = \dot{x} - \dot{x}_d + \lambda(x - x_d). \tag{18}$$

Indeed, a significant challenge within the SMC method lies in the careful definition of the sliding surface. However, one can assert that the sliding surface ideally mirrors the system's error. This error signifies the disparity that necessitates a reduction to zero within the intended system.

$$\begin{aligned} \dot{S} &= \ddot{x} - \ddot{x}_d + \lambda(\dot{x} - \dot{x}_d), \\ &\xrightarrow{\dot{x}=f(x)+u} u_{\text{eq}} : \dot{S} = 0 \rightarrow u_{\text{eq}} = X_d - \lambda \dot{e} \end{aligned} \tag{19}$$

In "Eqs. (19)", the u_{eq} stands for the equivalent control input, which is a part of the total control input specifically

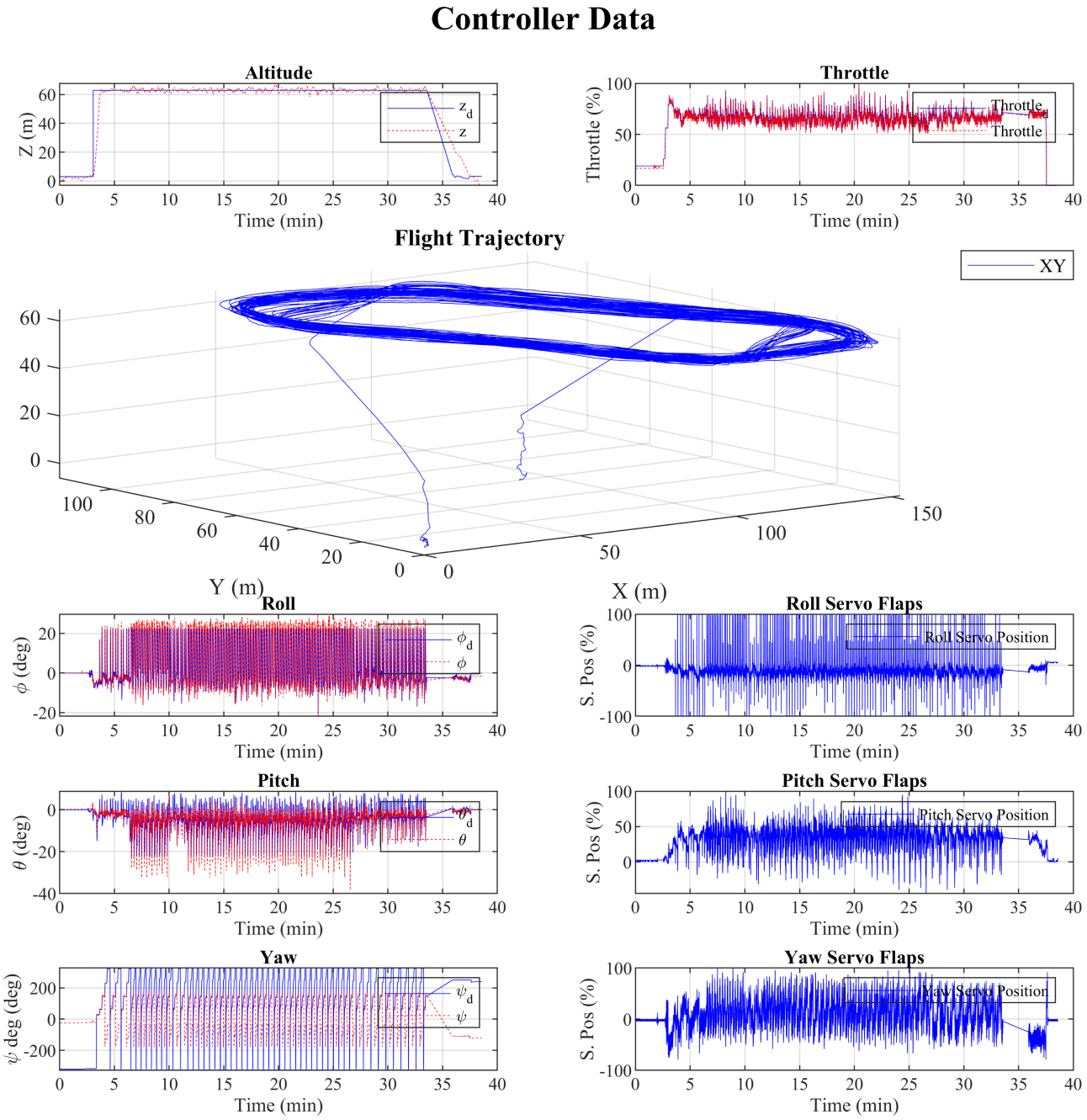

Fig. 10. Simulation: Attitude controller performance during a cruise flight, controlled by the presented robust controller and utilizing flap vanes.

designed to drive the system onto the sliding surface and maintains sliding mode behavior. As seen, the control input has appeared in the first derivative of the sliding variable. Therefore, the relative degree of the system is equal to 1. Moreover, the complete control input is defined, encompassing both the equivalent control input, denoted as u_{eq}, and the uncertain term of the system. This can be expressed as follows:

$$u = u_{\text{eq}} - d \times \text{sign}(s), \tag{20}$$

In "Eq. (20)", the term $\text{sign}(s)$ embodies the switching or uncertainty component within the control law. This term accommodates system uncertainties, external disturbances, or any unaccounted dynamics that could influence the system's behavior. Its purpose is to enhance the robustness of the control system when confronted with uncertain factors that might impact the system's performance. To determine the unknown parameter d, a Lyapunov candidate is introduced. This candidate is not only Positive-Definite (PD) itself but also has a Negative-Definite (ND) derivative, as shown in what follows. To mitigate the chattering phenomenon, which can cause undesirable high-frequency oscillations, the $\tanh s$ function is employed instead of the abrupt $\text{sign}(s)$ function. Additionally, for improved and swifter stability convergence, it is assumed that the derivative of the Lyapunov candidate is not only ND but also significantly more negative than a predefined positive value, μ. This choice ensures stability within a finite timeframe.

$$\begin{aligned}
&\textbf{updating : } \mathbf{u} = \mathbf{u_{eq}} - \mathbf{d} \times \tanh(\mathbf{s}),\\
&V(x) = S^2/2 \rightarrow dV(x)/dt = s\dot{s},\\
&\textit{necessitates that} : \dot{V}(x) \leq -\mu \rightarrow s\dot{s} \leq -\mu|s|\\
&\textit{knowing that} : \; s(x^{(n)} = Ax + Bu + \delta(x))\\
&\qquad\qquad = s(-db\tanh(s) + \delta(x))\\
&\rightarrow -db|s| + |s\delta(x)| = -db|s| + |s||\delta(x)| =\\
&\quad |s|(-db + |\delta(x)|) \leq -\mu|s|\\
&\rightarrow -db + k \leq -\mu \rightarrow d \geq (\mu + k)/b.
\end{aligned} \tag{21}$$

Hence, by adhering to the condition $d \geq (\mu + k)/b$, the stability of the system can be effectively ensured. This condition plays a pivotal role in bolstering the control system's ability to resiliently counter uncertainties and disturbances, thereby facilitating the achievement of both stability and precise tracking of the intended trajectory. Thus, in the context of the control law, the reformulation of the attitude controller concerning the azimuthal angle of the flap vanes can be expressed as

$$\begin{aligned}
U_{\text{roll}} &= I_x(\ddot{\delta}_{fv_d} - k_1\dot{e}_\phi) - k_1\tanh(k_3S),\\
U_{\text{pitch}} &= I_y(\ddot{\delta}_{fv_d} - k_2\dot{e}_\theta) - k_1\tanh(k_3S),\\
U_{\text{yaw}} &= I_z(\ddot{\delta}_{fv_d} - k_3\dot{e}_\psi) - k_2\tanh(k_1S).
\end{aligned} \tag{22}$$

Table 1. Controller parameters fine-tuned for practical flight scenarios.

Parameter	Value
k_1	1.236
k_2	0.911
k_3	1.568
b	0.88
d	4.01

Table 2. Specification of the final Duty Hopper prototype.

Component	Parameter	Value	Dimension
Fuselage	Mass	350	Kg
	Height	163	cm
	Width	311	cm
	I_{xx}	411.62	Kg.m^2
	I_{yy}	411.62	Kg.m^2
	I_{zz}	536.31	Kg.m^2
Propeller	Number	4	—
	Blade Number	5	—
	Blade Radii	67	cm
	Blade Tip Chord	10	cm
	Blade Tip Angle	7.5	deg
	Nominal Rotor Rev.	1200	rpm
	Thrust Factor	2.16e-2	N.m^2
Propeller Duct	Length	37	cm
	Outer Diameter	151	cm
	Inner Diameter	155	cm
	Arc Radii at Tip	7	cm
	Avg. Inlet air Velocity	135	m/s
	Avg. Exit air Velocity	63.56	m/s
Flap Vane	Number	8	—
	Number per Prop	8	—
	Height	27	cm
	Length	53	cm
	Avg. Width	8	cm
	Max Azimuthal Angle	±15	deg
Servo Flap	Number	4	—
	Avg. Speed	0.35	s/60°
	Input Signal	200	Hz
	Rated Torque	150	Kg.s

By using "Eqs. (22)", the constants k_i with $i \in \{1, 2, 3\}$ will be determined through trial and error during the implementation phase. Ultimately, as a result of applying the control law, the attitude controller interfaces with the position controller.

5. Results

In previous works [8, 9, 30], simulation results of different adaptive and robust approaches were presented, compared

to a well-tuned PID controller and discussed that contributed to the enhancement of the dynamic model and controller solutions. This paper exclusively presents simulation results comparing the optimized SMC with a fine-tuned cascade PID system, thereby presenting a series of real-world results. These results focus on five of the most successful missions performed by the redesigned and fine-tuned Duty Hopper prototype. Previously, the initial schematic of this prototype was explored in detail in [30]. Through successive iterations and improvements, this model has recently reached Technology Readiness Level 7 (TRL-7), signifying its readiness for practical deployment. The specification of the final model is summarized in "Table 2". During the tests, the final configuration, which includes the payload weighing 350 Kg, features each duct equipped with a single primary propeller comprising five blades (as discussed in aerodynamics enhancements in [9]). Additionally, the flap vanes installed per duct are interconnected in pairs, as illustrated in "Fig. 6". Each flap series is actuated by a servo high-torque metal steering gear capable of applying moments of up to 400 kg.s. Consequently, for the desired quad DF configuration, eight sets of flap

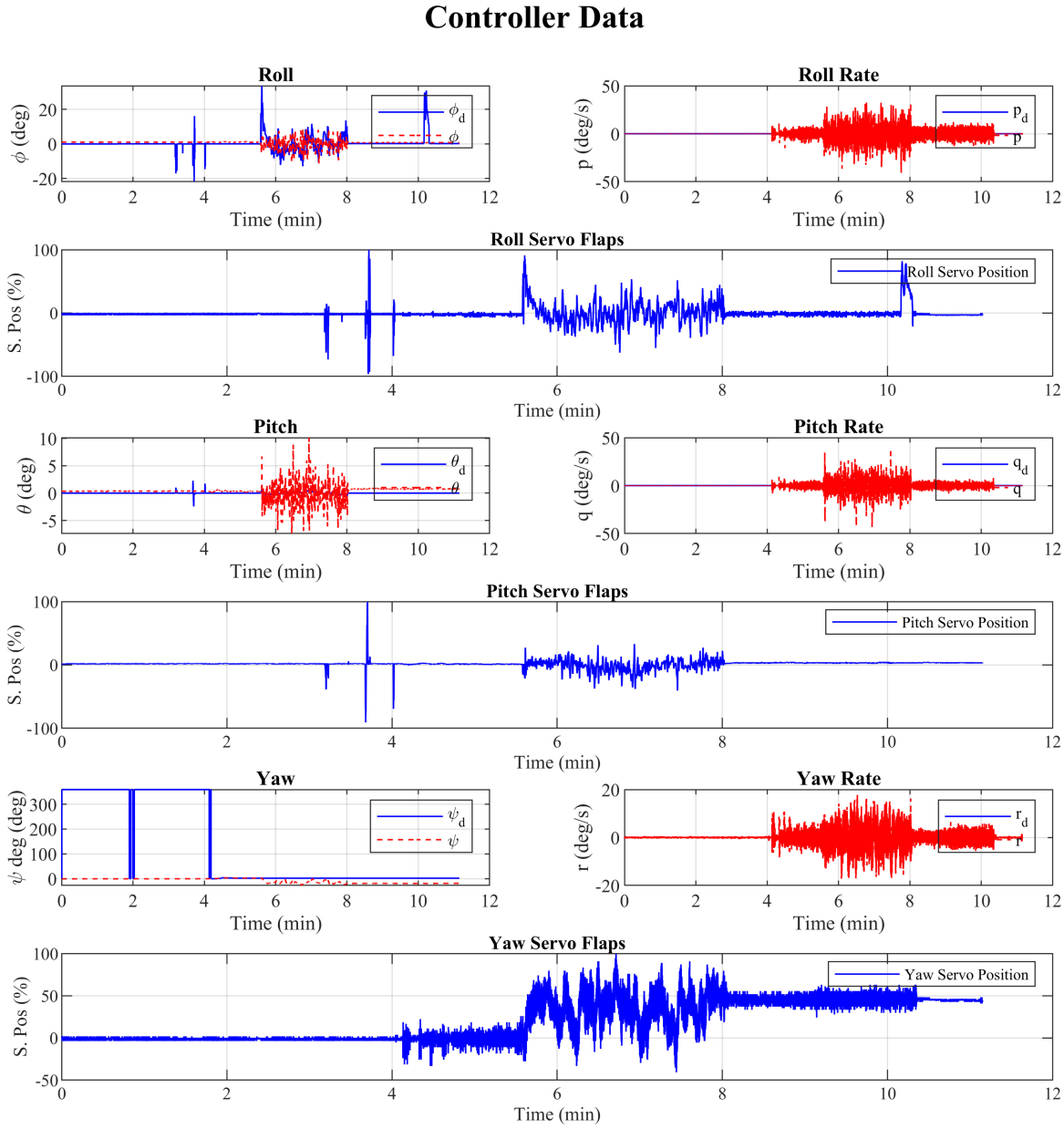

Fig. 11. Real Flight: Attitude controller performance during a hover flight, enhanced by TVC utilizing flap vanes to stabilize the system against uncertainties applied on the yaw loop.

vanes and four sets of servo flaps are deemed optimal for achieving peak performance.

5.1. *Simulation results*

Building upon previous research [9], the simulation process is conducted within the dynamic space of Gazebo on Ubuntu 18.04. The flap vanes joints were modeled as cylindrical bars connected to servo-simulated springs, incorporating presumed bandwidth and amplitude gain margins. Further details about the codified components models are available in [8, 9]. In the subsequent analysis, two figures illustrate the outcomes of two cruise flights conducted by the heavy Wild Hopper model over approximately 40 minutes for comparison. Figure 9 showcases the controller performance of a finely tuned PID controller. The top part depicts the altitude compared to the desired altitude, revealing a noticeable but manageable error. On the right, the total thrust of all propellers is presented, while the 3D plot illustrates the drone's trajectory throughout the flight. Zooming in on the movements, a five-line polygon of waypoints was

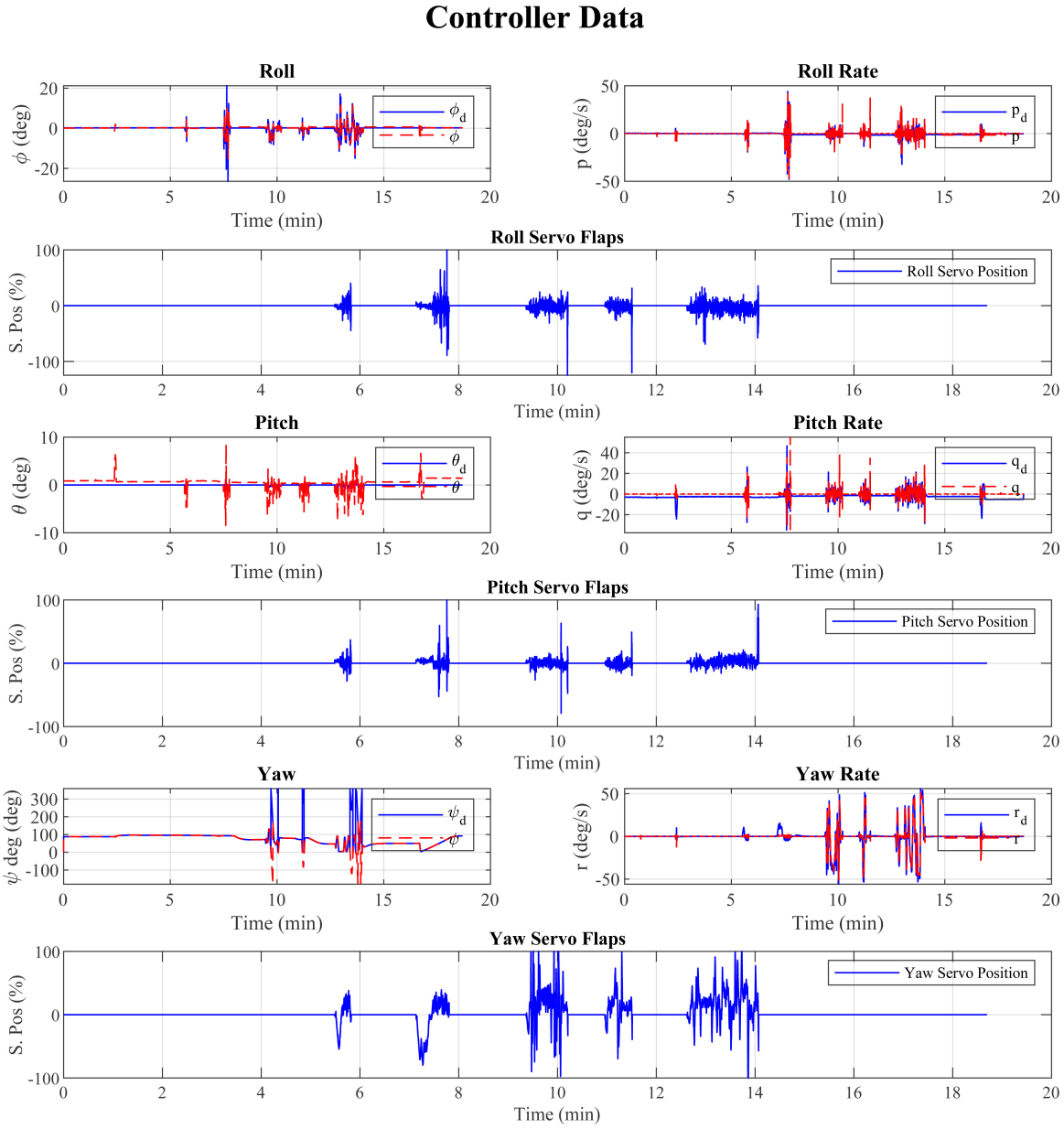

Fig. 12. Real Flight: Attitude controller performance during a hover flight, enhanced by TVC utilizing flap vanes to stabilize the system against uncertainties applied on the roll and pitch loops.

defined to observe attitude performance at turning points. Over time, trajectory errors accumulate in the integrator, especially at turning points. However, these errors diminished thanks to the cascade loop compensating for the deviated lines. Notably, some errors emerged during ascents since the waypoints were not horizontally aligned. This indicates that the PID controller struggled to stabilize effectively when altitude changes occurred simultaneously. Nevertheless, it demonstrated merely acceptable results during hover and cruise flights.

The second simulation flight utilized the robust method introduced in this paper. As depicted in "Fig. 10", the overall flight trajectory mirrors that of the PID controller. In this simulation, a rectangular flight plan was initially executed. However, halfway through the flight, the rectangle underwent a 20-degree horizontal rotation to assess potential controller parameter accumulation. Remarkably, the controller effectively stabilized the flight, showcasing minimal attitude errors in the roll, pitch, and yaw loops. In contrast to the PID controller, this time the ascending phase was

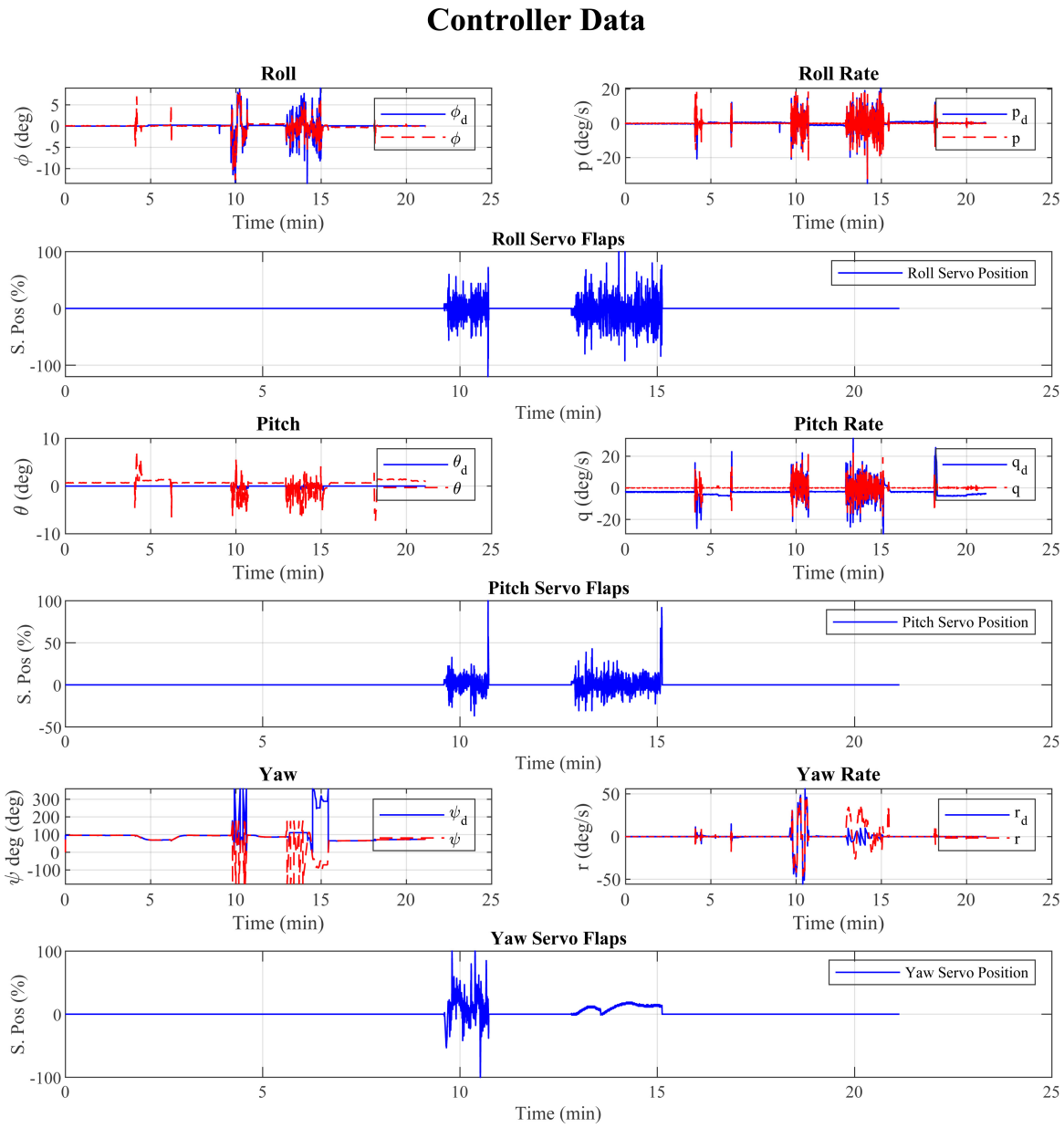

Fig. 13. Real Flight: Attitude controller performance during a cruise flight with a rectangular trajectory, enhanced by TVC utilizing flap vanes to stabilize the system against uncertainty applied on the roll and pitch loops.

more intense, and unexpectedly, moments of instability occurred during ascent that were beyond the controller's immediate control. However, the drone's swift movements effectively compensated for the instability, ensuring a safe landing.

5.2. *Real-world flight experiments*

Crucially, the practical tests incorporated the utilization of fine-tuned SMC parameters. These parameters were meticulously adjusted to guarantee precise control and steadfast stability in real-world flight scenarios, as defined in "Eqs. (22)" and detailed in "Table 1".

Hence, the parameter values presented in "Table 1" align with the AP employed during the flights, known as the Micropilot with dual CPU capabilities. Prior to the flights, rigorous examinations of the attitude controller applied to the AP were performed under stationary conditions. To facilitate the integration of these parameters into the AP's primary control loop, special Extender licenses were

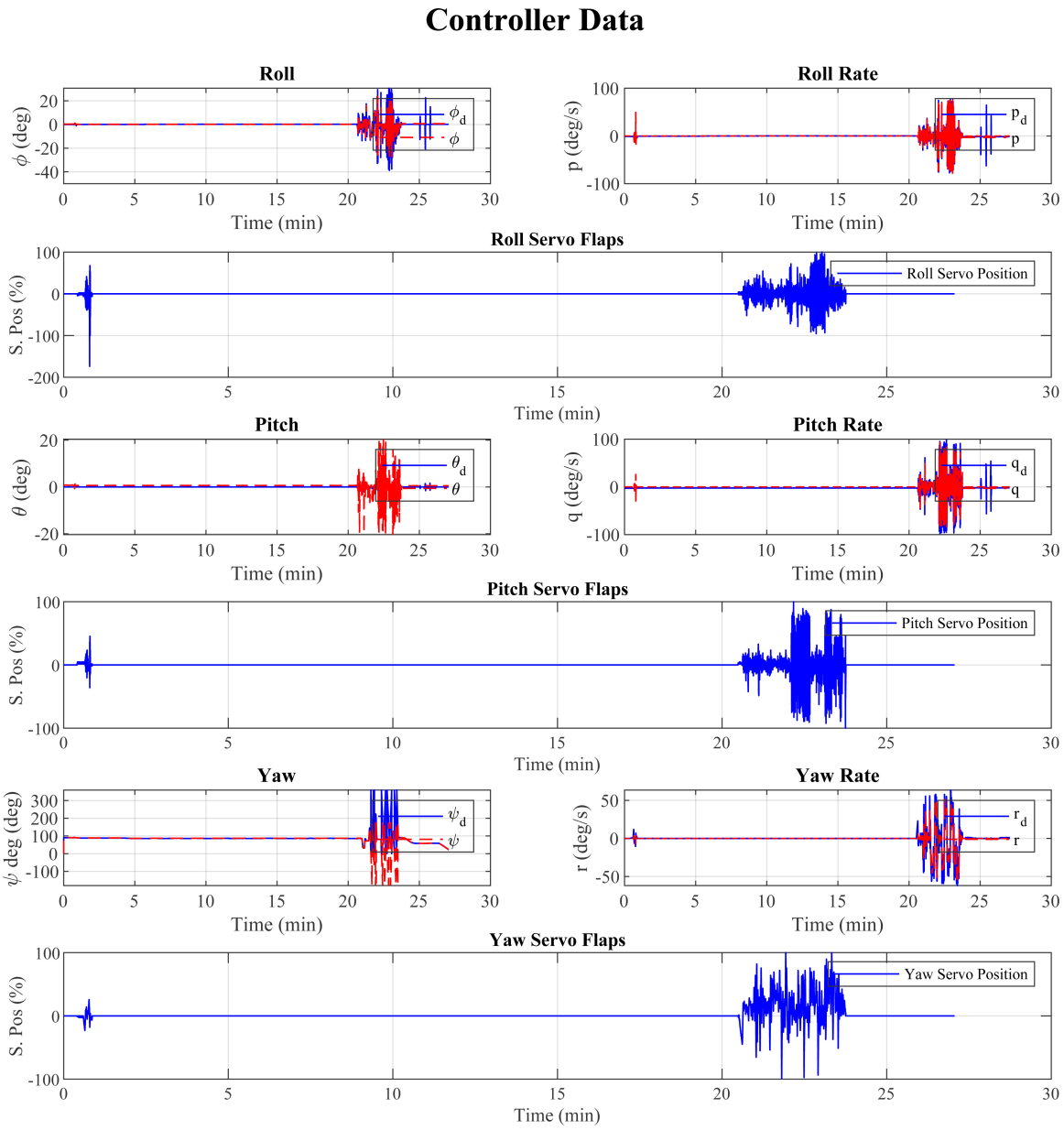

Fig. 14. Real Flight: Attitude controller performance during a cruise flight with a rectangular trajectory, enhanced by TVC utilizing flap vanes to stabilize the system against uncertainties applied on the yaw loop.

acquired, enabling the configuration of the firmware code and parameter adjustments through the Horizon user interface. Additionally, a simple plugin was developed within the application to facilitate parameter modification and tuning.

All the presented results share a common timeframe, with flight durations ranging from 11 to 27 min. These experiments primarily assess the efficiency of the attitude controller, with the position loop intentionally excluded from consideration. To aid clarity and ease of interpretation, we also include the rates of the Euler angles in our results, with a specific focus on the changes in roll, pitch, and yaw servo flap positions, presented in an comprehensive diagrams. Furthermore, it is important to note that the random noise equation employed for all flights remains consistent, as previously discussed in [9], and is consistently applied in the context of this research.

The first result illustrated in "Fig. 11", pertains to a brief hovering flight sequence. During this flight, we intentionally introduced random noise into the yaw controller loop for 60 ms, occurring in both the second and fourth minutes of the flight. The impact of this noise propagation is evident between the sixth and eighth minutes. However, as our diagrams vividly illustrate, the controller effectively managed this uncertainty, demonstrating its capability to stabilize the attitude even in the face of unexpected challenges.

The second flight, as shown in "Fig. 12", lasting approximately 19 min, featured two instances of random nonlinearity application during an almost hover flight, coupled with a few angle-turning trajectories. These nonlinearities were introduced once in the roll loop and once in the pitch loop. Notably, the overall system promptly re-established regulation. However, in the yaw loop, some interference became apparent due to accumulated errors introduced during the extended duration of the flight. In this instance, the adaptive parameters struggled to fine-tune the loop. Importantly, it is worth noting that the interference, while observable, remained within predefined limits as the yaw angle remained saturated.

The third flight, illustrated in "Fig. 13", comprised a 22-min cruise phase during which random noise was deliberately introduced into both the roll and pitch control loops. These uncertainties manifested as brief, 50-ms disturbances, with one occurring in the roll loop during the tenth minute and another in the pitch loop during the fifteenth minute of the flight. The results of this flight demonstrate the system's impressive recovery and adaptability, with adaptive parameters promptly adjusted before and during the flight to restore stability. This flight was extended to observe the assessment of accumulated errors in the yaw control loop. As depicted in the figure, the yaw rate effectively compensated for the nonlinearity, leading to a rapid decrease in yaw loop disturbances, highlighting the effectiveness of the system's adaptive capabilities.

The last flight, depicted in "Fig. 14", lasted for 27 min, following a rectangular trajectory. During the flight, a high noise was applied to the yaw loop precisely at the moment when the aircraft was making a turn within the rectangular path to evaluate the controller's performance under challenging conditions. As evident from the plots, the noise disturbance was applied at the 20th minute, leading to a response from the system that involved the coordinated use of both roll and pitch servo flaps. This cooperative action was necessary to counteract the nonlinearity observed in the system's behavior. Remarkably, the system successfully recovered within a minute, allowing the flight to continue without further issues.

6. Conclusions and Future Work

This paper consolidates three previous research efforts by the authors, introducing a novel controller state vector tailored for Multi-Ducted Fan (MDF) systems. The primary objective is to evaluate the effectiveness of an ARAC when applied to this specific system, employing a Thrust Vector Control (TVC) strategy through flap vanes and servo flaps at the duct's exhaust to regulate MDF attitude behavior. Brief dynamic equations are formulated to understand airflow dynamics, duct interaction, and the aerodynamic forces and moments involved in controller actuators. The controller's key concepts are outlined, and multiple flight tests assess its performance amid random disturbances, encompassing hover flights with roll, pitch, and yaw loop disturbances and cruise flights with attitude loop and servo flap disturbances. Outcomes demonstrate a satisfactory controller response in real flight scenarios, with the potential for further enhancements in industrial applications and varying temperature conditions. It is worth mentioning that TVC's adaptability and precise control make it an invaluable asset for heavy UAVs in various industrial settings to enhance maneuverability, improve stability, and the capability to counteract disturbances encountered during missions effectively. In future work, a focus will be placed on the enhancement of flap vane efficiency, with particular attention given to the optimization of their geometric profiles. The aim is to reduce drag and eliminate the need for auxiliary vanes, achieved through the integration of both lateral and longitudinal vane components, enabling the generation of yaw moments via diagonal vane rotation.

Acknowledgments

We would like to thank the University of Carlos III, campus Leganes, Madrid, for performing laboratories and hangers

through our research. We would also like to thank our colleagues at Drone Hopper for their support during the project. This work was conducted to complete the doctoral project of Mohammad Sadeq Ale Isaac with the support of Professor Pascual Campoy, and Doctor Ahmed Refaat Ragab. This work was supported by the ULTRADRON Project, funded by CDTI under the call number PTAP-20231017, focused on "Enabling Technologies for an Intelligent Logistics Unit with Drone Technology" and by the project INSERTION ref. ID2021-127648OBC32, "UAV Perception, Control and Operation in Harsh Environments," funded by the Spanish Ministry of Science and Innovation under the program "Projects for Knowledge Generating."

ORCID

Mohammad Sadeq Ale Isaac https://orcid.org/0000-0001-8773-7184
Pablo Flores Peña https://orcid.org/0009-0005-7219-6879
Marco Andrés Luna https://orcid.org/0000-0003-1036-7538
Ahmed Refaat Ragab https://orcid.org/0000-0002-6897-6048
Pascual Campoy https://orcid.org/0000-0002-9894-2009

References

[1] K. L. N. C. Prakash, S. K. Ravva, M. Rathnamma and G. Suryanarayana, AI applications of drones, in *Drone Technology: Future Trends and Practical Applications* (Wiley, 2023), pp. 153–182.
[2] Office of the Secretary of Defense, Unmanned aircraft systems roadmap: 2005–2030 (2005).
[3] T. Elmokadem and A. V. Savkin, Towards fully autonomous UAVs: A survey, *Sensors* **21**(18) (2021) 6223.
[4] S. A. H. Mohsan, N. Q. H. Othman, Y. Li, M. H. Alsharif and M. A. Khan, Unmanned aerial vehicles (UAVs): Practical aspects, applications, open challenges, security issues, and future trends, *Intell. Serv. Robot.* **16**(1) (2023) 109–137.
[5] A. I. Abrego, R. W. Bulaga and M. Rutkowski, Performance study of a ducted fan system, *American Helicopter Society Aerodynamics, Acoustics and Test and Evaluation Technical Specialists Meeting* (California, USA, 2002).
[6] A. Ko, O. Ohanian and P. Gelhausen, Ducted fan uav modeling and simulation in preliminary design, *AIAA Modeling and Simulation Technologies Conf. Exhibit* (2007), p. 6375.
[7] L. González-deSantos, News applications of UAVs for infrastructure monitoring: Contact inspection systems, *Eng. Proc.* **17**(1) (2022) 23.
[8] M. S. Ale Isaac, M. A. Luna, A. R. Ragab, M. M. Ale Eshagh Khoeini, R. Kalra, P. Campoy, P. Flores Peña and M. Molina, Medium-scale UAVs: A practical control system considering aerodynamics analysis, *Drones* **6**(9) (2022) 244.
[9] M. S. Ale Isaac, A. R. Ragab, M. A. Luna, M. M. Ale Eshagh Khoeini and P. Campoy, Thrust vectoring control for heavy UAVS, employing a redundant communication system, *Sensors* **23**(12) (2023) 5561.
[10] Y. Zeng, R. Zhang and T. J. Lim, Throughput maximization for UAV-enabled mobile relaying systems, *IEEE Trans. Commun.* **64**(12) (2016) 4983–4996.
[11] V. U. Castrillo, A. Manco, D. Pascarella and G. Gigante, A review of counter-UAS technologies for cooperative defensive teams of drones, *Drones* **6**(3) (2022) 65.
[12] M. Muehlebach and R. D'Andrea, The flying platform–a testbed for ducted fan actuation and control design, *Mechatronics* **42** (2017) 52–68.
[13] N. Wang, S.-F. Su, M. Han and W.-H. Chen, Backpropagating constraints-based trajectory tracking control of a quadrotor with constrained actuator dynamics and complex unknowns, *IEEE Trans. Syst. Man, Cybern. Syst.* **49**(7) (2018) 1322–1337.
[14] T. Manzoor, Z. Sun, Y. Xia and D. Ma, Mpc based compound flight control strategy for a ducted fan aircraft, *Aerosp. Sci. Technol.* **107** (2020) 106264.
[15] D. Invernizzi and M. Lovera, Trajectory tracking control of thrust-vectoring UAVs, *Automatica* **95** (2018) 180–186.
[16] M. Labbadi and M. Cherkaoui, Robust adaptive backstepping fast terminal sliding mode controller for uncertain quadrotor UAV, *Aerosp. Sci. Technol.* **93** (2019) 105306.
[17] E. Tobias and J. Horn, Simulation analysis of the controllability of a tandem ducted fan aircraft, *AIAA Atmospheric Flight Mechanics Conf. Exhibit* (2008), p. 6700.
[18] W. Fan, B. Xu, Y. Zhang, S. Tang and C. Xiang, Adaptive fault-tolerant control of a novel ducted-fan aerial robot against partial actuator failure, *Aerosp. Sci. Technol.* **122** (2022) 107371.
[19] H. Jiang, Y. Zhou, H. W. Ho and W. Hu, Adaptive model predictive control for engine-driven ducted fan lift systems using an associated linear parameter varying model, arXiv:2309.12552.
[20] Z.-H. Cheng and H.-L. Pei, Control effectiveness enhancement for the hovering/cruising transition control of a ducted fan UAV, *J. Intell. Robot. Syst.* **105**(4) (2022) 89.
[21] Z. Cheng and P. Hailong, A corridor-based flight mode transition strategy for agile ducted-fan tail-sitter UAV: Altitude-hold transition, *Chin. J. Aeronaut.* **36**(9) (2023) 330–345.
[22] M. Miwa, Y. Shigematsu and T. Yamashita, Control of ducted fan flying object using thrust vectoring, *J. Syst. Des. Dyn.* **6**(3) (2012) 322–334.
[23] B. Xu, X. Wang, C. Xiang, Y. Ma and W. Chen, Modelling and hovering control of a novel multi-tandem ducted fan vehicle, *2015 Int. Conf. Unmanned Aircraft Systems (ICUAS)* (IEEE, 2015), pp. 1346–1354.
[24] W. Fan, C. Xiang and B. Xu, Modelling, attitude controller design and flight experiments of a novel micro-ducted-fan aircraft, *Adv. Mech. Eng.* **10**(3) (2018), doi: 1687814018765569.
[25] K. Feng, J. Ji, Y. Zhang, Q. Ni, Z. Liu and M. Beer, Digital twin-driven intelligent assessment of gear surface degradation, *Mech. Syst. Signal Process.* **186** (2023) 109896.
[26] K. Feng, J. Ji, Q. Ni, Y. Li, W. Mao and L. Liu, A novel vibration-based prognostic scheme for gear health management in surface wear progression of the intelligent manufacturing system, *Wear* **522** (2023) 204697.
[27] A. Townsend, I. N. Jiya, C. Martinson, D. Bessarabov and R. Gouws, A comprehensive review of energy sources for unmanned aerial vehicles, their shortfalls and opportunities for improvements, *Heliyon* **6**(11) (2020).
[28] G. Wang, W. Samarathunga and S. Wang, Uninterruptible power supply design for heavy payload tethered hexaroters, *Int. J Emerg. Eng. Res. Technol.* **4**(2) (2016) 16–21.
[29] M. Adamski, Analysis of propulsion systems of unmanned aerial vehicles, *J. Marine Eng. Technol.* **16**(4) (2017) 291–297.

[30] M. S. A. Isaac, A. R. Ragab, E. C. Garcés, M. A. Luna, P. F. Peña and P. C. Cervera, Mathematical modeling and designing a heavy hybrid-electric quadcopter, controlled by flaps, *Unmanned Syst.* **10**(3) (2022) 241–253.
[31] J. Jeong, S. Kim and J. Suk, Control performance analysis on variable configuration of ducted-fan flight array, *Int. J. Aeronaut. Space Sci.* **21** (2020) 524–537.
[32] S. B. F. Asl and S. S. Moosapour, Adaptive backstepping fast terminal sliding mode controller design for ducted fan engine of thrust-vectored aircraft, *Aerosp. Sci. Technol.* **71** (2017) 521–529.
[33] C. Chen, T. Dong, W. Fu and N. Liu, On dynamic characteristics and stability analysis of the ducted fan unmanned aerial vehicles, *Int. J. Adv. Robot. Syst.* **16**(4) (2019), doi: 1729881419867018.
[34] J. Jeong *et al.*, Control system design for a ducted-fan unmanned aerial vehicle using linear quadratic tracker, *Int. J. Aerosp. Eng.* **2015** (2015) 364926.
[35] J. Yu, A. Jadbabaie, J. Primbs and Y. Huang, Comparison of nonlinear control design techniques on a model of the caltech ducted fan, *Automatica* **37**(12) (2001) 1971–1978.
[36] C. R. Kothari, *Research Methodology: Methods and Techniques* (New Age International, 2004).
[37] A. T. Bahill and B. Gissing, Re-evaluating systems engineering concepts using systems thinking, *IEEE Trans. Syst. Man Cybern. C (Appl. Rev.)* **28**(4) (1998) 516–527.
[38] B. W. Boehm, A spiral model of software development and enhancement, *Computer* **21**(5) (1988) 61–72.
[39] S. Shan, Z. Hou and S. Wang, Controller design and experiment of the ducted-fan flying robot, *2016 IEEE Int. Conf. Robotics and Biomimetics (ROBIO)* (IEEE, 2016), pp. 1852–1857.
[40] Y. Wang, C. Xiang, Y. Ma and B. Xu, Comprehensive nonlinear modeling and simulation analysis of a tandem ducted fan aircraft, in *Proc. 2014 IEEE Chinese Guidance, Navigation and Control Conf.* (IEEE (2014), pp. 255–261.
[41] W. Xiaoliang, C. Xiang, H. Najjaran and X. Bin, Robust adaptive fault-tolerant control of a tandem coaxial ducted fan aircraft with actuator saturation, *Chin. J. Aeronaut.* **31**(6) (2018) 1298–1310.
[42] Y. Zhang, C. Xiang, B. Xu, X. Wang and W. Fan, Comprehensive nonlinear modeling and attitude control of a novel tandem ducted fan vehicle, *2016 IEEE Int. Conf Aircraft Utility Systems (AUS)* (IEEE, 2016), pp. 50–56.
[43] H. Zhao, Development of a dynamic model of a ducted fan VTOL UAV, PhD thesis, RMIT University (2009).
[44] E. N. Johnson and M. A. Turbe, Modeling, control, and flight testing of a small-ducted fan aircraft, *J. Guid. Control Dyn.* **29**(4) (2006) 769–779.
[45] S. A. Emami and A. Banazadeh, Robustness investigation of a ducted-fan aerial vehicle control, using linear, adaptive, and model predictive controllers, *Int. J. Adv. Mechatron. Syst.* **6**(2–3) (2015) 108–117.

Mohammad Sadeq Ale Isaac received his M.S. and B.S. degrees from the University of Amirkabir, AUTMAV Laboraroy, and Khajenasir in 2019 and 2015, respectively. Currently, he is nearing completion of his PhD at the Centre for Automation and Robotics (CAR), Universidad Politécnica de Madrid (UPM-CSIC). He is the author of over 10 technical publications, proceedings, editorials, and books. Currently, he works in Wake-Eng as a flight dynamics engineer and ground control station visual interface software engineer. His research interests include Flight Dynamics, Nonlinear Control or UAVs, and Robotic Application topics.

Pablo Flores Peña is Aeronautical engineer and the CEO and CTO of the Drone Hopper Company, Madrid, Spain. He created the research center at Drone Hopper Company. Also, he holds IE MBA. He has more than 15 years of experience as Chief Engineer at Airbus Company.

Marco Andrés Luna is Ph.D. candidate at the Centre for Automation and Robotics (CAR), Universidad Politcnica de Madrid (UPM-CSIC) and SW engineer at Ahyres Company, Madrid, Spain. He obtained his B.S. degree in automation and control engineering from Universidad de las Fuerzas Armadas ESPE and his B.S. degree in automatic and robotics from the Polytechnic University of Madrid.

Ahmed Refaat Ragab is Postdoctoral Researcher at the University of Carlos III, and Drone Hopper Company, Madrid, Spain. He is a lecturer at October 6 University, Egypt. He was graduated from Air Defense College, Alexandria, Egypt. His field of interest is Unmanned Aerial Systems.

Pascual Campoy Cervera is Professor at the Higher Technical School of Industrial Engineers of the Polytechnic University of Madrid. He is the head of the research group "Vision for Unmanned Aerial Vehicles (UAVs)" of the Department of Automation, Electrical Engineering and Electronics and Industrial Informatics of the Centre for Automation and Robotics (CAR), Universidad Politécnica de Madrid (UPM-CSIC). The objective of his research group is to provide unmanned systems with greater autonomy through the use of computer vision techniques.

References

Abrego, A. I., Bulaga, R. W., & Rutkowski, M. (2002). Performance study of a ducted fan system. *American Helicopter Society Aerodynamics, Acoustics and Test and Evaluation Technical Specialists Meeting*.

Ale Isaac, M. S., Flores Pena, P., Andres Luna, M., Refaat Ragab, A., & Campoy, P. (2024). Sensing and control integration for thrust vectoring in heavy uavs: Real-world implementation and performance analysis. *Unmanned Systems*.

Ale Isaac, M. S., Luna, M. A., Ragab, A. R., Ale Eshagh Khoeini, M. M., Kalra, R., Campoy, P., Flores Peña, P., & Molina, M. (2022). Medium-scale uavs: A practical control system considering aerodynamics analysis. *Drones*, *6*(9), 244.

Ale Isaac, M. S., Ragab, A. R., Luna, M. A., Ale Eshagh Khoeini, M. M., & Campoy, P. (2023). Thrust vectoring control for heavy uavs, employing a redundant communication system. *Sensors*, *23*(12), 5561.

Andrievsky, B. R., Churilov, A. N., & Fradkov, A. L. (1996). Feedback kalman-yakubovich lemma and its applications to adaptive control. *Proceedings of 35th IEEE Conference on Decision and Control*, *4*, 4537–4542.

Asl, S. B. F., & Moosapour, S. S. (2017). Adaptive backstepping fast terminal sliding mode controller design for ducted fan engine of thrust-vectored aircraft. *Aerospace Science and Technology*, *71*, 521–529.

Bahill, A. T., & Gissing, B. (1998). Re-evaluating systems engineering concepts using systems thinking. *IEEE Transactions on Systems, Man, and Cybernetics, Part C (Applications and Reviews)*, *28*(4), 516–527.

Bin Junaid, A., Konoiko, A., Zweiri, Y., Sahinkaya, M. N., & Seneviratne, L. (2017). Autonomous wireless self-charging for multi-rotor unmanned aerial vehicles. *energies*, *10*(6), 803.

Boehm, B. W. (1988). A spiral model of software development and enhancement. *Computer*, *21*(5), 61–72.

Cabanas, M. F., Duque, S. B., González, J. D., González, F. P., & Fernández, M. G. (2021). Preliminary results of a hybrid thermoelectric propulsion system for a multirotor uas with active rectifying, electronic throttle control and supercapacitors. *Applied Sciences*, *11*(17), 7899.

Castrillo, V. U., Manco, A., Pascarella, D., & Gigante, G. (2022). A review of counter-uas technologies for cooperative defensive teams of drones. *Drones*, *6*(3), 65.

Chen, C., Dong, T., Fu, W., & Liu, N. (2019). On dynamic characteristics and stability analysis of the ducted fan unmanned aerial vehicles. *International Journal of Advanced Robotic Systems*, *16*(4), 1729881419867018.

Deutsch, C., Meneghini, C., Mermut, O., & Lefort, M. (2010). Measuring technology readiness to improve innovation management. *Proc. of The XXI ISPIM Conference*.

Dronetools. (2021). *Dronetools*. Retrieved April 3, 2021, from https://www.dronetools.es/

Elmokadem, T., & Savkin, A. V. (2021). Towards fully autonomous uavs: A survey. *Sensors*, *21*(18), 6223.

Emami, S. A., & Banazadeh, A. (2015). Robustness investigation of a ducted-fan aerial vehicle control, using linear, adaptive, and model predictive controllers. *International Journal of Advanced Mechatronic Systems*, *6*(2-3), 108–117.

Fan, W., Xiang, C., & Xu, B. (2018). Modelling, attitude controller design and flight experiments of a novel micro-ducted-fan aircraft. *Advances in Mechanical Engineering*, *10*(3), 1687814018765569.

Foxtech nova 2400 generator. (n.d.). Retrieved April 3, 2021, from https://www.foxtechfpv.com/foxtech-nova-2400-generator.html

González-deSantos, L. (2022). News applications of uavs for infrastructure monitoring: Contact inspection systems. *Engineering Proceedings*, *17*(1), 23.

Isaac, M. S. A., Ragab, A. R., Garcés, E. C., Luna, M. A., Peña, P. F., & Cervera, P. C. (2022). Mathematical modeling and designing a heavy hybrid-electric quadcopter, controlled by flaps. *Unmanned Systems*, *10*(03), 241–253.

Jeong, J., Kim, S., Suk, J., et al. (2015). Control system design for a ducted-fan unmanned aerial vehicle using linear quadratic tracker. *International Journal of Aerospace Engineering*, *2015*.

Jeong, J., Kim, S., & Suk, J. (2020). Control performance analysis on variable configuration of ducted-fan flight array. *International Journal of Aeronautical and Space Sciences*, *21*, 524–537.

Johnson, E. N., & Turbe, M. A. (2006). Modeling, control, and flight testing of a small-ducted fan aircraft. *Journal of guidance, control, and dynamics*, *29*(4), 769–779.

Ko, A., Ohanian, O., & Gelhausen, P. (2007). Ducted fan uav modeling and simulation in preliminary design. *AIAA modeling and simulation technologies conference and exhibit*, 6375.

Kothari, C. R. (2004). *Research methodology: Methods and techniques*. New Age International.

LNC Prakash, K., Ravva, S. K., Rathnamma, M., & Suryanarayana, G. (2023). Ai applications of drones. *Drone Technology: Future Trends and Practical Applications*, 153–182.

Miwa, M., Shigematsu, Y., & Yamashita, T. (2012). Control of ducted fan flying object using thrust vectoring. *Journal of System Design and Dynamics*, *6*(3), 322–334.

Mohsan, S. A. H., Othman, N. Q. H., Li, Y., Alsharif, M. H., & Khan, M. A. (2023). Unmanned aerial vehicles (uavs): Practical aspects, applications, open challenges, security issues, and future trends. *Intelligent Service Robotics*, *16*(1), 109–137.

Muehlebach, M., & D'Andrea, R. (2017). The flying platform–a testbed for ducted fan actuation and control design. *Mechatronics*, *42*, 52–68.

Naldi, R., Gentili, L., Marconi, L., & Sala, A. (2010). Design and experimental validation of a nonlinear control law for a ducted-fan miniature aerial vehicle. *Control Engineering Practice*, *18*(7), 747–760.

of the Secretary of Defense, O. (2005). Unmanned aircraft systems roadmap: 2005–2030.

Parshin, A., Morozov, V., Snegirev, N., Valkova, E., & Shikalenko, F. (2021). Advantages of gamma-radiometric and spectrometric low-altitude geophysical surveys by unmanned aerial systems with small scintillation detectors. *Applied Sciences*, *11*(5), 2247.

Peña, P. F., Ragab, A. R., Luna, M. A., Isaac, M. S. A., & Campoy, P. (2022). Wild hopper: A heavy-duty uav for day and night firefighting operations. *Heliyon*, *8*(6).

Ragab, A. R., Isaac, M. S. A., Luna, M. A., & Flores Peña, P. (2021). Wild hopper prototype for forest firefighting. *International Journal of Online & Biomedical Engineering*, *17*(9).

Ronchi, D., Limongiello, M., & Barba, S. (2020). Correlation among earthwork and cropmark anomalies within archaeological landscape investigation by using lidar and multispectral technologies from uav. *Drones*, *4*(4), 72.

Sadin, S. R., Povinelli, F. P., & Rosen, R. (1989). The nasa technology push towards future space mission systems. In *Space and humanity* (pp. 73–77). Elsevier.

Shan, S., Hou, Z., & Wang, S. (2016). Controller design and experiment of the ducted-fan flying robot. *2016 IEEE International Conference on Robotics and Biomimetics (ROBIO)*, 1852–1857.

Tobias, E., & Horn, J. (2008). Simulation analysis of the controllability of a tandem ducted fan aircraft. *AIAA atmospheric flight mechanics conference and exhibit*, 6700.

Townsend, A., Jiya, I. N., Martinson, C., Bessarabov, D., & Gouws, R. (2020). A comprehensive review of energy sources for unmanned aerial vehicles, their shortfalls and opportunities for improvements. *Heliyon*, *6*(11).

Viera-Torres, M., Sinde-González, I., Gil-Docampo, M., Bravo-Yandún, V., & Toulkeridis, T. (2020). Generating the baseline in the early detection of bud rot and red ring disease in oil palms by geospatial technologies. *Remote Sensing*, *12*(19), 3229.

Wang, Y., Xiang, C., Ma, Y., & Xu, B. (2014). Comprehensive nonlinear modeling and simulation analysis of a tandem ducted fan aircraft. *Proceedings of 2014 IEEE Chinese Guidance, Navigation and Control Conference*, 255–261.

Xiaoliang, W., Xiang, C., Najjaran, H., & Bin, X. (2018). Robust adaptive fault-tolerant control of a tandem coaxial ducted fan aircraft with actuator saturation. *Chinese Journal of Aeronautics*, *31*(6), 1298–1310.

Xu, B., Wang, X., Xiang, C., Ma, Y., & Chen, W. (2015). Modelling and hovering control of a novel multi-tandem ducted fan vehicle. *2015 International conference on unmanned aircraft systems (ICUAS)*, 1346–1354.

Yu, J., Jadbabaie, A., Primbs, J., & Huang, Y. (2001). Comparison of nonlinear control design techniques on a model of the caltech ducted fan. *Automatica*, *37*(12), 1971–1978.

Zeng, Y., Zhang, R., & Lim, T. J. (2016). Throughput maximization for uav-enabled mobile relaying systems. *IEEE Transactions on communications*, *64*(12), 4983–4996.

Zhang, Y., Xiang, C., Xu, B., Wang, X., & Fan, W. (2016). Comprehensive nonlinear modeling and attitude control of a novel tandem ducted fan vehicle. *2016 IEEE International Conference on Aircraft Utility Systems (AUS)*, 50–56.

Zhang, Y., Xiang, C., Xu, B., Wang, Y., & Wang, X. (2018). Design and implementation of a novel aerial manipulator with tandem ducted fans. *2018 IEEE/RSJ International Conference on Intelligent Robots and Systems (IROS)*, 4210–4217.

Zhang, Y., Xu, B., Xiang, C., Fan, W., & Ai, T. (2020). Flight and interaction control of an innovative ducted fan aerial manipulator. *Sensors*, *20*(11), 3019.

Zhao, H. (2009). *Development of a dynamic model of a ducted fan vtol uav* [Doctoral dissertation, RMIT University].

Annexes

A Scientific Dissemination

This appendix presents a list of related scientific contributions provided during the development of this thesis. Several scientific contributions have been provided through publications in well-known scientific journals and conferences, as given below:

A.1 Journals

Ale Isaac, M.S., Flores Pena, P., Andres Luna, M., Refaat Ragab, A., and Campoy, P. (2024). *Sensing and Control Integration for Thrust Vectoring in Heavy UAVs: Real-World Implementation and Performance Analysis.* Unmanned Systems, doi:10.1142/S2301385025500396.

Ale Isaac, M.S., Ragab, A.R., Luna, M.A., Ale Eshagh Khoeini, M.M., and Campoy, P. (2023). *Thrust Vectoring Control for Heavy UAVs, Employing a Redundant Communication System.* Sensors, 23(12), p.5561, doi:10.3390/s23125561.

Ale Isaac, M.S., Luna, M.A., Ragab, A.R., Ale Eshagh Khoeini, M.M., Kalra, R., Campoy, P., Flores Peña, P., and Molina, M. (2022). *Medium-Scale UAVs: A Practical Control System Considering Aerodynamics Analysis.* Drones, 6(9), p.244, doi:10.3390/drones6090244.

Isaac, M.S.A., Ragab, A.R., Garcés, E.C., Luna, M.A., Peña, P.F., and Cervera, P.C. (2022). *Mathematical Modeling and Designing a Heavy Hybrid-Electric Quadcopter, Controlled by Flaps.* Unmanned Systems, 10(03), pp.241-253, doi:10.1142/S2301385022500133.

Luna, M.A., **Ale Isaac, M.S.**, Ragab, A.R., Campoy, P., Flores Peña, P., and Molina, M. (2022). *Fast Multi-Uav Path Planning for Optimal Area Coverage in Aerial Sensing Applications.* Sensors, 22(6), p.2297, doi:10.3390/s22062297.

Flores Peña, P. Luna, M.A., **Ale Isaac, M.S.**, Ragab, A.R., Elmenshawy, K., Martín Gómez, D., Campoy, P., and Molina, M. (2022). *A Proposed System for Multi-UAVs in Remote Sensing Operations.* Sensors, 22(23), p.9180, doi:10.3390/s22239180.

Flores Peña, P., Ragab, A.R., Luna, M.A., **Isaac, M.S.A.**, and Campoy, P. (2022). *WILD HOPPER: A heavy-duty UAV for Day and Night Firefighting Operations.* Heliyon,

8(6), p.e09588, doi:10.1016/j.heliyon.2022.e09588.

Ragab, A.R., **Isaac, M.S.A.**, Luna, M.A., and Flores Peña, P. (2021). *WILD HOPPER Prototype for Forest Firefighting.* International Journal of Online & Biomedical Engineering, 17(9), doi:10.3991/ijoe.v17i09.25205.

Ragab, A. R., Peña, P. F., Luna, M. A., and **Isaac, M.S.A.** (2022). *Systemic Integrated Unmanned Aerial System.* International Journal of Online & Biomedical Engineering, 18(1), doi:/10.3991/ijoe.v18i01.26435.

A.2 Conferences

Luna, M. A., **Isaac, M.S.A.**, Fernandez-Cortizas, M., Santos, C., Ragab, A. R., Molina, M., and Campoy, P. (2023). *Spiral Coverage Path Planning for Multi-UAV Photovoltaic Panel Inspection Applications.* In 2023 International Conference on Unmanned Aircraft Systems (ICUAS), p. 679-686, IEEE.

A. R. Ragab, M. S. Ale Isaac, M. A. Luna, and P. F. Peña. (2021). *Unmanned Aerial Vehicle Swarming.* 2021 International Conference on Engineering and Emerging Technologies (ICEET), Istanbul, Turkey, 2021, p. 1-6, doi:10.1109/ICEET53442.2021.9659698.

Isaac, M.S.A., Naghash, A., and Mirtajedini, S.H. (2019). *Control and Guidance of an Autonomous Quadrotor Landing Phase on a Moving Platform.* In Proceedings of the IMAV Annual Conference of Autonomous Vehicles, Madrid, Spain, vol. 29.

B Industrial Projects

The section presents the main projects executed using the proposed approaches presented in this thesis.

FASTER Project (First responder Advanced technologies for Safe and efficient Emergency Response) - H2020 International Project (Grant Agreement ID: 833507): The thesis contributed to this project by providing a suitable firefighting solution with a liquid heavy payload. Link: FASTER Project Details

WILDHOPPER - Long Autonomy Solution for Heavy Payloads (Grant Agreement ID: 880642): The primary objective of the thesis was to offer a long autonomy solution for heavy payloads. Link: WILDHOPPER Project Details

C Data Availability

This section provides the link to the data repository and video demonstrations of all the algorithms and approaches presented in this thesis.

Data 1

Data 2

D Technology Readiness Level (TRL)

This section provides a brief table of the general terms, definitions, and descriptions for TRLs used in the engineering process of the doctoral project.

Table 1: TRL definitions and descriptions.

TRL	Definition	Hardware Description	Software Description	Exit Criteria
1	Basic principles observed and reported.	Scientific knowledge generated underpinning hardware technology concepts/applications.	Scientific knowledge generated underpinning basic properties of software architecture and mathematical formulation.	Peer-reviewed publication of research underlying the proposed concept/application.
2	Technology concept and/or application formulated.	Invention begins, practical application is identified but is speculative, and no experimental proof or detailed analysis is available to support the conjecture.	Basic properties of algorithms, representations, and concepts defined. Basic principles coded. Experiments performed with synthetic data.	Documented description of the application/concept that addresses feasibility and benefit.
3	Analytical and experimental critical function proof-of-concept.	Analytical studies place the technology in an appropriate context and lab-oratory demonstrations, modeling and simulation validate analytical prediction.	Development of limited functionality to validate critical properties and predictions using non-integrated software components.	Documented analytical or experimental results validating predictions of key parameters.
4	Component and/or breadboard validation in a lab environment.	A low-fidelity system/component breadboard is built and operated to demonstrate basic functionality and critical test environments, and associated performance predictions are defined relative to the final operating environment.	Key, functionally critical, software components are integrated, and functionally validated, to establish interoperability and begin architecture development. Relevant Environments de-fined and performance in this environment predicted.	Documented test performance demonstrating agreement with analytical predictions and definition of relevant environment.
5	Component validation in a relevant environment.	A medium fidelity system/component brass board is built and operated to demonstrate overall performance in a simulated operational environment with realistic support elements that demonstrates overall performance in critical areas. Performance predictions are made for subsequent development phases.	End-to-end software elements implemented and interfaced with existing systems/simulations conforming to the target environment. The end-to-end software system, tested in a relevant environment, meeting predicted performance. Operational environment performance predicted. Prototype implementations developed.	Documented test performance demonstrating agreement with analytical predictions and definition of scaling requirements.
6	System/subsyste m model or prototype demonstrated in a relevant environment.	A high fidelity system/component prototype that adequately addresses all critical scaling issues is built and operated in a relevant environment to demonstrate operations under critical environmental conditions.	Prototype implementations of the software demonstrated on full-scale realistic problems. Partially integrated with existing hardware/software systems. Limited documentation is available, and engineering feasibility is fully demonstrated.	Documented test performance demonstrating agreement with analytical predictions.
7	System prototype demonstration in an operational environment.	A high fidelity engineering unit that adequately addresses all critical scaling issues is built and operated in a relevant environment to demonstrate performance in the actual operational environment and platform (ground, air-borne, or space).	Prototype software exists having all key functionality available for demonstration and testing. Well integrated with operational hardware/software systems demonstrating operational feasibility. Most software bugs are removed. Limited documentation is available.	Documented test performance demonstrating agreement with analytical predictions.
8	The actual system is completed and qualified through tests and demonstrations.	The final product in its final configuration is successfully demonstrated through test and analysis for its intended operational environment and platform.	All software has been thoroughly debugged and fully integrated with all operational hardware and software systems. All user documentation, training documentation, and maintenance documentation are completed. All functionality is successfully demonstrated in simulated operational scenarios. V&V completed.	Documented test performance verifying analytical predictions.
9	The actual system has been proven through successful operations.	The final product is successfully operated in an actual mission.	All software has been thoroughly debugged and fully integrated with all operational hardware/software systems. All documentation has been completed. Sustaining software engineering support is in place. The system has been successfully operated in the operational environment.	Documented mission operational results.